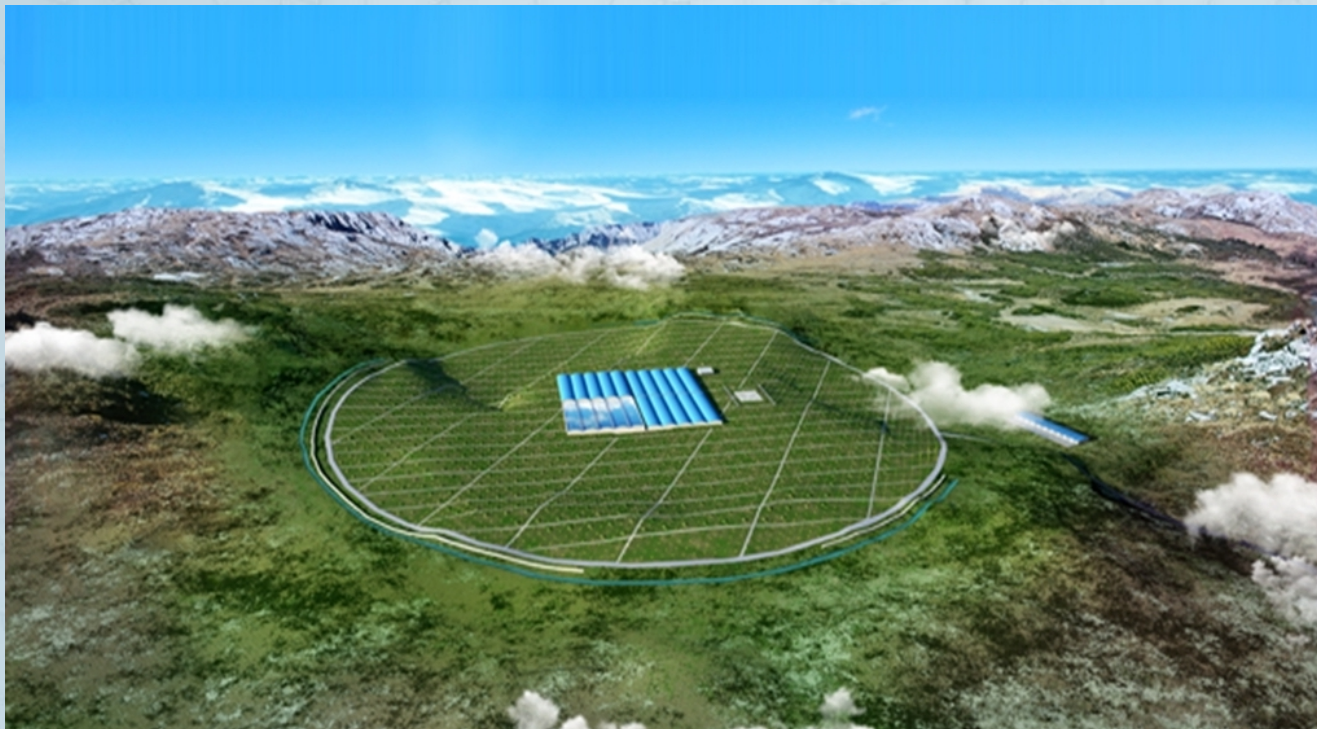




THE LARGE HIGH ALTITUDE AIR SHOWER OBSERVATORY

SCIENCE WHITE PAPER [☆]
(v3.2 DECEMBER 15, 2024)



December 15, 2024

X. Bai^{a,c}, B. Y. Bi^a, X. J. Bi^a, Z. Cao^{a,*}, S. Z. Chen^a, Y. Chen^r, A. Chiavassa^e, X. H. Cui^f, Z. G. Dai^g, D. della Volpe^{b,*}, T. Di Girolamo^{j,k}, Giuseppe Di Sciascio^u, Y. Z. Fan^h, J. Giacaloneⁱ, Y. Q. Guo^a, H. H. He^a, T. L. He^f, M. Heller^b, D. Huang^l, Y. F. Huang^g, H. Jia^l, L. T. Ksenofontovⁿ, D. Leahy^o, F. Li^h, Z. Li^{am,ag}, E. W. Liang^p, P. Lipari^q, R. Y. Liu^r, Y. Liu^s, S. Liu^h, X. Ma^a, O. Martineau-Huynh^m, D. Martraire^a, T. Montaruli^b, D. Ruffolo^t, Y. V. Stenkin^{v,w}, H. Q. Su^f, T. Tam^x, Q. W. Tang^y, W. W. Tian^f, P. Vallania^{z,aa}, S. Vernetto^d, C. Vigorito^{aa,ab}, J. C. Wang^{ak}, L. Z. Wang^f, X. Wang^{ac}, X. Y. Wang^{r,g}, X. J. Wang^l, Z. X. Wang^{ai}, D. M. Wei^h, J. J. Wei^h, D. Wu^f, H. R. Wu^a, X. F. Wu^h, D. H. Yan^{ak}, A. Y. Yang^f, R. Z. Yang^{aj}, Z. G. Yao^a, L. Q. Yin^a, Q. Yuan^h, Bing Zhang^{ae,af,ag}, B. Zhang^f, L. Zhang^{al}, M. F. Zhang^f, S. S. Zhang^a, X. Zhang^r, Yi Zhao^{a,ah}, X. X. Zhou^l, F. R. Zhu^{ah}, H. Zhu^f

^aKey Laboratory of Particle Astrophysics, Institute of High Energy Physics, CAS, P.O. Box 918, 100049 Beijing, China

^bDépartement de Physique Nucléaire et Corpusculaire, Université de Genève, 24 Quai Ernest-Ansermet, 1211 Genève, Switzerland

^cPhysics Department, South Dakota School of Mines and Technology, Rapid City, SD 57701, USA

^dIstituto Nazionale di Astrofisica, OATO, Torino, Italy

^eDipartimento di Fisica, Università degli Studi di Torino, Via Pietro Giuria 1, Torino, 10125, Italy

^fNational Astronomical Observatories, CAS, Beijing, 100012, China

^gSchool of Astronomy and Space Sciences, Nanjing University, Nanjing 210093, China

^hPurple Mountain Observatory, CAS, Nanjing 210008, China

ⁱLunar and Planetary Laboratory, University of Arizona, Tucson AZ 85721, USA

^jDipartimento di Fisica dell'Università di Napoli "Federico II", Complesso Universitario di Monte Sant'Angelo, via Cinthia, I-80126 Napoli, Italy

^kIstituto Nazionale di Fisica Nucleare, Sezione di Napoli, Complesso Universitario di Monte Sant'Angelo, via Cinthia, I-80126 Napoli, Italy

^lSchool of Physical Science and Technology, Southwest Jiaotong University, Chengdu 610031, China

^mLaboratoire de Physique Nucléaire et des Hautes Energies, CNRS-IN2P3, Universités Paris VI et VII, Paris, France

ⁿYu.G. Shafer Institute of Cosmophysical Research and Aeronomy SB RAS, 31 Lenin Ave., 677980 Yakutsk, Russia

^oDepartment of Physics & Astronomy, University of Calgary, Calgary, Alberta T2N 1N4, Canada

^pDepartment of Physics, Guangxi University, Nanning 530004, China

^qIstituto Nazionale di Fisica Nucleare, Sezione Roma1, Roma, Italy

^rDepartment of Astronomy, Nanjing University, Nanjing 210093, China

^sThe School of Physics, Shandong University, Jinan 250100, China

^tDepartment of Physics, Faculty of Science, Mahidol University, Bangkok 10400, Thailand

^uINFN, Sez. Roma Tor Vergata, Via della Ricerca Scientifica 1, I-00133 Roma, Italy

^vNational Research Nuclear University MEPhI (Moscow Engineering Physics Institute), 115409 Moscow, Russia

^wInstitute for Nuclear Research, Russian Academy of Sciences, 117312 Moscow, Russia

^xInstitute of Astronomy and Space Science, Sun Yat-Sen University, Guangzhou 510275, China

^ySchool of Science, Nanchang University, Nanchang 330031, China

^zOsservatorio Astrofisico di Torino dell'Istituto Nazionale di Astrofisica, via P. Giuria 1, I-10125 Torino, Italy

^{aa}Istituto Nazionale di Fisica Nucleare, Sezione di Torino, via P. Giuria 1, I-10125 Torino, Italy

^{ab}Dipartimento di Fisica dell'Università di Torino, via P. Giuria 1, I-10125 Torino, Italy

^{ac}Xinjiang Astronomical Observatory, CAS, Urumqi 830011, China

^{ad}Department of Astronomy, University of Massachusetts, Amherst, MA 01002, USA

^{ae}Department of Physics and Astronomy, University of Nevada, Las Vegas, NV 89154, USA

^{af}Department of Astronomy, School of Physics, Peking University, Beijing 100871, China

^{ag}Kavli Institute of Astronomy and Astrophysics, Peking University, Beijing 100871

^{ah}Southwest Jiaotong University, 610031 Chengdu, Sichuan, China

^{ai}Key Laboratory for Research in Galaxies and Cosmology, Shanghai Astronomical Observatory, Chinese Academy of Sciences, 80 Nandan Road, Shanghai 200030, China

^{aj}Max-Planck-Institut für Kernphysik, P.O. Box 103980, 69029 Heidelberg, Germany

^{ak}Key Laboratory for the Structure and Evolution of Celestial Objects, Yunnan Observatory, Chinese Academy of Sciences, Kunming 650011, China

^{al}Key Laboratory of Astroparticle Physics of Yunnan Province, Department of Astronomy, Yunnan University, Kunming 650091, China

^{am}Department of Astronomy, School of Physics, Peking University, Beijing 100871, China

Abstract

The Large High Altitude Air Shower Observatory (LHAASO) project is a new generation multi-component instrument, to be built at 4410 meters of altitude in the Sichuan province of China, with the aim to study with unprecedented sensitivity the spectrum, the composition and the anisotropy of cosmic rays in the energy range between 10^{12} and 10^{18} eV, as well as to act simultaneously as a wide aperture (one stereoradiant), continuously-operated gamma ray telescope in the energy range between 10^{11} and 10^{15} eV. The experiment will be able of continuously surveying the TeV sky for steady and transient sources from 100 GeV to 1 PeV, thus opening for the first time the 100-1000 TeV range to the direct observations of the high energy cosmic ray sources. In addition, the different observables (electronic, muonic and Cherenkov/fluorescence components) that will be measured in LHAASO will allow to investigate origin, acceleration and propagation of the radiation through a measurement of energy spectrum, elemental composition and anisotropy with unprecedented resolution. The remarkable sensitivity of LHAASO in cosmic rays physics and gamma astronomy would play a key-role in the comprehensive general program to explore the High Energy Universe. LHAASO will allow important studies of fundamental physics (such as indirect dark matter search, Lorentz invariance violation, quantum gravity) and solar and heliospheric physics.

In this document we introduce the concept of LHAASO and the main science goals, providing an overview of the project.

Keywords: LHAASO, TeV gamma-ray astronomy, Cosmic Ray physics, Solar-heliospheric physics, Air showers, EAS arrays,

[☆]This document is a collaborative effort.

*Corresponding Editors

Email addresses: caozh@ihep.ac.cn (Z. Cao), domenico.dellavolpe@unige.ch (D. della Volpe)

Contents

Introduction	2
1 The LHAASO experiment	4
1.1 The scintillator array	5
1.2 The muon detector array	5
1.3 The water Cherenkov detector array (WCDA)	5
1.4 The wide field of view Cherenkov telescope array (WFCTA)	5
1.5 Electron-Neutron Detector Array (ENDA)	6
2 GAMMA-RAY ASTRONOMY WITH LHAASO	8
2.1 Exploring the gamma ray sky above 30 TeV with LHAASO	8
2.1.1 Introduction	8
2.1.2 LHAASO sensitivity to gamma rays	10
2.1.3 LHAASO and sky survey	12
2.1.4 Galactic gamma ray astronomy	14
2.1.5 Diffuse galactic emission	17
2.1.6 Attenuation of gamma rays in space	17
2.1.7 Extragalactic gamma ray astronomy	19
2.2 Galactic gamma-ray Sources	22
2.3 Supernova Remnants	22
2.3.1 γ -ray observation of SNRs	22
2.3.2 Hadronic or leptonic origin of the γ -ray emission	23
2.3.3 Are SNRs PeVatrons?	26
2.4 Star-forming Regions	27
2.4.1 Cygnus region	27
2.4.2 W49A: a Galactic mini-starburst	27
2.5 Pulsars and Pulsar Wind Nebulae	30
2.5.1 High-energy TeV emission from pulsars	30
2.5.2 Pulsar wind nebulae	30
2.6 γ -ray binaries	32
2.7 The Galactic Center	34
2.7.1 Galactic center as a high energy emission source	34
2.7.2 γ -ray emission of the GC	34
2.7.3 The LHAASO sensitivity at 100 TeV energy range	35
2.7.4 Short summary	36
2.8 Giant Molecular clouds	37
2.8.1 GMCs as CR calorimeter	37
2.8.2 Young stellar associations inside GMCs	38
2.9 PeVatrons	38
2.10 Diffuse Galactic Gamma-Rays	41
2.10.1 Progresses on the observations of Galactic diffuse γ -rays	41
2.10.2 The outlook of LHAASO project on Galactic diffuse γ -rays above 30 TeV	42
2.10.3 Diffuse γ -ray constraints to Galactic neutrino flux	43
2.10.4 Short summary	44
2.11 Multi-wavelength study of Galactic cosmic rays	45
2.11.1 Background	45
2.11.2 The diffuse shock acceleration theory	46
2.11.3 CRs diffusive propagation and distribution	49

3 Extra-Galactic GAMMA-RAY ASTRONOMY WITH LHAASO	52
3.1 Upgrading of LHAASO/WCDA Towards Multi-messenger Observation	52
3.1.1 Introduction	52
3.1.2 LHAASO/WCDA Experiment and the Upgrading Plan	52
3.1.3 Performances and Prospects for Gamma Ray Astronomy	53
3.1.4 Summary	57
3.2 LHAASO Science: VHE observations of star-forming/starburst galaxies	58
3.2.1 VHE observations of star-forming/starburst galaxies	58
3.2.2 Implications of VHE observations	58
3.3 Measuring Extragalactic Background Light with LHAASO Observations of blazars .	61
3.3.1 Introduction	61
3.3.2 Attenuation of VHE photons	62
3.3.3 Fitting method	62
3.3.4 Perspective of LHAASO	62
3.3.5 Conclusion	63
3.4 Prospects for Gamma Ray Bursts detection with LHAASO	64
3.4.1 Introduction	64
3.4.2 The LHAASO experiment	65
3.4.3 The GRB model	66
3.4.4 The high energy spectrum	66
3.4.5 The light curve	66
3.4.6 The EBL absorption	68
3.4.7 The detector performance for the different configurations	68
3.4.8 The detector threshold and external trigger rate	69
3.4.9 Discussion and conclusions	70
3.5 Low multiplicity technique for GRB observation by LHAASO-WCDA	71
3.5.1 Introduction	71
3.5.2 WCDA experiment and trigger mode	72
3.5.3 Low multiplicity technique	72
3.5.4 Scientific prospect and conclusions	74
4 Multi-Messenger Astronomy with LHAASO	76
4.1 Introduction	76
4.2 VHE neutrino origin	76
4.3 Point sources	76
4.3.1 Diffuse emission	77
4.3.2 UHECR origin	77
4.3.3 Transient searches	77
4.4 Studies of Active Galactic Nuclei with LHAASO	79
4.4.1 LHAASO and Signatures of UHECRs in Gamma-rays from Blazars	80
4.4.2 LHAASO and Cosmic TeV Gamma-Ray Background Radiation	82
4.4.3 LHAASO and New Physics	83
4.4.4 Concluding remarks	84
5 Cosmic Ray Physics with LHAASO	86
5.1 Study of the acceleration of cosmic rays in supernova remnants with LHAASO	86
5.1.1 Introduction	86
5.1.2 Maximal energy of CRs accelerated in SNRs	86
5.1.3 Transition from galactic to extragalactic component of CRs	86

5.2	Cosmic rays physics around knee energies	89
5.2.1	Current status of experimental results	89
5.2.2	Future Prospects and the LHAASO contributions	91
5.3	Cosmic proton spectrum from 30 TeV to 10 PeV measured by hybrid detectors of LHAASO	94
5.3.1	LHAASO Experiment	94
5.3.2	Simulation and quality events selection	94
5.3.3	Shower Energy Reconstruction	95
5.3.4	Mass sensitive parameters	96
5.3.5	Hydrogen Event Selection	99
5.3.6	Hydrogen and Helium Event Selection	99
5.3.7	Conclusion	101
5.4	Measuring Spectrum of heavy component of cosmic rays above 10 PeV Using LHAASO KM2A and WFCTA	103
5.4.1	Introduction	103
5.4.2	Detector Arrays in LHAASO	103
5.4.3	Composition sensitive parameters and their measurements	106
5.4.4	Summary	109
5.5	Contribution of ENDA to LHAASO	111
5.5.1	Motivation	111
5.5.2	Detector Principle	111
5.5.3	Progress of ENDA	114
5.6	Prospective for radio-detection of air showers at the LHAASO site	116
5.6.1	Introduction	116
5.6.2	Status of Extensive Air Shower detection	116
5.6.3	Benefit of radio-measurements for LHAASO	120
5.6.4	LHAASO and GRAND	121

6 Fundamental Physics, Heliosphere Physics and Interdisciplinary Researches with LHAASO 123

6.1	High Energy Emissions of Gamma-Ray Bursts and Constraints on Lorentz Invariance Violation	123
6.1.1	Introduction	123
6.1.2	High Energy Emission of Gamma-ray Bursts	123
6.1.3	Detecting GRB High Energy Photons with LHAASO	124
6.1.4	GRB High-Energy Emission Models and Diversities	125
6.1.5	Constraining Extragalactic Background Light	126
6.1.6	Constraining Lorentz Invariance Violation	127
6.2	Suggestions for Section on Solar-Heliospheric Science	129
6.2.1	Types of data	129
6.2.2	Sun shadow and advance warning of the interplanetary magnetic field for space weather forecasting	129
6.2.3	Loss-cone anisotropy and advance warning of shock arrival for space weather forecasting	133
6.2.4	Forbush decreases due to solar storms	133
6.2.5	Modulation of the cosmic ray flux with the solar cycle	134
6.2.6	27-day variations	134
6.2.7	Sidereal anisotropy	135
6.2.8	Diurnal anisotropy	136
6.2.9	Short-time variations	137

6.2.10	Moon shadow and geomagnetic field variations	138
6.3	LHAASO research topics about CME shock and SNR shock	139
6.3.1	Topic-1: CME's shadow	139
6.3.2	Topic-2: Particles acceleration in SNR shock	141
6.4	Investigating a possible link between cosmic ray flux and Earth's climate	144
6.5	Detection of MeV-range γ -rays from thundershowers	144
6.6	Geophysical researches with environmental neutrons flux	145
6.7	Effects of the near-earth thunderstorms electric field on intensity of the ground cosmic ray electron at YBJ	146
6.7.1	Introduction	146
6.7.2	Simulation Parameters	146
6.7.3	Simulation Results	147
6.7.4	Discussion	149
6.7.5	Conclusion	150
6.8	Effects of thunderstorms electric field on the energy of cosmic ray electron	151
6.8.1	Introduction	151
6.8.2	Simulation setup	152
6.8.3	Simulation results	152
6.8.4	Conclusion	155

List of Figures

1	Layout of the LHAASO experiment. The insets show the details of one pond of the WCDA and of the KM2A array constituted by two overlapping arrays of electromagnetic particle detectors (ED) and of muon detectors (MD). The telescopes of the WFCTA, located at the edge of a pond, are also shown.	4
2	Left: ED and MD simulation Number of events is normalized to a year of flux from the Crab. Right: WCDA only simulation. proton and γ , remaining ratio = $N_{survive}/N_{totaltriggered}$. compactness = $N_{firedPMT}/NPE_{offcoreMAX}$	10
3	Differential sensitivity (multiplied by E^2) of LHAASO to a Crab-like point gamma ray sources compared to other experiments. The Crab nebula data obtained by different detectors [1] is taken into account, and the spectral index of -2.6 is extrapolated and extended to 1 PeV.	11
4	Observation time (hours) per day as a function of the source declination, for 3 values of the maximum zenith angle. The area under the curves is proportional to the total exposure (observation time \times solid angle).	12
5	Sky map in galactic coordinates, showing the positions of the known TeV sources. The red line represents the celestial equator. The green lines limits the region of the sky that culminates at zenith angles smaller than 40° at the LHAASO site. The sources are indicated by different colors according to their type: galactic, extragalactic, unidentified (note that the three sources denoted as “galactic” around the position r.a.= 83° and dec.= -69° are actually in the Large Magellanic Cloud).	13
6	Energy spectrum of the CRAB nebula measured by different experiments.	15
7	Differential spectra (multiplied by E^2) of the TeV gamma ray sources visible by LHAASO extrapolated to 1 PeV, compared to the LHAASO sensitivity. The dashed red line represents the Crab nebula flux, as measured by ARGO-YBJ [2] extrapolated to 1 PeV as a power law.	15
8	Extragalactic gamma ray absorption according to [3]. Top left: EBL and CMB intensity as a function of wavelength. The starlight peaks at $\sim 1 \mu\text{m}$, the dust emission at $\sim 100 \mu\text{m}$, and the CMB blackbody radiation at $\sim 10^3 \mu\text{m}$. Top right: CMB and EBL number density as a function of photon energy. Bottom left: opacity as a function of gamma ray energy. Bottom right: attenuation of gamma ray flux as a function of gamma ray energy.	18
9	Ratio between the observed and the intrinsic flux of 39 extragalactic objects in the LHAASO field of view, with known redshift. The red curve indicate the blazar Mrk421, one of the closest sources.	19
10	Locations of SNRs and unidentified TeV γ -ray sources in Galactic coordinates, compared with the field-of-view of LHAASO (grey region) [4]. Black dots represent SNRs from Green ¹ , red filled circles and magenta stars show TeV and GeV γ -ray SNRs ¹ [5], blue triangles represent the unidentified TeV γ -ray sources, and cyan triangles represent two super-bubbles which were detected in TeV γ -ray bands.	23
11	Expectation of the LHAASO project on the historical SNR spectrum [4].	24
12	Expectation of the LHAASO project on SNRs interaction with molecular clouds spectrum [4].	25
13	SED of SNR Cas A (left) and Tycho (right). The black solid line represents the total emission from zone1 (solid) and zone 2 (dashed) with components: synchrotron (red), inverse Compton (green), and p-p collision (blue).	25
14	Hadronic emission spectra expected for four SNRs that interact with molecular clouds using the diffusive proton model [6, 7].	26
15	Expectation of the LHAASO project on Cygnus Cocoon by using one year MC data [4], compared with the measurement of Fermi-LAT [8], ARGO-YBJ [9], Milagro[10, 11].	28

16	Modeling the Fermi-LAT data of source NGC 3603 [12] with the different proton cutoff energies: 3000 TeV (black), 100 TeV (green) and 10 TeV (red), compared with the LHAASO's sensitivity curve (gray).	29
17	The spectrum of the nebula around the Geminga pulsar measured by Milagro [13], HAWC [14] and MAGIC [15].	31
18	Differential spectra of LS I +61° 303 during a flaring period from the VERITAS observations in 2014, together with those average spectra in previous publications (from [16]).	33
19	The image of very-high-energy γ -ray emission from the direction of the GC region (adopted from [17]).	34
20	The spectra of very-high-energy γ -ray for the point and diffuse emission (adopted from [17]).	35
21	The effective area of LHAASO for γ -rays from GC direction	36
22	The sensitivity of LHAASO for γ -rays from GC direction	37
23	The γ -rays flux produced in a molecular clouds with a M/d^2 value of 10^6 (M_{\odot}/kpc^2), the angular size is 20 arcdeg ² . The CR spectrum measured by AMS-02 extrapolated to 10 PeV with and without a hardening are used in deriving the γ -ray flux. The LHAASO sensitivity are estimated by considering the source extension.	39
24	left: the image of Fermi bubbles. right: Spectral energy distribution of Fermi bubbles. Figures are taken from [18].	42
25	The predicted DGE flux respectively at Cygnus region (left) and $25^{\circ} < l < 100^{\circ}$, $ b < 5^{\circ}$ (right) observed by LHAASO experiment.	43
26	The extrapolated energy spectrum of the Fermi bubbles in hadronic model (black solid line) according to [19] and the integral sensitivity of one quarter LHAASO project (red solid line).	43
27	The γ -ray spectra predicted by different knee models[20] and the LHAASO sensitivity (grey dash line).	44
28	The sensitivity of LHAASO-WCDA and LHAASO-KM2A [21].	47
29	The basic parameters for SKA [22].	48
30	Radio to X-ray synchrotron spectrum of the northeastern part of RCW 86. A curve model is needed to fit spectrum [23].	49
31	optical depth vs observation frequency of typical HII region and planetary nebulae. The solid line is for HII with temperature $T_e=10000$ K, electron density $n_e=100 \text{ cm}^{-3}$, size $\Delta l=10$ pc. The dashed line is for planetary nebulae with temperature $T_e=10000$ K, electron density $n_e=3000 \text{ cm}^{-3}$, size $\Delta l=0.1$ pc.	50
32	(The distribution of HII regions and planetary nebulae along Galactic latitude.	51
33	The layout of the scintillator counter (small dots) array, muon counter (big dots) array, water Cherenkov detector (rectangle in the center) array and 18 wide field of view Cherenkov telescopes (small rectangles) in the LHAASO complex of multi-detector array of 1.3 km^2	52
34	Two simulated events recorded by one of the pools of WCDA induced by 1 TeV gamma ray (upper) and 2 TeV proton (lower), respectively.	53
35	The integrated sensitivity of LHAASO (in pink) comparing with other experiments. The part of the curve below 10 TeV is the contribution of WCDA optimized with the cuts described in text.	54
36	The differential sensitivity of LHAASO (in red) comparing with other experiments. Below 300 GeV, both estimates with 8" PMT configuration (dashed line) and 20" PMT configuration (solid line) are plotted. It is noticed that WCDA with 20" PMTs is almost as same sensitive as FERMI/LAT at 70 GeV.	55

37	The SED of TXS 0506+056 during the flare within 20 days after the neutrino event IC-170922A. It is reported in Ref. [24] including sensitivity curves of HAWC, HESS and VERITAS experiments. The upgraded LHAASO sensitivity is also plotted in the same figure (light blue) from 30 GeV to 100 TeV.	56
38	Expectation of the LHAASO project on Mrk501, compared with the measurement of Fermi-LAT, ARGO-YBJ[25].	56
39	Spectral energy distribution for NGC 2146 obtained in the analysis of the 68 months of Fermi/LAT data. The black solid line represents the best-fit power law in the range of 0.2-100 GeV and the dashed line is the extrapolation to higher energies.	59
40	Left: 1-dimensional marginalized probability distributions of the fitting parameters ξ_i . Right: Fitting results of the EBL intensities with simulated LHAASO spectra of 45 blazars, compared with the input EBL model [26]. We also show the constraints with the current blazar data as derived in [27] for comparison.	63
41	A comparison of the LAT and GBM fluencies in the [0.1-10] GeV and [10-1000] keV range respectively. Black (red) squares are for long (short) GRBs; dashed lines indicate LAT-GBM fluence ratio of 0.1, 1.0, 10.0 (bottom to top).	67
42	Distribution of measured GBM fluencies for Long (black) and Short (red) GRBs in the [10-1000] MeV range.	67
43	Distribution of T_{90} durations for Long (black) and Short (red) GRBs detected by Fermi-GBM.	67
44	Distribution of redshift for Long (black) and Short (red) GRBs detected by Fermi-GBM. Dashed lines show the subsamples of Long and Short GRBs observed simultaneously by Fermi-GBM and Swift-BAT detectors.	67
45	Expected angular resolution of the WCDA for internal events and $N_{fit} \geq 20$ (see text).	69
46	Effective areas of the WCDA for gamma rays (left) and protons (right) for four zenith windows and $N_{fit} \geq 10$ (see text).	69
47	Distribution of number of hit. Solid line is a power law fit to the number of hits to infer low multiplicity due to threshold effect.	74
48	Sensitivity using the low multiplicity as a function of spectral index. The 5σ discovery potential is shown as a function of spectral index for various values of a sharp high-energy spectral cutoff. The duration of the burst is fixed to 1s and the zenith angle is fixed to 0° . Data from 2 GRBs are corrected for duration and inserted for comparison [28] [29].	75
49	One SED of Mrk 421. [from 30].	80
50	Cosmogenic model of [31] for the non-variable and hard TeV spectrum of 1ES 0229+200. [from 31].	81
51	A spectrum of UHECR-induced cascade gamma-rays for Mrk 421 (dotted line) and the historical TeV data of Mrk 421 (points). The data are obtained through the SED Builder of ASDC (http://tools.asdc.asi.it). The cascade gamma-rays are calculated by using the TRANSPORTCR code [32]. The injection spectrum of protons is assumed to be a power-law with an exponential cutoff. We take the index of 2.6 and the cutoff energy of 10^{19} eV. The EBL model of [3] is used in the calculation. The solid line is the one-year differential sensitivity of LHAASO.	81
52	GeV background radiation measured by <i>Fermi</i> gamma-ray space telescope, and the upper and lower limits on TeV background [33]. [from 33].	82
53	TeV spectrum of 1ES 0229+200 with the consideration of LIV (dotted line). The points are the HESS data of 1ES 0229+220. The EBL model of [34] is used in the calculation. The dashed line is the one-year differential sensitivity of LHAASO.	83

54	CR intensities at the Solar system as a function of kinetic energy. Experimental data obtained in the CAPRICE [35], BESS [36], ATIC-2 [37], CREAM [38], JACEE [39] and KASCADE [40] experiments are shown as well.	87
55	Mean logarithm of the CR nucleus atomic number as a function of energy. Calculations corresponded to ankle and dip scenarios are shown by solid and dashed lines respectively [41]. Experimental data obtained in the ATIC-2 [42], JACEE, KASCADE [43], Auger [44], HiRes at $\epsilon < 10^{18}$ eV [45], HiRes at $\epsilon > 10^{18}$ eV [46] and Yakutsk [41] experiments are shown. Open and solid symbols corresponds to QGSJET and SIBYLL models respectively.	88
56	N_μ/N_e calculated for EAS observed at the LHAASO altitude above sea level (4410 m) in the ideal case of a full coverage experiment without detection errors.	92
57	The total number of photoelectrons N_{pe} as a function of the impact parameter R_p for primary protons. The color scale represents the shower energies in bins of $\Delta \log_{10}(E/1\text{TeV}) = 0.2$, covering primary energies from 30 TeV to 10 PeV.	95
58	Energy resolution is about 20% and the bias is less than 3% for the light component energy spectrum. E_{rec} is the reconstruction energy from a specific table of a mixture of protons and helium nuclei and E_{true} is the primary energy. The error bars represent the energy resolution.	96
59	p_{max} - p_C map.	97
60	p_{max} - p_μ map.	98
61	p_{max} - p_μ map.	98
62	Aperture of the hybrid experiment. Solid circles represent the aperture for the selected H events.	99
63	The contamination fraction (%) of events of heavy composition other than protons that survive through the H selection cuts. The Hörandel model is assumed in the simulation.	100
64	The number of proton like events in each energy bin measured by hybrid experiments of LHAASO per year after the composition selection. The Hörandel model is assumed in the simulation.	100
65	Aperture of the hybrid experiment. Solid circles represent the aperture for the selected $H\&He$ events.	101
66	The contamination fraction (%) of events of heavy composition other than $H\&He$ that survive through the $H\&He$ selection cuts. The Hörandel model is assumed in the simulation.	102
67	The number of $H\&He$ like events in each energy bin measured by hybrid experiments of LHAASO per year after the composition selection. The Hörandel model is assumed in the simulation.	102
68	The layout of the scintillator counter (small dots) array, muon counter (big dots) array, water Cherenkov detector (rectangle in the center) array and the location of the wide field of view (FoV) Cherenkov telescope (small squares) array in the LHAASO experiment (left panel). The FoV of the telescopes in the entire northern sky map. The azimuth angle 90° is the north direction. Curves in the sky indicate the trajectories of the moon in one year.	105
69	The wavelength response function of relevant components of the telescope including mirrors, filter, Winston cones and the SiPMs. The response of the cones is an average over all incident angles. The overall response function is also shown here.	105

70	A 20 PeV iron shower event hit in the array with the $R_p \sim 200m$ to the telescopes. The registered scintillator counter map and muon counter map are shown in the left two panels. The image of the shower taken by the telescopes is shown in right. The ‘cross’ mark in the right panel indicates the arrival direction of the event determined by the scintillator array.	106
71	Distributions of inverted muon contents ($1/C_\mu$) in showers with 5 groups of species, <i>i.e.</i> iron (in pink), Mg-Al-Si (blue), C-N-O (green), Helium (red) and proton (black). Left, events are evenly distributed among 5 species; Right, with the assumption of composition in[47]	107
72	Relationship between vertical X_{max} and the angular offset of the centroid of the shower image from the arrival direction (left) and corresponding resolution of X_{max} (right). The solid curve is the resolution function of showers that have impact parameter $R_p < 200m$ and the dashed curve is for $R_p > 200m$, respectively	108
73	Distributions of vertical X_{max} of showers with 5 groups of species, <i>i.e.</i> iron (in pink), Mg-Al-Si (blue), C-N-O (green), Helium (red) and proton (black). Left, events are evenly distributed among 5 groups of species; Right, with the assumption of composition in[47].	108
74	Left: The correlation between $1/C_\mu$ & X_{max} for 5 groups of species of iron (in pink), Mg-Al-Si (blue), C-N-O (green), Helium (red) and proton (black). The cuts indicated by the two lines can be applied to select the iron samples with a purity about 85% from all measured CR events. Right: The expectation of the pure iron spectrum over an energy range from 10 to 100 <i>PeV</i> with LHAASO in one year observation. The knee structure will be significantly measured if it is as the assumption of model in [47]	109
75	The energy resolution function of the pure iron showers using the total numbers of Cherenkov photons in the shower images (left) which is symmetrical Gaussian function with the mean of 1% and standard deviation of 18% according to the fit indicated by the smooth curve. In the right panel, the systematic offset (spots) and the resolution (squares) of the energy reconstruction for the pure iron events as functions of shower energy are plotted. It is noticed that the resolution is nearly a constant over the energy range.	109
76	Simulation results: At the same energy, for example, 1PeV, proton has both secondary hadrons M_h and hadron energy E_h and then neutrons M_n about one order higher than ones of Fe [48].	112
77	Left: Scheme of the EN-detector. Right top: Photo of the ZnS(Ag)+LiF scintillator used in PRISMA-YBJ. Right bottom: Photo of the ZnS(Ag)+B ₂ O ₃ scintillator used in LHAASO-ENDA.	113
78	Left: pulse shape of noise and neutron. Right: Separation between noise and neutron in the coordinate system of $Q_{trigger}$ vs Q_{total}	113
79	The shape of the signals from the neutron detectors at PRISMA-YBJ. Upper plot: the pulse from 0 to 2.5 ms. The large peak in the first bin is generated by the EAS electrons. Middle plot: the pulse from 0 to 0.25 ms. Lower plot: the pulse from 0.6 to 0.8 ms (note the different scale on the vertical axis). The small peaks following the first peak are generated by thermal neutrons.	114
80	Location of ENDA inside LHAASO.	115
81	configuration of ENDA-64 (left) and ENDA-400 (right).	116

- 82 Left: radio-energy estimator S_{radio} as a function of the cosmic-ray energy measured with the Auger surface detector. Green filled circles denote air showers with at least five stations with signal. Open circles denote events with less than five stations with signal and use the surface detector core position. A 17% energy resolution could be achieved for events with 5+ stations triggered. Taken from [49]. Right: correlation of the shower energy reconstructed with Tunka-Rex radio and Tunka-133 air-Cherenkov measurement. Taken from [50]. 118
- 83 Radio profiles in arbitrary units for a proton shower with $X_{max} = 794 \text{ g/cm}^2$ (left panel) and an iron shower with $X_{max} = 573 \text{ g/cm}^2$ (right panel). Both showers have an energy of $2.3 \cdot 10^{17} \text{ eV}$ and a zenith angle of 49 degrees. Taken from [51]. 119
- 84 Distribution of reconstructed zenith (left) and azimuth angles for the 465 EAS radio candidates selected in the 317 live days of TREND data (black squares). Also shown are the expected distributions for air showers initiated by protons with $E = 10^{17} \text{ eV}$ (green empty squares). 120
- 85 Multiband light curves of GRB 080916C. It can be seen that the light curve in LAT (high-energy) band has a 5 s delay compared with GBM (low-energy) band. The first LAT peak coincides with the second GBM peak. Adopted from Ref. Abdo et al. (2009a). 124
- 86 A schematic figure of three spectral components of Fermi GRBs: (I) A Band-type broken power-law component with non-thermal origins; (II) a quasi-blackbody component that is likely from GRB photosphere; and (III) an extra power-law with a possible high-energy cut-off. Adopted from Ref. [52]. 125
- 87 Illustration of the solar wind and interplanetary magnetic field. The solar wind is emitted radially from the Sun in all directions at all times. The spiral magnetic field lines connect plasma that originated from the same location on the rotating solar surface. Note that the turbulent magnetic field lines (solid lines) do not coincide with the mean magnetic field lines (dashed lines). The Earth might be located near the bottom of the figure. 130
- 88 Smoothed monthly international sunspot number (using 5-month boxcar smoothing) and McMurdo neutron monitor count rate as a function of time. The long-term drift at McMurdo has been corrected following [53]. A neutron monitor count rate indicates the Galactic cosmic ray flux, which undergoes “solar modulation” in association with solar activity. Solar modulation includes dramatic 11-year variations with the sunspot cycle, and a 22-year variation with the solar magnetic cycle, seen here in changes in the solar modulation pattern between positive ($A > 0$) and negative ($A < 0$) magnetic polarity. [54]. 131
- 89 Seasonal variation in the sun shadow observed by the ARGO-YBJ experiment in cosmic rays at median energy 5 TeV. The observation period for each map is one astronomical season in the Northern Hemisphere. The smoothing radius is 1.2° and the pixels are $0.1^\circ \times 0.1^\circ$. Each map shows the fractional change in the cosmic ray flux (color scale) and the statistical significance of the change (contours). Each contour represents an integral value of the significance (in units of the standard deviation), with darker contours every 5 units. Maps for the Spring and Summer seasons show stronger significance because the Sun was higher in the sky at the ARGO-YBJ site in Tibet. The fractional change suddenly weakened in Spring 2010, in association with a sudden increase in IMF variability, whereas the sunspot number and some other generic indicators of solar activity started to increase rapidly only in Spring 2011. 132

90	<i>Reversed time plots in day of year (DOY) for Carrington (solar) rotation 2071 (between 2008 June 12 and 2008 July 10). Top panel: Synoptic map of the solar corona as observed by the EUVI-A imager in the Fe II 195 bandpass. Upper three graphs: Data of the diurnal anisotropy and flux of Galactic cosmic rays (GCRs) as measured by PSNM at Doi Inthanon. Lower graphs: Hourly interplanetary plasma parameters from the ACE and OMNIWeb databases in GSE coordinates. When the high speed solar wind streams pass the Earth they reduce the cosmic ray flux. Each dotted-dashed line represents a boundary between magnetic polarities of the streams. After the rapid solar wind speed increase of DOY 177, there was a strong, long-lasting enhancement in the diurnal anisotropy of GCRs. This is attributed to an extra $\mathbf{B} \times \nabla n$ anisotropy with a latitudinal gradient in association with the coronal hole (dark region) morphology [55].</i>	135
91	<i>Relative intensity map of TeV cosmic rays as measured by ARGO-YBJ, showing the sidereal anisotropy [56].</i>	136
92	<i>The schematic diagram of the CME's shadow.</i>	139
93	<i>The observation from the spacecraft. The energy distribution shows a double power law with a "break" at \sim2-5MeV [57].</i>	140
94	<i>Simulated energy spectrum of 13,Dec,2006 shock event shows a "break" occurred at \sim5MeV in the $E^2 \cdot F(E)$ representation [58].</i>	140
95	<i>The schematic diagram of the SNRs shock interacted with nearby MCs [59].</i>	142
96	<i>The spectral energy distribution obtained for IC 443 and W44 at different energy range from multiple spacecraft [60].</i>	142
97	<i>Percent change of particle number as a function of electric field at YBJ(The illustration is the enlarged view of the total number in reducing range)</i>	147
98	<i>Percent change of the total number of electrons and positrons as a function of positive electric field strength for different primary energies at YBJ.</i>	148
99	<i>Percent change of electrons and positrons as a function of atmospheric depth for different primary energies shower in different positive fields.</i>	148
100	<i>Percent of electrons and positrons number as a function of atmospheric depth in absence electric field.</i>	149
101	<i>Percent of electrons and positrons number as a function of atmospheric depth in different negative fields.</i>	150
102	<i>Percent of electrons and positrons number as a function of atmospheric depth in different positive fields</i>	150
103	<i>Number of electrons and positrons as a function of atmospheric depth in an electric field of 1.7 kV/cm (left) and -1.7 kV/cm (right). [Electric field area: 457-599 g/cm²]</i>	153
104	<i>Total number of electrons and positrons as a function of atmospheric depth in electric field strength of 0.4 kV/cm. (electric field area: 457-599 g/cm²)</i>	154
105	<i>The ratio distribution of electrons and positrons in energy range 1-30 MeV as a function of energy in absence of a field at the altitude of 4400 m</i>	154
106	<i>Energy distribution of electrons and positrons in electric field of -1.7 kV/cm and the same in absence of a field at the altitude of 4400 m</i>	155
107	<i>Electron energy spectra at 4400 m altitude in different fields</i>	155
108	<i>Electron energy spectra at different altitudes in an electric field of -1.7 kV/cm</i>	155
109	<i>The change of particle number as a function of energy in an electric field of 0.4 kV/cm at the altitude of 4400m</i>	156
110	<i>Positron energy spectra at different altitudes in an electric field of 0.4 kV/cm</i>	156

List of Tables

1	Properties of the GMCs in the FOV of LHAASO. The estimated distance and position are obtained from Dame et al, 1987. The mass values listed in the second column are calculated from the CfA maps (see [61] for detail).	38
2	Effective area at different energy for low multiplicity	73
3	Background rate at different low multiplicity	74
4	Comparison of the ratio between the active detection area (of the electromagnetic and muonic EAS components) and the effective area of LHAASO experiments with those of some of the more recent experiments operating in the knee energy range. The Ice-Top experiment has no surface muon detectors, high energy muons are measured by the IceCube detector thus limiting the solid angle.	92

INTRODUCTION

Introduction

The **Large High Altitude Air Shower Observatory (LHAASO)** project[62] is a new generation instrument targeting a deep investigation of the “*High Energy Universe*”, that is the study of the systems and mechanisms that can produce particles with energy as high as 10^{20} eV, i.e. 7 orders of magnitude larger than the maximum energy obtained in accelerators, and with a center mass energy (for interactions with nucleons at rest) of the order of 430 TeV, 30 times the nominal LHC energy. The remarkable sensitivity of LHAASO in cosmic ray physics and gamma-ray astronomy will play a key-role in the comprehensive general program to explore the “*High Energy Universe*”. LHAASO will open for the first time the 100-1000 TeV range to the direct observations of the high energy cosmic ray sources.

The first phase of LHAASO will consist of the following major components:

- 1 km² array (LHAASO-KM2A) composed of electromagnetic particle (ED) and muon detectors (MD). The ED detectors are divided into two parts: a central part including 4901 scintillator detectors of 1 m² active area arranged on a triangular grid with 15 m pitch covering a circular area with a radius of 575 m and an outer guard-ring up to a radius of 635 m instrumented with further 294 EDs arranged on a grid of 30 m pitch. The 1171 MD detectors are interspersed on the same 1 km². Each MD is an underground water Cherenkov tanks with a 6 m radius arranged on a grid with a 30 m pitch, achieving a total sensitive area for muons of $\sim 42,156$ m²).
- A close-packed, surface water Cherenkov detector facility with a total area of about 78,000 m² (LHAASO-WCDA).
- 18 wide field-of-view air Cherenkov telescopes (LHAASO-WFCTA).

LHAASO will be installed at high altitude (4410 m a.s.l., 600 g/cm², 29° 21' 31" N, 100° 08'15" E) in the Daochen site, Sichuan province, P.R. China, with the aim of studying with unprecedented sensitivity the spectrum, the composition and the anisotropy of cosmic rays in the energy range between 10^{12} and 10^{18} eV, as well as to act simultaneously as a wide aperture (about 2 sr), continuously operating gamma-ray telescope in the energy range between 10^{11} and 10^{15} eV.

Therefore, LHAASO is the only experiment strategically built to cover the exploration of several energy decades with a unique installation. A set of observations will be carried out in a coherent way, simplifying the problem of a correct interpretation of the results.

LHAASO will enable studies in cosmic ray physics and gamma-ray astronomy that are unattainable with the current suite of instruments:

- 1) LHAASO will study in detail the high energy tail of the spectra of most of the γ -ray sources observed at TeV energies, opening for the first time the 100–1000 TeV energy range to the direct observations of the high energy cosmic ray sources. The acceleration mechanism of cosmic ray particles at energies higher than 1 PeV is expected to be uncovered by finding and deep investigating the sub-PeV gamma ray sources.

When new wavelength bands are explored in astronomy, previously unknown sources and unknown types of sources are discovered. LHAASO’s wide field of view provides therefore a unique discovery potential.

- 2) LHAASO will perform an *unbiased sky survey of the Northern sky* with a detection threshold of a few mini Crab unit at sub-TeV/TeV energies and around 100 TeV in one year. This sensitivity grants a high discovery potential of flat spectrum Geminga-like sources not observed at GeV energies. This unique detector will be capable of continuously surveying the γ -ray sky for steady and transient sources from about 100 GeV to 1 PeV.

From its location LHAASO will observe at TeV energies and with high sensitivity about 30 of the sources catalogued by Fermi-LAT at lower energy [63], monitoring the variability of 15 AGNs (mainly blazars) at least.

- 3) The sub-TeV/TeV LHAASO sensitivity will allow to observe AGN flares that are unobservable by other instruments, including the so-called TeV orphan flares. Multi-wavelength observations of AGN flares from radio to TeV probe the environment up to within ~ 0.01 pc from the supermassive black hole constraining models of gamma-ray production and acceleration of charged particles.
- 4) LHAASO will map the Galactic *diffuse gamma-ray emission* above few hundreds GeV and thereby measure the cosmic ray flux and spectrum throughout the Galaxy with high sensitivity. The measurement of the space distribution of diffuse γ -rays will allow to trace the location of the CR sources and the distribution of interstellar gas.
- 5) The high background rejection capability in the 10 – 1000 TeV range will allow LHAASO to measure the *isotropic diffuse flux of ultrahigh energy γ radiation* expected from a variety of sources including dark matter and the interaction of 10^{20} eV CRs with the 2.7 K microwave background radiation. In addition, LHAASO will be able to achieve a limit below the level of the IceCube diffuse neutrino flux at 100 TeV – 10 PeV, thus constraining the origin of the IceCube astrophysical neutrinos.
- 6) LHAASO will allow the reconstruction of the energy spectra of different cosmic ray mass groups in the $10^{13} – 10^{18}$ eV with unprecedented statistics and resolution, thus tracing the light and heavy components through the knee of the all-particle spectrum.
- 7) LHAASO will allow the measurement, for the first time, of the CR anisotropy across the knee separately for light and heavy primary masses.
- 8) The different observables (electronic, muonic and Cherenkov/fluorescence components) that will be measured in LHAASO with high resolution will allow a detailed investigation of the role of the hadronic interaction models, therefore investigating if the EAS development is correctly described by the current simulation codes.
- 9) LHAASO will look for signatures of WIMPs as candidate particles for DM, mainly as spectral continuum gamma-ray features, with high sensitivity for particles masses above 10 TeV. Moreover, axion-like particle searches are planned, where conversion of gamma-rays to/from axion-like particles can create distinctive features in the spectra of gamma-ray sources and/or increase transparency of the universe by reducing the Extragalactic Background Light (EBL) absorption. Testing of Lorentz invariance violation as well as the search for Primordial Black Holes and Q-balls will also be part of the scientific programme of the experiment.

In the next decade CTA-North and LHAASO are expected to be the most sensitive instruments to study Gamma-Ray Astronomy in the Northern hemisphere from about 20 GeV up to PeV.

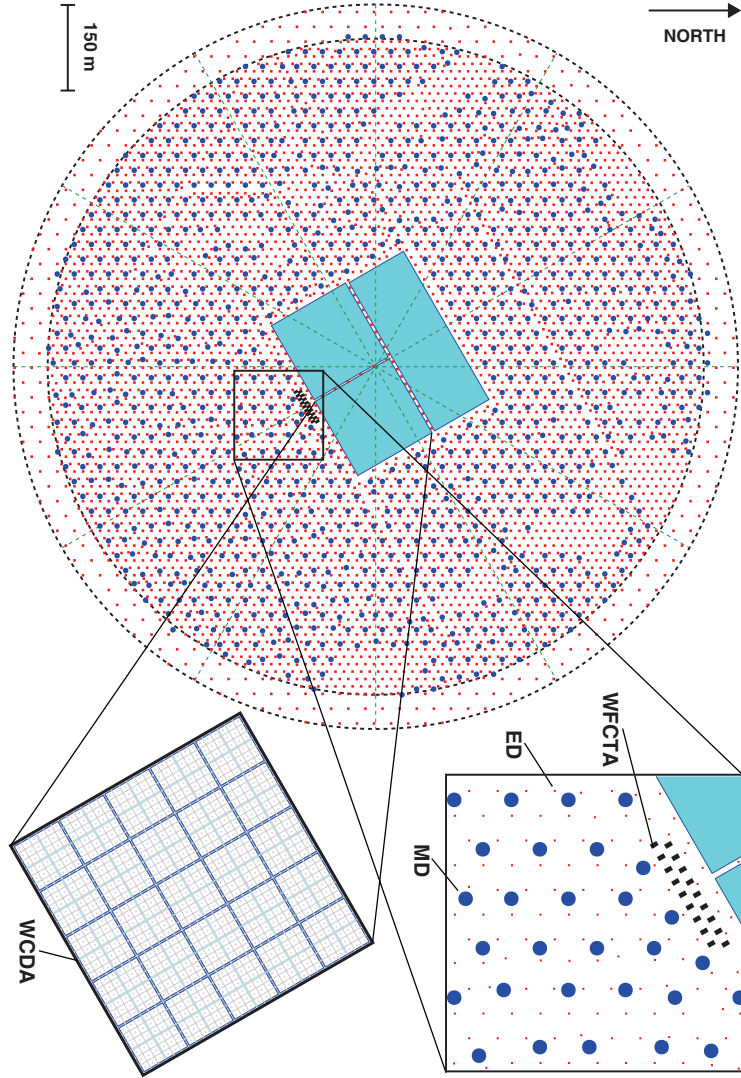


Figure 1: Layout of the LHAASO experiment. The insets show the details of one pond of the WCDA and of the KM2A array constituted by two overlapping arrays of electromagnetic particle detectors (ED) and of muon detectors (MD). The telescopes of the WFCTA, located at the edge of a pond, are also shown.

1. The LHAASO experiment

The first phase of LHAASO will consist of the following major components[62] (see Fig. 1):

- 1 km² array (LHAASO-KM2A) for electromagnetic particle detectors (ED), 1 m² each in size, divided into two parts: a central part including 4901 scintillator detectors (15 m spacing) to cover a circular area with a radius of 575 m and an outer guard-ring instrumented with 294 EDs (30 m spacing) up to a radius of 635 m.
- An overlapping 1 km² array of 1171 underground water Cherenkov tanks 36 m² each in size, with 30 m spacing, for muon detection (MD, total sensitive area $\sim 42,156$ m²).
- A close-packed, surface water Cherenkov detector facility with a total area of about 78,000 m² (LHAASO-WCDA).
- 20 wide field-of-view air Cherenkov telescopes (LHAASO-WFCTA).

LHAASO will be located at high altitude (4410 m a.s.l., 600 g/cm², 29° 21' 31" N, 100° 08' 15" E) in the Daochen site, Sichuan province, P.R. China.

1.1. The scintillator array

The array is composed of 4901 scintillator detectors (Electromagnetic particle Detector, ED) deployed in a grid with a spacing of 15 m between different modules to cover a circular area with a radius of 575 m. This central part is surrounded by an outer guard-ring instrumented with 294 EDs (30 m spacing) up to a radius of 635 m, mainly to improve the identification and the reconstruction of showers with the core outside the instrumented area. Each ED will be covered by a 0.5 cm thick lead plate (~ 1 r.l.) to improve the angular resolution and to lower the energy threshold exploiting the pair production of secondary photons. The measured time resolution of a typical ED module is less than 2 ns. To accomplish the physics program of KM2A, the EDs have been optimised to measure a wide range of particle densities, from $1/\text{m}^2$ to $\sim 10,000/\text{m}^2$.

1.2. The muon detector array

The array of muon detectors (MD) is composed of 1171 water Cherenkov tanks deployed in a grid with a spacing of 30 m. The detectors are buried under 2.5 m of soil (about 12 radiation-lengths) to reduce the punch-through due to the shower electromagnetic particles. Therefore, the muon energy threshold is 1.3 GeV. Each cylindrical concrete tank contains a water bag with a diameter of 6.8 m and a height of 1.2 m to enclose the pure water. The inner layer is made of Tyvek 1082D (DuPont) which is an opaque material with excellent strength, good flexibility, and high diffuse reflectivity for near-UV light (>95%). Tyvek is non-woven material made of high-density polyethylene, which minimises the possibility of chemicals leaching into the water volume. A PMT sits at top center of the water bag and looks downwards through a highly transparent window into the water. The total area of the MD is $\sim 36 \text{ m}^2$. The measured time resolution is about 10 ns. The overall signal charge resolution for vertical single muon signals is estimated to be about 25%.

1.3. The water Cherenkov detector array (WCDA)

The water Cherenkov detector array, covering an area of about $78,000 \text{ m}^2$ area, is constituted by 3120 detector units divided into 3 separate arrays. Every array is a single water pond 4.5 m deep. Two of them with an effective area of $150 \times 150 \text{ m}^2$ contain 900 detector units each. The third pond with an area of $300 \times 110 \text{ m}^2$ contains 1320 detector units. Each detector unit has a $5 \times 5 \text{ m}^2$ area and is divided by black plastic curtains vertically hung in the water to attenuate scattered light. The curtains of the cells are made in black plastic to minimise late light from reflections. A pair of 8" and 1.5" PMTs in each unit of first $150 \times 150 \text{ m}^2$ pond and a pair of 20" and 3" PMT in each unit of the other two ponds are anchored at the center of the cell bottom. To guarantee an attenuation length of near-ultra-violet light longer than 20 meters a water purification system will be operated.

The measured counting rate was at least 35 kHz for each cell, with an expected minimum of 12.5 kHz given by cosmic rays. This very high single counting rate does not allow a simple majority but requires a topological one, with different trigger levels. The basic element is given by a 3×3 cells matrix, whose signal is collected by a custom FEE and sent to a station where a suitable trigger is generated and the corresponding data are recorded. This approach is quite new and is called "trigger-less" and allows the maximum DAQ flexibility. For example, overlapping the clusters (corresponding to 12×12 cells) by shifting them by 30 m and requiring a coincidence of at least 12 PMTs within 250 ns in any cluster, a trigger rate of 70 KHz is expected. This approach is particularly effective In the search for GRBs, as it will be discussed in the section [3.4](#).

1.4. The wide field of view Cherenkov telescope array (WFCTA)

The array of wide field of view Cherenkov telescopes will be made by 18 detectors. Each Cherenkov telescope consists of an array of 32×32 SiPMs and a 4.7 m^2 spherical aluminised mirror. It has a field of view of $16^\circ \times 16^\circ$ with a pixel size of approximately $0.5^\circ \times 0.5^\circ$. The telescope unit together with the power supply and a slow control system are installed in a $4.8 \text{ m} \times 2.5 \text{ m} \times 2.6 \text{ m}$ shipping container. A

1.5 Electron-Neutron Detector Array (ENDA)

wide band filter from 310 nm to 550 nm is installed in front of the SiPM staffed camera to filter out the most night sky background dominated by long wavelength component above 550 nm. The telescopes will be located at the center of the KM2A array, close to the edges of a water Cherenkov pond which will provide the position of the reconstructed shower cores with a few meters resolution. Different configurations of the telescopes in the array will be used to optimise the sensitivity to the measurement of the CR energy spectrum and composition in different energy ranges (see sec. 5.3).

1.5. Electron-Neutron Detector Array (ENDA)

The idea of a novel type of array for EAS study proposed in 2001 has been developed in 2008 as the PRISMA (PRImary Spectrum Measurement Array) project. It is based on a simple idea: as hadrons are the main EAS component forming its skeleton and resulting in all its properties at an observational level, the hadron component should also be the main component to be measured in experiments. Therefore, we have developed a novel type of EAS array detector (en-detector) capable to record the hadronic component through thermal neutron detection and also the electron component. The detector looks like a usual EAS detector but with a specific thin inorganic scintillator sensitive to thermal neutrons and to charged particles as well. Distributing 400 these detectors over an area of $100 \times 100 \text{ m}^2$ on the Earth's surface (ENDA) one can obtain a huge hadron calorimeter along with EAS array capable to measure both neutron and electron components over the array area.

GAMMA-RAY ASTRONOMY WITH LHAASO

2. GAMMA-RAY ASTRONOMY WITH LHAASO

2.1. Exploring the gamma ray sky above 30 TeV with LHAASO

Executive summary The gamma ray sky above a few tens of TeV is almost completely unexplored, since past and present telescopes have been able to record only few photons of energy larger than 30 TeV. On the other hand the study of the emission in this energy range is of great importance for the understanding of the physical mechanisms that generate the high energy radiation.

The LHAASO observatory has the potential to extend the study of gamma ray emission to the energy range 30–300 TeV with the unprecedented sensitivity of $\sim 3 \times 10^{-18}$ photons $\text{s}^{-1} \text{cm}^{-2} \text{TeV}^{-1}$ at 100 TeV for an observation time of one year.

The telescope will be continuously monitoring a large portion of the sky around the zenith direction, corresponding to almost 60% of the celestial sphere for observations with a maximum zenith angle of 40° . For the the most energetic events, the extension of the field of view to larger zenith angles will increase the sky coverage allowing observations close to the galactic center.

It should be stressed that gamma ray observations above a few tens of TeV are essential for the unambiguous identification of the “PeVatrons”, the galactic sources of cosmic rays around the so called “knee” in the spectrum at a primary energy around $E_0 \simeq 3000$ TeV. These sources are known to exist, but remain elusive. The LHAASO observations have the potential to either discover these sources or set very important constraints on their properties. The LHAASO sensitivity is sufficient to provide measurements on the emission in the 10–100 TeV range and above for most of the known TeV galactic sources.

Concerning extragalactic astronomy, the absorption of gamma rays due to the Extragalactic Background Light (EBL) hampers the study of the higher energy range of the source spectra, however the measurement of photons above 10–20 TeV from nearby objects could bring valuable information on the the density of the EBL itself in the infrared region.

Finally, the possible detection of photons from extragalactic objects of energy above the expected absorption cutoff, could open a window on unexpected scenarios and extend our horizon beyond the paradigms of the standard physics.

2.1.1. Introduction

During the last twenty years, the achievements in Gamma Ray astronomy both in the GeV energy range with space borne instruments (like EGRET, AGILE and Fermi) and in the TeV region with ground based detectors (like Whipple, HESS, MAGIC, VERITAS, MILAGRO and ARGO-YBJ), produced extraordinary advances in high energy astrophysics, with the detection of a large number of sources (more than 3000 in the Fermi catalogue), about 170 of them emitting up to TeV energies.

These sources belong to different classes of objects, both galactic (like pulsars, pulsar wind nebulae, supernova remnants, compact binary systems, etc.) and extragalactic (like active galactic nuclei and gamma ray bursts), in which the emission of high energy photons can be produced by different mechanisms. All these results are deeply modifying our understanding of the “non-thermal Universe”. The field is extremely dynamic: the observations continuously provide new results, often unexpected and surprising, while the theory makes efforts to clarify the structure of the sources and the mechanisms operating in the acceleration regions.

In this scenario a strong interest is addressed to the development of new instruments able to make more precise observations, with a better sensitivity and in a more extended energy range. This interest brought to new ambitious projects, like CTA (Cherenkov Telescope Array [64]), HAWC (High Altitude Water Cherenkov [65]), HiSCORE (Hundred Square-km Cosmic Origin Explorer [66]), and LHAASO.

Most results of TeV Gamma Ray Astronomy has been obtained with Imaging Atmospheric Cherenkov Telescopes (IACT), directional instruments with a field of view limited to a few square degrees, that can make observations only in clear and moonless nights. These are obvious limitations in a field of research

2.1 Exploring the gamma ray sky above 30 TeV with LHAASO

aimed to discover unknown sources, and where most of objects have variable emissions, in some case explosive and unpredictable as Gamma Ray Bursts, whose emission can last only a few tens of seconds.

Air shower detectors, detecting the secondary particles of gamma ray induced showers reaching the ground, do not have these limitations, since they can continuously observe the whole overhead sky. Air shower detectors like MILAGRO and ARGO-YBJ, even if with a lower sensitivity with respect to Cherenkov telescopes, have obtained relevant achievements. Starting from their results, new instruments based on the same concepts, but with a much higher sensitivity, like HAWC and LHAASO, have been designed to complement in a natural way the observation of future IACTs.

As pointed out before, the fundamental idea of LHAASO is the development of an instrument able to measure the cosmic ray spectrum, composition and anisotropy in a wide energy range ($\sim 1\text{-}10^5$ TeV) and at the same time to be a sensitive gamma ray telescope at energies from ~ 300 GeV to 1 PeV. In particular, the LHAASO design makes the detector particularly competitive in the gamma ray energy range above a few tens of TeVs, an energy region almost completely unexplored. So far, no photons of energy above 100 TeV have been observed from any source, and above 30 TeV the data are very poor. Only a few sources have been observed to emit photons at these energies, and the data are affected by large uncertainties since the sensitivity of current instruments is not enough to determine clearly the spectral shape.

Actually, gamma ray astronomy at and above 100 TeV is of extreme importance since it is related to one of the most puzzling aspects of high energy astrophysics: the identification of cosmic rays sources. Presently there is a general consensus that cosmic rays with energy up to the so called “knee” of the spectrum (2-4 PeV), and probably even up to 10-100 PeV, are accelerated inside our Galaxy. Supernova remnants (SNR) are long since believed the most likely sources, because the shock wave of the expanding shell could provide the conditions suitable to accelerate particles to relativistic energies, and secondly, the frequency of Supernova explosions and their energy release could provide the total energy budget of cosmic ray in the Galaxy [67].

This idea, however, is still lacking a clear experimental evidence. Actually TeV gamma rays have been observed from a number of supernova remnants, demonstrating that in SNRs some kind of acceleration occurs. However the question whether TeV gamma rays are produced by the decay of π^0 from protons or nuclei interactions, or by a population of relativistic electrons via Inverse Compton scattering or bremsstrahlung, still need a conclusive answer.

AGILE and Fermi observed GeV photons from two young SNRs (W44 and IC443) showing the typical spectrum feature around 1 GeV (the so called “ π^0 bump”, due to the decay of π^0) related to hadronic interactions [68]. This important measurement however does not demonstrate the capability of SNRs to accelerate cosmic rays up to the knee and above. A key observation would be the detection of gamma rays of energy as high as a factor 10 - 30 times less than the maximum energy of galactic cosmic rays. The observation of a gamma ray power law spectrum with no break up to 100 TeV would be a sufficient condition to proof the hadronic nature of the interaction, since the Inverse Compton scattering at these energies is strongly suppressed by the Klein-Nishina effect.

Recently ICECUBE reported a first evidence of neutrinos of astrophysics origin of energy 0.4 - 1 PeV [69]. The nature of such a flux has been object of intense discussions and different hypothesis have been expressed about the galactic or extragalactic origin of the signal. If neutrinos were extragalactic the gamma rays generated by the same processes would be absorbed by the Cosmic Microwave Background (CMB) through pair production and would not be observable at Earth (see the discussion ahead), but in case of a galactic origin of a fraction of the measured neutrino flux, it would be important to detect a photon signal of comparable energy.

LHAASO, thanks to the large area of the array KM2A and the high capability of background rejection, can reach sensitivities above 30 TeV about 100 times higher than that of current instruments, offering the possibility to monitor for the first time the gamma ray sky up to PeV energies.

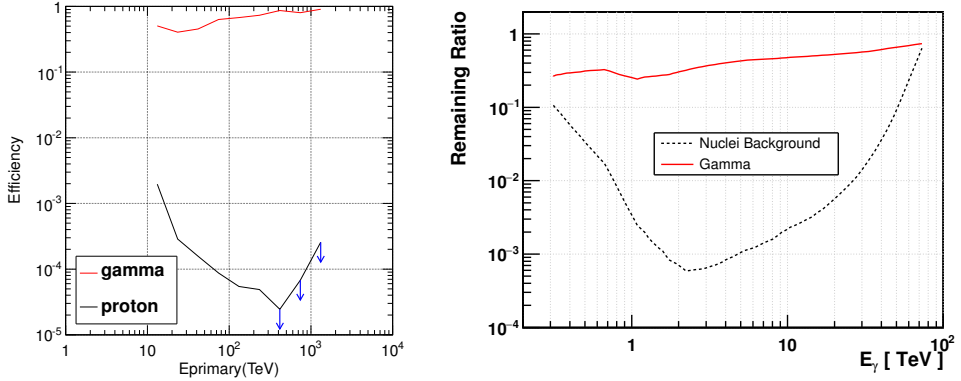


Figure 2: Left: ED and MD simulation Number of events is normalized to a year of flux from the Crab. Right: WCDA only simulation. proton and γ , remaining ratio = $N_{\text{survive}}/N_{\text{totaltriggered}}$. compactness = $N_{\text{firedPMT}}/NPE_{\text{offcoreMAX}}$.

2.1.2. LHAASO sensitivity to gamma rays

LHAASO can study gamma ray sources over almost 4 decades of energy. Fig. 3 shows the differential sensitivity in one year of measurement, obtained by simulating the response of the detector to a gamma ray flux from a source like the Crab nebula one. In the same figure the Crab nebula spectrum is also shown as a reference flux. The LHAASO sensitivity curve is the combination of two components, the first relative to the water Cherenkov detector (WCDA), operating in the energy range $\sim 0.3 - 10$ TeV, the second relative to the KM2A array, sensitive to energies above 10 TeV [70].

Using proton and gamma flux from the Crab direction (zenith within $8^\circ \sim 45^\circ$, spectrum index $\gamma = 2.7$), the simulated efficiency of gamma and proton that pass the hadron rejection cuts is shown on the left in Fig. 2. The simulation includes the ED, MD, and WCDA components of the LHAASO. The hadron rejection cut uses the parameter $C = \log_{10} \left(\frac{N_\mu}{N_{\text{em}}^{1.33}} \right)$. For each simulated energy, the value of the cut is defined by maximizing the Q-value defined as $Q = \frac{N_{\gamma, \text{survive}}/N_{\gamma, \text{inject}}}{\sqrt{N_{p, \text{survive}}/N_{p, \text{inject}}}}$.

Above 10 TeV the measurement of the muon component in the showers allows a very efficient rejection of cosmic ray showers. According to simulations the fraction of cosmic rays that survives the discrimination cuts is 0.01 and 0.004 % at 10 and 30 TeV, respectively, while above ~ 150 TeV is found to be less than 0.0001%. This means that above ~ 150 TeV the study of the gamma emission from a point source can be considered as background free, because after applying the rejection procedure the expected background in a cone around a source is less than one event in one year. Note that changing the observation time, the energy threshold for the background free regime change too.

The minimum flux has been evaluated dividing each energy decade in 4 bins, and requiring a statistical significance of 5 standard deviations per bin and a minimum number of 10 events. In the background free regime, the only request is the detection of at least 10 events. It is interesting to note that in the background free regime, the sensitivity increases linearly with the observation time instead of the square root of time, as in presence of background.

According to simulations, the minimum gamma ray flux detectable by LHAASO is less than 3% of the Crab flux in the energy range $\sim 1-5$ TeV and about 10% Crab around 100 TeV. In Figure 3 the sensitivity curves of other detectors (some in operation, some in project) are also reported. It has to be noted, however, that for a general convention the sensitivity of air shower detectors is reported for one year of operation, while that of Cherenkov telescopes is relative to 50 hours of “on source” measurement. Note that EAS arrays observe every day all the sources in the field of view for a fixed time interval depending on the source declination, while IACTs observe only one source at the time, and only in the season of the year when the source culminates during night time.

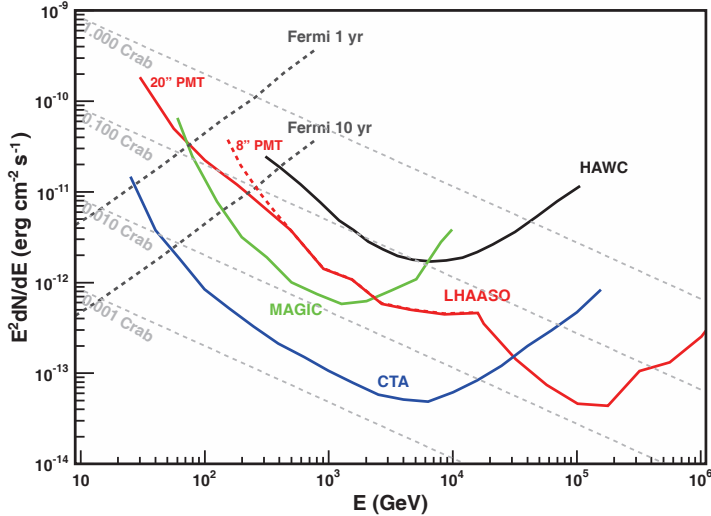


Figure 3: Differential sensitivity (multiplied by E^2) of LHAASO to a Crab-like point gamma ray sources compared to other experiments. The Crab nebula data obtained by different detectors [1] is taken into account, and the spectral index of -2.6 is extrapolated and extended to 1 PeV.

The differences in observation times for which the sensitivity curves are evaluated makes the comparison of different detectors not so straightforward. To evaluate the effective performance of different instruments, one must first determine the type of the observation to be done (sky survey, single source follow-up, observation of a flare/burst, etc.). In the observation of a single source during a flare, for example, lasting a certain number of hours, one must consider the sensitivity curves for *that* observation time. This correction however is not simply obtained by shifting the curves by an amount proportional to the square root of time, because some energy regions can be background free. Due to the different background regime, the sensitivity curves can change shape changing the observation time. Decreasing (increasing) the time with respect to the time used in the figure, the background also decreases (increases) and the measurement can be background free at a lower (higher) energy.

Actually, the two techniques - Cherenkov Telescopes and EAS array - are complementary, each of them exploring different aspects of the gamma ray emission. Below 10 TeV, observing a single source, a telescope array as CTA has a higher sensitivity compared to EAS arrays like HAWC and LHAASO. Thanks to the better angular and energy resolution, a Cherenkov telescope can study more in detail the source morphology and spectral features. EAS arrays however have the possibility to monitor a source all days of the year, that in case of active galactic nuclei (AGNs) or variable sources in general, it's a clear advantage. Moreover, thanks to the large field of view, they have a much bigger chance to catch unpredictable transient events like flares.

Concerning LHAASO-WCDA and HAWC, their geographical positions (China and Mexico, respectively) allow the observation of the same source at different times during the day, increasing the covering time.

At higher energies LHAASO-KM2A is clearly the most sensitive instrument. According to Fig. 3, at 30 TeV the LHAASO sensitivity is comparable to that of CTA-South and 4 times better than that of CTA-North. Above this energy the sensitivity rapidly increases. The minimum observable flux at 100 TeV is $\sim 3 \times 10^{-18}$ photons $s^{-1} cm^{-2} TeV^{-1}$, about a factor ~ 13 (65) lower than that of CTA-South (CTA-North).

At 1 PeV the minimum flux is $\sim 10^{-19}$ photons $s^{-1} cm^{-2} TeV^{-1}$. At the same energy, the combined air shower/neutrino detector Ice-Top/Ice-Cube, located at the South Pole, reports a minimum observable gamma ray flux ranging from $\sim 10^{-19}$ to 10^{-17} photons $s^{-1} cm^{-2} TeV^{-1}$ (depending on the source

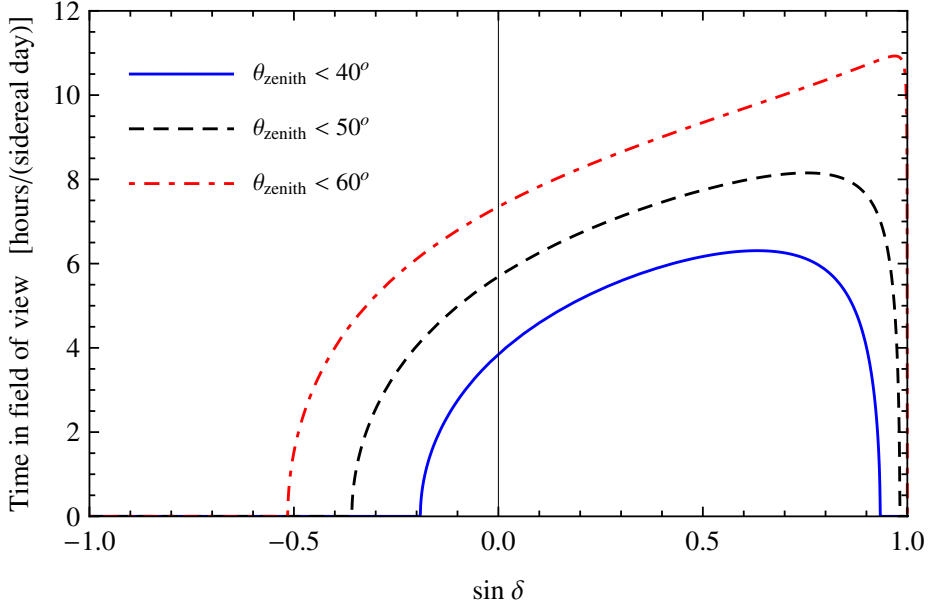


Figure 4: Observation time (hours) per day as a function of the source declination, for 3 values of the maximum zenith angle. The area under the curves is proportional to the total exposure (observation time \times solid angle).

declination) for sources on the galactic plane in 5 years of measurements [71]. It has to be noted, however, that at these energies the observations can be seriously hampered by pair production with the Cosmic Microwave Background (CMB) photons, that can affect the fluxes of galactic sources with a distance larger than a few kpc (see Section 5).

2.1.3. LHAASO and sky survey

One of the most interesting aspect of LHAASO is the large field of view (FOV) and the capability to monitor every day a consistent fraction of the sky. In principle the FOV can include all the sky above the horizon, but the sensitivity decreases at large zenith angles.

Considering only the region of the sky that culminates at zenith angles smaller than 40° , every day LHAASO (located at latitude 29° North) can survey the declination band from -11° to $+69^\circ$ (about 56% of the whole sky) that includes the galactic plane in the longitude interval from $+20^\circ$ to $+225^\circ$. Most of this region will be observed by LHAASO with unprecedented sensitivity. For the the most energetic events, the extension of the field of view to larger zenith angles will increase the sky coverage allowing observations close to the galactic center. Fig. 4 shows the observation time per day as a function of the source declination, for different values of the maximum zenith angle.

In the past, the air shower detectors ARGO-YBJ and Milagro have surveyed about the same region of the sky visible by LHAASO, at energies above 0.3-1 TeV and ~ 10 TeV respectively, with a sensitivity of about 0.3 Crab units [72, 73]. The new EAS array HAWC, in full operation since 2015, has a sensitivity ~ 4 times lower than that expected for LHAASO in the 1-10 TeV region, but more than 100 times lower at 100 TeV. Concerning Cherenkov telescopes, their limited field of view and duty cycle prevent a survey of large regions of the sky. In the past a fraction of the galactic plane have been surveyed by IACTs with an excellent sensitivity in the TeV energy range. HESS performed a survey of the galactic plane between longitude -110° and 65° in the latitude band $\pm 3.5^\circ$ with a sensitivity of ~ 0.02 Crab units at energies above 100 GeV [74], that led to the discovery of more than 60 sources, while VERITAS surveyed the Cygnus region between longitude 67° and 82° with a sensitivity of about 0.04 Crab units [75].

It is interesting to compare the performance in sky survey of LHAASO and the future array CTA. Let's consider a survey of the galactic plane in a longitude interval of 200° and a latitude band from -4°

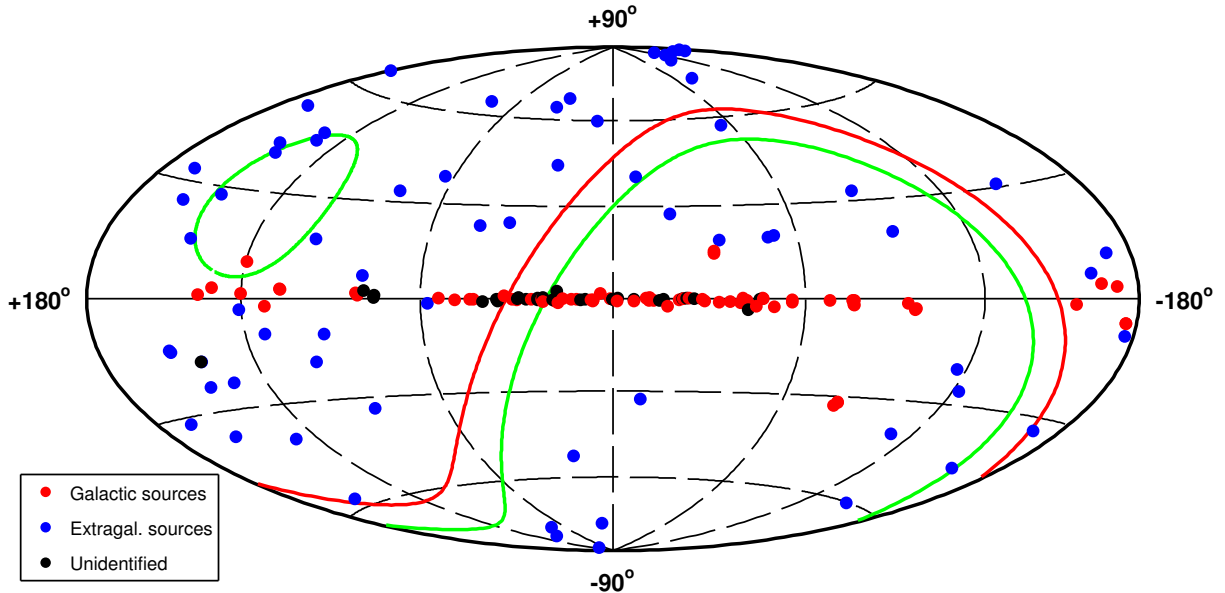


Figure 5: Sky map in galactic coordinates, showing the positions of the known TeV sources. The red line represents the celestial equator. The green lines limits the region of the sky that culminates at zenith angles smaller than 40° at the LHAASO site. The sources are indicated by different colors according to their type: galactic, extragalactic, unidentified (note that the three sources denoted as “galactic” around the position $r.a. = 83^\circ$ and $dec. = -69^\circ$ are actually in the Large Magellanic Cloud).

to $+4^\circ$. A detector like CTA, with its limited field of view, must scan the whole region with different pointings. The number of pointings determines the maximum observation time that can be dedicated to any location. Assuming a field of view of 5° radius and a decrease of sensitivity of about 50% at a distance of 3° from the center (according to the design of SSTs, the CTA-South small area telescopes planned to work at the highest energies), a reasonable step for pointings could be 4° . With this step, 100 pointings are necessary to cover the entire region. Since in one year a Cherenkov telescope can make observations for a total time of ~ 1300 hours (assuming the use of the silicon photomultipliers that allow the data taking also in presence of the Moon), every source can be observed for ~ 13 hours. At 1 TeV, the CTA-South sensitivity in 13 hours is still higher than that of LHAASO in one year. At ~ 25 TeV LHAASO starts to become more sensitive than CTA. Above 30 TeV, the CTA-South sensitivity is no more limited by the background but by the number of detected events (that must be at least equal to 10), hence it must be rescaled linearly with the time. According to this rough estimation, LHAASO would be ~ 4 and 50 times more sensitive than CTA-South at 30 and 100 TeV, respectively.

The LHAASO performance is more impressive in case of an *all sky* survey, where assuming a region of 7 steradians to be scanned, the number of CTA pointings would be as large as ~ 1600 and every location would be observed for less than one hour. In this case the LHAASO sensitivity would be more than ~ 60 and 800 times higher than that of CTA-South for energies of 30 and 100 TeV, respectively.

Finally, in the comparison with CTA-North (that will be located in the Canary island of La Palma at about the same latitude of LHAASO and will observe about the same sky), LHAASO will gain a further factor 4-5 due to the lower sensitivity of the Northern array with respect to the Southern one. Furthermore, it has to be noted that the CTA-North telescopes will have a field of view with a radius not larger than 4° and consequently the number of pointings necessary to cover the region to be scanned will be larger by at least 40% with respect to the value used above, decreasing correspondingly the observation time and the sensitivity.

2.1.4. Galactic gamma ray astronomy

According to the online TeV source catalogue TeVCat [76] at the time of writing the number of known sources is 169. Among them, 60% belong to our Galaxy and 40% are extragalactic (mostly active galactic nuclei of blazar type). About 1/3 of galactic sources are still unidentified, 1/3 are pulsar wind nebulae (PWN), and the remaining are supernova remnants, compact binary systems and massive star clusters. Note the the sensitivity of the current instruments allowed the detection of three “galactic” sources inside an extragalactic object, the Large Magellanic Cloud.

The sky map in Fig. 5 shows the position of all the sources in galactic coordinates. The sky region that culminates at zenith angle smaller than 40° , delimited by green lines in the figure, includes 84 objects, 23 galactic, 47 extragalactic, and 14 still unidentified. All the unidentified sources but one, lay on the galactic plane, being probably galactic objects that cannot be identified due to the number of possible associations in their positional error box.

The spectrum of the galactic sources has been generally measured in the energy range from a few hundreds GeV to 10-20 TeV, and for most of them it is consistent with a power-law behavior. The precise measurement at higher energies would be of extreme interest to understand the emission mechanisms of gamma rays, that for most of the sources is still not understood, and will surely help in the source identification.

So far, only six sources have data above 30 TeV. They are all galactic and are among the most luminous objects of the TeV sky: the supernova remnant RX J1713.7-3946, the pulsar wind nebulae Crab and Vela-X, and the three MILAGRO extended sources MGROJ2031+41, MGROJ2019+37 (actually resolved in two different sources by VERITAS), and MGROJ1908+06, all them probably pulsar wind nebulae too. Their spectrum above 30 TeV is however known with large uncertainties.

Pulsar wind nebulae are the most common type of galactic source. They are believed to be the product of the ultra-relativistic e^\pm wind emitted by young pulsars with large spin-down rates, interacting with magnetic and radiation fields around the pulsar. Other leptons can also be accelerated in the shock produced in the collision of the wind with the environment matter. All these relativistic leptons produce synchrotron and Inverse Compton (IC) radiation.

The Crab nebula, the most luminous TeV source and the first to be detected at TeV energies at the beginning of the Cherenkov telescopes era in 1989, is the most famous example of this class of objects. Its spectral energy distribution (SED) shows a double-humped structure. The first one, extending from radio waves to ~ 1 GeV, is due to synchrotron emission, the second one, peaking at ~ 100 GeV is the product of IC scattering of electrons off low energy photons (synchrotron, thermal and cosmic microwave (CMB) photons). The SED is well defined up to 10-20 TeV. Above this energy is not precisely known. Fig. 6 shows the high energy Crab spectrum measured by different ground based experiments [2, 77, 78, 79, 80]. Even considering the large error bars, a disagreement is evident among the higher energy data. The HEGRA spectrum is a power law with a weak steepening above 10 TeV whereas MAGIC and HESS measurements show a more evident spectral curvature in all the energy range considered. The precise measurement of the high energy emission, the “end” of the spectrum, would bring important information on the particle acceleration and the magnetic and radiation fields in the pulsar environment, constraining some parameters that the lower energy spectrum alone cannot determine unambiguously.

The high energy measurement would also be of great importance in understanding the intriguing phenomena of the Crab nebula flares. Since long considered the “standard candle” for gamma ray astronomy, the Crab nebula has unexpectedly shown a variable behavior in the 100 MeV-1 GeV energy range, with strong flares lasting hours/days [81, 82, 83], and rate variations on time scales of months [84], that are still waiting for a shared interpretation. During flares, the SED shows a new hard component above 100 MeV, generally interpreted as synchrotron emission of a new population of electrons accelerated to energy up to 10^{15} eV, whose origin is still not understood. A TeV flux enhancement in coincidence with GeV flares have been reported by ARGO-YBJ [85], but with low statistical significance, and has not been confirmed by later measurements by the more sensitive Cherenkov experiments

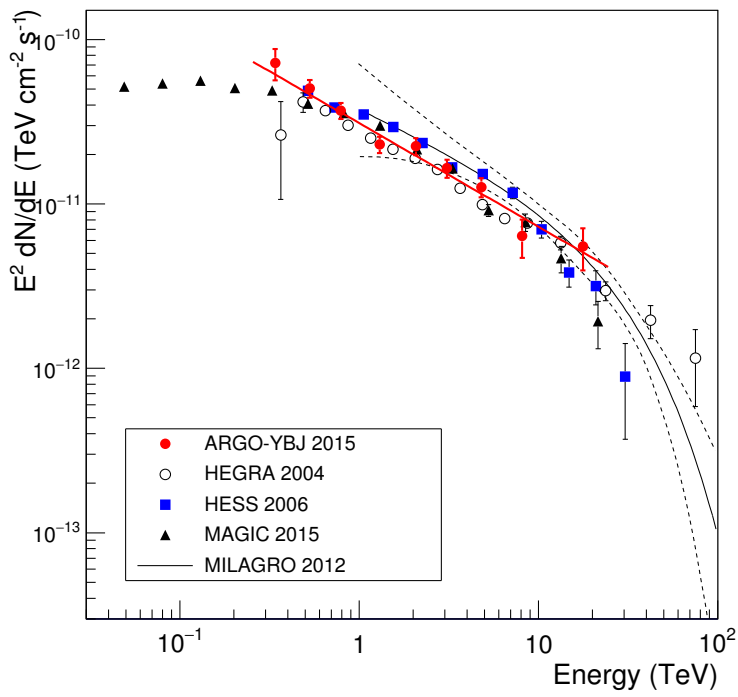


Figure 6: Energy spectrum of the CRAB nebula measured by different experiments.

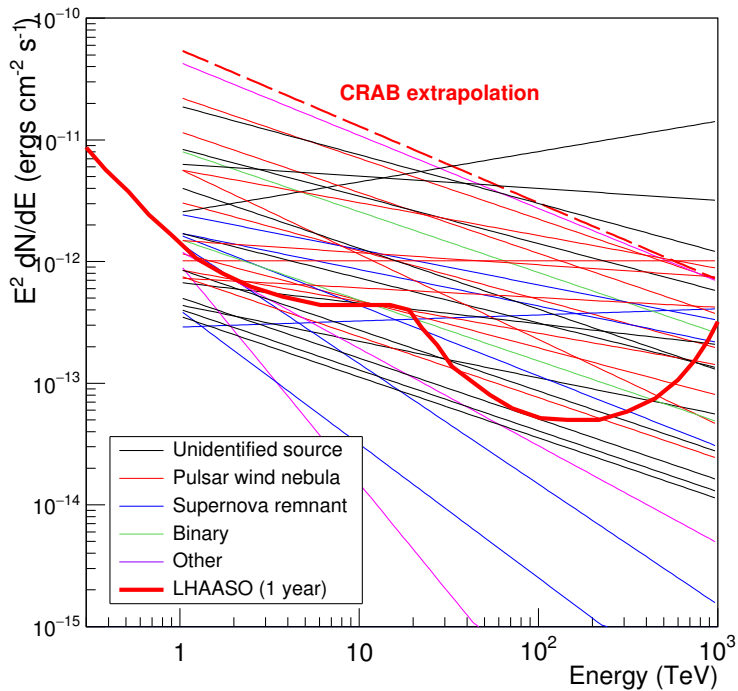


Figure 7: Differential spectra (multiplied by E^2) of the TeV gamma ray sources visible by LHAASO extrapolated to 1 PeV, compared to the LHAASO sensitivity. The dashed red line represents the Crab nebula flux, as measured by ARGO-YBJ [2] extrapolated to 1 PeV as a power law.

[86, 87]. The question of the possible existence of an Inverse Compton emission associated to the GeV flares remains open, in particular in the energy region around and above 100 TeV, where the IC emission is more likely to occur. LHAASO is the most suitable detector for such a study, due to the high sensitivity at these energies and to the possibility of observing the Crab nebula for 5-6 hours every day of the year.

Besides the Crab nebula, LHAASO can perform accurate spectra measurements above 30 TeV for most of the known TeV galactic sources visible from its location. To give a quantitative idea of the LHAASO capabilities, it is useful to compare the detector sensitivity with the fluxes of such sources.

Out of 84 sources crossing the detector field of view with a zenith angle less than 40° , 23 are associated with known galactic objects, while 13, even if not yet associated with certitude with a source, lay on the galactic plane, and can be reasonably considered galactic too. For 35 out of these 36 galactic sources the flux has been measured and reported in [76] and for 24 of them a spectral index is available, ranging from 1.75 to 3.1, with an average value of 2.4.

Fig. 7 shows the spectra of 35 objects extrapolated to 1 PeV (with the same spectral index measured in the TeV region) compared to the LHAASO one-year sensitivity. The spectral index has been set to 2.5 for the sources without an available spectral measurement. It should be specified that for a correct comparison the LHAASO sensitivity should be calculated for each source using its individual spectrum, angular extension and declination, while in the figure the sensitivity refers to a Crab-like source. The spectra extrapolations are clearly unrealistic, since the real spectra likely would show steepening or cutoffs at some energy, but the purpose of the figure is to show that the flux of almost all the considered sources is above the LHAASO sensitivity. LHAASO can study in detail the behavior of the higher energy emission of most of the sources, down to fluxes of $\sim 3 \times 10^{-18}$ photons $s^{-1} \text{ cm}^{-2} \text{ TeV}^{-1}$, at 100 TeV in one year of measurement. These high energy data are likely to play a crucial role for the understanding of the properties of the sources.

Among galactic sources, shell supernova remnants are probably the most interesting to be studied at high energy because the detection of an emission above 100 TeV could be the footprint of hadronic acceleration. In general, from an emission of hadronic origin, one expects a gamma ray spectrum showing the “ π^0 bump” followed by a power law with a slope consistent with parents spectrum slope up to 50-100 TeV, or even more, depending on the parent nuclei maximum energy. A leptonic emission (Inverse Compton scattering of electrons with a power law spectrum) would produce a flatter power law gamma ray spectrum, but with a gradual steepening due to the Klein-Nishina effect. The position of the break depends on the energy of the target photons. For example, electrons with a spectral index of -2.2, scattering off cosmic microwave background (CMB) photons, would produce a gamma ray spectrum of index -1.6 in the Thomson regime, that gradually steepens up to -3.2 in the Klein Nishina regime. At 100 TeV the flux is already suppressed by a factor of 3 with respect to the extrapolation of the spectrum before the break.

Actually, in a SNR one could expect a combination of the two emissions, leptonic and hadronic, with different weights depending on many parameters, as the density of target material for hadronic interaction, the magnetic field strength, the age on the Supernova, etc. that make difficult to identify the emission origin. However, the observation of a spectrum extending above 100 TeV would be a strong indication of a hadronic emission.

So far, only one remnant, SNR RX J1713.7-3946, has data above 30 TeV (actually, the spectrum reaches almost 100 TeV [88]). In this case the spectrum steepens above a few TeV and does not show the “ π^0 bump”, being more consistent with a leptonic emission [89]. All other TeV SNRs have data up to 15 TeV at maximum, Based on the new data, RX J0852.0-4622 [90], Cas A [91], and RCW 86 [92] have a high-energy cutoff around few TeV. but all the spectra are power law with no cutoff or steepening in the observed energy region.

In the LHAASO field of view there are six shell SNRs (Tyco [93], CAS A [94], W51 [95], IC443 [96], W49B [97] and SNR G106.3+2.7 [98]). The measured spectra show a power law behavior without

any cutoff up to the maximum energy reached by the current instruments, that ranges from ~ 2 to 15 TeV for the sources considered. It should be noted that a recent result of VERITAS [99] shows an updated spectrum of Tycho, steeper than the one reported in the figure, that would make the LHAASO measurement more challenging for this source.

Besides the observation of known sources, given the LHAASO capabilities in sky survey, new galactic sources will likely be discovered at high energy, since objects with fluxes at 1 TeV below the current instruments sensitivity but with hard spectra (i.e. spectral index < 2) would be easily detectable by LHAASO above ~ 10 TeV.

2.1.5. Diffuse galactic emission

The diffuse gamma ray emission from the galactic plane is mainly produced by the interactions of cosmic rays with the interstellar gas. The study of the diffuse flux at 30-100 TeV energies would be of extreme importance to understand the propagation and the confinement of the parent cosmic rays in the Galaxy and their source distribution.

The diffuse emission in the TeV range has been measured by ARGO-YBJ, that reports a differential flux of 6×10^{-10} photons $\text{cm}^{-2} \text{s}^{-1} \text{TeV}^{-1} \text{sr}^{-1}$ at 1 TeV, in the galactic longitude interval 25° – 100° for latitudes between $\pm 5^\circ$, consistent with the extrapolation of the Fermi-DGE model for the same region [100]. At higher energies, the best upper limits have been obtained by the air shower array CASA-MIA from 140 TeV to 1.3 PeV with the data recorded in 5 years [101]. At 140 TeV the CASA-MIA 90% confidence level flux upper limit is $F < 1.8 \times 10^{-15}$ photons $\text{cm}^{-2} \text{s}^{-1} \text{TeV}^{-1} \text{sr}^{-1}$, a value very close to the extrapolation of the Fermi-DGE model at the same energy. It has to be noted however that the region studied by CASA-MIA (the longitude interval 50° – 200°) only partially overlaps the region of ARGO-YBJ and likely contains a lower average diffuse flux, being more distant from the galactic center.

A rough evaluation of the LHAASO sensitivity to the galactic diffuse flux can be obtained by multiplying the point source sensitivity given in Fig. 3 by the correction factor $f = (\Omega_{PSF} \Omega_{GP})^{-1/2}$, where Ω_{PSF} is the observation angular window, related to the detector point spread function (PSF) and Ω_{GP} in the solid angle of the galactic plane region to be studied. According to this simple calculation (that however does not take into account the different path in the sky of the galactic plane region with respect to the Crab nebula), the 5 sigma minimum flux detectable by LHAASO in one year in the longitude interval 25° – 100° would be $F_{min} \sim 7 \times 10^{-16}$ photons $\text{cm}^{-2} \text{s}^{-1} \text{TeV}^{-1} \text{sr}^{-1}$ at 100 TeV. This value is a factor ~ 6 lower than the extrapolation of the Fermi-DGE model at the same energy ($F_{DGE} \sim 4 \times 10^{-15}$ photons $\text{cm}^{-2} \text{s}^{-1} \text{TeV}^{-1} \text{sr}^{-1}$), showing that LHAASO will likely be able to study the properties of gamma rays produced by the interaction of cosmic rays with energy up to the “knee” of the spectrum.

2.1.6. Attenuation of gamma rays in space

A major problem to face when working at high energy, is the absorption of gamma rays due to pair production in the interstellar and intergalactic space. The process causes an attenuation of the gamma ray flux, usually expressed as $I = I_0 \exp^{-\tau}$, where the value of the optical depth τ depends on the gamma ray energy, the source distance and the density and energy of the target photons along the gamma ray path to Earth. The absorption increases with the gamma ray energy and the source distance, being particularly effective for extragalactic sources, but at sufficiently high energy can affect also the flux of galactic objects.

In general, the spectral energy distribution of target photons, both in interstellar and intergalactic space shows three broad peaks: the first one centered in the optical band ($\lambda \sim 1 \mu\text{m}$), mostly due to stellar light, the second one in the infrared band ($\lambda \sim 100$ – $200 \mu\text{m}$), due to light absorbed and re-radiated by dust, and the third one due to the Cosmic Microwave Background.

Pair production occurs when the energy in the center of mass exceeds two electron masses, namely $E_\gamma \times E_{ph} > 2 m_e^2 c^4 / (1 - \cos\theta)$, where θ is the angle between the two photons. The cross section is maximum when $E_\gamma(\text{TeV}) \times E_{ph}(\text{eV}) = 1.07 / (1 - \cos\theta)$. This means that gamma rays of ~ 1 TeV mostly interact with photons of ~ 1 eV (starlight), gamma rays of ~ 100 TeV interact with infrared photons,

2.1 Exploring the gamma ray sky above 30 TeV with LHAASO

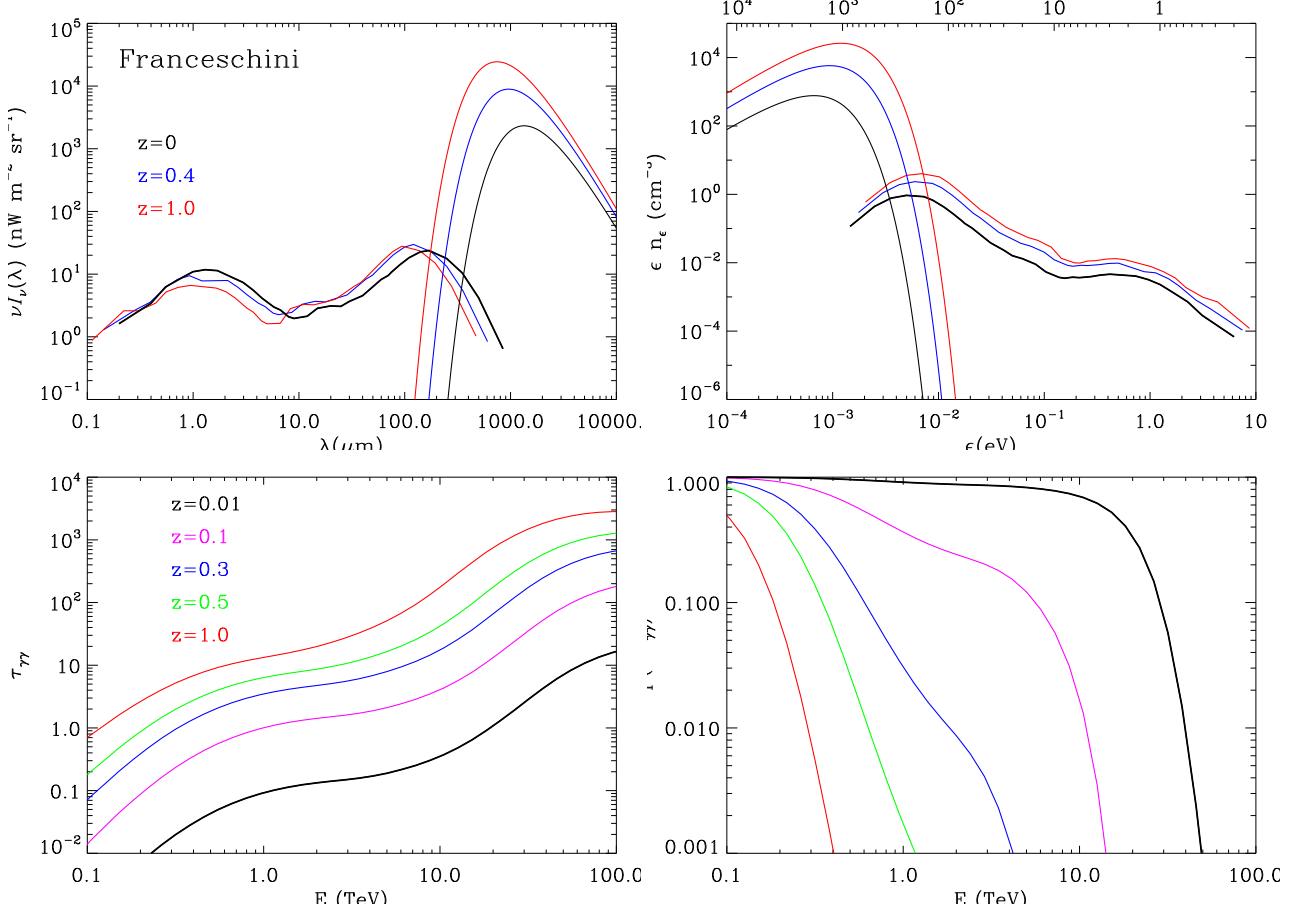


Figure 8: Extragalactic gamma ray absorption according to [3]. Top left: EBL and CMB intensity as a function of wavelength. The starlight peaks at $\sim 1 \mu\text{m}$, the dust emission at $\sim 100 \mu\text{m}$, and the CMB blackbody radiation at $\sim 10^3 \mu\text{m}$. Top right: CMB and EBL number density as a function of photon energy. Bottom left: opacity as a function of gamma ray energy. Bottom right: attenuation of gamma ray flux as a function of gamma ray energy.

and gamma rays of ~ 1 PeV with CMB. The three radiation components generate different absorption features in the source spectra, observable as changes in the spectrum slope. The precise evaluation of these spectrum features depends on the exact knowledge of the low energy radiation intensity. CMB is precisely measured, while the intensity of optical and infrared photons has large uncertainties. For this reason the evaluation of the opacity parameter is mostly indirect, based on assumptions and models, especially in the extragalactic case.

Concerning galactic sources, the absorption depends on the relative position of the source and the Sun inside the Galaxy, that determines the amount of target photons along the gamma ray path. According to [102], up to ~ 10 TeV the gamma ray attenuation would be less than a few percent for every source position. At ~ 100 TeV the flux of a source close to the galactic center would be reduced by 20%. The reduction is smaller for a source located in more peripheral regions, unless the source is beyond the galactic center, for which the absorption can reach almost 50%. Above ~ 200 TeV the CMB becomes effective and the absorption depends on the distance rather than on the position in the Galaxy: at ~ 2 PeV, about 70% of the flux of a source at the distance of the galactic center (8.5 kpc) is absorbed, while at 20 kpc the absorbed flux is 95%. From these calculations it is evident that the absorption is not an obstacle for galactic gamma ray astronomy up to a few hundred TeV, while at higher energies it can seriously hamper the observations.

The situation is more problematic for extragalactic astronomy. The absorption of gamma rays from ~ 1 TeV to ~ 200 TeV is mostly due to the Extragalactic Background Light, that includes light from

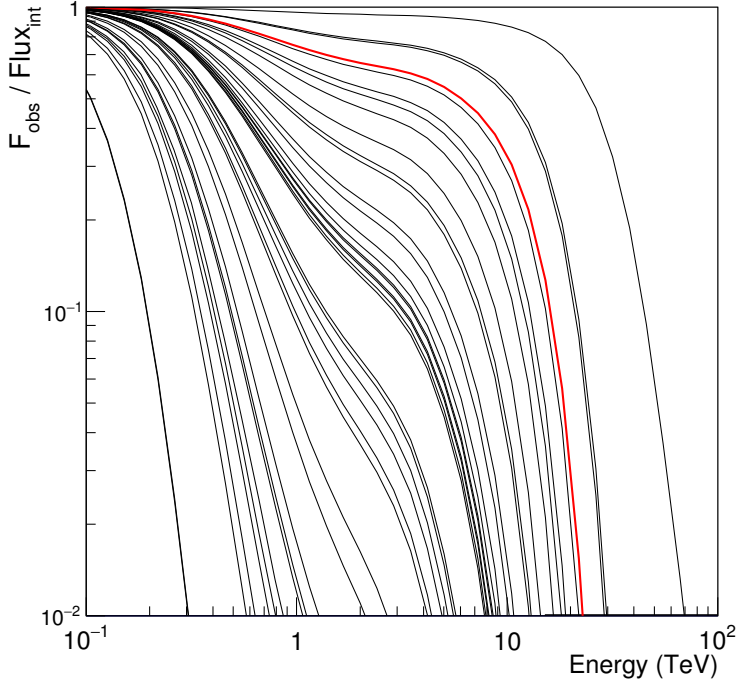


Figure 9: Ratio between the observed and the intrinsic flux of 39 extragalactic objects in the LHAASO field of view, with known redshift. The red curve indicate the blazar Mrk421, one of the closest sources.

stars/AGNs and dust emission, and whose intensity is related to the whole Universe history, star formation and galaxy evolution. The absorption above 200 TeV is mostly due to CMB. The measurement of EBL is however extremely difficult, in particular in the infrared region. A lower limit to the EBL has been obtained integrating the light of all the resolved galaxies.

The optical depth τ is generally expressed as a function of the gamma ray energy and the source redshift z . The evaluation of τ requires the modeling of the EBL spectrum at different redshifts. Fig 8 shows the EBL intensity and the τ values obtained by Franceschini et al. [3], as reported in the review article [103]. According to these results, gamma rays above 30 TeV from a source at $z=0.01$ are 90% absorbed. At $z=0.03$ (that is the redshift of the *closest* blazars observed at TeV energies, Mrk421 and Mrk501) the flux above ~ 20 TeV is 95% absorbed. Increasing the energy or the redshift, the absorption becomes stronger and can seriously limit the study of most extragalactic sources.

2.1.7. Extragalactic gamma ray astronomy

A wide FOV experiment with a large duty cycle like LHAASO is suitable to the observation of variable sources as AGNs. As for galactic sources, the measurements of AGNs high energy spectra would be of extreme importance for the understanding of the emission mechanisms, but the observations are seriously hampered by the absorption of gamma rays during their travel to Earth.

In the sky region of declination between -11° and $+69^\circ$ there are 47 extragalactic objects known as TeV emitters. Most of them are active galactic nuclei of the blazar class, whose redshift, measured for 39 of them, ranges between 0.0044 and 0.94. Fig.9 shows the flux attenuation as a function of energy for the 39 sources with known distance, obtained using the parametrization of [3]. According to these calculations, the possibility to observe a signal above 30 TeV from an extragalactic source appears limited to the very close objects. Even Mrk421 ($z=0.031$), one of the most luminous blazars of the sky, could be observable at these energies only during particularly strong flares.

Presently there are only three sources closer than Mrk421 in the LHAASO field of view: the ra-

2.1 Exploring the gamma ray sky above 30 TeV with LHAASO

dio galaxy M87 (z=0.0044), the radio galaxy NGC1275 (z=0.018), and the (probably) blazar IC310 (z=0.019). M87 and IC310 have hard spectra and their possible detection at high energy depends on the flux during active states. NGC1275 have a very soft spectrum and the detection seems unlikely.

It is interesting to mention the starburst galaxy M82 at z=0.0007, the closest extragalactic source, that culminates at a zenith angle of almost 41° and for this is not included in Fig. 9. M82 is a steady source, one of the two starburst galaxies detected at TeV energies, with a TeV flux $\sim 1\%$ of the Crab nebula. Starbursts are galaxies with a high star formation rate, probably triggered by a previous collision with an other galaxy. They host a large amount of gas where massive stars are formed, causing a high rate of supernova explosions. If supernova remnants are the sites where cosmic rays are accelerated, one expects a large flux of cosmic rays inside these galaxies and a consequent high flux of gamma rays produced by the interactions of cosmic rays with the ambient gas. The measurement of the spectrum at high energy would be of great value to understand the origin of gamma rays. The observation of a de-absorbed spectrum that extends up to 100 TeV as a power law would be a strong support of the hadronic origin of gamma rays and of the idea that supernova remnants accelerate cosmic rays. M82 is a very interesting object to be studied, but its position in the sky makes challenging the detection by LHAASO, whose success will depend on the high energy flux and spectral slope, that now is known with large errors in the TeV energy range [104].

Besides the study of the sources physics, one can use extragalactic objects to study the EBL itself, observing the spectral features due to the EBL absorption in nearby objects. Making reasonable assumptions on the intrinsic source spectra, from the observation of the position and shape of the spectral break of gamma ray sources at different z , one can infer the spectrum of EBL, and get information on the Universe history and evolution (see [105] for a review).

In the past, the unexpectedly hard spectra observed in some blazar after the correction for the absorption according to the existing EBL models, provided upper limits on the background light at optical/near-infrared wavelengths, leading to the rejection of the models predicting the largest absorptions [106]. More recently, the measurement of the spectra of 150 blazars at different redshifts by Fermi-LAT at energies above 1 GeV allowed the measurement of the EBL intensity in the optical-UV band [107]. Similarly, the observation by HESS of almost 20 blazar spectra at energies above ~ 100 GeV provided the spectrum of the EBL at energies of the optical “bump” [108]. An even more recent work [109], using 86 spectra of blazars measured by different experiments, with minimal assumptions on the intrinsic spectra, reports an evaluation of the EBL spectrum from 0.3 to 100 μm , that appears to be very close to the lower limit given by the integrated light of resolved galaxies. All these measurements are consistent with an EBL intensity lower than what previously expected.

The EBL infrared region at $\lambda \sim 10\text{-}70 \mu\text{m}$ is particularly difficult to measure because of the foreground light due to the interplanetary dust (zodiacal light) and could be determined, or at least constrained, by the spectra of “nearby” extragalactic objects. LHAASO, with its sky survey capability, could increase the sample of these objects and study their spectral features above 10 TeV to probe the EBL in the infrared region.

The discovery that the Universe is more transparent to gamma rays than previously thought and the detection of more and more distant TeV blazars (as the gravitationally lensed blazar B0218+357 at z=0.944 [110], and the Flat Spectrum Radio Quasar PKS 1441+25 at z=0.939 [111]), open the possibility of new scenarios, in which high energy gamma rays can be observed even from very distant sources.

A further decrease in the level EBL is practically impossible, because it is already close to the lower limit obtained by the galaxy count. A detection of TeV gamma rays from objects at $z > 1$ would need new approaches to explain or avoid extremely hard intrinsic blazar gamma-ray spectra.

One possibility is that gamma rays observed from high redshifts are the results of cascades from ultra-high energy ($\sim 10^{17} - 10^{19}$ eV) cosmic rays [112]. Cosmic rays below the GZK cutoff do not lose a significant part of their energy in interactions with background photons and can travel over large

cosmological distances, producing photons closer to the observer via electromagnetic cascades initiated by interactions with CMB and EBL photons. As long as the the magnetic field along the path is small enough ($< 10^{15}$ Gauss), ultra energetic protons can travel almost rectilinearly and the broadening of both the proton beam and the cascade electrons can be less than the typical point spread function of detectors. This idea however has to face some problems with the energetics of the emission and the trajectory deflection, that requires very stringent limits on the magnetic fields, and to the fact that so far no statistical significant excess in ultra high energy cosmic rays have been observed from the direction of AGNs.

A more exotic scenario, beyond the standard particle physics, is based on the existence of a hypothetical axion-like particle (ALP), a very light pseudo-scalar spin-zero boson, that coupling with the electromagnetic field, can mix with photons and generate oscillations. The oscillation of VHE photons into ALPs in ambient magnetic fields would decrease the opacity of the Universe, as ALPs propagate unimpeded over cosmological distances [113].

An other unconventional way to increase the transparency of the Universe is to modify the cross section of the photon-photon collision and pair production processes. The Lorentz-invariance violation, predicted by quantum-gravity theories when approaching the Planck energy scale (i.e. 1.22×10^{28} eV), would produce a shift in the energy threshold for pair production at high energies. Despite a difference of fifteen orders of magnitude between the gamma rays observed on Earth and the Planck energy scale, the pair-production threshold could be already affected at around 15 TeV. The optical depth would decrease as the photon energy increases, leading to a re-emergence of the gamma ray flux at high energy [114].

Thanks to its high sensitivity at higher energy and capability to measure at the same time a large number of sources, LHAASO can collect a big sample of spectral data from sources at different redshifts, and probe all these unconventional and attractive hypothesis, that could open a window on a new physics.

2.2. Galactic gamma-ray Sources

Executive summary: In the γ -ray sky, the highest fluxes come from Galactic sources: supernova remnants (SNRs), pulsars and pulsar wind nebulae (PWNe), star forming regions, binaries and micro-quasars, giant molecular clouds, Galactic center, and the large extended area around the Galactic plane. The mechanisms of γ -ray emission and the physics of the emitting particles, such as the origin, acceleration, and propagation, as well as the condition for emission are of very high astrophysical significance. A variety of theoretical models have been suggested for the relevant physics and emission energies $E \geq 10^{14}$ eV are expected to be crucial in testing them. In particular, this energy band is a direct window to test at which maximum energy a particle can be accelerated in the Galactic sources and whether the most probable source candidates such as Galactic center and SNRs are “PeVatrons”.

Designed aiming at the very high energy (VHE, > 100 GeV) observation, LHAASO will be a very powerful instrument in the astrophysical studies. Over the past decade, great advances have been made in the VHE γ -ray astronomy. So far, more than 170 VHE γ -ray sources have been observed, and 42 of these Galactic sources fall in the LHAASO field-of-view. With a sensitivity of 10 milli-Crab, LHAASO can not only provide accurate spectrum for the known γ -ray sources, but also search new TeV γ -ray sources [4]. In the following sub-sections, the observation of all the galactic sources with LHAASO will be discussed in details.

2.3. Supernova Remnants

2.3.1. γ -ray observation of SNRs

Among Galactic γ -ray point sources, SNRs are considered to be one of the most plausible candidates for acceleration of cosmic-rays up to PeV energies [115, 116, 117]. According to Dave Green’s Galactic SNR catalogue ¹, 295 SNRs have been detected up to now. Most of these SNRs have been detected in low energy bands. In the GeV energies range, the Fermi-LAT collaboration reported their first SNR catalog based on three year’s survey data, in which 12 firm identifications and 11 possible associations with SNRs were found [5]. In the TeV energies range, there have been at least 23 SNRs or SNR candidates detected up to now, 10 of which are also GeV γ -ray emitters ². Furthermore, there are 34 unidentified TeV γ -ray sources which do not have clear counterparts in other wavelengths. Unlike from the Fermi unidentified sources, which are expected to be dominantly constituted by active galactic nuclei [118], most of the unidentified TeV sources are located in the Galactic plane (see Fig. 1) and could be potential SNRs. Fig.10 illustrates the locations of those sources (symbol) and their visibility by LHAASO (shaded region). In total, 92 out of 295 SNRs in Green Catalog, 6 GeV SNRs or SNR candidates, 2 TeV SNRs and 6 GeV-TeV SNRs are in the field of view of LHAASO. Besides, 17 TeV unidentified sources locate in the field of view of LHAASO.

Moreover, it has been found that some SNRs could emit TeV γ -rays while in GeV energy band there was no observation results, such as G106.3+2.7 and HESS J1912+101. G106.3+2.7 was first observed by DRAO at radio energy range [119]. In 2000, Pineault & Joncas confirmed the object as a SNR, with an estimated age of 1.3 Myr and distance of 12 kpc [120]. The pulsar PSR J2229+6114 is located at the northern edge of the remnant’s head and it is associated with boomerang-shaped radio and X-ray emitting wind nebula. At GeV energy band, the EGRET source 3EG J2227+6122 is compatible with the pulsar position, as well as the main bulk of the radio remnant [121]. At TeV energy band, VERITAS reported the total flux from the SNR G106.3+2.7 above 1 TeV is about $\sim 5\%$ of the Crab Nebula in 2009 [98]. HESS J1912+101 is plausibly associated with the PSR J1913+1011, which is detected by H.E.S.S. experiment. The integral flux between 1-10 TeV is 10% of the Crab Nebula and the measured energy spectrum can be described by a power-law with a photon index ~ 2.7 . From the current observation on these two TeV SNRs, we can conclude that LHAASO might discover a number of SNRs compared to conservative predictions based on the current SNR catalogs.

¹<http://www.mrao.cam.ac.uk/surveys/snrs/>

²<http://tevcat.uchicago.edu/>

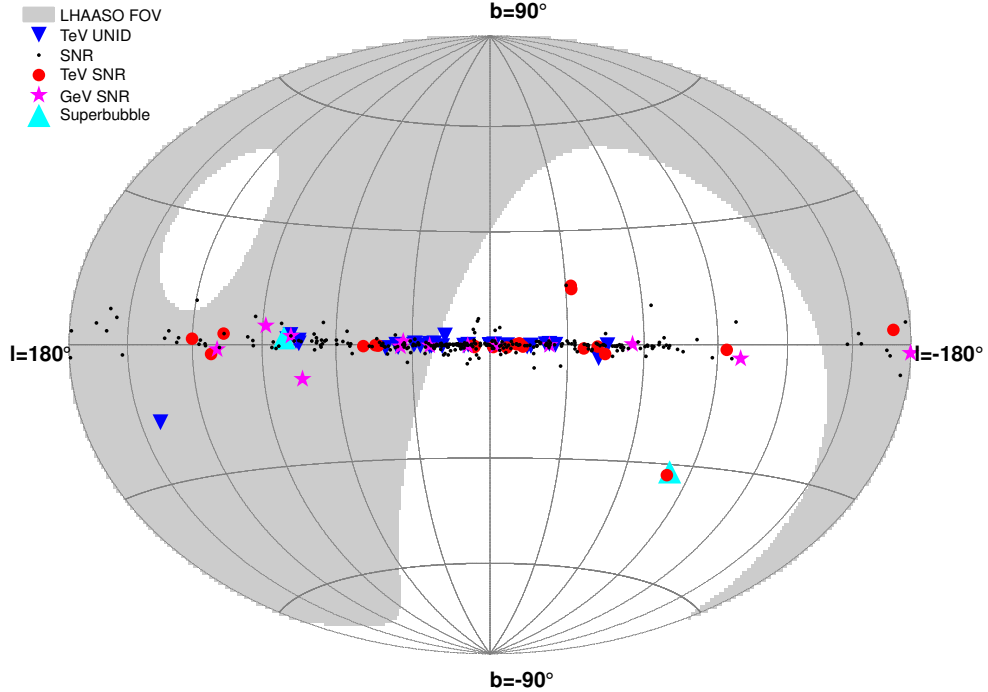


Figure 10: Locations of SNRs and unidentified TeV γ -ray sources in Galactic coordinates, compared with the field-of-view of LHAASO (grey region) [4]. Black dots represent SNRs from Green¹, red filled circles and magenta stars show TeV and GeV γ -ray SNRs¹ [5], blue triangles represent the unidentified TeV γ -ray sources, and cyan triangles represent two super-bubbles which were detected in TeV γ -ray bands.

2.3.2. Hadronic or leptonic origin of the γ -ray emission

Generally, there are two types of scenarios for the production of high-energy γ -rays from SNRs: the leptonic interaction via inverse Compton(IC) scattering of background photos by relativistic electrons and hadronic interaction via decay of neutral pions produced by inelastic collisions of relativistic ions with ions in the background plasma [122, 123, 6, 7].

Up to now, the evidence for efficient leptonic acceleration in SNRs is now clearly established [124, 125]; however, the question of whether SNRs are efficient hadron accelerators is more difficult to answer. The recent observation of γ -ray spectrum for W44 and IC443 by Fermi shows that accelerated protons and nuclei via hadronic interactions with ambient gas and subsequent π^0 decays into γ -rays [126, 68], but no observations above 10 TeV region have succeeded in identifying hadronic acceleration. According to the current experiment results [127, 96, 128], the measurement of spectrum is up to several TeV and the error value is not enough to explain the emission mechanism in high energy region. With the wide FOV, LHAASO is suitable not only to measure their SEDs but also carry out morphologic investigations on those sources at high energies.

Young SNRs, typified by Tycho and Cassiopeia A (Cas A), are believed to be energetic accelerators of relativistic particles. Tycho's SNR, which appeared in 1572 [129], has been observed from radio to TeV γ -ray band [130, 131, 132, 133, 134, 93]. At the GeV range, Fermi-LAT reported a 5σ detection of GeV γ -ray emission from Tycho, which can be described by a power-law with a photon index 2.3 ± 0.2 [135]. At the TeV range, VERITAS observed that the total flux of Tycho above 1 TeV is $\sim 0.9\%$ of Crab Nebula and the spectrum index between 1 TeV and 10 TeV is about 1.95 ± 0.51 in 2011. But in 2015, the spectrum index is 2.92 ± 0.42 [99]. If the spectral index is about 2 up to 10 TeV as the VERITAS reported in 2011, it implies that the corresponding spectrum of primary protons extends without a significant steepening or a cutoff to at least several hundred TeV [136, 67]. Due to the large uncertainties of the

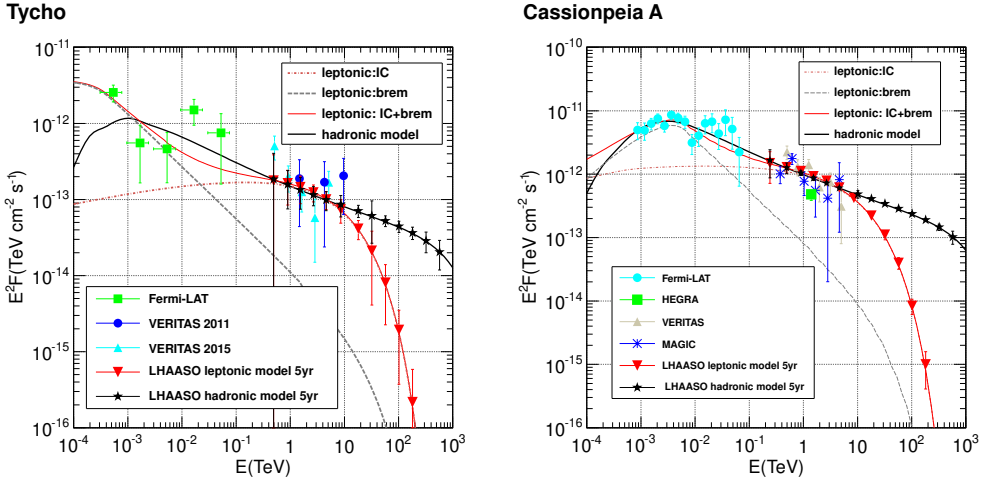


Figure 11: Expectation of the LHAASO project on the historical SNR spectrum [4].

data sets of Fermi and VERITAS, the energy spectrum from GeV to TeV can be described by a broad range of function, which is not enough to constrain the high energy γ -ray emission.

Cas A, which might appear in 1680, is the youngest of the historical Galactic SNRs [126, 137]. It is one of the best studied objects with both thermal and non-thermal broad-band emission ranging from radio wavelengths to TeV γ -rays [138, 94, 137, 139]. TeV γ -ray observations revealed a rather modest γ -ray flux, compared to the synchrotron radio through X-ray emission, which further strengthens the argument for a rather high magnetic field. In the GeV range, Fermi-LAT observation suggests that leptonic model can not fit the turnover well at low energy because the bremsstrahlung component that is dominant over IC below 1 GeV has a steep spectrum, and hadronic emission describing the γ -ray spectrum by a broken power-law is preferred. However, because the observed TeV γ -ray fluxes have large statistical uncertainties, it can not be judged yet whether the TeV γ -rays are generated by interactions of accelerated protons and nuclei with the ambient gas or by electrons through bremsstrahlung and inverse Compton scattering. And the maximum energy of the observed TeV γ -ray is only several TeV, the question whether Cas A accelerates particles to PeV energy is still open.

At the LHAASO site, the effective observation time is 6.2 hours per day for Tycho and 6.8 hours per day for Cas A with zenith angle less than 45° . Tycho culminates with a zenith angle of 34° and Cas A culminates with a zenith angle of 29° . The expected spectrum of Cas A from 0.3 TeV to 1 PeV is shown in Fig.11, we can see that from 300 GeV to 500 TeV, the statistic error of data obtained by LHAASO will be less than 10%. Due to the Klein-Nishina effect, the spectrum dominated by electrons is much softer than the hadronic emission above 10 TeV, and the expected result of LHAASO with a low statistic error can give a reasonable explanation on the high energy range. These estimations show that the LHAASO observation would be just sufficient not only to give the final judgement for the hadronic/leptonic models but also to confirm whether the historical SNRs are PeVatrons or not.

Middle-aged SNRs that are associated with γ -ray emission are usually in interaction with molecular clouds and feature hadronic emission in γ -rays. As one of the well studied middle-aged SNRs, IC 443 possesses strong molecular line emission regions that makes it a case for an SNR interacting with molecular clouds. The X-ray emission of IC 443 is primarily thermal and peaked towards the interior of the northeast shell, indicating that IC 443 is a thermal composite or mixed-morphology SNR. Fermi [140] in the GeV band and VERITAS [96], and MAGIC [141] in the TeV band detected the γ -ray emission from IC 443 and obtained the spectra up to 1 TeV, but there is not yet observation at higher energies, which is very important for determination on γ -ray emission mechanism.

The middle-aged SNR W51C (G49.2-0.7) also interacts with the molecular clouds. The W51 region was heavily studied as it is known to host several objects. It contains three main components: two star-

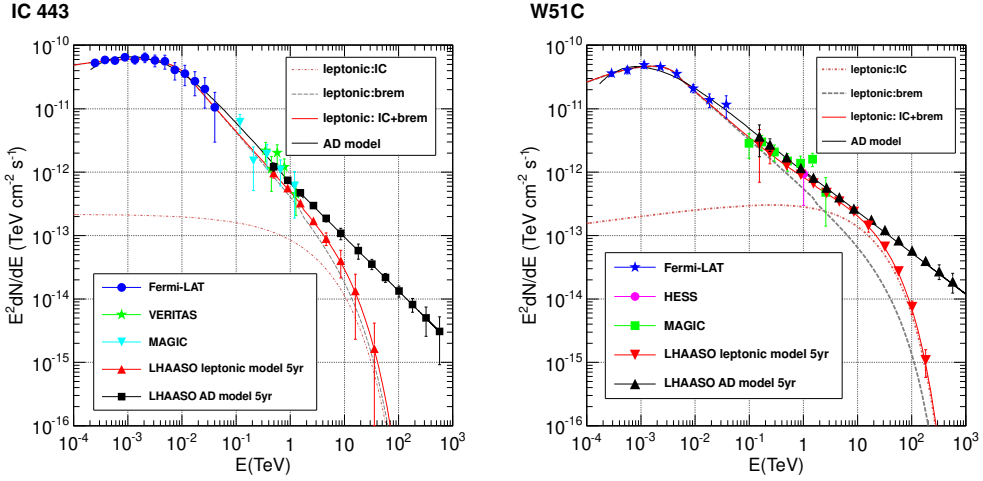


Figure 12: Expectation of the LHAASO project on SNRs interaction with molecular clouds spectrum [4].

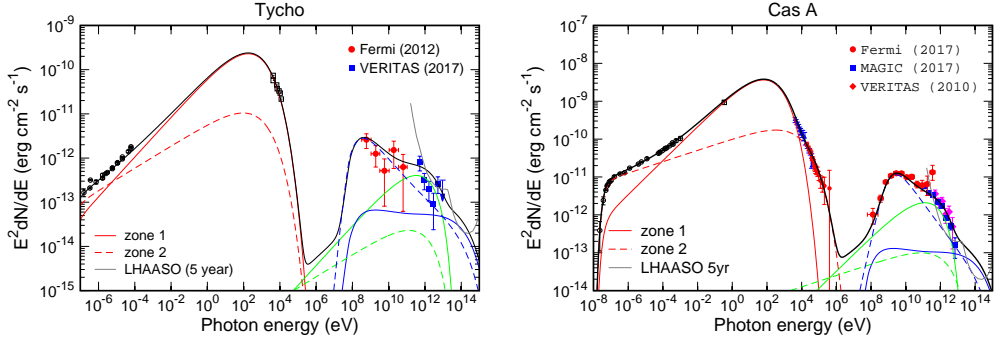


Figure 13: SED of SNR Cas A (left) and Tycho (right). The black solid line represents the total emission from zone1 (solid) and zone 2 (dashed) with components: synchrotron (red), inverse Compton (green), and p-p collision (blue).

forming regions W51A and W51B surrounded by very giant molecular cloud, and SNR W51C. W51C is a radio-bright SNR at a distance of 6 kpc from Earth with an estimated age of $\sim 3 \times 10^4$ yr [142]. W51C is visible in X-rays showing both a shell type and center filled morphology. Shocked atomic and molecular gases have been observed, providing direct evidence on the interaction of W51C shock with a large molecular cloud [143, 95]. The GeV spectral result provided by Fermi indicates that leptonic model is difficult to explain γ -rays production and the most reasonable explanation is that hadronic interaction taking place at the shocked shell of W51C emits GeV γ -rays [144]. Moreover, MAGIC and H.E.S.S. also indicates the γ -ray emission from W51C tends to be dominated by π^0 -decay up to several TeV [145, 143, 95]. But this still has uncertainties for the acceleration mechanism above 10 TeV.

At the LHAASO site, the effective observation time is 6.53 hours per day for IC 443 and 6.0 hours per day for W51C with zenith angle less than 45° . IC 443 culminates with a zenith angle of 8° and W51C culminates with a zenith angle of 16° . The expectation of LHAASO is given in Fig. 12, compared with the measurement of Fermi, MAGIC and VERITAS. From 300 GeV to 500 TeV, the statistic error of data obtained by LHAASO will be less than 10%. The discrepancy between the expectations from the two models will reach more than 5 sigma above 20 TeV. It indicates that LHAASO will make a great contribution to the acceleration measurement in the TeV range, providing the final judgement on leptonic or hadronic origin.

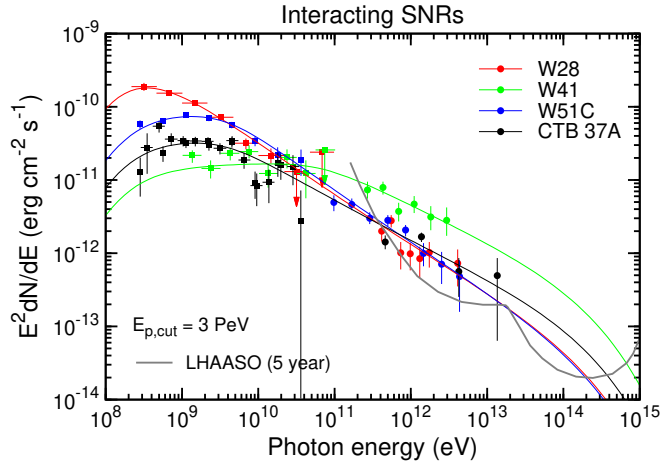


Figure 14: Hadronic emission spectra expected for four SNRs that interact with molecular clouds using the diffusive proton model [6, 7].

2.3.3. Are SNRs PeVatrons?

LHAASO will be powerful in showing whether Galactic SNRs are PeVatrons or not. Whether young SNRs are PeVatrons or not may have an effect on their γ -ray spectra. With 158h of high quality data, MAGIC collaboration [91] updated the TeV gamma-ray spectrum of SNR Cas A and revealed a high-energy cutoff of 3.5 TeV with 4.6σ significance. This spectral feature seems to rule out Cas A as a PeV particle accelerator if the TeV γ -ray emission has a hadronic origin. However, the cutoff also can be explained by the leptonic process in a two-zone model [146]. In this model, the electrons accelerated by the forward shock (zone 1) dominantly contribute the TeV γ -rays via the inverse Comptonization, while the GeV γ -rays are mainly produced by the protons accelerated by the inward/reverse shock (zone 2) (see Fig. 13). Thus, the proton spectrum does not need a cutoff, implying that Cas A can still be treated as a PeVatron. Moreover, the hadronic γ -rays from zone 1 can dominate the hundreds of TeV range if the total energy in the relativistic protons accelerated by the forward shock reaches the order of 10^{48} erg, which is also sufficient to supply the high-energy component of CR ions in the frame of SNR origin of Galactic CRs [147]. This two-zone model also could be applied to the Tycho SNR and explain the very soft TeV spectrum observed by VERITAS (see the right panel of Fig. 13). The spectral data obtained with LHAASO can thus be used to determine the maximum energy to that energetic protons can be accelerated by the SNR shock wave.

Using the hadronic interaction model for the diffusive protons [6, 7], Fig. 14 shows the expected hadronic spectra of the middle-aged SNRs W28, W41, W51C, and CTB37A for a proton energy cutoff at 3PeV, which are within the detection ability at the TeV photon energy for 5-yr LHAASO observation.

2.4. Star-forming Regions

Star-forming regions are the factories of stars, containing young OB stars and related super-bubbles with strong collective stellar winds. The wind shocks and turbulence created by the collective stellar winds can accelerate particles to the relativistic regime. So they are the potential CR sources. On the one hand, the recent measurements of ^{60}Fe abundance in CRs [148] indicate that a substantial fraction of CRs could be accelerated in young OB star clusters and related super-bubbles. Furthermore, the measurements of the Galactic diffuse γ -ray emission show that the CRs have a similar radial distribution as OB stars rather than SNRs [149, 150]. On the other hand, super-bubbles do have sufficient kinetic energy, supplied by supernova explosions therein or collective stellar winds, to provide the flux of the locally measured CRs [151]. Meanwhile, these objects should be visible in γ -rays due to the freshly accelerated CRs interacting with ambient gas. In this regard a principal question is whether these objects can operate also as PeVatrons, i.e. whether they can provide the bulk of the locally observed CRs up to the so-called knee around 1 PeV. The most straightforward and unambiguous answer to this question would be the detection of γ -rays with a hard energy spectrum extending to energies well beyond 10 TeV.

2.4.1. Cygnus region

The Cygnus region of the Galactic plane is the famous region in the northern sky for the complex features observed in radio, infrared, X-rays, and γ -rays. It contains a high density interstellar medium and is rich in potential CR acceleration sites such as Wolf-Rayet stars, OB associations, and SNRs. This region is home of a number of GeV γ -ray sources detected by Fermi-LAT [152] and several noteworthy TeV γ -ray sources detected by Milagro, ARGO-YBJ in the past decade. The Cygnus Cocoon, located in the star-forming region of Cygnus X, is interpreted as a cocoon of freshly accelerated CRs related to the Cygnus super-bubble. The extended TeV γ -ray source ARGO J2031+4157 (or MGRO J2031+41) is positionally consistent with the Cygnus Cocoon discovered by Fermi-LAT at GeV energies in the Cygnus super-bubble, and another TeV source MGRO J2019+37 is a mysterious source only being detected by MILAGRO [10, 11] above 20 TeV and VERITAS [75] above 1 TeV. The reason for the hard SED from such a spatially extended region is totally unknown. The discovery of this kind of sources and the more detailed multi-wavelength spectroscopic investigations can be an efficient way to explain the radiation mechanism of them.

Figure 15 shows all the spectral measurements by Fermi-LAT [8], ARGO-YBJ [9], Milagro [11], and the expectation results with LHAASO. One year observation of LHAASO will be sufficient to give a judgement on the different energy cutoff models from 300GeV to several hundred TeV. It will provide important information for investigating the particle acceleration within the super-bubble.

2.4.2. W49A: a Galactic mini-starburst

As a part of the W49 complex [153], the powerful thermal radio continuum source W49A is one of the brightest Galactic giant radio H II regions ($\sim 10^7 L_\odot$) and is identified as an active star-forming region. It is located in a giant molecular cloud with a total mass of $\sim 10^6 M_\odot$ [154, 155] and is the best Galactic analog to the starburst phenomenon seen in other galaxies. This region contains ~ 40 ultracompact H II regions, each hosting at least one massive star (earlier than B3) [156], and the brightest water maser cluster in our Galaxy [157]. Based on the proper motion of the strong H₂O masers, the distance is estimated to be 11.4 ± 1.2 kpc [158]. These massive stars can output a copious amount of kinetic energy via stellar winds, which may be sufficient to accelerate CRs. Two expanding shells as well as remnants of two gas ejections were found in W49A [159]. The shells may be driven by the massive stars and have a total kinetic energy of $\sim 10^{49}$ ergs. The gas ejections are likely to have the same origin as the expanding shells and a total energy of $\sim 10^{50}$ ergs. All these observational results make it as a likely potential γ -ray source. Indeed, the observations of HESS telescopes toward the direction of W49A reveal an excess of TeV γ -rays with a significance of more than 4.4σ [97], although the GeV emission has not been reported.

Cygnus Cocoon

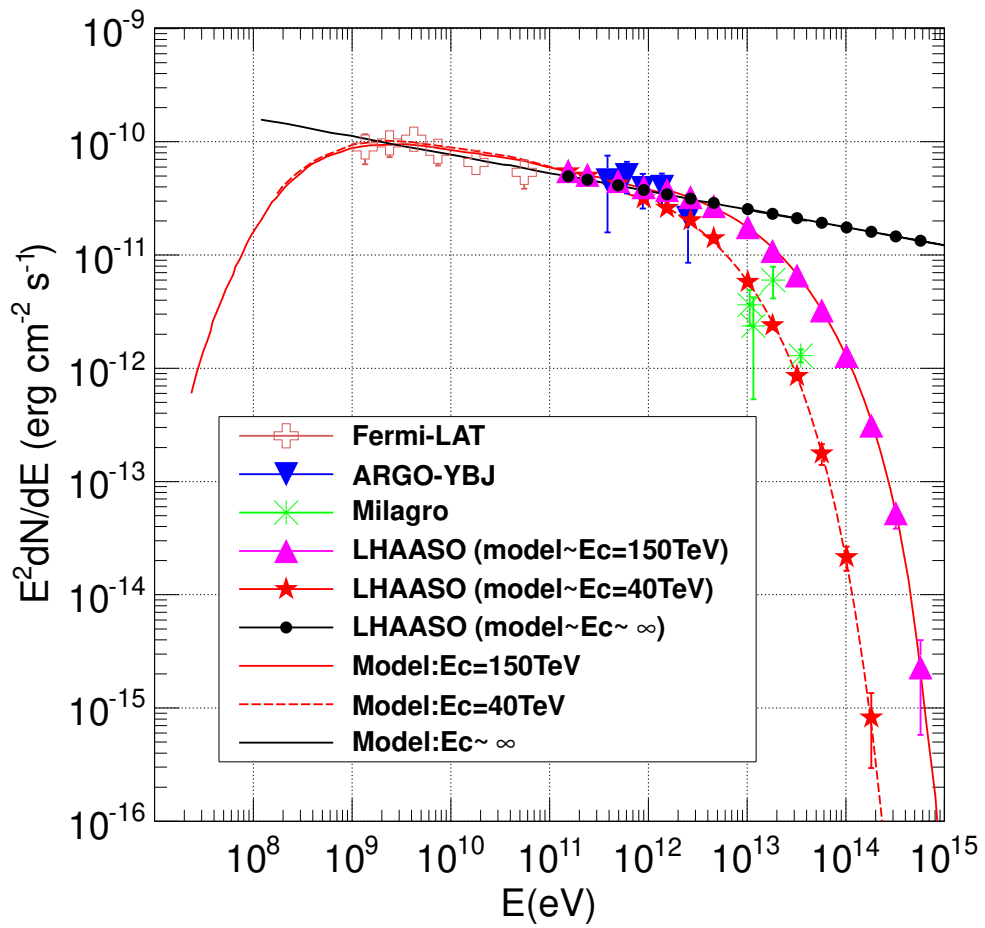


Figure 15: Expectation of the LHAASO project on Cygnus Cocoon by using one year MC data [4], compared with the measurement of Fermi-LAT [8], ARGO-YBJ [9], Milagro[10, 11].

However, another star-forming region NGC 3603 was detected by Fermi-LAT as an extended source with radius of 1.1° at a significance level of more than $\sim 10\sigma$ [12]. Although NGC 3603 is not located in the field of view of LHAASO, its properties in the GeV band may give some clues to explore the TeV γ -rays for the other star-forming regions. The spectrum of NGC 3603 in energy range from 1 to 250 GeV didn't show any sign of cutoff and can be well fitted with a single power law with a photon index of $\Gamma \approx 2.3$, indicating the existence of the particles with multi-TeV energies at least. In Figure 16, the Fermi-LAT data are modeling via the hadronic scenario with different proton cutoff energy. As can be seen, LHAASO observation toward the other star-forming regions, including W49A, may help us to answer what energy particles can be accelerated up to PeV in the star-forming regions.

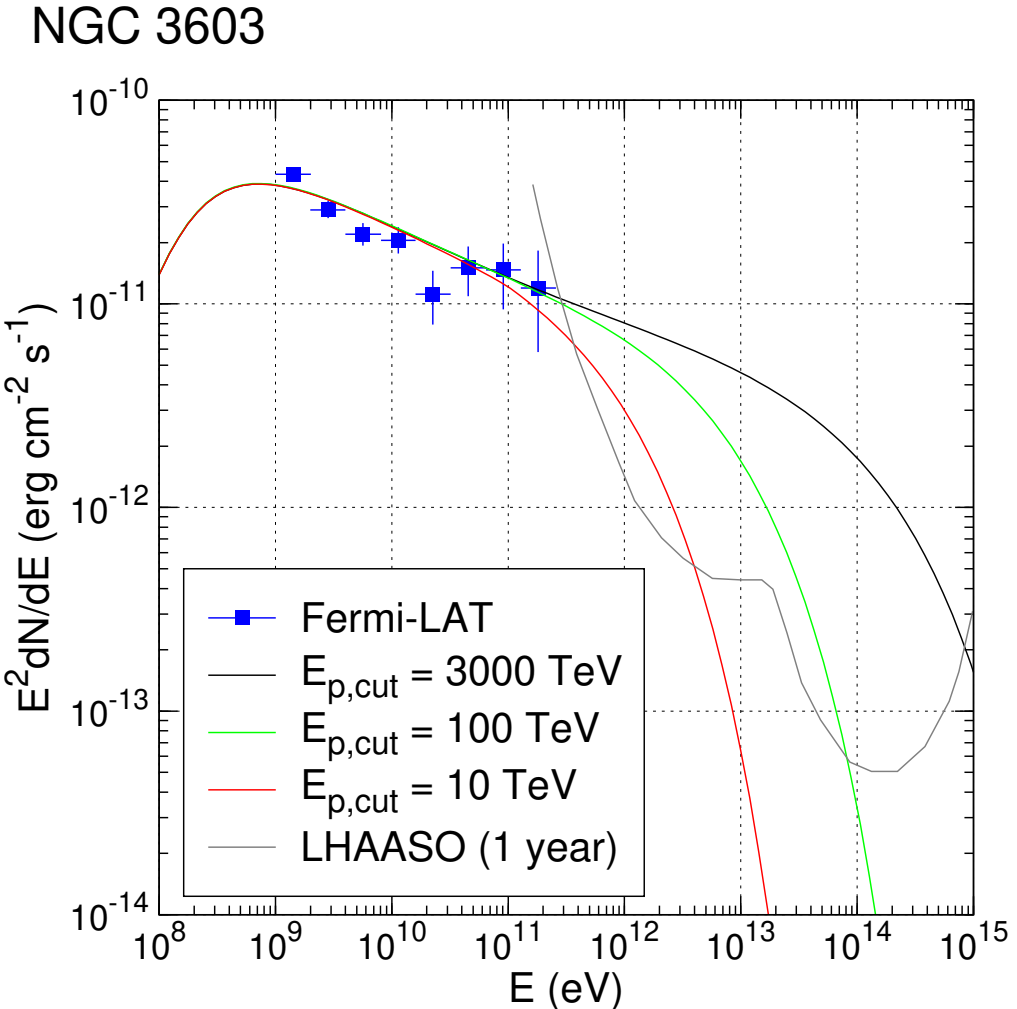


Figure 16: Modeling the Fermi-LAT data of source NGC 3603 [12] with the different proton cutoff energies: 3000 TeV (black), 100 TeV (green) and 10 TeV (red), compared with the LHAASO's sensitivity curve (gray).

Further consideration of LHAASO targets of candidate PeVatrons harbored in star forming regions will be given in §2.9.

2.5. Pulsars and Pulsar Wind Nebulae

2.5.1. High-energy TeV emission from pulsars

Thanks to *Fermi Gamma-ray Space Telescope (Fermi)*, which was launched in 2008 June, we have learned from its observations that pulsars are the dominant γ -ray $0.1 - 100$ GeV sources in our Galaxy [5]. Thus far more than 200 pulsars have been detected by *Fermi*, and from the studies we now know that pulsars generally have γ -ray emission described by a power law with exponential cutoff at several GeV. Such a spectral shape matches the theoretical expectations, as the emission arises due to curvature radiation from the magnetosphere (near the magnetic poles) of a pulsar (e.g., [160]). It was certainly a surprise when 100 GeV pulsed emission from the Crab pulsar was detected by *VERITAS* [161], and recently the *MAGIC* Collaboration has recorded the photons with energies up to 1.5 TeV [162]. In addition, pulsed photons above 50 GeV from the Vela pulsar were also detected [163]. Is such high energy emission only seen from the brightest, young pulsars? Not really! In a recent paper, [164] have reported the detection of up to 200 GeV photons from an old, so-called millisecond pulsar (MSP; they spin rapidly, at periods of several milliseconds).

The detection of photons above 100 GeV challenges the theoretical understanding of the pulsar emission mechanisms, because all the pulsar emission models predict a cutoff in the curvature radiation of pulsars as large as ~ 100 GeV. Currently the inverse-Compton scattering process in the outer magnetosphere or the pulsar wind region is considered to produce the pulsed emission detected in the > 10 GeV band from the Crab pulsar (see, e.g., [165, 166]). Alternatively a non-stationary outer-gap scenario has also been proposed recently by [167], in which the observed spectrum of a pulsar is the superposition of emission from the variable outer gap structures.

LHAASO will certainly explore the high-energy TeV emission from pulsars, helping by finding a full sample of them and setting constraints for theoretical modeling. We note that high-energy γ -ray emission is seen from 27 pulsars, as reported in the first *Fermi* catalog of sources above 10 GeV [168]. Among them 20 sources were found to have pulsed γ -ray-ray emission in the > 10 GeV band, including 17 young pulsars and three MSPs. These sources could be good targets for LHAASO.

2.5.2. Pulsar wind nebulae

Pulsars are powered by their fast rotation, and most of the rotational energy of a pulsar is released in a form of the pulsar wind (see, e.g., [169]). The high-energy, relativistic particles in the pulsar wind interact with the ambient medium around a pulsar forming a terminal wind shock. Particles at the shock emanate synchrotron radiation, making the pulsar wind nebula (PWN) bright from radio to X-ray energies. At GeV and TeV γ -ray energies, it is believed that the inverse Compton (IC) scattering process gives rise to emission, with Lorentz factor of $\sim 10^6$ electrons up-scattering background infrared photons to GeV/TeV range. The modeling of a broad-band spectrum of a PWN thus allows us to study its particle population, magnetic field, and dynamical evolution (after the birth of the pulsar; e.g., [170, 171, 172]). Thus far, more than 30 PWNe or candidates have been detected at TeV energies, and *Fermi* has been able to have detected a few of them [173]. Part of the sample will certainly be investigated by LHAASO. With LHAASO's great sensitivity at TeV and large-sky area monitoring capability, it is conceivable that more PWNe will be detected, allowing to obtain a full sample of them in the northern sky.

Apart from SNRs, PWNe are also believed to be a kind of Galactic cosmic ray source. According to the Hillas criteria [174], the particles with energy below the knee energy can be effectively trapped by the magnetic fields of PWNe. Thus, PWNe can store a large amount of energy in relativistic protons if pulsars or PWNe can continuously produce energetic protons. Based on the outer-magnetospheric gap model, Cheng et al. [175] pointed out that the Crab pulsar can produce relativistic protons if $\vec{\Omega} \cdot \vec{\mu} > 0$, where $\vec{\Omega}$ and $\vec{\mu}$ are the angular velocity and magnetic moment of the star, respectively. Recently, it is suggested that the PWNe inside SNRs can further accelerate the relativistic protons accelerated by the SNR shocks up to the energy of 1 PeV and hence such PWNe may also be PeVatrons [176]. If a PWN locates in dense environments and contains relativistic protons, the hadronic emission from the energetic

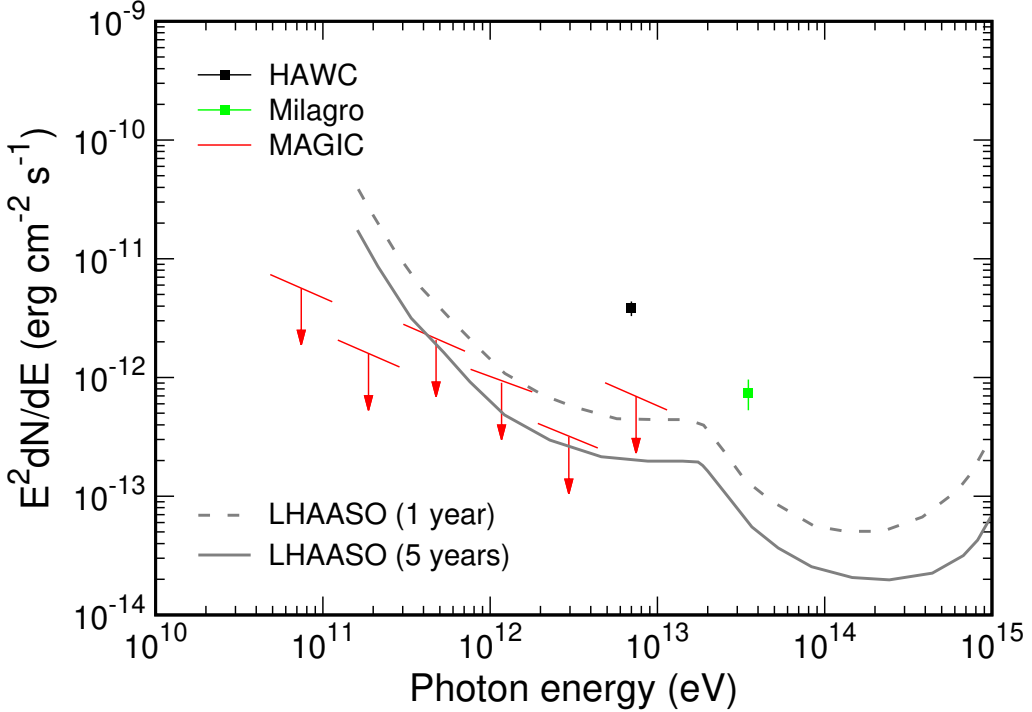


Figure 17: The spectrum of the nebula around the Geminga pulsar measured by Milagro [13], HAWC [14] and MAGIC [15].

protons may have a significant contribution to the GeV-TeV γ -rays [177]. Indeed, the lepton-hadronic model has been applied to some PWNe to explain their broadband spectra, e.g. in the cases of Vela X [178] and G54.1+0.3 [179]. With LHAASO’s great capacity of detecting γ -rays up to energy of ~ 100 TeV, it may help us testing the protons acceleration in PWNe and understanding of CRs’ origin.

Space experiments (PAMELA [180], Fermi [181], i AMS-02 [182]) have revealed an excess of high-energy positrons relative to the standard predictions for secondary production in the ISM. In order to explain this positron excess, it can be confirmed that significant quantities of TeV positrons should be produced within the local volume (the surrounding \sim kpc), but the source of positrons is still in debates. PSRs and/or PWNe are widely suggested to be the dominant sources of the local population of TeV electrons and positrons, which can account for the observed positron excess [183, 184, 185, 186, 187]. Among the known pulsars, Geminga (PSR J0633+1746) and B0656+14 (PSR J0659+1414) are the potential sources due to their short distance to us. These pulsars are each relatively young (370 and 110 kyrs, respectively) and are located within a few hundred parsecs of the solar system (250^{+230}_{-80} and 280^{+30}_{-30} pc, respectively [188]). The electrons and positrons released by PSRs can diffuse into the surrounding medium and produce γ -rays. Indeed, the extended TeV γ -ray emission (2° – 3° radius) surrounding the Geminga pulsar has been reported by Milagro [13] and HAWC [14], although the observations by the MAGIC telescopes³ show no significant detection above 50 GeV [15]. The extended TeV γ -ray emission from B0656+14 also has been detected by HAWC [14]. Based on the HAWC results, Hooper et al. [187] calculate the expected contributions from the two PSRs to the local positron spectrum via fitting the γ -ray spectrum and conclude that PSRs are likely sources of the local TeV positron. In figure 17, the observed results for Geminga and the LHAASO’s sensitivity are shown. As can be seen, LHAASO has the ability to accurately measure the γ -ray spectrum from 200 GeV to 100 TeV, which will give more stronger constraints on the properties of these PSRs and test the PSR scenario of the positron excess, thus settling the dispute between the MAGIC and HAWC observations.

³It is difficult for imaging atmospheric Cherenkov telescopes (IACTs) to detect the large extended sources.

2.6. γ -ray binaries

A new class of high-mass X-ray binaries (HMXBs) have been discovered as strong γ -ray emitters: PSR B1259–63, LS 5039, LS I +61° 303, HESS J0632+057, and 1FGL J1018.6–5856 (see [189] for a review). Other recent candidates such as PSR J2032+4127 have also been reported [190]. These γ -ray binaries contain a compact object orbiting an OB companion star, emitting non-thermal emission from radio to TeV γ -rays that are modulated on the orbital period. Studying the emissions from γ -ray binaries can probe the surroundings of compact objects at AU scale, which is a largely unexplored distance scale. The complexity of the immediate environment of γ -ray binaries also shed light on physical processes that are poorly understood.

The detection of very high energy (VHE) γ -rays (above 100 GeV) by the current imaging atmospheric Cherenkov Telescopes (IACTs) from all known γ -ray binaries, gives hint for very efficient particle acceleration in these systems. Indeed, there is no lack of particle acceleration sites for γ -ray binaries: the interaction of the pulsar wind (for those the compact object is a pulsar) with the strong wind of a massive star, accretion onto a compact object and/or jet activities (similar to micro-quasars), and a relativistic outflow interacting with the ISM at a larger scale. Micro-quasars or interacting stellar binaries are also observed to emit γ -rays above 60 MeV, e.g., in Cygnus X-1 [191], Cygnus X-3 [192], V 404 Cyg [193], and Eta Carinae [194].

γ -ray binaries, such as LS 5039, have a very high efficiency of particle acceleration. The very good sensitivity of LHAASO in the energy band of 10–100 TeV or above will allow us to probe the acceleration mechanism, the magnetic field strength, stellar wind densities, and short-term variability of the acceleration and/or radiation regions. This is because the opacity and orbital dependence of γ - γ absorption, and the angular dependence of the inverse-Compton emission, or other sources of variability, are less important in this energy range than in sub-TeV energy band. In addition, the spectrum of the emission also depends on whether the accelerated particles are leptons or hadrons.

LHAASO, being an excellent all-sky detector at the TeV to multi-TeV energies, are a good monitor of the TeV transient sky, including transient phenomena related to γ -ray binaries.

For γ -ray binaries, the most surprising transient behavior came from the GeV observations of PSR B1259-63. During late 2010 to early 2011, the Fermi-LAT observed PSR B1259-63 through a periastron passage, for the first time since its launch in 2008. Before and during the passage, the LAT detected a weak emission above 100 MeV. Unexpectedly, a GeV flare occurred 30 days after the passage, with a flux about an order of magnitude higher than the pre-periastron value. The flare continued about three months after the periastron passage [195, 196]. It turned out that the GeV flare was seen again in 2014 periastron at a similar orbital phase as in 2011. The major obstacle to understand the GeV flare is that it occurred at an orbital phase well after the second/post-periastron disk crossing, and did not correspond to any activities in other wavelengths as of 2011. Although PSR B1259-63, visible only from southern hemisphere, is not visible to LHAASO, this highlights the possibility that any VHE emission from γ -ray binaries can be unpredictable and transient, which is best probed by an all-sky detector like LHAASO.

In fact, previously unexpected ‘flares’ of VHE emission was already seen before. LS I +61° 303 is one of the most studied γ -ray binary but the nature of its compact object is still under debate because of the poorly constrained mass of the compact object and the inclination angle of the system. Radio to γ -ray emission are all modulated at the orbital period (26.5 days) and even at the super-orbital period of 1667 ± 8 days. VERITAS observations of LS I +61° 303 clearly observed VHE flares in two consecutive orbits in similar orbital phase (October and November 2014; [16]). The 0.3–20 TeV flux of the VHE flare is about a factor of 2–5 above that of the average flux measured previously, and the flare spectrum does not show any cut-off up to 20 TeV. With the planned sensitivity of LHAASO, it is possible that the VHE emission can be seen by LHAASO, if such elevated TeV level remains for months.

Although leptonic scenario prevails to explain the multi-wavelength emissions from γ -ray binaries, if hadrons are also accelerated in the complicated binary environment, they might also contribute to

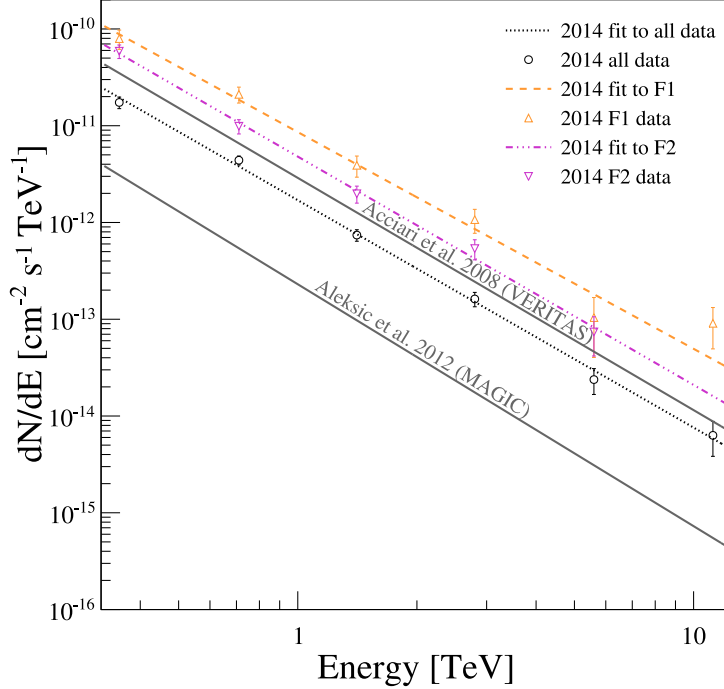


Figure 18: Differential spectra of LS I +61° 303 during a flaring period from the VERITAS observations in 2014, together with those average spectra in previous publications (from [16]).

>10 TeV emission. An observational ‘evidence’ for hadronic emission is a low-significance neutrino signal (pre-trial p -value is 0.087) from HESS J0632+057 reported by the IceCube collaboration [197]. Although this signal is fully compatible with the background fluctuation after taking the trial factor into account, if similar events are detected in the future, it could increase the likelihood of a >10 TeV emission from accelerated hadrons.

Chances are that there are more γ -ray binaries to be discovered, based on the fact that known γ -ray binaries tend to be nearby. Paredes et al. [198] estimate that the total number of γ -ray binaries in our Galaxy is about 50, but this number can depend on the duty cycle of γ -ray emission: VHE emission in HESS J0632+057, LS I +61° 303, and PSR B1259–63 is strongly dependent on orbital phase and in some sources the orbital periods can be (very) long, e.g., the 30–50-year orbital period binary pulsar PSR J2032+4127 has only been recently discovered by long-term monitoring (i.e., years) by the Fermi-LAT. With its very large field of view at all times, LHAASO will be the best instrument to observe known and yet-to-discover γ -ray binaries at energies above 100 GeV.

2.7. The Galactic Center

2.7.1. Galactic center as a high energy emission source

It is well known that the Galactic Center (GC), with a supermassive black hole ($\sim 4 \times 10^6 M_\odot$), is a good laboratory for the study of high energy astrophysical phenomena. Currently, the overall behavior of the GC is quite silent now, except some continuous weak activities. Transient X-ray events with a 2–10 keV energy output up to 10^{35} erg s $^{-1}$ are observed from the GC on a regular basis, as well as transient events at MeV/GeV energies. Flares from the X-ray binaries located in the GC region can reach luminosities up to 10^{37} erg s $^{-1}$. However, there are sufficient evidences to prove that the GC has violent activities in the past, such as X-ray outbursts [199] and the Fermi-Bubbles [200]. During the violent activities, the accretion of stars and gas by the supermassive black hole could be effective to accelerate particles. The maximum energy that protons can achieve by diffusive shock acceleration is [201]

$$E_{\max} \sim eBR \approx 10^{14} \left(\frac{B}{G} \right) \left(\frac{M}{4 \times 10^6 M_\odot} \right) \left(\frac{R}{10R_g} \right) \text{ eV} \quad (1)$$

where B is the magnetic field and R is the size of the acceleration region. As in [201], we assume the acceleration takes place within 10 Schwarzschild radii ($R_g \sim 10^{12}$ cm) of the black hole. To accelerate protons to above \sim PeV requires magnetic field strength of tens of G in the acceleration region [202, 203]. Such a condition could be reached in the very central region of the GC [201, 204]. On the other hand, if the acceleration takes place in larger regions, the required magnetic field could be smaller. When the accelerated CRs diffuse out of the GC, hadronic interaction with the ISM will happen and produce similar amount of γ -rays and neutrinos. The observations of high energy γ -ray emissions can shed new light on the acceleration mechanism at the GC. In fact, with the state of art technologies, current γ -ray observations have provided unprecedented sensitivity in studying the acceleration activities in the GC.

2.7.2. γ -ray emission of the GC

The very high energy γ -rays from hundreds of GeV to tens of TeV in the direction of the GC have been observed by several atmospheric Cherenkov telescopes such as CANGAROO [205], VERITAS [206, 207], HESS [208, 209, 210, 211], and MAGIC [212]. The diffusive γ -ray emission is also observed at Galactic Center Disk (GCD) range by HESS experiment [209]. Fig. 19 shows the image of very-high-energy γ -ray emissions. More interesting thing is that the map of the central molecular zone as seen in γ -rays demonstrates a strong correlation between the brightness distribution of very-high-energy γ -rays and the locations of massive gas-rich complexes. This points towards a hadronic origin of the diffuse emission, where the γ -rays result from the interactions of relativistic protons with the ambient gas.

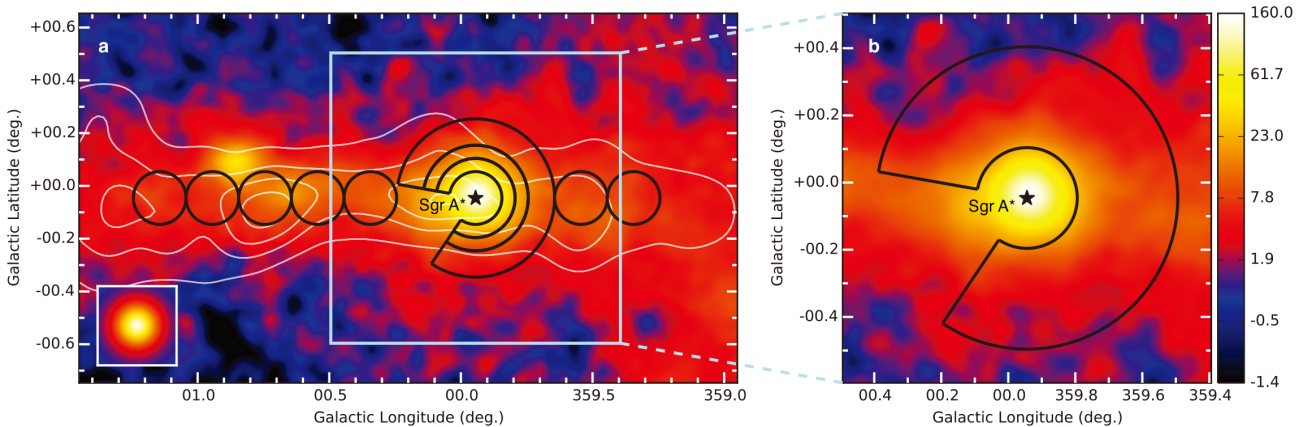


Figure 19: The image of very-high-energy γ -ray emission from the direction of the GC region (adopted from [17]).

Fig. 20 shows the spectra of very-high-energy γ -rays for the GC point and diffuse emission. The best-fit to the data found that the spectrum with power law index ~ 2.3 can extend the energies up to

tens of TeV, without any indication of a cutoff or a break. It is suggested that such a γ -ray spectrum, arising from hadronic interactions, is detected in general for the first time. Since these γ -rays result from the decay of neutral pions produced by p-p interactions, the derivation of such hard power-law spectrum implies that the spectrum of the parent protons should extend to energies close to 1 PeV. Simultaneously, the spectral index at TeV energy range for the GC point source is the as that of the diffusive one, which may possibly share the same origin: GC supermassive black hole. The result supports that the γ -ray emissions come from \sim PeV energy protons and the most plausible accelerator is the GC [17].

However, the γ -ray emission from the point source in GC has a break power law spectrum at tens of TeV. The best fit of the cut-off can be described by exponential function in high energy [213]. While adopting the traditional model of ISRF, the absorption effect is too small to explain the observed cut-off spectrum of HESS J1745-290 [213]. The alternative solution attributes it to the intrinsic cut-off, which characterizes the acceleration limit of the flaring event with the critical energy $E_c \sim 200$ TeV for protons. Let's look into the diffuse γ -ray emission at GC region. The uncertainty at tens of TeV in the γ -ray spectrum leads to the poor ability to discriminate the different energy cutoff of protons. It is to say that the observation of γ -ray emission at \sim 100 TeV energy will play a very important role to determine the acceleration ability of GC in the future.

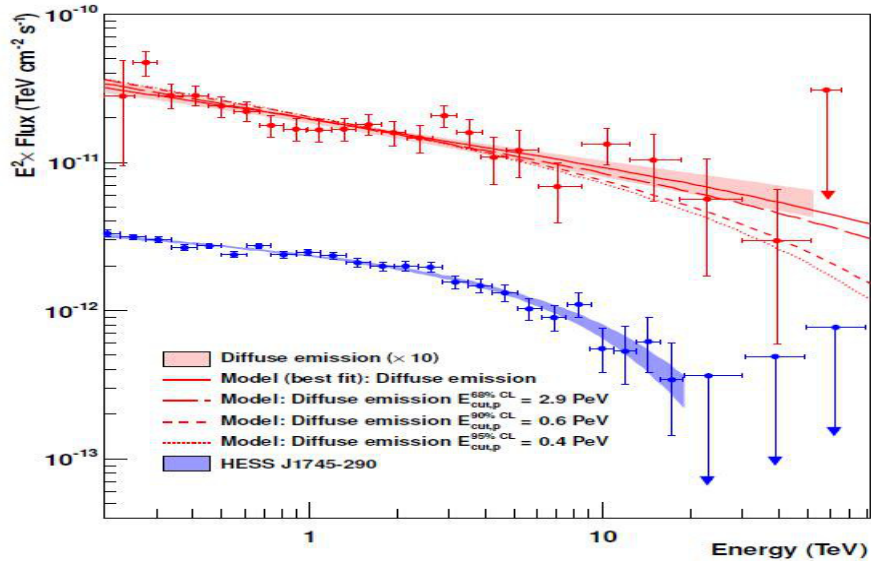


Figure 20: The spectra of very-high-energy γ -ray for the point and diffuse emission (adopted from [17]).

2.7.3. The LHAASO sensitivity at 100 TeV energy range

The LHAASO, a km^2 scale CR/ γ -ray observatory, is proposed to decipher the origin of CRs by discovering 100 TeV γ -ray emission [62]. One of the major detectors (KM2A), with an effective area of 1 km^2 , is composed of 5195 scintillator electron detectors (EDs) with 1 m^2 each and a spacing of 15 m, and 1171 muon detectors (MDs) with 36 m^2 each and a spacing of 30 m. At 10 TeV, the effective area of KM2A can reach about 0.3 km^2 , the angular resolution is about 0.86° , and the energy resolution for γ -rays is about 42%. The corresponding values are 0.8 km^2 , 0.5° , 33% at 30 TeV, and 0.9 km^2 , 0.3° , 20% at 100 TeV respectively. With the large area of MD array, KM2A will reject the hadronic shower background at a level of 10^{-4} at 50 TeV and even 10^{-5} at higher energies, so that γ -rays samples can reach background free above 100 TeV. The highest sensitivity of KM2A is $\sim 1\%$ of the Crab nebula flux in the energy range of 50-100 TeV for one year observation.

The problem is that the GC in LHAASO field of view is with the zenith angle of $\sim 65^\circ$, which will seriously reduce the sensitivity of LHAASO. So the special analysis technology for wide field of view should develop to study the γ -ray emission from the GC region based on the simulation. The air shower development in the atmosphere has been generated with the CORSIKA v7.405 code [70].

The electromagnetic interactions are described by the EGS4 package while the hadronic interactions are reproduced by the QGSJET model. The low-energy hadronic interactions are described by the FLUKA package. Cosmic ray spectra have been simulated in the energy range from 10 TeV to 10 PeV. About 8-yrs showers have been sampled in the zenith angle interval from 55° to 70° . For γ -rays, we produce $2e^4$ events at every energy point including: 50, 100, 200, 500, 1000 TeV. The experimental conditions (trigger logic, time resolution, electronic noises, etc.) have been taken into account via a GEANT4-based fast simulation code and analyzed with the same reconstruction code.

The event selection is performed for the reconstructed simulation data. Firstly, the reconstructed core position within 500 m is selected. The adopting of 500 m radius is based on the Muon detector. Secondly, to keep the event with good quality, the sigma is less than 1.0. By doing so, a part of events with worse core and angle resolution can be rejected. Due to the large zenith angle, the secondary particles induced into detector is reduced and only tens of them can be recorded. Particularly, the events with old age become worse and should be rejected. So the selection of $29 * age + nHits > 60$ is performed. Lastly, we apply the Muon detector selection with the number of Muon less than 0.1. By doing above selection, the backgrounds of CRs can be rejected to zero. Fig. 21 is the effective area of KM2A array. It can reach $\sim 5e^3$ m² at 50 TeV, $\sim 3e^4$ m² at 100 TeV and larger than $\sim 2e^5$ m² above 200 TeV. Owing to the zero background, 10 γ -ray events detected can be defined 5σ level, Fig. 22 shows the sensitivity of LHAASO with one year observation. It is obvious that the LHAASO have enough sensitivity to observe this source at above 100 TeV. However, if the protons can not be accelerated to \sim PeV, LHAASO can not have enough sensitivity.

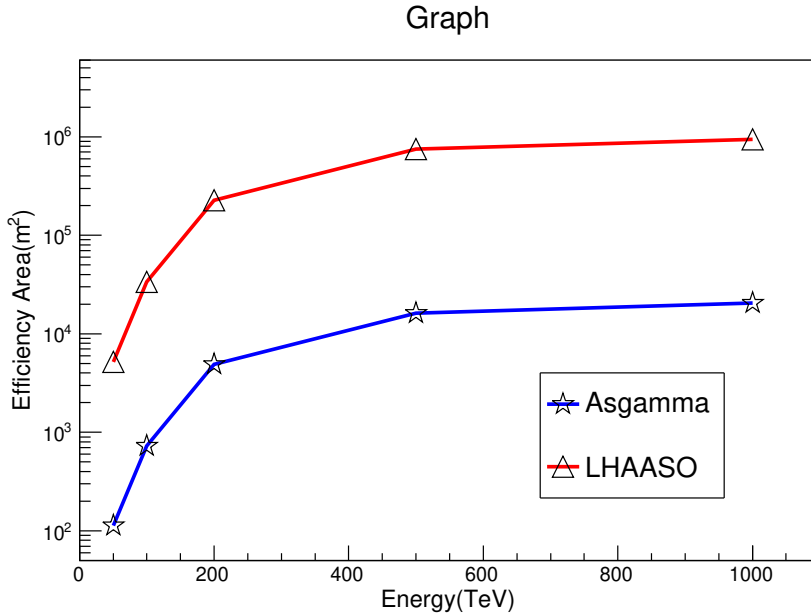


Figure 21: The effective area of LHAASO for γ -rays from GC direction

2.7.4. Short summary

Galactic cosmic rays can reach energies of \sim PeV. The first PeV accelerator, GC, has been evidenced by HESS experiment based on the observation of γ -ray emission at tens of TeV. However, the uncertainty at tens of TeV for the spectrum of γ -rays leads to the poor ability to discriminate the different energy cutoff of protons. We employ the MC simulation to examine the LHAASO sensitivity to Galactic center at 100 TeV energy range and see that the LHAASO has enough sensitivity with one year observation to detect this source at above 100 TeV if the proton can be accelerated to PeV energy. On the contrary, if the maximum energy is \sim 200 TeV, the LHAASO can not have enough sensitivity to detect it.

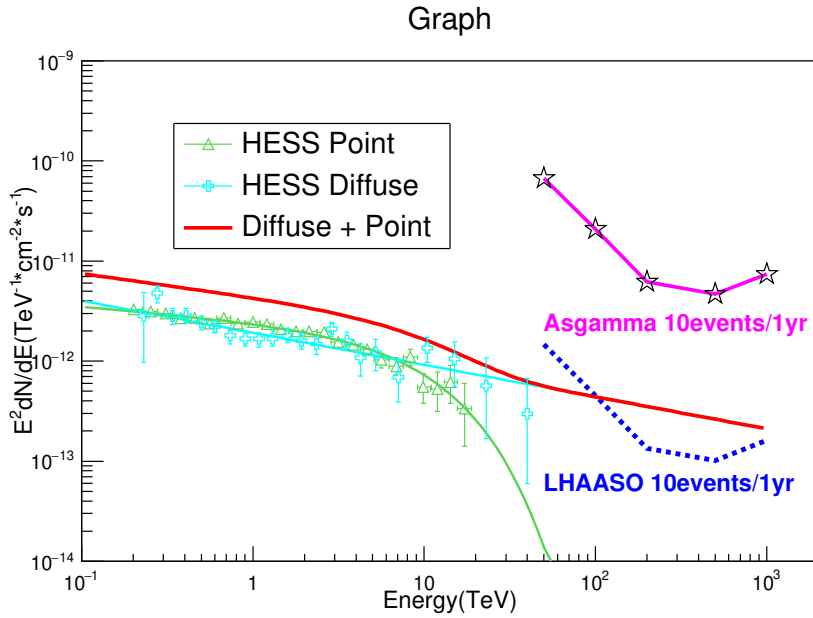


Figure 22: The sensitivity of LHAASO for γ -rays from GC direction

2.8. Giant Molecular clouds

A giant molecular cloud (GMC) has a typical mass of 10^5 solar mass and a density of more than 100 cm^{-3} . The molecular gas in GMCs can be observed and measured via molecular lines, such as the rotational transition lines of CO. Furthermore the infrared emission from the dust inside GMCs provides an alternative way to study the gas contents. GMCs are the birth place of young stars and thus also harbor HII regions and bubble-like structure. GMCs are also regarded as γ -ray emitters. The main γ -ray production mechanisms inside GMCs are the decay of neutral pions produced in the collision of cosmic ray (CR) nuclei with the ambient gas, inverse Compton scattering (IC) of relativistic electrons on background radiation fields, and bremsstrahlung of relativistic electrons. Due to the high gas density, pion-decay dominates the other mechanisms above about 100 MeV[214]. In the energy range of LHAASO, the IC and bremsstrahlung are further suppressed due to the high energy cutoff at several TeV observed in the CR electron spectrum [215]. The dominance of pion-decay mechanism in γ -ray production makes it an ideal place to measure CR density beyond the solar system. Several famous GMCs locate inside the field of view (FOV) of LHAASO. Their positions, mass, and distances are listed in Table 1. The predicted γ -ray flux from GMCs are proportional to the value M/d^2 , which are also listed in Table 1.

2.8.1. GMCs as CR calorimeter

The current paradigm of cosmic rays (CRs) postulates that, because of the effective mixture of CRs during their propagation in the interstellar magnetic fields, the CR density locally measured in the Earth's neighborhood should correctly describe the average density of CRs throughout the Galactic disk [216]. However, small variations of CRs on large (kpc) scales do not exclude significant fluctuations on smaller scales, particularly in the proximity of young CR accelerators. Therefore, it is not obvious that the locally measured component of CRs can be taken as an undisputed representative of the whole Galactic population of relativistic particles. In particular, it is possible that the flux of local CRs might be dominated by the contribution of a few nearby sources. However, the density of CRs in different parts of the Galaxy can be probed uniquely through observations of γ -rays from GMCs [217, 218, 219]. On GeV band the investigations in this regard have already been done on the nearby GMCs in Gould belt [220, 221, 222, 61] as well as on Sgr B complex in Galactic center [223]. But on TeV band the GMCs are still left undetected. One reason for the non-detection of GMCs is the extended size of these objects and the limited FOV of Imaging Atmospheric Cherenkov Telescope (IACT). In contrast, the

Table 1: Properties of the GMCs in the FOV of LHAASO. The estimated distance and position are obtained from Dame *et al.*, 1987. The mass values listed in the second column are calculated from the CfA maps (see [61] for detail).

Region	M [$10^5 M_\odot$]	D [pc]	l [$^\circ$]	b [$^\circ$]	M/d^2 [($10^5 M_\odot/\text{kpc}^2$)]	size [arcdeg 2]
ρ Oph	0.12	165	356	+18	8.4	68
Orion B	0.78	500	205	-14	3.9	22
Orion A	1.2	500	213	-18	5.2	28
Mon R2	1.1	830	214	-12	1.7	19
Taurus	0.30	140	170	-16	15.0	101
Polaris flare	0.055	230	130	+26	0.96	40

high sensitivity and large FOV of LHAASO will provide a unique opportunity to detect such objects and measure the CR density in TeV-PeV band in different position of the Galaxy. To show the detection prospect we plot the predicted γ -ray flux as well as the LHAASO sensitivities for a typical GMCs with a M/d^2 value of $10^6 (M_\odot/\text{kpc}^2)$ in Figure 23. It should be mentioned that the sensitivities for extended sources are estimated as $F_{ext} = F_{ps} * (\Omega_{ext}/\Omega_{psf})$, where F_{ext} and F_{ps} are sensitivities for the extended source and point source, respectively, and Ω_{ext} and Ω_{psf} are the angular size of extended source and point spread function, respectively. Thus the detection capacity of GMCs depends on their angular size. Indeed, the GMCs show filamentary morphology and the γ -ray emission region is much smaller than that listed in Table 1. Thus the estimation of LHAASO sensitivities in Figure 23 is very conservative and should be regarded as an upper limit.

In addition to the absolute CR fluxes at different positions of the Galaxy, it would also possible to measure the spectral property of CRs using the γ -ray observations on GMCs. Recently a hardening in CR spectrum above 200 GeV was reported by several observations [224, 225, 42]. This effect can be observed in the γ -ray flux in the nearby GMCs given the hardening extends to more than 100 TeV. To illustrate the effect we plot in Figure 23 the predicted γ -ray flux in GMCs with and without such a hardening. Furthermore, the γ -ray above 100 TeV are already produced by CRs with the energy close to the *knee*. Thus, LHAASO observation of γ -rays from GMCs in this energy range will provide an alternative method in measuring the CR spectral property near the *knee*.

2.8.2. Young stellar associations inside GMCs

Young star associations and corresponding super bubbles are considered to be the origin of a substantial fraction of Galactic CRs [226, 227]. Fermi LAT has detected a cocoon like structure near the young star association of Cygnus OB2 with a hard spectrum and argue that this is produced by fresh accelerated CRs [8]. The GMCs harbored various young star associations and young HII regions. For example, the Orion Nebula Cluster (ONC) in the Orion A molecular cloud and NGC 2024 in the Orion B molecular cloud are the two largest clusters in the youngest subgroup of Orion OB1, with ages less than 2 Myr [228]. These young star clusters are also potential accelerating sites of the CRs. Although these young accelerators are not observed in GeV band, one can not exclude the possibility that they would dominate in multi-TeV ranges, due to their hard spectra. In this case the CR density inside GMCs are contaminated by the embedded acceleration and GMCs can no longer be regarded as CR calorimeters. Furthermore, if the hard spectra in these young structures are detected in multi-TeV energy range, this would be a strong evidence for the existence of *PeVatron*, which will be discussed in detail in an independent section (§2.9).

2.9. *PeVatrons*

The hard spectrum in multi-TeV range without cutoff is considered as the sign of hadronic origin of the emissions. This is because the Klein-Nishina (KN) effects will introduce a break in the spectrum

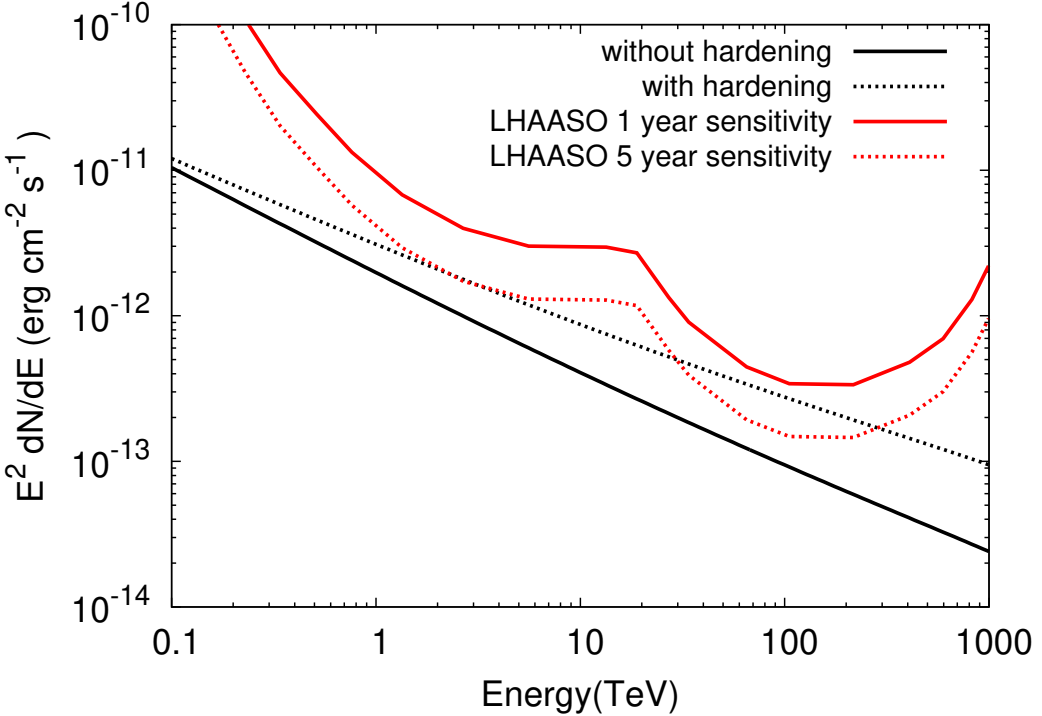


Figure 23: The γ -rays flux produced in a molecular clouds with a M/d^2 value of 10^6 (M_\odot/kpc^2), the angular size is 20 arcdeg 2 . The CR spectrum measured by AMS-02 extrapolated to 10 PeV with and without a hardening are used in deriving the γ -ray flux. The LHAASO sensitivity are estimated by considering the source extension.

of IC scattering off CMB photons at this energy range, even if there is no cutoff in electron spectrum. Thus such a hard spectrum can only be produced by CRs protons with energy up to PeV. This argument has been adopted for the PeVatrons in Galactic center observed by H.E.S.S. [229] (also see §2.7).

As a result, all the hard TeV sources without detected high energy cutoff can be regarded as candidates for PeVatrons. Several famous young SNRs, such as Cassiopeia A and Tycho, are detected by Air Cherenkov telescopes without cutoff up to several TeV. As already discussed in the section “SNRs” (see §2.3, §2.3.3) such objects should be regarded as PeVatron candidates. Along with young SNRs, the unidentified TeV sources without cutoff should also be examined. One recent example is the H.E.S.S detection of hard spectra up to more than 20 TeV without cutoff in the source HESS J1641-463 [230]. However, the limited statistics cannot rule out a cutoff at higher energy caused by KN effects. By comparison, the much higher sensitivity of LHAASO at the energy range of 10–100 TeV provides an ideal window to study the spectral property of the PeVatron candidate. Although HESS J1641-463 is located beyond the LHAASO FOV, there are still a few unidentified Galactic source in the northern sky with hard spectra.

One remarkable example is TeV J2032+4130 in Cygnus region (§2.4.1), which is also related with the Fermi Cygnus cocoon [8]. The hard spectra (index of -2) and non-detection of cutoff at TeV range has been reported by Veritas [75]. Furthermore, the study on Fermi Cygnus cocoon reveals that the Cygnus region indeed harbors CR acceleration site and fresh CRs. The Cygnus region, as well as other star-forming regions (see §2.4), is a very promising target to hunt for PeVatrons.

Another interesting source is HESS J1848-018. H.E.S.S measurement has revealed a spectral index of -2.8 [231], which makes it unlike a PeVatron. However, the recent HAWC observations [232] reveal a much higher flux at high energy and thus a harder spectra. The difference may comes from the diffusive nature of this source. The source is spatially correlated with the star forming region W43, which has a similar environment as that of the Cygnus cocoon (§2.4.1). We note that, at GeV range, the Cygnus cocoon also has a spatial extension of more than 3 degrees. Indeed, if the CRs are accelerated in the

super-bubbles surrounding the young star clusters, the γ -ray emission should be diffuse due to the low ambient density in the cavities. Such diffuse structure can hardly be detected by IACT due to the very limited FOV. LHAASO, however, with much larger FOV and continuous exposure, has the capability to detect such structures.

In conclusion, in addition to the strong indication of the Galactic center (§2.7), the hard unassociated TeV sources noted here, SNRs (§2.3), PWNe (§2.5.2), and star-forming regions (§2.4) considered in the previous sections can be Galactic PeVatron candidates. Whether high energy cutoff is present at dozens of TeV is crucial to identify the PeVatron nature of these sources. The energy range of LHAASO is perfectly suitable to study their spectral features. On the other hand, the PeVatrons can also be diffusive rather than compact, and such kind of sources can hardly be detected by the former IACT but would be very promising to be detected by LHAASO.

2.10. Diffuse Galactic Gamma-Rays

It is recognized that the γ -rays above 100 MeV chiefly spring from the diffuse emission. Three major mechanisms are thought to be responsible for the creation of γ -rays, and they are respectively[233]: the decay of neutral pions which are generated through the inelastic collisions between CRs (mostly protons and heliums) and ISM, the inverse Compton scattering of high energy electrons off interstellar radiation field, as well as the bremsstrahlung of CR electrons with interstellar gas. Each process is dominant in different parts of the γ -ray spectrum.

Observation of these diffuse emission is beneficial in acquiring the following knowledge: 1.) spatial distributions of hadronic and leptonic components of CRs, 2.) origin and propagation of cosmic CRs in the Galaxy, 3.) composition and allocation of interstellar medium, and 4.) large-scale distribution of Galactic magnetic field and turbulence. Moreover as the Galactic diffuse emission often represents the natural background to many different signals, a thorough understanding of diffuse Galactic γ -ray emission (DGE) is also essential for deducing the spectra of other components of the diffuse emission, unveiling the undiscovered γ -ray sources, enhancing the measurement accuracy of the position and spectral energy distribution (SED) of galactic or extragalactic point/extended sources and even searching for the sign of dark matter annihilation or decay.

2.10.1. Progresses on the observations of Galactic diffuse γ -rays

The observation of diffuse γ -rays started with the OSO-III satellite in 1968[234]. The measurements have been dramatically ameliorated during the surveys of SAS-2[235], COS-B[236], COMPTEL[237, 238], HEAO 1[239] and EGRET[240]. With the launch of a new generation telescope, Fermi Large Area Telescope (LAT), it maps the γ -ray sky up to a few hundreds of GeV with unprecedented accuracy[241, 242], which deepens our understanding of the generation and propagation of Galactic CRs. In lower energies, the SPI instrument on INTEGRAL observatory has extended the observations of CR-induced diffuse emissions into the hard X-ray range[243, 244]. As for the higher energies, subject to very low flux and limited area of space-based detector, the observations above TeV have been carried out principally on ground-based instruments, such as Whipple[245], HEGRA[246], Milagro[10], HESS[247], ARGO-YBJ[100] and so on.

Higher-quality data enable us to model the DGE based on CR transport and interactions in magnetic halo[248, 249, 250, 241, 242]. In the GeV energy range, the EGRET data show a significant excess in all directions (called “GeV excess”) with respect to the predictions supposing the same CR spectrum in the Galaxy as that at the Earth. But this excess has not been confirmed by the following observation of Fermi-LAT at intermediate Galactic latitudes[251]. Up to now, the DGE model generated by the numerical package GALPROP well conforms the observations at both high and intermediate latitudes published by the 21-month Fermi-LAT survey[241]. But in the Galactic plane the models all underestimate the data above a few GeV, especially toward the inner Galaxy. This has been reconfirmed in the renewed measurements by Fermi-LAT[242]. Possible explanations include the contribution from the unresolved point source population such as pulsars, SNRs, PWNe, spectral variations of CRs or even dark matter annihilation/decay[252, 253]. Recently Guo et al.[254] suggest that a hard CR component within the Galactic plane can self-consistently explain the excess of diffuse γ -rays at the inner Galaxy, the observed B/C and \bar{p}/p ratio. For the diffuse TeV γ -rays, the Milagro telescope made the first observation towards the Galactic disk and corroborated the existence of diffuse TeV γ -ray emission[255, 256]. In the Galactic plane, the Cygnus region inhabits abundant CR sources and large column density of matter, and is recognized as the brightest γ -ray region in the entire northern sky[256]. Milagro telescope performed the observations of Cygnus region and found the diffuse TeV γ -ray emission[10]. Subsequently ARGO-YBJ experiment carried out similar observation as well[100], whose data agree well with the measurements of Fermi-LAT at lower energies. Meanwhile, HESS telescope array also performed surveys at both Galactic plane[247] and center[209, 17].

Probably, the most spectacular discovery about the extended emission in recent years is the so-called Fermi Bubbles[200, 18]. The Fermi bubbles are two giant lobes, roughly symmetrically distributed at

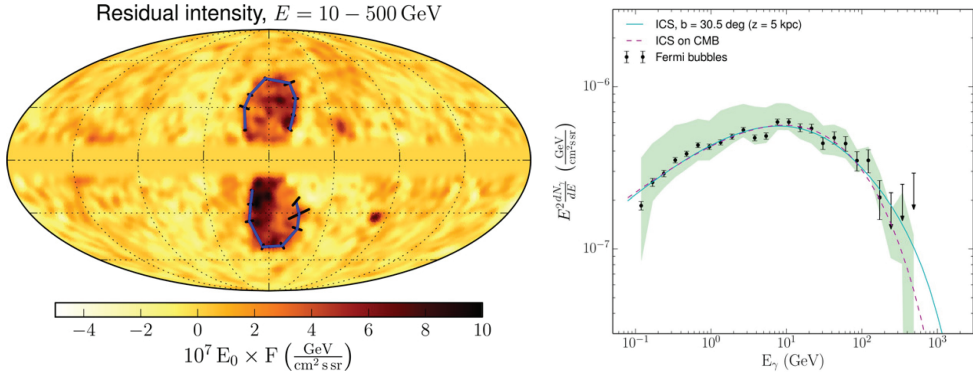


Figure 24: left: the image of Fermi bubbles. right: Spectral energy distribution of Fermi bubbles. Figures are taken from [18].

two sides of the Galactic center. Each bubble owns an oval emission region with sharp edge, which extends over several kilo-parsecs beyond the Galactic plane. Compared with the diffuse γ -rays, the Fermi bubbles have a visibly harder γ -ray spectrum with index ~ -2 , see Figure 24. So far the origin of Fermi bubbles is still on debate. Many theories have been proposed including jet radiation of massive black hole at the Galactic center, shock wave from accretion events of the central black hole, shock wave from supernova explosions near the Galactic center and so forth (see [257] and references therein).

2.10.2. The outlook of LHAASO project on Galactic diffuse γ -rays above 30 TeV

Nevertheless the above intriguing findings only reach to energies around tens of TeV at most, while for the higher energy, i.e. 100 TeV γ -rays, the observations so far are still poor. One main part of the LHAASO project, KM2A (one KM^2 Array), is designed to observe the γ -rays above 30 TeV. It is composed of a 1 km^2 array of electron detectors (ED) and muon detectors (MD). By detecting muon content in the air shower simultaneously, one can effectively identify γ -ray photons from the large background of CRs. The large detection area and high capability of background rejection enable the sensitivities of LHAASO experiment to reach ~ 100 times higher than that of current instruments above 30 TeV[70, 258]. It will also be the first time to monitor γ -ray sky at PeV energies.

1. The observations of diffuse γ -rays above tens of TeV LHAASO project plans to map the DGE above a few hundreds GeV throughout the Galaxy with high sensitivity. It is going to perform an unbiased sky survey of the northern sky with a detection threshold of ~ 0.03 Crab unit at TeV energies and ~ 0.1 Crab around 100 TeV by one year operation, respectively, which is capable of continuously surveying the γ -ray sky from 100 GeV to 1 PeV. For the LHAASO sensitivity to the DGE flux, it can be evaluated roughly according to the point source sensitivity multiplied by a correction factor $f = (\Omega_{\text{PSF}} \Omega_{\text{GP}})^{-1/2}$, in which Ω_{PSF} is the observation angular window, related to the detector point spread function (PSF), and Ω_{GP} is the solid angle of a certain region in the Galactic plane. Therefore according to the above rough evaluation, after one year observation towards the longitude interval $25^\circ - 100^\circ$, the $5-\sigma$ minimum flux detectable by LHAASO can reach as low as $F_{\text{min}} \sim 7 \times 10^{-16}$ photons $\text{cm}^{-2} \text{ s}^{-1} \text{ eV}^{-1} \text{ sr}^{-1}$ at 100 TeV, which is about 6 times lower than the extrapolation of the Fermi-DGE model at the same energy[70, 258]. Figure 25 shows the predicted DGE flux observed by one quarter LHAASO project after one year run, at Cygnus region (left) and $25^\circ < l < 100^\circ$, $|b| < 5^\circ$ (right), respectively. It can be seen that LHAASO is very sensitive to 100 TeV γ -ray photons. Hence we could expect a better measurements for the DGE at this energy range, especially the presence of exponential cutoff at TeV energies.

2. Diffuse γ -ray constraints to the origin of the Fermi bubbles

Part of Fermi bubbles are in LHAASO's wide field of view. If the γ -rays stem from the interaction between the CRs and molecular gas within the bubbles, the spectral index is anticipated to be harder,

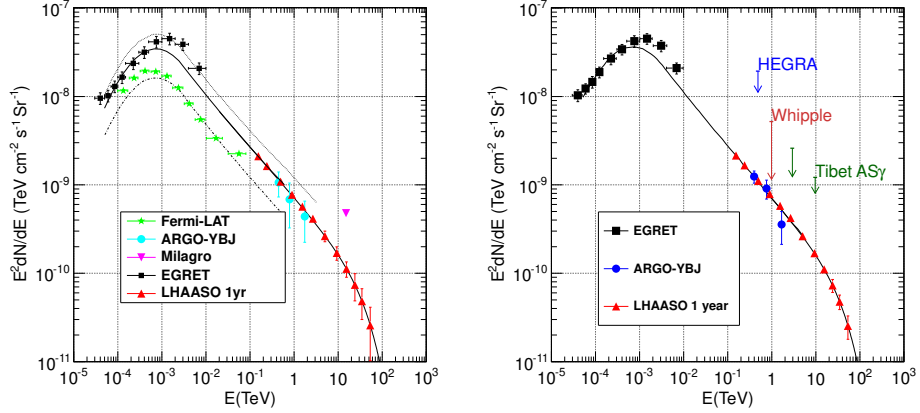


Figure 25: The predicted DGE flux respectively at Cygnus region (left) and $25^\circ < l < 100^\circ$, $|b| < 5^\circ$ (right) observed by LHAASO experiment.

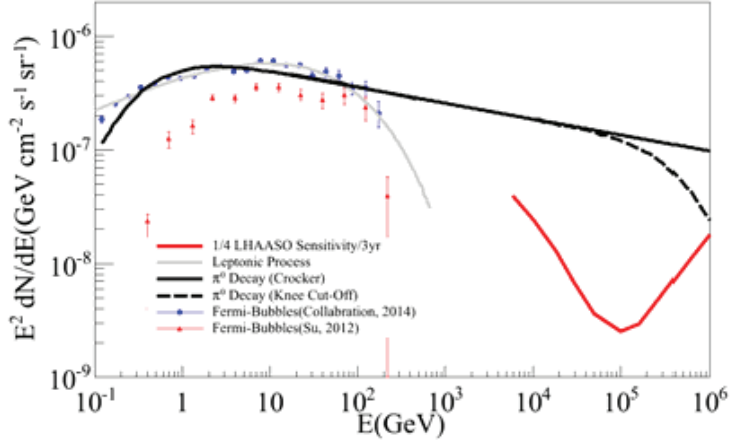


Figure 26: The extrapolated energy spectrum of the Fermi bubbles in hadronic model (black solid line) according to [19] and the integral sensitivity of one quarter LHAASO project (red solid line).

thus the spectra of γ -rays could extend to 100 TeV. According to the sensitivity of LHAASO, it can make precise measurement between 10–100 TeV and thus offer the support to the acceleration mechanism of CRs within Fermi bubbles and hadronic origin of γ -rays. Figure 26 shows the energy spectrum of the Fermi bubbles extrapolated according to the hadronic model of [19] (black solid line) and the integral sensitivity of one quarter LHAASO project (red solid line).

3. Diffuse γ -ray constraints to the CR knee region The origin of the CR knee has been a mystery since its discovery. So far there are various models proposed to explain the break of all particle spectrum at the knee region. However, due to the large uncertainties of the measurement of individual composition, it is hard to further testify these hypotheses. In [20], Guo et al. argue that the different models about the knee region could generate distinct DGE spectra, in which a knee-like structure also appears at about hundreds of TeV due to the different CR compositions around PeV energies. Thus the measurement of the DGE at hundreds of TeV could use to distinguish the models of the knee region. Figure 27 shows the γ -ray spectra predicted by different knee models, and the grey dash line is the expected LHAASO sensitivity.

2.10.3. Diffuse γ -ray constraints to Galactic neutrino flux

The IceCube collaboration has recently reported the discovery of high-energy extraterrestrial neutrino flux[259]. After two years' operation, the IceCube experiment has observed 28 neutrino events

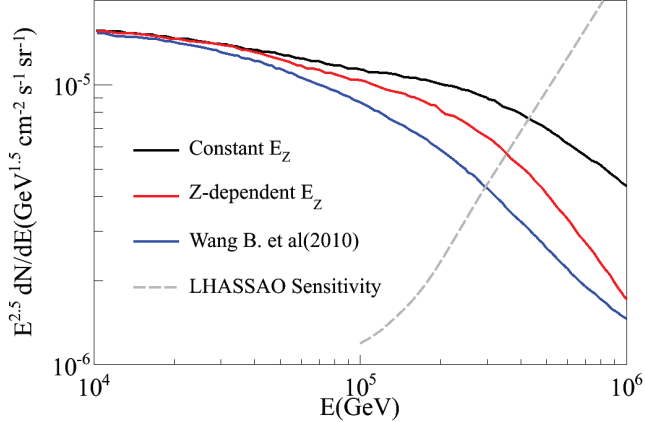


Figure 27: The γ -ray spectra predicted by different knee models[20] and the LHAASO sensitivity (grey dash line).

between 30 TeV and 1.2 PeV, which is far above the 10.6 events evaluated from conventional atmospheric background. It declares that we have entered into a new era of neutrino astronomy. The interactions between CRs and interstellar medium could also generate neutrinos as well as γ -rays. Thus the neutrinos detected by the IceCube may partly originate from Galaxy. The DGE could effectively impose restrictions on the origin of the Galactic neutrinos and the contribution of the Galactic neutrino flux[260, 261, 20, 262, 263]. The measurement of the DGE above hundreds of TeV by the coming LHAASO can provide more stringent constraints.

2.10.4. Short summary

γ -ray astrophysics has made a remarkable progress. Especially recent observations of the DGE obtained by both space- and ground-based instruments have significantly changed and deepened our understanding of the origin and transport of the CRs in the Galaxy. While already being investigated at GeV energies over several decades, assessments of the DGE at TeV energies remain sparse and lots of terra incognita is going to be uncovered in the future. LHAASO ground array is promising to provide more detailed observations of VHE DGE above tens of TeV and open a new window at PeV energies.

2.11. Multi-wavelength study of Galactic cosmic rays

Executive summary: Cosmic rays were discovered more than 100 years ago. Theoretical studies and multi-wavelength observations have provided plenty of evidences indicating that the shock wave of supernova remnants are the best site to accelerate Galactic cosmic rays. However Galactic cosmic rays' origin, propagation and distribution are still far from well-known. With the next generation telescopes, such as LHAASO and SKA, we may make one giant leap for understanding Galactic cosmic rays by finding the PeVatrons, measuring the magnetic field amplification, examining the energy conversion rate and nonlinear effect, increasing evidence for TeV CRs diffusive propagation and studying their distribution in our Galaxy.

2.11.1. Background

On 7th August 1912, Austrian Physicist Dr. Hess found that the flux of ionizing radiation measured in atmosphere increased when altitude rises. He wrote the sentence in his paper: The results of my observation are best explained by the assumption that a radiation of very great penetrating power enters our atmosphere from above. This is the discovery of cosmic rays (CRs). Now we know that CRs are mainly comprised of proton with about 10% fraction of helium and a spot of heavy element nuclei and electrons. The energy spectrum of CRs has the form of a power law with two bends at about 4 PeV (i.e., knee) and 4 EeV (i.e., ankle) respectively. CRs with energy lower than the knee are usually known as Galactic CRs.

Supernova remnants (SNRs) are known as the best origination candidate for Galactic CRs (other candidates include pulsar wind nebulae, X-ray binaries, Galactic centre, super-bubbles and so on). The basic idea was first proposed by Baade and Zwicky in 1934. They noticed that if the Galactic supernova rate is about 2-3 per century with each explosion releasing kinetic energy of about 10^{51} erg and 10% of the energy is used to accelerate CRs, the observed CRs energy density in our Galaxy, about 1 eV cm^{-3} , could be naturally explained. Further theoretical studies gave the detail accelerating mechanism: diffuse shock acceleration (DSA).

Multi-wavelength observations have provided lots of evidence supporting SNRs as the origin of Galactic CRs: (1) Radio observations display bright filaments and twisty structures of SNRs which are predicted by DSA. (2) The average spectral index, α , of SNRs is about 0.5 ($S_v \propto v^{-\alpha}$) indicating a particle energy index, γ , of about 2 ($\gamma = 1+2\alpha$). (3) The magnetic fields derived from observing OH 1720 MHz masers in the SNRs shocked regions are significantly amplified to magnitude of mG. (4) X-ray observations detect synchrotron emissions from young SNRs showing electrons have been accelerated up to 100 TeV and the magnetic fields are amplified to 100-600 μG . (5) Molecular spectral line observations detect enhanced ionization rate surrounding SNRs. (6) Many SNRs interacting with molecular clouds or neutral hydrogen clouds, which are identified by infrared, centimeter, millimeter and sub-millimeter observations, are also GeV and/or TeV emitting objects. (7) The two components of optical H α line discovered support the existence of CRs induced shock precursor. (8) *Fermi* satellite has detected the pion bump feature from SNRs IC443 and W44 giving the first direct evidence that both SNRs accelerate CRs to GeV.

A combination of DSA and CRs propagation in our Galaxy is usually referred as the SNR paradigm. The theoretical and observational works mentioned above are in favor of this paradigm. However, many questions in the paradigm are still open. Multi-wavelength observations from next generation telescopes especially LHAASO and SKA should play a key role in solving the problems in DSA theory, CRs diffusive propagation and distribution.

See Ref. [264]

See Ref. [265]

2.11.2. The diffuse shock acceleration theory

Some key predictions or requirements of DSA are that: SNRs could accelerate CRs to the knee, i.e., about 4 PeV; magnetic field amplification is needed to accelerate CRs; the energy conversion rate should be high, i.e., larger than 10%, and CRs should have important nonlinear effect on the structure of the shock [266, 267].

The CRs are usually traced by 4 emission processes. For electrons, the tracers are synchrotron radiation ($\propto N_{CRe}B^2$, where N_{CRe} is the column density of electron, B is the magnetic field strength), bremsstrahlung ($\propto N_{CRe}N_H$, where N_H is the column density of neutral and molecular hydrogen) and inverse Compton (IC) scattering ($\propto N_{CRe}N_*$, where N_* mean the column density of background photon density). For protons, the tracer is neutral pion decay ($\propto N_{CRp}N_H$, where N_{CRp} is the column density of protons). The first process usually dominates in the radio band and sometimes appears in the X-ray band. The last three processes contribute important radiation in the γ -ray band. The key to illustrate SNRs as the origin of Galactic CRs is to separate the hadronic process from the leptonic processes. Since both bremsstrahlung and pion decay are in proportion to N_H , their relative intensity is determined by the density ratio between electrons and protons (K_{ep}). Because K_{ep} is usually smaller than 0.01, bremsstrahlung could be easily distinguished from pion decay (see the estimation from [268]). The main confusion is from IC.

Multi-wavelength observations are so far the best way to solve the problem. From synchrotron radiation (radio and X-ray bands), we could investigate the electron energy index which can be used to restrict the IC radiation. Furthermore, the ratio of electron energy loss between synchrotron radiation and IC is $P_{sy}/P_{IC} = U_B/U_{ph}$, where U_B and U_{ph} are the energy densities of magnetic field and background photon field. Higher magnetic field strength will lead to less IC radiation. The OH 1720 MHz maser (centimeter band), X-ray synchrotron radiation (X-ray band) can be used to estimate the magnetic field strength. The background photon field is usually treated as the 3 K cosmic background radiation. However, for some SNRs, the infrared radiation from dust (infrared band) also has a great contribution to the photon field. For pion decay, it depends on the material distribution which can be inferred by the molecular lines observation (centimeter, millimeter/sub-millimeter band), dust observation (infrared band) and X-ray observation.

(1) Pevatrons

In the γ -ray band, there are two crucial spectral windows to distinguish pion decay from leptonic processes. The first one is the sub-GeV window. In this window, the spectrum of pion decay is characterized by the pion bump—rises steeply below ~ 200 MeV. This feature has been observed as the first direct evidence for accelerating proton at GeV. Since the current ongoing γ -ray satellites are not sensitive at this band, further MeV-GeV telescopes, such as PANGU [269], may complete the large sample investigation. Another window is the band well beyond 10 TeV, such as 100 TeV. In this band, the γ -ray contribution from the IC component is greatly suppressed due to the Klein-Nishina effect. The hadronic origin could be established through detailed modeling with multi-wavelength information. So far, LHAASO has the best sensitivity at the energy above 10 TeV (see Figure 28). It will not only give the first SNR observation above 30 TeV, but also greatly reduce the error bar of the data which is critical to reduce the possibility that the observed data, sometimes, could be well fitted by different models. Some young SNRs should be PeVatrons is a key prediction of SNR paradigm theory, while LHAASO will play a great role in verifying it.

(2) Magnetic field amplification

Magnetic field amplification is a prediction of sufficient CRs acceleration and is also required if SNRs can accelerate CRs to PeV. LHAASO could give direct evidence of PeVatrons, but the pro-

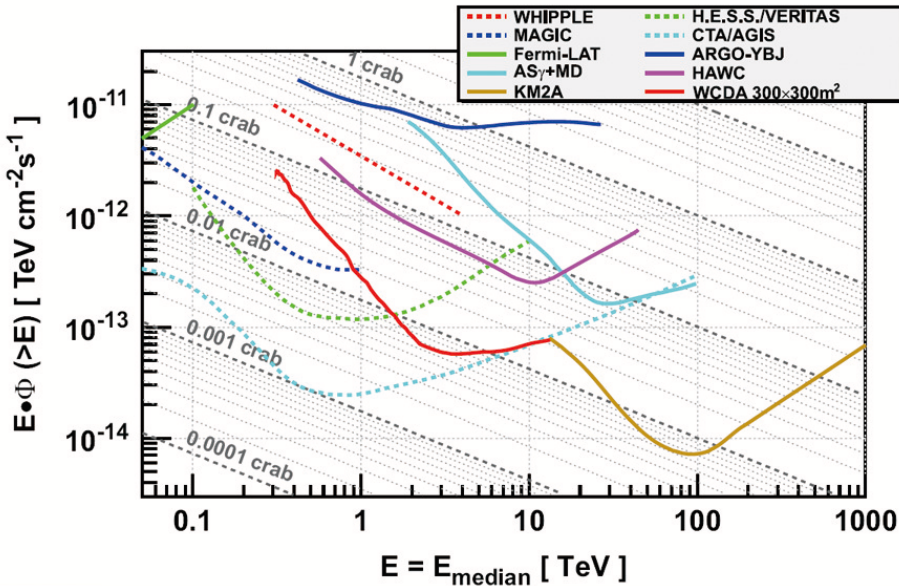


Figure 28: The sensitivity of LHAASO-WCDA and LHAASO-KM2A [21].

cess of how the CRs are accelerated to PeV is not within its reach. As mentioned above, previous magnetic field strength studies are mainly based on OH 1720 MHz maser and X-ray synchrotron radiation observations. Both studies indicate significant magnetic field amplification. The OH 1720 MHz masers only appear in shocked molecular cloud with density of about 10^5 cm^{-3} . That means the magnetic field strength measurement is constrained to a compact region. For most parts of an SNR, OH maser observation is not able to measure the magnetic field strength. For young SNRs, X-ray synchrotron emission is only identified in narrow regions close to shock front. So, does magnetic field amplification really appear in the whole region of an SNR?

The Zeeman effect of neutral hydrogen has been used to measure the magnetic field strength of the interstellar medium. The difficulty of this method is the superposition of different hydrogen clouds within narrow velocities. Recently, observations have shown that some SNRs are associated with high velocity neutral hydrogen clouds [270]. Since those clouds are distinct from background ones, to measure their magnetic fields is possible. SKA with its sensitivity, angular resolution and big field of view (see Figure 29), will bring us a chance to map the magnetic field strength with great details in the large area of an SNR. It could help to reveal where the magnetic field amplification happens and how large the amplification can reach.

Magnetic field amplification is believed to be associated with density turbulence. This turbulence will cause scattering, scintillation of background and might cause the background point source to become an "extended" one. The scintillation of pulsars has been widely used to detect interstellar cloud physical properties to study the Kolmogorov spectrum. When a pulsar is located behind a SNR, even behind the shock region, we could use it to detect the turbulence in the shock region with the same method used to study the interstellar electron clouds. Since most pulsars are faint (previous studies usually use pulsars with flux larger than 20 mJy at 400 MHz), a more sensitive telescope like SKA is needed to do this work.

(3) Energy conversion rate and nonlinear effect

To explain the observed CRs energy density, an energy conversion rate of about $\sim 10\%$ is needed. In the nonlinear DSA theory, the conversion rate in effective CRs acceleration shock can reach up to 50 %. However it is not true for some SNRs. One case is Cas A. Abdo et al. (2010) claimed [271],

2.11 Multi-wavelength study of Galactic cosmic rays

Table xxx: Parameters for Comparable Telescopes															
$A_{\text{eff}}/T_{\text{sys}}$	m^2/K	60	265	276	250	100	61	1250	321	124	1150	65	391	1000	1630
FoV	deg^2	0.25	0.25	0.015	0.13	0.65	14	0.0017	0.86	0.25	0.003	30	18	27	0.49
Receptor Size	m	25	25	101	45	64	39	300	13.5	25	225	12	15	35	15
Fiducial frequency	GHz	1.4	1.4	1.4	1.4	1.4	0.12	1.4	1.4	1.4	1.4	1.4	1.67	0.11	1.67
Survey Speed FoM	$\text{deg}^2\text{m}^{-1}\text{K}^{-2}$	9.00×10^2	1.76×10^4	1.14×10^3	8.13×10^2	6.50×10^4	5.21×10^4	2.66×10^3	8.86×10^4	3.84×10^3	3.97×10^4	1.27×10^5	2.75×10^4	2.70×10^7	1.30×10^6
Resolution	arcsec	$10\text{-}150 \times 10^3$	1.4 - 44	420	2	660	5	88	11	16	192	7	0.9	11	0.22
Baseline or Size	km	217	1 - 35	0.1	27	0.064	100	0.5	4	2.7	225	6	50	50	200
Frequency Range	GHz	1.3-1.8, 4-8, 22-24	1 - 50	0.2 - 50+	0.15, 0.23, 0.33, 0.61, 1.4	0.44 to 24	0.03 - 0.22	0.1 - 3	0.7 - 2.5, 0.7 - 10	0.3 - 8.6	0.3 - 10	0.7-1.8	0.65-1.67	0.050-0.350	0.35-14
Bandwidth	MHz	400	1000	400	450	400	4	800	1000	160	1000	300	500	250	770
Cont. Sensitivity	$\mu\text{Jy}\cdot\text{hr}^{1/2}$	27.11	3.88	5.89	6.13	16.26	266.61	0.92	3.20	20.74	0.89	28.89	3.72	2.06	0.72
Sensitivity, 100 kHz	$\mu\text{Jy}\cdot\text{hr}^{1/2}$	1714	388	373	411	1029	1686	82	320	830	89	1582	263	103	63
SEFD	Jy	46.0	10.4	10.0	11.0	27.6	45.2	2.2	8.6	22.3	2.4	42.5	7.1	2.8	1.7

Notes to Table														
eMERLIN	Frequencies non-contiguous													
JVLA	Multiple antenna configurations													
GBT	Single dish													
GMRT	Frequencies non-contiguous													
Parke's MB	Multi-beam (13)													
LOFAR	Parameters for all NL stations													
FAST	Single dish													
MeerKAT	SKA Precursor													
WSRT	Frequencies non-contiguous													
Arecibo	Single dish													
ASKAP	SKA Precursor													
SKA1-survey	Multi-beam (36)													
SKA1-low														
SKA1-mid														
Notes: All (cont'd)	Fiducial frequency: Most Parameters	$\Omega_{\text{FoV}} = (\pi/4)(66\text{A}/\text{Dish})^2$	Mixed 13.5-m & 15-m dishes	FoV based on 15-m dishes	Under construction	Planned								
	SEFD derived from $A_{\text{eff}}/T_{\text{sys}}$	Sensitivity derived from SEFD & BW	Sensitivity derived from SEFD & BW	Gray shading: <400 MHz capable	System efficiency assumed 100%	SEFD: System Equivalent Flux Density								

Figure 29: The basic parameters for SKA [22].

only less than 2 % of the total energy is used to accelerate CRs. LHAASO may push this study further by measuring and modeling many SNRs energy spectra with high sensitivity and broad energy coverage and give more accurate conversion rate estimates to a sample of SNRs.

A general condition for the 10 % conversion rate is a Galactic supernova explosion rate of 2-3 per century. Considering the typical life time of about 10^5 years for an SNR, a conversion rate of ~ 10 % means that the total number of Galactic SNRs is at least larger than 1000. This is much larger than 300 SNRs currently detected in our Galaxy. Is this gap real or just because we miss lots of SNRs due to observation selection effects? For the first one, we need reconsider the theory of SNR paradigm. For the second one, we need to find the missing ones. Previous Galactic radio surveys are usually sensitivity limited or resolution limited which lead to the failed detection of old, faint, large remnants or young, small remnants. The ability of SKA (high resolution, sensitivity and big field of view) gives us a chance to discover the missing SNRs in our Galaxy. It will answer how many SNRs are in our Galaxy and even tell us how the SNRs are distributed in our Galaxy. The total number of SNRs is critical to answer whether they are the main accelerator of Galactic CRs. The distribution of SNRs affect the CRs injection model which is important when modeling the diffuse γ -ray emission of our Galaxy.

Another way to find SNRs is to identify the lower energy counterparts of unidentified GeV/TeV sources. One example is the discovery of SNR G353.6-0.7 which is the first SNR discovered at TeV band and then identified at radio band [272]. Till now, more than 120 TeV sources have been discovered, however, more than 1/3 of them have no lower energy counterparts [273]. It is undoubtedly that LHAASO will find more TeV sources and some of them should be SNRs. The combination of SKA and LHAASO, will identify those missing SNRs, which allows us a compelling population study of the conversion rate problem.

When the energy is effectively converted to CRs, the shock structure will be modified which will lead to a curvature of electron spectrum with spectral hardening at high energy. This effect has been detected for a few SNRs (see Figure 30), but there are still lack of a large sample and spatial detailed study, e.g. more obvious nonlinear effect towards TeV SNRs. To do this study, the SKA

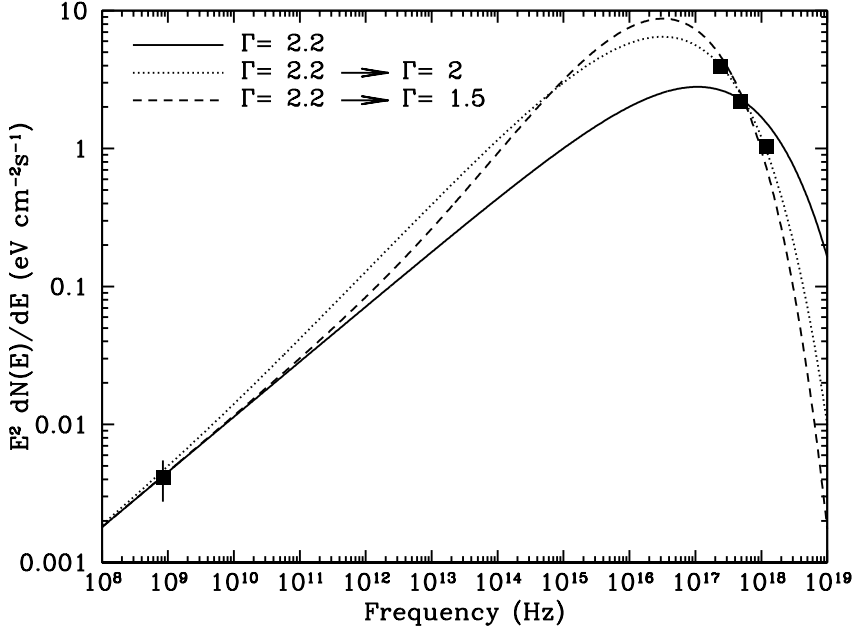


Figure 30: Radio to X-ray synchrotron spectrum of the northeastern part of RCW 86. A curve model is needed to fit spectrum [23].

and LHAASO need work together.

2.11.3. CRs diffusive propagation and distribution

When the CRs are accelerated to high energy and the shock velocities slow down, the CRs will propagate diffusively from SNRs to the Galaxy. These CRs interact with interstellar medium forming the non-thermal background diffuse emissions from radio to γ -ray bands.

(1) Propagation

The escaped CRs take energy away from their mother SNRs. Therefore it is a possible explanation why some TeV bright SNRs have a very low energy conversion rate. One case for CRs escape is from the *Fermi* observation of W44 in the GeV band [274]. While, for young SNR like Cas A, the escaped CRs should have very high energy. These CRs interact with materials to produce TeV emission. Compared with CTA, LHAASO has higher sensitivity to extended sources which make it perfect equipment to detect the TeV halo surrounding young SNRs. Since pion decay also depends on the material density, the infrared, centimeter or millimeter observations are also needed to derive the density distribution surrounding SNRs. High energy CRs will escape earlier and faster than lower energy CRs, so the halo may also have a GeV/TeV ratio change with distance away from the SNR. But the angular resolution of LHAASO is low, so CTA is more suitable for this kind of study.

(2) Distribution At a certain frequency, the Modeling this emission will show the column information of The distribution along the line-of-sight can be get with the absorption measurements of HII regions and planetary The large number of these two types of sources will reveal a 3D emissivity distribution of all-sky radiation. This extra

Two challenges are the spatial distribution and spectral energy distribution of CRs. Two methods can be used to measure the CRs distribution. One is modeling the diffuse emission from radio to γ -ray bands. Another one is measuring the emissivity of electron from radio observations with the help of absorption from HII regions and planetary nebulae. The first one will only give two dimen-

sional information and the second one may map the three dimensional electron distributions.

By employing the 21 months *Fermi* data, [241] used the GALPROP software to analyze the Galactic diffuse γ -ray emission. Their work achieves great success on reproducing the observed γ -ray emission and giving the γ -ray composition and distribution from electrons and protons respectively. However, they do not consider whether the electrons and protons, which are used to model γ -ray emission, could produce the observed radio emission or not. A combination modeling of radio and γ -ray is necessary. However, the angular resolution of current radio surveys in frequency of a few tens MHz to a few hundreds MHz is poor (usually worse than 1 degree) and can not effectively separate point sources from diffuse emission. SKA can provide the needed high resolution low frequency radio data and LHAASO will supplement the high energy TeV data.

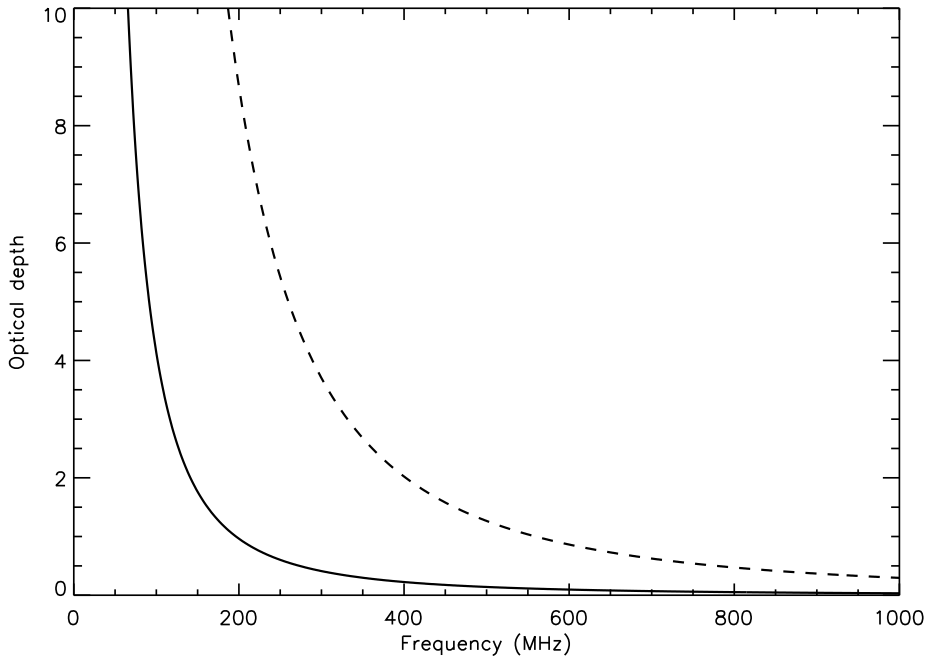


Figure 31: optical depth vs observation frequency of typical HII region and planetary nebulae. The solid line is for HII with temperature $T_e=10000$ K, electron density $n_e=100 \text{ cm}^{-3}$, size $\Delta l=10 \text{ pc}$. The dashed line is for planetary nebulae with temperature $T_e=10000$ K, electron density $n_e=3000 \text{ cm}^{-3}$, size $\Delta l=0.1 \text{ pc}$.

Generally speaking, if we could get the synchrotron emission and magnetic field information at each position, it is possible to give a three dimensional model of electron distribution in our Galaxy. The only problem is how to get the distance information for synchrotron emission. A long time ago, people have noticed that HII regions can absorb the background low frequency radio emission though free-free absorption. This gives us a chance to estimate averaged foreground synchrotron emissivity as the background emission has been screened. Furthermore, if there are many HII regions distributed close to one line of sight, we could even estimate the emissivity between those HII regions. Figure 31 displays the relation between optical depth and frequency for typical HII regions and planetary nebulae. Figure 32 shows the spatial distribution of HII regions and planetary nebulae. For HII regions, they are big, so easy to be detected. Their distances are also easily determined. However, the total number of known HII regions is small and they are mainly located on the Galactic plane. For planetary nebulae, their distribution is wider than HII regions, so can be used to estimate the emissivity of middle latitude regions. The total number of planetary nebulae is big and planetary nebulae become optical thick at higher frequency which mean they can measure the emissivity at broader region and dynamical range. The disadvantages

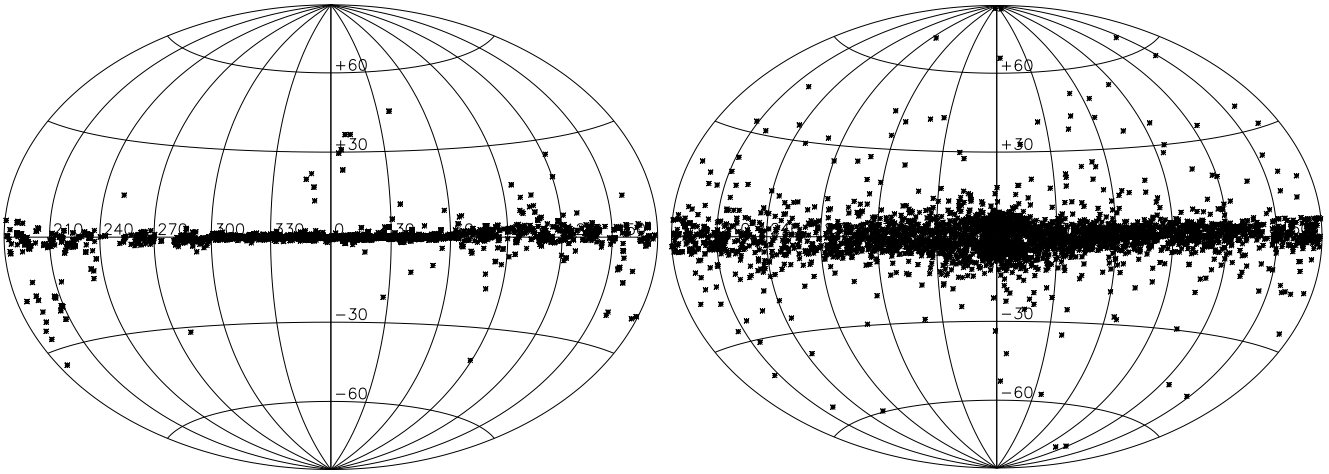


Figure 32: (The distribution of HII regions and planetary nebulae along Galactic latitude.

are that their sizes are small and measuring the distances are not easy for most of them.

Currently, only a few tens absorptions from HII regions have been detected and no absorption detections for planetary nebulae. The main problem is due to the poor angular resolution and sensitivity of current low frequency radio surveys. SKA has enough resolution (such as a few arc-second) and sensitivity to carry out this study. This will be a great step to know the CRs-electron's distribution in our galaxy.

EXTRA-GALACTIC GAMMA-RAY ASTRONOMY WITH LHAASO

3. Extra-Galactic GAMMA-RAY ASTRONOMY WITH LHAASO

3.1. *Upgrading of LHAASO/WCDA Towards Multi-messenger Observation*

Executive summary: LHAASO is planning to enhance its sensitivity at energies around 100 GeV by utilize MCP staffed 20" PMT in the Water Cherenkov Detector Array. The effective area for gamma ray detection will reach to 1800 m^2 and differential sensitivity to 0.2 CU at 50 GeV. It will be the very useful survey detection for transient phenomena at 50 GeV in the northern sky. LHAASO is expected to play an important role in the multi-messenger observation with the upgrading.

3.1.1. *Introduction*

The first multi-messenger observation of gravitational wave (GW) event GW170817 by LIGO and VIRGO GW observatories together with many other Electro-magnetic (EM) wave observations, such as FERMI[275] and the multi-wavelength campaign on the possible EM partner of the very high energy neutrino IceCube-170922A detected by IceCube experiment[24] are very significant progresses in astroparticle physics in the past year. They opened new windows for exploring the high energy phenomena in the universe. This, however, becomes a challenge to Large High Altitude Air Shower Observatory (LHAASO) experiment with its original proposal which is designed to target the high energy (above several hundred GeV) gamma ray sources and charged particles at even higher energies up to a few EeV. At energies lower than 300 GeV, the gamma ray detection sensitivity is not sufficient to detect those sources which is typically faint. In order to enhance the sensitivity below 100 GeV, we proposed to enlarge the sensitive area of the photo cathode of the water Cherenkov detector (WCD) in the LHAASO array. In this paper, we are going to briefly describe the LHAASO experiment and its WCD Array as well as the upgrading plan in particular in the second section, and the performance of WCDA in gamma ray astronomy with the the enhancement at low energy region in third section. The whole upgrading plan is summarized in the forth section.

3.1.2. *LHAASO/WCDA Experiment and the Upgrading Plan*

LHAASO is a multipurpose complex of EAS detection consisting of four major detector arrays[62], ie. 5195 scintillation counters (ED) and 1171 muon detectors (MD) covering an area of 1.3 km^2 , 78,000 m^2 water Cherenkov detector (WCD) with 3120 gap-less detecting units, and 18 wide field of view Cherenkov telescopes watching over the sky above the whole complex with a coverage of 4608 square degree. As shown in Figure 68, the WCDA in the center of the array is divided into 3 components as 3 independent water pools, namely two smaller pools with the area of $150 \text{ m} \times 150 \text{ m}$ each and the larger one with the area of $300 \text{ m} \times 110 \text{ m}$.

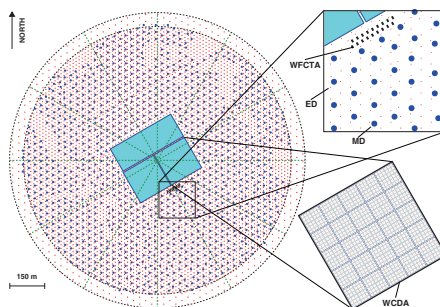


Figure 33: The layout of the scintillator counter (small dots) array, muon counter (big dots) array, water Cherenkov detector (rectangle in the center) array and 18 wide field of view Cherenkov telescopes (small rectangles) in the LHAASO complex of multi-detector array of 1.3 km^2 .

The firstly built pool in south-west has 900 WCD units, 25 m^2 each, equipped by a large (8") PMT for timing and a small (1.5") PMT for pulse size at the center of each unit 4 m beneath the water surface, and measures shower directions with a resolution better than 0.2° above 10 TeV and 1.0° above

600 GeV. Only direct Cherenkov light generated by the shower particles is collected by the upwards watching PMTs. To suppress the cross talking effect and improve the timing resolution, black plastic divisions are installed between units. The Front End Electronics (FEE) of the large PMTs is designed to have the timing resolution of 0.5 ns. The dynamic range of the detector is enlarged very much by using the small PMT. This enables the measurement of the detailed particle density distribution in the shower cores without significant saturation even for energetic showers up to 10 PeV and achievement of the core location resolution better than 3 m over a wide energy range. This is designed for the identification of the primary particle species in the cosmic ray composition and spectrum measurements. It is also very useful in locating the shower inside the pool with minimal loss of good detected events. The pool is planned to be turned on for operation early 2019.

Low energy showers are small in terms of total number of particles that reach to the pools, therefore the total Cherenkov signal generated by those secondary particles in every detector unit is faint, even for units being near the cores of the showers. In order to enhance the gamma ray detecting sensitivity at low energies, enlarging the sensitive photo-cathode area of the PMT in the same size unit could be one effective way to catch the faint signals. LHAASO's upgrading plan is along with this approach, namely to replace the 8" PMTs by 20" PMTs in the rest two pools of 55,500 m² in total. The customized design of the PMTs using multi-channel-plate (MCP) instead of the traditional dynodes enables good uniformity between PMTs as well as the Transit Time Spreads (TTS) less than 7 ns, Cathode Transit Time Distribution (CTTD) less than 2 ns and long lifetime. The photo cathode is a factor of 6.25 larger than the 8" tube, therefore the dynamic range is also shrunk by the same factor. In order to compensate the loss, a 3" PMT is installed beside the large PMT in each unit, read out only for the pulse size by a simplified version of FEE covering 4 orders of amplitudes in number of photo-electrons.

3.1.3. Performances and Prospects for Gamma Ray Astronomy

Gamma ray induced showers are different from showers induced by charged CR nuclei in terms of the hits distribution in the pool. In general, the later is more spread out than the former ones as shown in Figure 34, where two MC simulated events due to 1 TeV gamma ray and 2 TeV proton are compared with each other. Even more significantly, the CR events have many "hot spots", the populated hits, outside the core region, while the gamma ray events are much cleaner beyond some distance from the core. This enables us to identify the gamma events out of the CR background, nevertheless they are

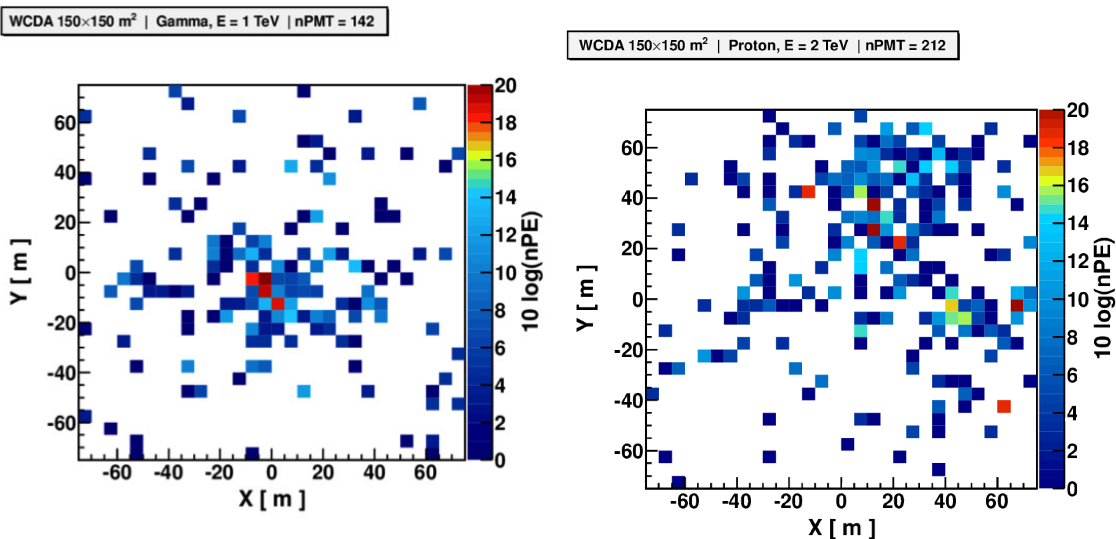


Figure 34: Two simulated events recorded by one of the pools of WCDA induced by 1 TeV gamma ray (upper) and 2 TeV proton (lower), respectively.

much more ($10^{4\sim 5}$) than gamma ray signals even if within a very small angular region defined by the point-spread-function (PSF) near the sources. By eliminating the events which have the most populated

hit in the outer region, 45 m from the core, greater than certain number of photoelectrons, N_{th} , the CR background will be suppressed to very low in the nearby region of sources. Making balancing between the elimination of the background CR events and the loss the gamma-like signal events to maximize the sensitivity, it is found that N_{th} increases with the number of hits that are involved in the shower front fit, denoted as N_{fit} which measures the shower energy, i.e. proportional to $N_{fit}/\log N_{fit}$. Other parameters characterize the distribution of hits in the whole pool area, such as hit density in the outer region, are used in the identification of gamma ray events. This results an effective area for gamma ray detection of about 230 m^2 at 50 GeV and $30,000 \text{ m}^2$ at 1 TeV, respectively, if all 3 pools were equipped by 8" PMTs. The corresponding sensitivity of the gamma ray point-like source detection is plotted in Figure 35 as a function of gamma ray energy.

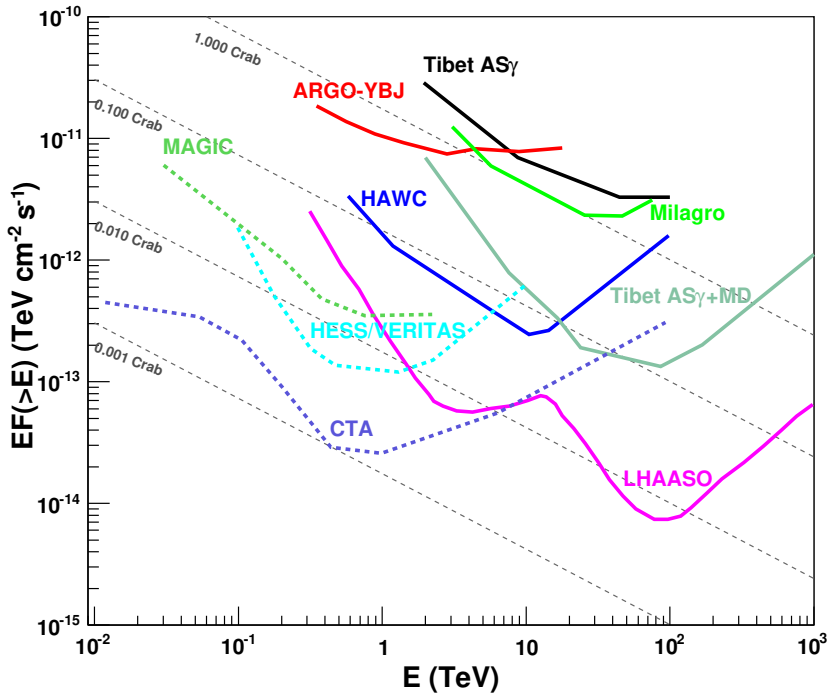


Figure 35: The integrated sensitivity of LHAASO (in pink) comparing with other experiments. The part of the curve below 10 TeV is the contribution of WCDA optimized with the cuts described in text.

With this configuration, LHAASO has a survey power for discovering all sources that are brighter than 7 mini crab unit above 1 TeV. Taking into account the wide field of view of $\sim 1/7$ of the entire sky and the constant exposure time of 24 hours, LHAASO is very significant in finding new sources. It is actually estimated that about 40 new AGNs[276] could be discovered within one year after it is fully operated. It is also expected that LHAASO will make a deeper survey inside our galaxy comparing with what has been done by HAWC experiment[277].

1. Enhancement at Low Energy With the upgraded configuration using 20" PMTs in the other two pools, the effective area at energies below 300 GeV is significantly enlarged, i.e. reaches to $1,800 \text{ m}^2$ at 50 GeV and $44,000 \text{ m}^2$ at 1 TeV. The corresponding differential sensitivity around 50 GeV is expected to be 0.2 crab unit per a quart decade of energy which is compatible with the space borne detector FERMI/LAT, as shown in Figure 36. The difference, however, is that the effective area is a factor of 1,800 larger than the later. This means that more than 1000 photons are expected to be recorded if the gamma ray burst event GRB090510 happened again in the field of view of LHAASO. In the event, FERMI/LAT recorded a single gamma photon at 30 GeV[28]. This opens a window for the multi-wavelength campaign in a much convenient way because of the clock-round operation of LHAASO. With any global alarm for transient phenomena, such as GBR, it is easy for LHAASO to recall the data

in the window in which the alarm was ringing. Not only the status of the source at T_0 can be observed, but also it is in principle possible to find any pre-emission of gamma rays if there were.

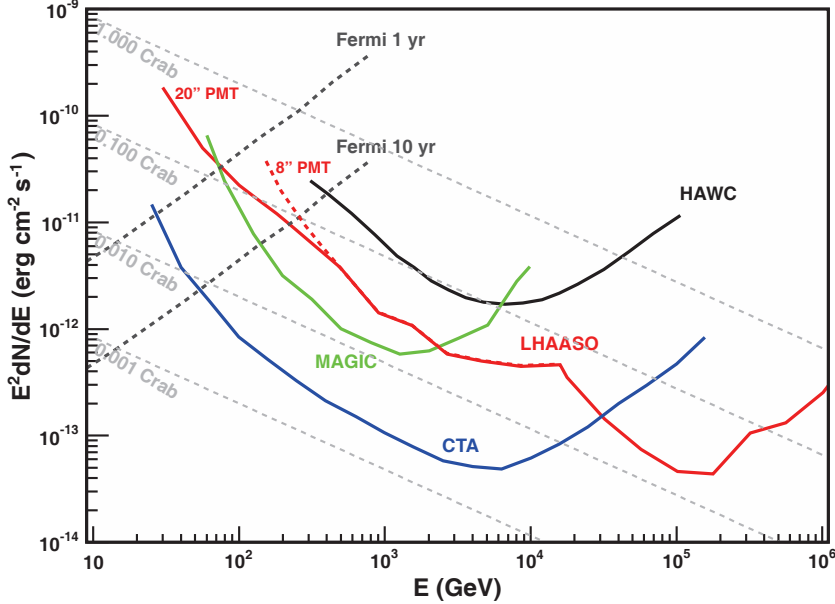


Figure 36: The differential sensitivity of LHAASO (in red) comparing with other experiments. Below 300 GeV, both estimates with 8" PMT configuration (dashed line) and 20" PMT configuration (solid line) are plotted. It is noticed that WCDA with 20" PMTs is almost as same sensitive as FERMI/LAT at 70 GeV.

With such a sensitivity, LHAASO will be a transient phenomenon finder as well. An alarm trigger algorithm is going to be operated to constantly watch all interested AGNs in LHAASO's FoV for any excess in various time windows, e.g. from few seconds to hours. It is useful for monitoring any AGN flare, e.g. if its emission level rises to be greater than 1 crab unit within an hour, an alarm will be broadcasted to the whole community.

2. Prospects for Multi-messenger Exploring Investigating sources with multi-messengers is very powerful in viewing of inside mechanism of high energy phenomena in the universe, particularly for possible common origins of the messengers, such as neutrinos, gamma rays, charged particles and gravitational waves. However, to identify the sources and verify the association, all corresponding detectors are required for sufficient sensitivities. As an example, we investigated the possible association between the ultra high energy muon neutrino event IC-170922A detected by IceCube experiment[24] and the blazer TXS 0506+056 which had a faint flare within 20 days after the neutrino event in multiple wavelength bands, including JX-ray (SWIFT), gamma ray (FERMI-LAT) and very high energy gamma ray (MAGIC). The SED of the blazer during the flare is reported in Ref. [24] and is quoted here in Figure 37 over a very wide energy range. Also shown in the figure, sensitivity curves of several experiments, including HAWK, HESS, VERITAS and upgraded LHAASO. According to this, LHAASO will play a significant role in such multi-messenger observation by covering an important energy range starting from, as low as, 30 GeV to few hundred TeV.

For other blazars including BL Lac objects and flat-spectrum radio quasars, the most extreme sub-class of active galactic nuclei (AGNs), LHAASO has a high duty cycle and a large field of view to monitor flares of them continuously. In Figure 38, the flare on Mrk501 for 35 days is measured by Swift, Fermi-LAT and ARGO-YBJ (See Ref.[25]). It clearly differs from the stable emission which fits well with the Synchrotron Self-Compton (SSC) model. Assuming the similar flare occurs again, the prediction for LHAASO's observation is plotted in Figure 4 and LHAASO will give an accurate spectrum at TeV region which can be the key to explain the radiation mechanism of flare. LHAASO

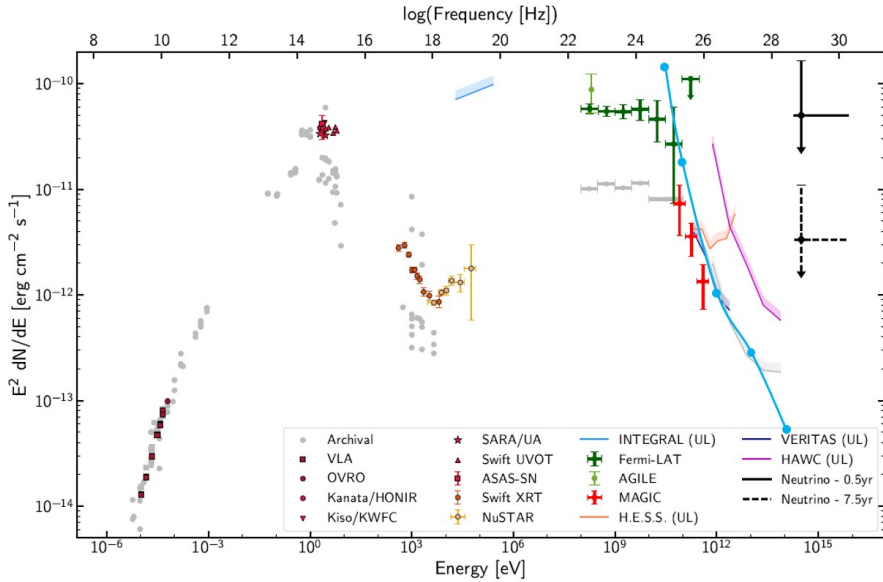


Figure 37: The SED of TXS 0506+056 during the flare within 20 days after the neutrino event IC-170922A. It is reported in Ref. [24] including sensitivity curves of HAWC, HESS and VERITAS experiments. The upgraded LHAASO sensitivity is also plotted in the same figure (light blue) from 30 GeV to 100 TeV.

not only serves as a global alarm system for the high energy flares, but also opens a great opportunity to identify the emitting mechanism during the flares. The potential of LHAASO in these researches, including exploring on new physics such as intergalactic magnetic field detection and Lorentz invariance tests, has been discussed in depth elsewhere (See Ref.[278]).

Mrk 501

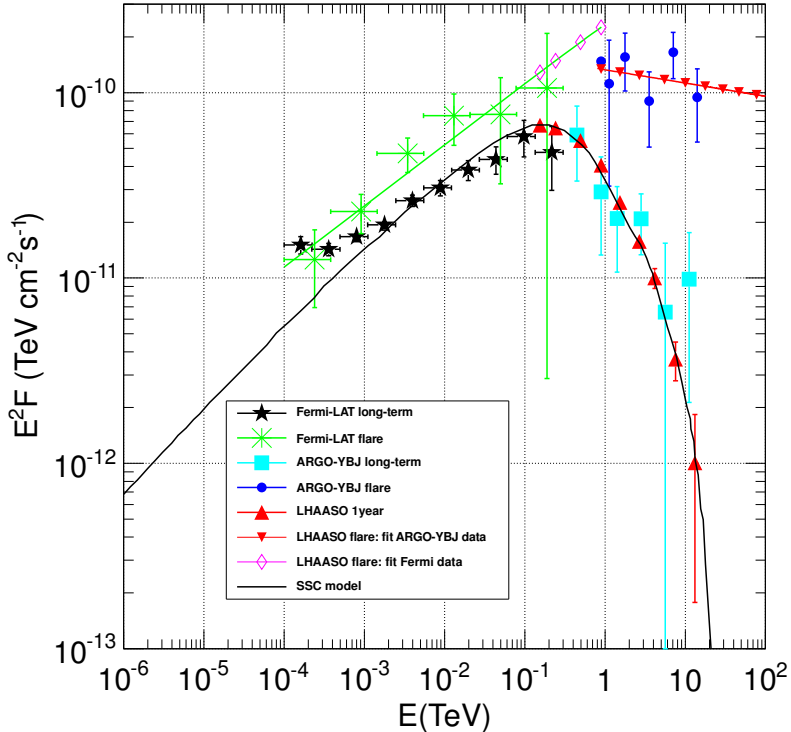


Figure 38: Expectation of the LHAASO project on Mrk501, compared with the measurement of Fermi-LAT, ARGO-YBJ[25].

3.1.4. Summary

LHAASO has made its upgrading plan by replacing the 8" PMTs in 70% of area of the central water Cherenkov detector with 20" PMTs. The first part, 30% of the total area of the detector, is under construction and going to be operated in early 2019. The whole array, including the scintillator counter array and muon detector array and Cherenkov telescopes, will be built up by 2021. With the upgraded configuration, the gamma ray detecting sensitivity below 300 GeV will be boosted to be about 0.2 crab unit per quarter decades of energy around 50 GeV and as same sensitive as FERMI at 70 GeV. LHAASO therefore will play a significant role in surveying for new sources brighter than 7 mini-crab-unit above 1 TeV in the northern sky and monitoring for transient phenomena in its FoV of the size of 1/7 sky at any moment. The LHAASO effective area of 1800 m^2 around 50 GeV is going to be useful tool in the multi-messenger observation involving ultra high energy neutrino or gravitational wave detections.

3.2. LHAASO Science: VHE observations of star-forming/starburst galaxies

abstract. Detections of high-energy gamma-ray emission from star-forming and starburst galaxies by *Fermi* suggest that these galaxies are huge reservoirs of cosmic rays and these cosmic rays convert a significant fraction of their energy into gamma-rays by colliding with the interstellar medium. We propose that LHAASO observes nearby star-forming and starburst galaxies within about 20 Mpc. With its high sensitivity at energies above 10 TeV, LHAASO will be able to probe the acceleration and propagation of PeV cosmic rays in these galaxies. As the processes producing VHE gamma-rays are accompanied by high energy neutrinos, the TeV-PeV gamma-ray flux of these galaxies can be used to study their contribution to the cosmic TeV-PeV neutrino background recently detected by IceCube.

3.2.1. VHE observations of star-forming/starburst galaxies

It is generally believed that Galactic cosmic rays (CR) are accelerated by supernova remnant (SNRs) shocks. CR protons interact with the interstellar gas and produce neutral pions (schematically written as $p + p \rightarrow \pi^0 + \text{other products}$), which in turn decay into gamma-rays ($\pi^0 \rightarrow \gamma + \gamma$). The high SN rate in star-forming and starburst galaxies implies high CR emissivities, so they are predicted to be bright gamma-ray sources. Ackermann et al. (2012) examined a sample of 69 dwarf, spiral, and luminous and ultraluminous infrared galaxies using 3 years of data collected by the Large Area Telescope (LAT) on the Fermi Gamma-ray Space Telescope (Fermi). They find further evidence for quasi-linear scaling relations between gamma-ray luminosity and total infrared luminosity which apply both to quiescent galaxies of the Local Group and low-redshift starburst galaxies. Nearby star-forming and starburst galaxies, such as M82 and NGC 253 are also detected at very high-energy (VHE) gamma-rays by e.g. HESS, VERITAS [104, 279]. But so far only quite a few galaxies have been detected. Moreover, no starburst galaxies have been detected above 10 TeV. With LHAASO, which has much higher sensitivity at energies above 10 TeV, one may expect that much more star-forming and starburst galaxies can be detected above 10 TeV and even above 100 TeV, as long as the galaxies are within the distance where VHE photons have not been absorbed by extragalactic background light (EBL) (typically within about 10-20 Mpc). At such high energy photons can only be produced by PeV cosmic rays, so LHAASO can probe the acceleration of PeV cosmic rays in these galaxies.

By extrapolating the TeV flux of M82 to the energy at 10 TeV, we find that the predicted flux at is $2 \times 10^{-13} \text{ TeV cm}^{-2} \text{ s}^{-1} (E/10 \text{ TeV})^{-0.2}$. NGC253 has a similar predicted flux above 10 TeV. These fluxes are above the sensitivity of LHAASO, so we expected that M82 and NGC 253 may be detected by LHAASO above 10 TeV. Since these two starburst galaxies are at distances of 2 – 3 Mpc, we expected that they may be detected even above 100 TeV by LHAASO.

Recently, Tang et al. (2014) [280] reported the detection of gamma-ray emission above 200 MeV from a luminous infrared galaxy NGC 2146, which is at a distance of 15.2 Mpc. Using this galaxy as an example, we here estimate the detectability of similar galaxies by LHAASO. Using the GeV flux and the spectrum of NGC 2146, we estimate the VHE flux assuming a simple power-law extrapolation. As can be seen from 39, the predicted energy flux is $E^2 dN/dE \simeq 10^{-13} \text{ TeV cm}^{-2} \text{ s}^{-1} (E/1 \text{ TeV})^{-0.1}$ at TeV energies, which is within the reach of LHAASO. Note that at a distance of 15.2 Mpc, the absorption by EBL is not severe for 10-100 TeV photons. Therefore, we propose that LHAASO perform systematic observations of nearby star-forming and starburst galaxies within 10-20 Mpc. The main candidates include M 82, NGC 253, NGC 2146, NGC 4945, NGC1068 and etc.

3.2.2. Implications of VHE observations

The gamma-ray luminosity of starbursts depends not only on the CR intensity, but also on the efficiency of converting CR proton energy into pionic gamma-rays. This efficiency in turn depends on the ratio of the timescale of pion production to the escape time of protons. Protons escape by advection with galactic winds or by diffusion. The gamma-ray flux at 100 TeV will thus not only give us information

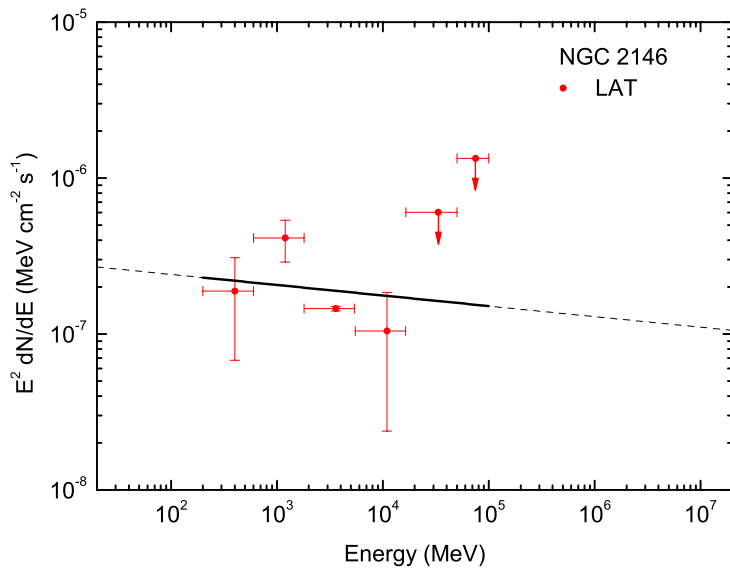


Figure 39: Spectral energy distribution for NGC 2146 obtained in the analysis of the 68 months of Fermi/LAT data. The black solid line represents the best-fit power law in the range of 0.2-100 GeV and the dashed line is the extrapolation to higher energies.

about the acceleration of PeV cosmic rays, but also tell us physics about the transport of these cosmic rays in galaxies.

Proton-proton collisions in starbursts not only produce neutral pions, but also produce charged pions, which then decay and produce neutrinos. Loeb & Waxman [281] argued that supernova remnants in starburst galaxies accelerate CR protons and produce high-energy neutrinos. Chang et al. (2015) [282] calculated the accumulated neutrino flux by using the infrared luminosity function of star-forming galaxies recently obtained by the Herschel PEP/HerMES survey. Recently, the IceCube Collaboration reported 37 events ranging from 60 TeV to 3 PeV within three years of operation, corresponding to a 5.7σ excess over the background atmospheric neutrinos and muons [69]. One attractive scenario for this excess is that they are produced by cosmic rays in starburst galaxies [283, 284]. But whether neutrinos in starburst galaxies can extend to sub-PeV/PeV energies is uncertain, given that normal supernova remnants are usually believed to accelerate protons only to PeV energy. It was suggested that hypernova remnants in starburst galaxies, by virtue of their fast ejecta, are able to accelerate protons to EeV energy [285] and produce sub-PeV/PeV neutrinos [284]. Future observations of nearby star-forming and starburst galaxies at 100 TeV will enable us to study the neutrino flux produced in such galaxies. One can then further study the total contribution to the cosmic neutrino background by all star-forming and starburst galaxies in the universe and hence pin down the starburst galaxy origin for IceCube neutrinos.

3.3. Measuring Extragalactic Background Light with LHAASO Observations of blazars

Executive summary: The extragalactic background light (EBL) contains important information about stellar and galaxy evolution. It leaves imprint on the very high energy γ -ray spectra from sources at cosmological distances due to the process of pair production. We have proposed a direct method to *measure* the EBL intensities by extracting the collective attenuation effects in a number of γ -ray sources at different redshifts. This method employs a Markov Chain Monte Carlo fitting algorithm to derive the EBL intensities and the intrinsic spectral parameters of γ -ray sources simultaneously, without prior assumption of the EBL shape. With larger sample of extragalactic sources, primarily blazars, and better spectral measurements by LHAASO, we expect to improve the measurement of EBL substantially.

3.3.1. Introduction

The extragalactic background light (EBL) is the diffuse radiation from ultraviolet to far infrared wavelengths, spread isotropically in the universe (for a review of EBL, see [103, 286]). The EBL originates from the radiative energy releases of all the stars, other extragalactic sources and diffuse emissions since the epoch of recombination. Therefore its intensity and spectral shape hold crucial information about the formation and evolution of stellar objects and galaxies throughout the cosmic history. The EBL is one of the fundamental quantities in cosmology.

Direct measurement of EBL is, however, very difficult due to the contamination of the foreground emission from the solar system zodiacal light and the Galactic stellar and interstellar emissions [287]. Technically, it also requires the absolute calibration of the instruments, and the understanding all measurement uncertainties. Given the difficulties, direct measurements provide just lower and upper limits of EBL intensity. A strict lower limit on the EBL intensity is provided by the integrated light from resolved galaxies, e.g. in optical by the Hubble Space Telescope [288] and in infrared by the Spitzer telescope [289]. The upper limit can be derived from the uncertainties of the absolute measurement of EBL [103].

Another indirect, but effective way to study the EBL is through the observation of very high energy (VHE) γ -rays. The VHE γ -rays from extragalactic sources are attenuated by the process of electron/positron pair production, $\gamma_{\text{VHE}} + \gamma_{\text{EBL}} \rightarrow e^+e^-$, when propagating to the Earth [290]. With the rapid development of ground based γ -ray imaging atmospheric Cherenkov telescopes (IACT), quite a few VHE γ -ray sources from cosmological distances have been detected, most of which are blazars, a subgroup of active galactic nuclei (AGN), with relativistic jet pointing towards the observer. With reasonable assumption of the intrinsic blazar spectra we can set an upper limit of the EBL intensity by comparing the observed spectra with the intrinsic spectra [291]. The observations of blazars H 2356-309 and 1ES 1101-232 at redshifts $z = 0.165$ and $z = 0.186$, respectively by HESS has set a strong upper limit of EBL, close to the lower limit set by galaxy counts, at the near infrared wavelength [106]. The MAGIC observation of 3C 279 at $z = 0.536$ set upper limit at the optical band [292]. In [293] Mazin and Raue gave a comprehensive study of EBL based on eleven blazars over a redshift range from 0.03 – 0.18. They explored a large number of hypothetical EBL scenarios and set robust constraints on EBL over a wide wave-length range. With the Fermi observation of blazar spectra at GeV to ~ 100 GeV more stringent constraints on EBL are shown recently (e.g., [294, 295, 296, 297, 298]). These studies seem to indicate that the Universe is more transparent than we had expected.

The power of this indirect method to study EBL is limited due to the fact that the intrinsic spectrum of each blazar is unknown. Therefore it is hard to disentangle the absorption effect by EBL from the intrinsic emission nature for a specific observation. The usual practice in the literature is to reconstruct the blazar intrinsic spectrum from the observation by first assuming an EBL model. The EBL model is rejected if it results in an unphysical intrinsic spectrum, for example, the reconstructed intrinsic spectrum follows a power law with an extremely hard spectral slope or even shows an exponential rise at the high energy end. Recently with large sample of γ -ray blazars, the EBL intensities were derived through a likelihood fit with given spectral template of the EBL [107, 108].

With the fast increasing number of γ -ray sources and better measurements of their spectra, we propose to directly *measure* the EBL intensities through extracting the collective absorption effects in a number of sources at different redshifts, using a global fitting method [27]. The method employs the Markov Chain Monte Carlo (MCMC) global fitting algorithm to fit the intrinsic source spectra and EBL simultaneously. Different from the previous studies in the literature, we make no assumption of the EBL spectral shape in the fitting. Instead the EBL intensities are approached as free parameters in a series of discrete energy bins, which are allowed to vary during the fitting. The application to a few sources by the current IACTs illustrate that this method can give effective measurement of both the intensities and shape of the EBL [27]. The derived results are consistent with the upper limits obtained with γ -ray observations as well as the theoretical modeling from galaxy evolution.

3.3.2. Attenuation of VHE photons

The observed VHE γ -ray spectrum after absorption by the EBL is commonly expressed as

$$F_{\text{obs}}(E) = e^{-\tau(E,z)} F_{\text{int}}(E), \quad (2)$$

where $F_{\text{int}}(E)$ is the intrinsic spectrum of the source at redshift z . The strength of the attenuation by EBL is described by the optical depth $\tau(E, z)$ as a function of energy E and the source redshift z . The optical depth τ is expressed as [299]

$$\tau(E, z) = \int_0^z dl(z') \int_{-1}^{+1} d\mu \frac{1-\mu}{2} \cdot \int_{\epsilon'_{\text{thr}}}^{\infty} d\epsilon' n'(\epsilon', z') \sigma(E', \epsilon', \mu), \quad (3)$$

where the variables with prime are the quantities at redshift z' , $dl = cdt = \frac{c}{H_0} \frac{dz'}{(1+z')\sqrt{\Omega_M(1+z')^3 + \Omega_\Lambda}}$ is the differential path traveled by the VHE photon, $\mu = \cos \theta$ with θ the angle between the momenta of VHE and EBL photons, $n'(\epsilon', z') = n(\epsilon'/(1+z'), z=0)(1+z')^3$ is the EBL number density at redshift z' , and σ is the pair production cross section. ϵ'_{thr} is the threshold energy for γ -ray energy $E' = E(1+z')$ with an angle $\cos \theta = \mu$ with the EBL photon. The cross section is peaked at a wavelength $\lambda/\mu\text{m} \sim 1.24E/\text{TeV}$ [300]. Therefore the observation of VHE γ -ray spectra can probe EBL at the wavelength from optical to far infrared, while it is not sensitive to UV band by the IACT data. The cosmological parameters used in this work are $\Omega_M = 0.274$, $\Omega_\Lambda = 1 - \Omega_M$, $H_0 = 70.5 \text{ km s}^{-1} \text{ Mpc}^{-1}$ [301].

3.3.3. Fitting method

We assume the intrinsic spectrum of blazar, F_{int} , is of log-parabola shape ($F \propto E^{-\alpha-\beta \log E}$). The blazar spectrum is commonly modeled by the synchrotron-self-Compton (SSC) scenario, which shows a concave γ -ray spectrum in general. If the measured energy range is not very wide, the simple power-law can actually give a quite good description to the observations. However, at least for some sources, deviation from single power-law distribution of the spectrum, even corrected for the absorption effect, has been observed [302]. Therefore we adopt the log-parabola form of the intrinsic spectrum. It has been tested that the log-parabola assumption of the intrinsic spectrum will give robust results of the EBL [27].

No prior assumption about the EBL shape is adopted in this study. We divide the wavelength range of EBL from $0.1 \mu\text{m}$ to $100 \mu\text{m}$, which is relevant for γ -rays between 100 GeV and 100 TeV , into 10 bins logarithmically. Within each bin the intensity νI_ν is assumed to be a constant ξ_i . Then we can fit the 10 ξ_i s, as well as the intrinsic source parameters of each source (nuisance parameters), from a set of observed γ -ray spectra $F_{\text{obs}}(E)$.

3.3.4. Perspective of LHAASO

We explore the potential of LHAASO to measure the EBL intensities with this method. We first generate simulated observations of the blazar spectra with LHAASO-WCDA [303]. In [303] we studied

the detectability of the blazars with LHAASO-WCDA, based on the Fermi AGN sample. The spectra of the Fermi AGNs, with known redshift measurements and within the field of view of LHAASO, are directly extrapolated to TeV energies based on the Fermi measurements. Then we apply the EBL absorption to the extrapolated spectra to derive the detected spectra of the sources. Comparing to the sensitivity of WCDA, we find that there will be about 30 – 40 Fermi blazars, mostly BL Lacs, could be detectable by LHAASO-WCDA in a few years’ survey. The actual number of sources may be higher, due to the unexpected flaring activities of the blazars and the sources without redshift measurements. However, the sources which do not have redshift measurements will not be able to be used to constrain the EBL.

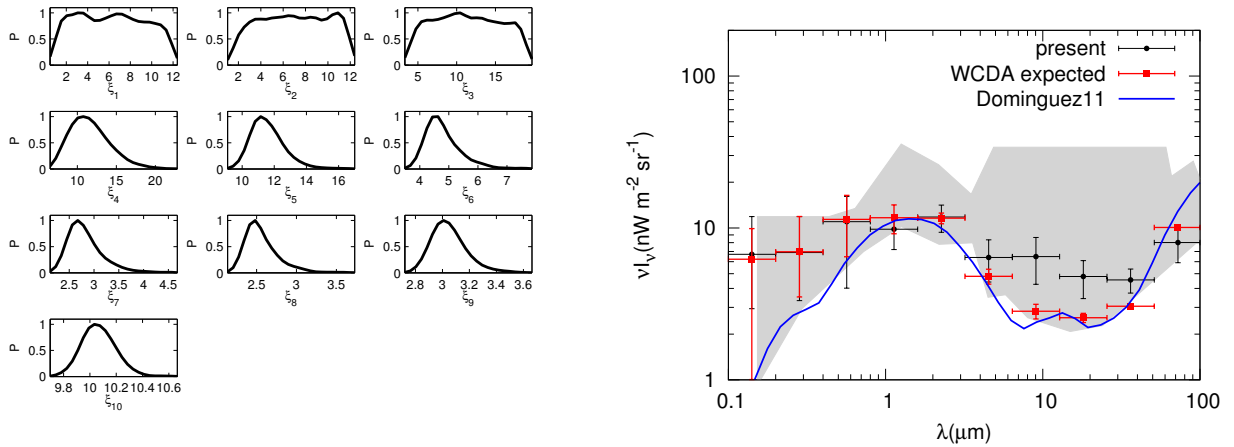


Figure 40: Left: 1-dimensional marginalized probability distributions of the fitting parameters ξ_i . Right: Fitting results of the EBL intensities with simulated LHAASO spectra of 45 blazars, compared with the input EBL model [26]. We also show the constraints with the current blazar data as derived in [27] for comparison.

Taking the EBL model by Dominguez et al. (2011; [26]) as an example, we find that 45 sources with redshifts in the third LAT AGN catalog (3LAC; [304]) will be detectable by LHAASO-WCDA for one year sky survey. We simulate the spectral measurements of these sources following [303]. Fitting to these simulated spectra enables us to have a measurement of the EBL intensities, as shown in Figure 40. We can see that the EBL intensities above $\sim 1 \mu\text{m}$ can be well constrained with the expected LHAASO data. At shorter wavelengths the constraints become weaker, due to the relatively high energy threshold of LHAASO. The fitting results reproduce the input EBL model well, illustrating the robustness of this method. Compared with the results obtained with the present (sub-)sample of blazars [27], we find that LHAASO will have significant potential to improve the measurements of the EBL intensities.

3.3.5. Conclusion

We propose to *measure* the EBL with a global fitting methods, based on the VHE γ -ray observations of extragalactic blazars by LHAASO. This method does not assume the spectral shape of EBL, but parameterizes the EBL intensities in different wavelength bins as a constant parameter. The intrinsic spectra of the sources and the EBL intensities are fitted simultaneously using an MCMC algorithm. With simulated observations of blazars by LHAASO, we show that the EBL intensities can be well measured. A large sample of sources with good spectral measurements, which is the object of LHAASO, is very essential for improving our understanding of the EBL.

3.4. Prospects for Gamma Ray Bursts detection with LHAASO

Executive summary The LHAASO (Large High Altitude Air Shower Observatory) experiment, currently under design, is planned to be installed in the Sichuan Province (China) at 4410 m a.s.l. with the aim of studying the highest energy gamma-ray sources and cosmic rays in the wide energy range from hundreds of GeV to hundreds of TeV. Among its different components, optimized to study different energy regions, the WCDA (Water Cherenkov Detector Array) will be one of the most important. Three ponds, for a total surface of $78,000\text{ m}^2$, will be equipped with 3120 PMTs to detect the Cherenkov light produced by ultra-relativistic particles. Each PMT will monitor a volume cell of $5\times 5\times 4.5\text{ m}^3$. Data (signal amplitude, with a threshold set at 1 pe level, and arrival time) from each PMT are collected and sent to a DAQ system able to build and record events with all multiplicities starting from a single PMT fired. For small numbers, the primary energy for gammas corresponds to a few GeV, overlapping with the actual satellite detectors energy range. In this paper, the scheme to calculate the expected rate and typology of GRBs detectable in follow-up mode with LHAASO is described and discussed.

3.4.1. Introduction

Gamma Ray Bursts are among the most powerful sources in the sky, with an energy spectrum extending from radio to gamma rays of tens of GeV (for a review see e.g. [305, 306]). They occur with a frequency of a few per day, and originate from the entire universe.

GRBs are divided into two classes depending on their duration. The short ones last up to 2 seconds and show a harder spectrum with a mean peak energy of 490 keV. It is believed that their origin is due to the merger of two compact objects such as neutron stars or black holes. Long GRBs have durations greater than 2 seconds with a softer spectrum and a peak at about 160 keV. In this case it is thought that the origin is due to the collapse of the nucleus of a type Ib/c Supernova, and in fact, the coincidence between these two phenomena has already been observed in many cases. The shape of the spectrum is well described in most cases by the Band function, characterized by two power laws smoothly connected. Although the majority of the ejection is concentrated in the energy region between keV and MeV, some photons have been observed up to tens of GeV using detectors in space on board the CGRO satellite and more recently Fermi and AGILE.

Until now all the experimental data in the MeV - GeV energy range were obtained from detectors onboard satellites, but due to their small size and the rapid fall of GRB energy spectra they hardly cover the energy region above 1 GeV. The detection on ground can be done by two kinds of detectors able to provide a much larger effective area: telescopes for the atmospheric Cherenkov light and EAS arrays.

With their enormous size, the Cherenkov telescope recently installed at HESS and those planned for the CTA observatory allow the detection of gamma rays with an energy threshold as low as 20 GeV. However, the necessity of working during nights with clear skies and no or few moon light limits the efficiency to 10-15 %. Furthermore, apart very seldom serendipitous observations or specific pointing strategies to cover a wider sky region, the field of view of less than about 5° prevents the study of short GRBs and of the prompt phase of long GRBs, since the repointing requires a minimum time of about 100 seconds. So far, all major Cherenkov detectors (MAGIC, HESS, VERITAS) have tried to point the GRBs following the afterglow but without success. In the case of CTA it is expected a coincident detection of 0.5 - 2 GRBs per year [307] depending on the assumed high energy spectral features, satellite alert rate and array performance.

The EAS arrays have on the contrary a large field of view (nominally 2 sr, limited only by the atmospheric absorption) and high efficiency (up to 100%), but the need to reveal enough secondary particles to reconstruct the arrival direction and energy of the primary increases the threshold to around 100 GeV.

An alternative mode consists in the measurement of the counting rates of the detectors at time intervals of the order of a fraction of second ("single particle technique") [308, 309, 310], and then in the search for an excess in coincidence with a GRB detected by a satellite. With this technique it is

not possible to measure the arrival direction of the excess, but the threshold energy can be lowered to about 1 GeV. Both techniques have been used by various extensive air shower arrays, such as EASTOP, Chacaltaya, Milagro and more recently ARGO-YBJ which has studied the richest sample of GRBs ever analyzed by a detector on ground (over 200 events) [9]. Even in this case there has been no clear detection.

The HAWC experiment, an extensive air shower array with an area of 22,000 m² fully operating in Mexico since spring 2015 at an altitude of 4100 m a. s. l., has made a detailed study on the possibility of detecting GRBs with both techniques, estimating an overall detection rate of 1.55/y for short GRBs and 0.25/y for long ones [311, 312]. The shower technique was found to be preferred with the idea of lowering the threshold energy down to 50 GeV. In this paper a method similar to that used for CTA and HAWC to calculate the expected rate and features of detectable GRBs has been applied to LHAASO.

3.4.2. The LHAASO experiment

The LHAASO experiment, planned to be installed in the Sichuan Province (P.R. of China) at 4410 m a.s.l., is currently under design to study cosmic rays and photons in the energy range 0.1 - 1000 TeV. This very wide interval is obtained combining different air shower detection techniques covering different energy windows. At the lower end, from 100 GeV to 30 TeV, the Water Cherenkov Detector Array (WCDA) is one of the major components of LHAASO. It is made of three ponds, covering a total surface of 78,000 m². Each pond is divided into 900 cells (5×5 m² each, with a depth of 4.5 m) seen by one PMT located at the cell floor centre and looking up to detect the direct Cherenkov light produced by the relativistic particles of the showers. In order to maximize the detector performance a large simulation campaign has been carried out to optimize both the cell dimensions and depth and the number of PMTs for each cell. The results show that a higher PMT density, obtained with both smaller cells and higher number of PMTs per cell gives a better performance in terms of angular resolution and sensitivity, but weighting these results with a cost estimate the 5×5 m² cells seen by a unique PMT offer the most effective layout [313]. Besides simulations, a prototype water Cherenkov detector has been built and operated in Beijing and an engineering array corresponding to 1% of one pool (3×3 cells equipped with one 8" Hamamatsu R5912 PMT each) has been implemented at the ARGO-YBJ site (Yangbajing Cosmic Ray Laboratory, 4300 m a.s.l., P.R. of China). The measured counting rate was about 35 kHz for each cell, with an expected minimum of 12.5 kHz given by cosmic rays. Since LHAASO will be located at a similar height, we foresee a counting rate close to this value. This very high single counting rate does not allow a simple majority but requires a topological one, with different trigger levels. The basic element is given by a 3×3 cells matrix, whose signal is collected by a custom FEE and sent to a station where a suitable trigger is generated and the corresponding data are recorded. This quite new approach is called "trigger-less" and allows the maximum DAQ flexibility. For example, overlapping the clusters (corresponding to 12×12 cells) by shifting them of 30 m and requiring a coincidence of at least 12 PMTs within 250 ns in any cluster, a trigger rate of 70 KHz is expected. In the search for GRBs, this approach is particularly effective. For very low multiplicities, starting from 3, the number of random coincidences does not allow the reconstruction of the arrival direction, and moreover the huge amount of events prevents the storage of data. However, if an on-line alert is provided by satellites, as for the case of Cherenkov telescopes, the DAQ can switch to this very low multiplicity mode for a limited amount of time (\sim minutes) and knowing the arrival direction the random coincidences can be strongly suppressed. Even if for these very low multiplicity events (\sim 3-10 hits) the angular resolution is very poor (\sim 10-15°) and the primary energy is very badly reconstructed, the background is highly reduced with respect to the single particle technique, where the contribution comes from the whole sky. Providing a buffer to store continuously some hundreds of seconds of low multiplicity data, the GRBs can be followed since the beginning covering the delay of the alert transmission. To sum up, the GRB search will be done by LHAASO using the WCDA data in three different ways, depending on multiplicity:

- for $n=1,2$ or slightly higher number of particles, the DAQ will simply count the number of events in a fixed time window with the corresponding multiplicity and the search will be done in "scaler mode", looking for a statistical excess in the counting rate of all the PMTs in the detector;
- for $n \gtrsim 10$ the events are reconstructed one by one and an excess is looked for in the GRB direction. Since all these data are recorded, this search can be done off-line with unlimited GRB duration;
- for the intermediate multiplicities, data are recorded for a fixed time window before and after the real-time alert given by satellites. If successful, this technique will cover for the first time for EAS arrays the energy region between a few GeV and 100 GeV with some directional information.

In order to evaluate the rate and typology of GRBs detectable by LHAASO, several ingredients must be laid together and precisely a GRB model, a parametrization as a function of energy of the detector performance (effective area and angular resolution) and some hypotheses on the expected external trigger rate. All these items will be presented and discussed in the following sections.

3.4.3. The GRB model

To compare our results with CTA and mainly HAWC, we decided to use the same approach found in [307] and [314]. In these papers, a set of pseudo-GRBs has been simulated sampling their features from the experimental ones measured by Fermi (GBM and LAT) and Swift (BAT) satellites. At first, we assume that the external trigger will be given by Fermi-GBM. For each parameter, a different distribution has been considered for short ($T_{90} \leq 2$ s) and long ($T_{90} > 2$ s) GRBs, and no correlation among them has been considered.

3.4.4. The high energy spectrum

We suppose a high energy emission in the 1-1000 GeV energy range as a simple power law with fixed spectral index and no intrinsic cutoff, that will be given exclusively by Extragalactic Background Light (EBL) absorption. To quantify this high energy contribution, we used the correlation between the fluencies measured by GBM and LAT, respectively in the low and high energy bands. Figure 41 shows this correlation, updated with all the 21 GRBs with fluence calculated in the same time window. The points are very scattered, and for short GRBs (red squares) only 3 events were measured by both detectors. Nevertheless we followed the assumptions made in [60] that the LAT fluence in the 100 MeV-10 GeV energy range is about 10% of the GBM fluence in the 10 keV-1 MeV energy range for long GRBs, while for short ones the amount is 100%.

Figure 42 shows the low energy fluence measured by GBM (red: short GRBs; black: long GRBs). For the high energy emission of our pseudo-GRBs we sampled from these distributions a fluence that is reported to the 100 MeV-10 GeV energy region using the quoted percentages. Since the fluence distribution for long GRBs is shifted towards larger values by about a factor of 10 with respect to the short ones, the high energy scaling produces a close distribution for short and long GRBs. For the high energy spectrum we used a spectral index $\alpha = -2$, since for long GRBs with an additional power law this is the mean value measured by LAT. For short GRBs we used $\alpha = -1.6$, the same value used in [314]. The assumption that all short and long GRBs have an additional high energy power law with spectral index -1.6 and -2, respectively, and without any cutoff in all the considered energy range is quite raw and optimistic, but in any case it allows us to compare our results with the expected sensitivity of HAWC.

3.4.5. The light curve

As pointed out by Ghisellini et al. in [315], the GRB light curve can be modeled as a constant flux during the T_{90} measured by GBM, followed by a power law fall-off with index $\gamma=1.5$. Due to its expected higher sensitivity and to the fact that it will lose the prompt phase of most GRBs, CTA made this assumption in [307] to estimate the rate of detectable GRBs. We decided instead to follow the approach used for HAWC, i.e., we sampled the T_{90} distribution showed in Figure 43 obtained by Fermi-GBM for long GRBs (black line), while we used a fixed GRB duration of 2 s for short GRBs.

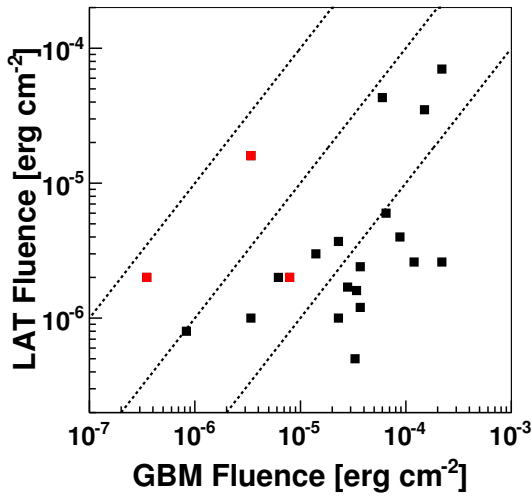


Figure 41: A comparison of the LAT and GBM fluences in the [0.1-10] GeV and [10-1000] keV range respectively. Black (red) squares are for long (short) GRBs; dashed lines indicate LAT-GBM fluence ratio of 0.1, 1.0, 10.0 (bottom to top).

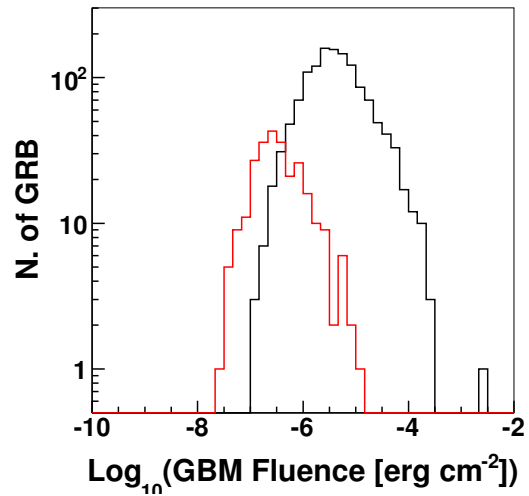


Figure 42: Distribution of measured GBM fluences for Long (black) and Short (red) GRBs in the [10-1000] MeV range.

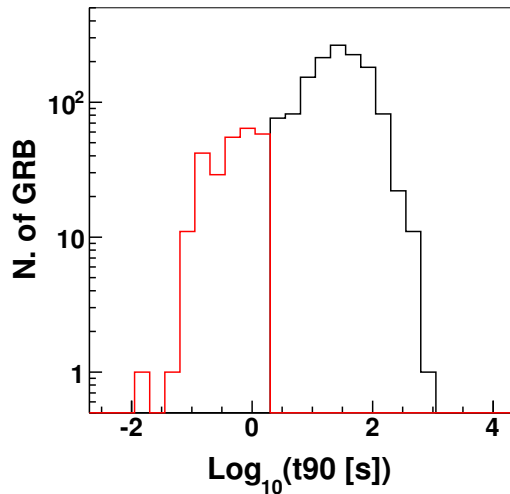


Figure 43: Distribution of T_{90} durations for Long (black) and Short (red) GRBs detected by Fermi-GBM.

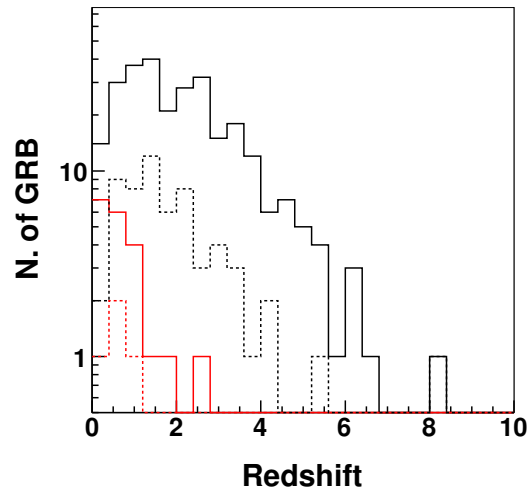


Figure 44: Distribution of redshift for Long (black) and Short (red) GRBs detected by Fermi-GBM. Dashed lines show the subsamples of Long and Short GRBs observed simultaneously by Fermi-GBM and Swift-BAT detectors.

3.4.6. The EBL absorption

The interaction of very high energy photons with the EBL produces e-pairs and thus a quite sharp spectral cutoff. This absorption depends on the redshift and GRBs are cosmological objects, with a mean value $z \simeq 2$. Many models of EBL attenuation have been published in the last decades, with a general trend towards an increase of transparency due to the observation of very high energy photons at larger redshifts [316]. In this work we used the model by Kneiske et al. [317]. Since the energy resolution of the Fermi-GBM instrument does not allow the detection of clear spectral lines, the GRB distance is obtained sampling the redshift distributions measured by Swift-BAT. Figure 44 shows these distributions for long (black line) and short (red line) GRBs. We apply the EBL cutoff starting from $z=0.1$ and up to 1 TeV, the maximum energy after which the source spectrum is totally absorbed. This choice is due to the fact that $z=0.1$ corresponds roughly to a cutoff energy of 1 TeV in our model. An important point to be checked is that the higher sensitivity of Swift-BAT with respect to Fermi-GBM could distort the redshift distribution, so we selected the subsample of GRBs detected by both. The corresponding distribution (dashed black and red lines for long and short GRBs respectively) is also shown in Figure 44 and does not show significant deviations from the whole data set.

3.4.7. The detector performance for the different configurations

The sensitivity of an EAS array to any gamma-ray source and in particular to GRBs is given by the angular resolution and the effective area for primary photons. Both of these depend on the primary energy and on the zenith angle (however, the dependency of the angular resolution on the zenith angle is small). The expected performance of the detector is evaluated by means of a detailed Monte Carlo simulation that reproduces the development of gamma-ray showers in the atmosphere and the interaction of the secondary EAS particles with the detector. For each pseudo-GRB the expected signal S is calculated integrating from 1 GeV to 1 TeV:

$$S = \int_{1 \text{ GeV}}^{1 \text{ TeV}} S_\gamma(E) \times EBL(E, z) \times A_{eff}^\gamma(E, \theta) \times T_{90} \, dE \quad (4)$$

where $S_\gamma(E)$ is the sampled GRB spectrum, $EBL(E, z)$ the EBL absorption, $A_{eff}^\gamma(E, \theta)$ the photons effective area and T_{90} the burst duration. The peak energy E_{peak} is defined as the energy corresponding to the maximum of the signal function before integration. For GRBs, E_{peak} is typically less than 100 GeV.

The zenith angle of the pseudo-GRB is randomly chosen in the range from 0 to 50 degrees, with a uniform distribution in the corresponding solid angle. To calculate the expected background B , the same Monte Carlo simulation is run for primary protons, obtaining an effective area $A_{eff}^p(E, \theta)$ as a function of energy and zenith angle. The expected background B is calculated integrating in the same energy range 1 GeV-1 TeV:

$$B = \int_{1 \text{ GeV}}^{1 \text{ TeV}} S_p(E) \times A_{eff}^p(E, \theta) \times T_{90} \times \Omega(E_{peak}) \, dE \quad (5)$$

where $S_p(E)$ is the cosmic ray spectrum and $\Omega(E_{peak})$ the solid angle corresponding to the angular resolution for $E = E_{peak}$. As angular resolution, we use the Ψ_{70} aperture that maximizes the signal to noise (i.e. S/\sqrt{B}) ratio keeping 71.5% of the signal with an aperture of 1.58σ .

For the cosmic ray spectrum, all the primary nuclei from p to Fe have been simulated and then grouped into five mass sets (p, He, CNO, NeMgSi, Fe). As a first step, the effective area has been obtained considering a cosmic ray flux made by only protons, normalized to obtain a counting rate equivalent to that produced by all the five mass groups using the Hörandel primary composition [47]. For each primary particle (in our case photons and protons) this simulation procedure, that is very CPU-consuming requiring the generation of a huge amount of events, must be repeated for each trigger condition and several zenith angles. Figure 45 shows the angular resolution for internal events ($r < 160$

m) and trigger multiplicity $N_{fit} \geq 20$, where N_{fit} corresponds to the total number of hits for each event after an iterative cleaning procedure to discard the random hits on the basis of the temporal features of the shower front. Figure 46 shows the effective areas for gammas (left) and protons (right) in steps of 15° for zenith angle from 0° to 60° and trigger multiplicity $N_{fit} \geq 10$. These results have been obtained using CORSIKA [318] for the development of EASs from gamma rays and protons, and a custom software derived by the Milagro one for the detector response. The complete set of simulations for the different trigger conditions is currently undergoing.

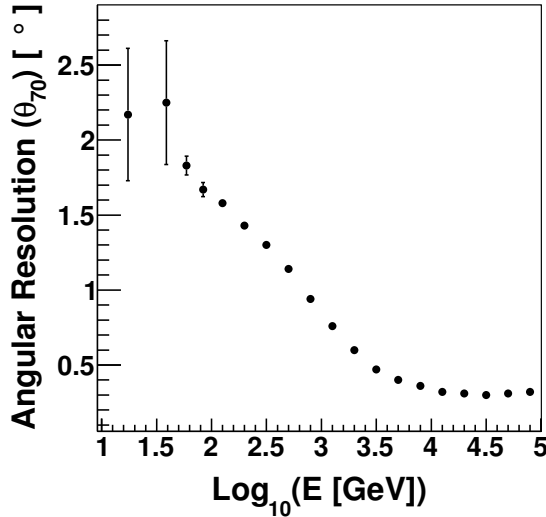


Figure 45: Expected angular resolution of the WCDA for internal events and $N_{fit} \geq 20$ (see text).

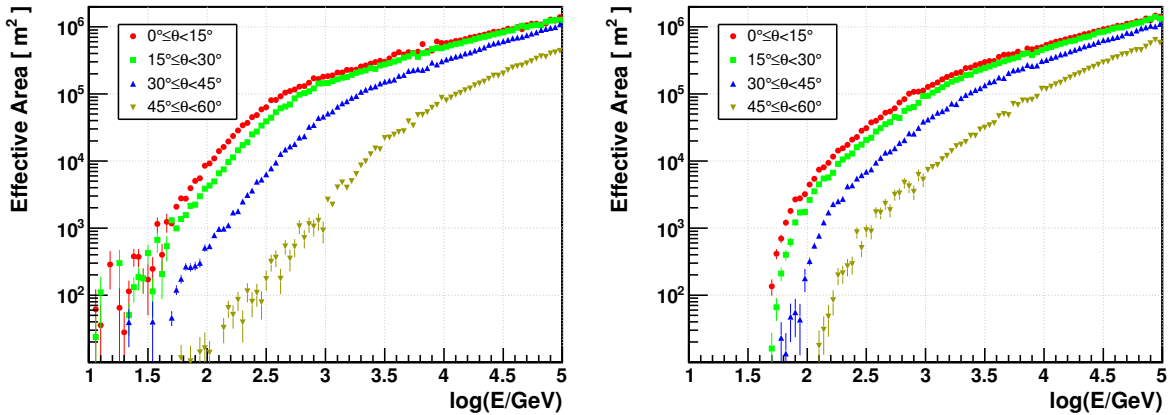


Figure 46: Effective areas of the WCDA for gamma rays (left) and protons (right) for four zenith windows and $N_{fit} \geq 10$ (see text)).

3.4.8. The detector threshold and external trigger rate

The confidence level of a detection is obtained requiring a signal greater than a given number of background fluctuations. A value of 5 s.d. has been set as the detector threshold, and to properly calculate the signal significance, equation (17) of [319] was used. Once the fraction of detectable GRBs has been derived, an external trigger rate must be provided. According to [320], Fermi/GBM detected GRBs with a mean detection rate of $\sim 250 \text{ yr}^{-1}$ in its f.o.v. of 8.74 sr. This corresponds to more than 700 GRBs yr^{-1} from the whole sky taking into account that GBM has a duty cycle of about 50%. The

3.4 Prospects for Gamma Ray Bursts detection with LHAASO

LHAASO angular acceptance up to 50° in zenith angle is 2.24 sr, with a full sky coverage of 17.9%. The expected trigger rate in GBM follow-up observations is thus 45 yr^{-1} , while in independent mode we foresee ~ 130 "GBM-like" GRBs per year. These values will be used to normalize in time our pseudo-GRBs data set.

3.4.9. *Discussion and conclusions*

CGRO/EGRET in the past and recently Fermi/LAT have clearly demonstrated the emission of GeV photons from GRBs. Nevertheless, this VHE emission is quite unusual and the presence of a hard power-law contribution to the spectrum has not been confirmed for all the GRBs seen by LAT. Moreover, the extrapolation to the GeV region is made over several orders of magnitude, with a fixed ratio between low and high energy fluencies that roughly fits reality. The expected fraction of detectable GRBs is largely dependent on the adopted GRB model, and for this reason we decided to use as much as possible the same assumptions made by CTA and mainly by HAWC to make the results comparable. Presently, our GRB model is defined together with all the calculation details. The determination of the effective area and angular resolution for gamma rays and protons and for the different trigger conditions is currently under way and the very first results on the GRBs detectability and typology for some trigger conditions by LHAASO-WCDA are under check.

3.5. Low multiplicity technique for GRB observation by LHAASO-WCDA

Executive summary: Detection of GeV photons from GRBs is crucial in understanding the most violent phenomenon in our universe. Due to the limited effective area of space-born experiment, very few GRBs are detected with GeV photons. Large area EAS experiments at high altitude can reach a much larger effective area around 10 GeV, for which single particle technique is usually used to lower the threshold energy but its sensitivity is poor due to losing primary direction information. To reach an energy threshold as low as 10 GeV and keep the primary direction information at the same time, low multiplicity trigger is required, but random coincidences rather than cosmic ray showers overwhelms the signals, and it is a great challenge for traditional trigger logic and reconstruction algorithm to discriminate the signals from the noises. A new method is developed for LHAASO-WCDA(Large High Altitude Air Shower Observatory-Water Cherenkov Detector Array) to work under low multiplicity mode. With this technique, the LHAASO detector can even work under multiplicity as low as 2 while keeping the direction information at the same time. The sensitivity and expectation of LHAASO-WCDA with low multiplicity technique to GRBs are presented.

3.5.1. Introduction

Gamma Ray Bursts(GRBs) are among the most powerful events in the Universe, and have been the subject of observational studies from radio to multi-GeV energies. Satellites with instruments sensitive to hard gamma-rays, such as CGRO and Fermi LAT, have extended the observations from 30 MeV to tens of GeV. GRB130427A [321] that was observed up to 94 GeV, or 126 GeV once corrected for redshift, shows that GRBs are capable of producing very-high-energy photons. On the present, several GRBs have been observed above 10 GeV [322, 28, 29, 323, 60]. It is unknown up to what energy the spectrum extends, as present-day observations are limited by effective area, in the case of space-based instruments, and by slewing constraints and energy threshold for ground-based Imaging Air Cherenkov Telescopes. Studying the spectrum beyond 10 GeV is crucial in understanding GRB mechanisms themselves, and also allows us to probe cosmological phenomena such as extra-galactic background light (EBL) and it may be used to constrain Lorentz invariance violation.

Currently three major classes of high-energy detectors exist: Satellite detectors, Imaging Atmospheric Cherenkov Telescopes (IACTs) and Extensive Air Shower (EAS) particle detector arrays. Satellites can observe very wide fields of view (e.g. 2.4sr or 19% of 4π sr for Fermi LAT) and have close to a 100% operational duty cycle. On the other hand, the limited physical size of satellites prevents them from obtaining enough statistics to reach energies greater than tens of GeV. Operating above 50 GeV IACTs that have been designed for fast slewing (1 min). EAS detector arrays, such as WCDA, benefit from a very large field of view (2 sr or 16% of 4π sr) and near 100% duty cycle that will allow for observations in the prompt phase. They are also sensitive to energies beyond those covered by satellites. EAS observatories, in particular WCDA, are thus useful high-energy GRB detectors that complement the observations by satellites such as Fermi.

For EAS detectors, at present, two methods can be used to analysis the sensitivity and capabilities of detection of GRBs by WCDA: Shower mode method, Single particle technique (SPT) and Low multiplicity technique. Shower model method is a regular analysis method, threshold-energy is about 100 GeV, but GRBs with 100 GeV photons are very few. SPT can detect GRBs with 10 GeV photon but poor in sensitivity due to losing direction information. So taking advantage of characteristic of trigger mode of WCDA, a new method, low multiplicity technique is developed for GRBs detection, which can reach such energy like tens of GeV and reserve direction information at the same time. In this proceeding we will present the sensitivity and capabilities of low multiplicity technique for detection of GRBs by WCDA and show the observatory's ability to measure possible high-energy emission from GRBs.

3.5.2. WCDA experiment and trigger mode

Targeting gamma astronomy in energy band from 100 GeV to 30 TeV, the WCDA is one of the major components of the LHAASO, covering an area $90,000 \text{ m}^2$, has been proposed to be built at Daocheng County (4300 m a.s.l.), GanZizhou, SiChuan, China. It is made of four ponds, $150 \times 150 \text{ m}^2$ each. Each pond is divided into 900 cells ($5 \times 5 \text{ m}^2$ each partitioned by 0.5 mm-thick black curtains made of black polyethylene lines, with an effective water depth of 4 m) seen by one PMT located at the cell floor center and looking up to detect the direct Cherenkov light produced by the relativistic particles of the showers.

The measured counting rate was about 36 kHz for each cell, which is much higher than the noise of PMT itself. So a new trigger technique based on "Trigger-less" is proposed for large area WCDA: each PMT will output a L1 (Level 1) single trigger signal of 250 ns after hit and over threshold, and if there is another over-threshold signal in the same 250 ns period, which will be taken as a new signal and trigger signal will extend 250 ns; namely the total array is divided into 81 trigger cluster ($60 \text{ m} \times 60 \text{ m}$ each, including $12 \times 12 = 144$ PMTs) Horizontally and vertically, and then judge whether hit multiplicity is bigger than 12 at the falling edge of the clock of each trigger cluster. When any trigger cluster satisfies this selection, then output one L2 trigger signal and produce total trigger. In this trigger system, if single counting rate produced by cosmic ray is less than 50 kHz, random coincidence trigger rate produced by single counting can be controlled smaller than 1 kHz, and trigger rate of 70 kHz produced by air shower ($> 10 \text{ GeV}$) is expected.

3.5.3. Low multiplicity technique

(1) Challenge in low multiplicity trigger for WCDA

In order to lower the threshold energy and reserve the primary direction information at the same time for GRBs detection, Low multiplicity technique is produced taking advantage of LHAASO-WCDA trigger technique based on "trigger-less", wide field of view and full duty cycle, only observatory array like LHAASO-WCDA with these three characteristics can do this. We have known the counting rate was 36 kHz for each PMT, and about 10^8 Hz for the whole array (3600 cells), which is much higher than signal from cosmic ray, so it's impossible for WCDA to trigger or reconstruct correctly the true events. Then how to discriminate the signals from the noise, it's a great challenge for traditional trigger logic and reconstruction algorithm? A new method is developed for LHAASO-WCDA to work under low multiplicity mode.

Lowering down the huge background rate from single rate is crucial for this method. Three steps are taken to realize this goal. firstly, we take the GRB alert as an "event" trigger for follow-up observation. As we know, typical delay of a GRB alert is about 1 minute, when a GRB alert comes, DAQ takes the GRB alert as an "event" trigger for low multiplicity technique and stores all the data in the pipeline and data of a certain time duration after the alert before reconstructing the shower core and direction for follow up observation. This implies that the GRB position is known from other observations. The time and duration of the burst are also assumed known, which allows one to efficiently reject the background by defining a restrictive time window. There is no any problem and hardware-free for WCDA. Secondly, we localize the shower, namely lower the total single rate. we can consider events with a distance from center of the array $< 50 \text{ m}$, and with zenith angle $< 40^\circ$, after doing so, the total number of noise hits is reduced by a factor of 10, but it's still too high for a multiplicity as low as 3. At last, we shrink the trigger time window through hit time transformation. After this transformation, the coincidence time window can be reduced by a factor of ~ 30 , in which the average number of noise hits can be reduced by a factor of ~ 30 , from 3 to 0.1, it's good for low multiplicity trigger.

In this method, all hits are to be saved, and the running time window should be applied on each hit, otherwise, shower hits can be separated into adjacent windows.

(2) Signal simulation for low multiplicity technique

Gamma-ray showers are simulated with CORSIKA with an $E^{-2.0}$ spectrum at different energy. The detector response model developed for WCDA is used at an altitude of 4300 m using a GEANT4

	$nhit \geq 1(m^2)$	$nhit \geq 2(m^2)$	$nhit \geq 3(m^2)$
10GeV	36986	4699	1710
20GeV	94533	18941	8214
50GeV	297410	88885	46175
100GeV	537151	224280	139644

Table 2: Effective area at different energy for low multiplicity

based code. The lowest energy for primary gamma showers was set to 10 GeV. The signal rate in the low multiplicity technique is the number of PMT hit after detector response and before direction and position reconstruction.

The signal rate S is given by:

$$S(\theta) = \int dE \frac{dN}{dE} A_{eff}^{lowmultiplicity}(E, \theta) \quad (6)$$

Where dN/dE is the photon spectrum and $A_{eff}^{lowmultiplicity}$ is the detector effective area. Depends on several variables and here only energy E and zenith angle are treated. In this proceeding, only results of $\theta = 0$ are presented, and other direction will be considered later. The effective area of WCDA for gamma rays for different low multiplicity is shown in the Table1.

(3) Background for low multiplicity technique

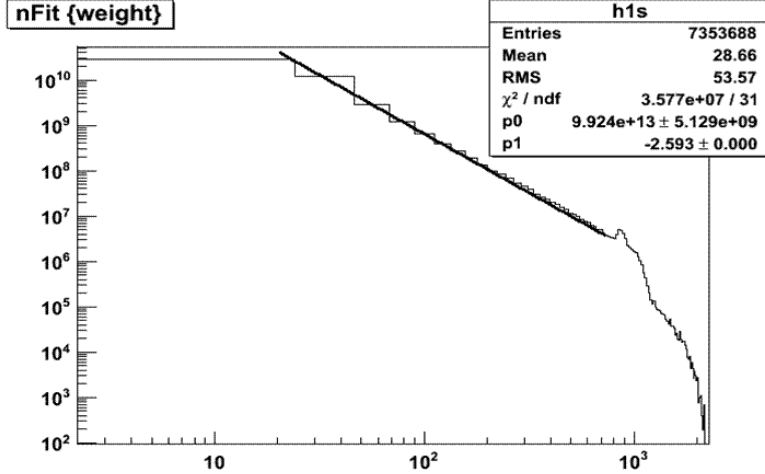
Galactic cosmic rays are simulated with CORSIKA for multiple species with an $E^{-2.62}$ spectrum: protons, He, C, O, Ne, Mg, Si, Fe. The galactic cosmic ray spectrum is re-weighted to measurement by J.R. Hoerandel [324]. Background rate mainly includes occasional noise from cosmic rays and random coincidence noise. Fig 47 is the distribution of hit number from cosmic ray background by simulation, from this figure, we can infer the occasional noise rate is 4.3×10^6 Hz for $nhit \geq 1$, 1.6×10^6 Hz for $nhit \geq 2$ and 8.4×10^5 Hz for $nhit \geq 3$ by fitting the distribution of number of hits with a power law.

For random coincidence noise, firstly, we take the pipe line with a time duration of 200 seconds, to save all the data when a GRB alert comes and after the alert. Secondly, we localize the shower, considering events with a distance from the center of < 50 m, then the total Number of noise hits is reduced by a factor of 10, i.e. from 30 hits ($10^8 Hz \times 300 \times 10^{-9}s = 30$ hits) reduced to 3 hits in trigger time window of 300 ns. The random coincidence noise rate is about $8e7$ Hz for $nhits \geq 3$, about 300 times higher than shower rate (with direction information). Secondly, we shrink the trigger time window, namely perform hit time transformation: GRB direction cosines are (l, m, n) , for each hit (x, y, z, t) , we can define $tr = t - (lx + my + nz)/C$, where C is light velocity in vacuum, Automatically removed those far from GRB direction and shower direction information is obtained without direction reconstruction. After this transformation, the coincidence time window can be reduced from 300 ns to 10 ns, in which the average number of noise hits is reduced from 3 to 0.1, good for low multiplicity trigger. For low multiplicity trigger, the running time window was applied on each hit, then the random coincidence rate is about $5e5$ Hz ($nhits \geq 3$ for mean noise hit of 0.1), lowering down a factor of 100. For different low multiplicities, the random coincidence noise rate and the Background rate are presented in the following Table2.

(4) Sensitivity of low multiplicity technique to GRBs

For low multiplicity, the sensitivity of WCDA to GRBs depends on a number of factors, including the GRB emission time scale, emission spectrum and redshift, as well as on the signal and background estimation of the experiment. To calculate WCDA's sensitivity, we simulate gamma ray spectrum according to the power-law $dN/dE \propto E^{-2}$ with an arbitrary reference flux normalization. This injection spectrum can be weighted for any other spectral shapes. In which we take into account attenuation of VHE gamma rays due to interaction with extragalactic background light, the Franceschini et al. [3] model is used.

	occasional noise rate(Hz)	random coincidence noise rate(Hz)	background rate(Hz)
$\text{nhit} \geq 1$	4.3×10^6	10^8	1.04×10^8
$\text{nhit} \geq 2$	1.6×10^6	9.5×10^6	1.11×10^7
$\text{nhit} \geq 3$	8.4×10^5	4.6×10^5	1.30×10^6

Table 3: Background rate at different low multiplicity

Figure 47: Distribution of number of hit. Solid line is a power law fit to the number of hits to infer low multiplicity due to threshold effect.

Given a signal rate $S(\theta)$, background rate B then the significance of a given observation is :

$$\text{Sig} = S(\theta)T_{90}/\sqrt{BT_{90}} = \sqrt{T_{90}/B} \int dE \frac{dN}{dE} A_{\text{eff}}^{\text{lowmultiplicity}}(E, \theta) \quad (7)$$

We have used various spectra of the type $dN/dE \propto E^{-\gamma}$ with sharp high-energy cutoffs to determine the sensitivity of the low multiplicity technique to GRBs. The sensitivity is defined as the flux detectable at 5σ significance. A range of spectral indices gamma between -3 and -1 and a range of cutoffs between 10 GeV and 10 TeV were tested, and effects of the EBL are also considered.

Figure 48 shows WCDA's sensitivity curve of different GRB emission spectra on the expected sensitivity of WCDA using the low multiplicity ($\text{nhit} \geq 3$) calculated with equation compared to GRBs that have been detected by Fermi LAT. Assuming that the burst occurs at a zenith angle of 0° and lasts 1 second at a distance of redshift of $z = 0.5$ [3]. Data for GRBs 090510 and 090902b, extracted from [28] and [29] are shown for comparison. We conclude that the most promising cases for detection with high significance are GRBs such as GRB 090510 and GRB 090902b if the high-energy cutoff is above 30 GeV. Fermi LAT observations of these two GRBs were made up to 30 GeV without any indication of a cutoff. If high-energy emission from GRBs extends beyond 30 GeV, then WCDA will become even more significant due to limited physical size of Fermi LAT.

3.5.4. Scientific prospect and conclusions

A new method was developed to detect GRBs at energy as low as 10 GeV and reserve source direction information using EAS array, like LHAASO-WCDA. From above analysis, we can conclude, WCDA, will have the capability of detecting GRBs at high energies. The simulations presented in this proceeding show that WCDA will be able to detect GRBs with characteristics similar to those of some of the brightest GRBs seen by Fermi LAT. As opposed to Fermi LAT, with a fixed physical size, the effective of the method of the low multiplicity increases with energy. Thus this method will expand upon the energy sensitivity of current detectors. Also WCDA is a wide field of view detector with near 100%

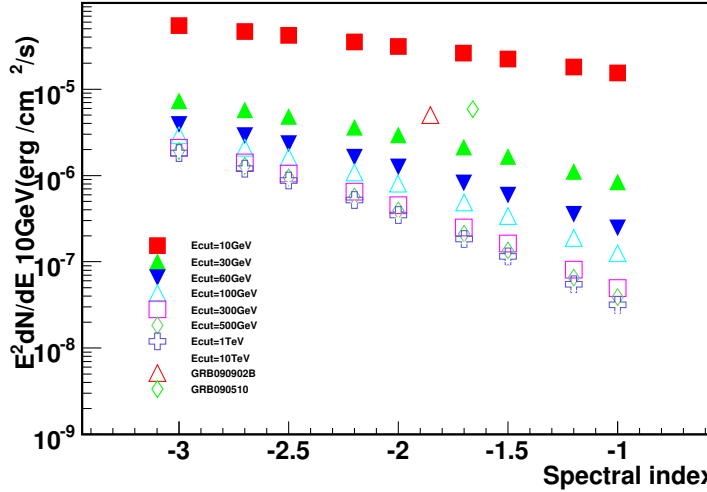


Figure 48: Sensitivity using the low multiplicity as a function of spectral index. The 5σ discovery potential is shown as a function of spectral index for various values of a sharp high-energy spectral cutoff. The duration of the burst is fixed to 1s and the zenith angle is fixed to 0° . Data from 2 GRBs are corrected for duration and inserted for comparison [28] [29]

duty cycle, it will be able to make GRB observation in the prompt phase. WCDA, in union with satellite or other ground based detectors, will be able to measure the high-energy GRB components including a possible high-energy cutoff. Important astrophysical information will be deduced from spectral cutoffs such as the Lorentz boost factor of GRB jets, the effects of the EBL and the maximum energy to which GRBs accelerate particles.

For low multiplicity technique, how to pick up the true events and analysis the data? This is still the question to be solved. In this proceeding, we present the result with GRBs alert information, at further step, we also can do without GRBs alert and work alone taking advantage of large field of view of WCDA, then CPU power maybe is a huge challenge.

4. Multi-Messenger Astronomy with LHAASO

abstract. The discovery of gravitational waves (GWs) marked the dawn of multi-messenger astronomy era. Combining observations of multi-messengers help in boosting the sensitivity of source searches, and probe various aspects of the source physics. In this work I will discuss how LHAASO observations of very high energy (VHE) gamma rays in combination with telescopes for the other messengers can help in solving the origins of VHE neutrinos and ultra high energy cosmic rays (UHECRs), and searching the GW sources and the VHE gamma rays from transients.

4.1. Introduction

Recently IceCube collaboration reported the discovery of very high energy (VHE) astrophysical neutrinos [69], and LIGO/VIRGO collaboration also reported the detection of gravitational waves (GWs) for the first time [325]. These discoveries opened new windows to explore the universe, and marked the dawn of the multi-messenger astronomy. The combination of observations of electromagnetic waves (EM), cosmic rays (CRs), neutrinos and GWs will provide a boost in the sensitivity of detecting sources, and explore various aspects of the physics of astrophysical objects. LHAASO, being a wide field of view (FOV), high duty cycle, and high sensitivity TeV gamma-ray telescope, will play an important role in the multi-messenger astronomy era. In this paper, we will discuss how the combination of LHAASO with the other telescopes observing different messengers helps in probing the universe.

4.2. VHE neutrino origin

IceCube has detected a diffuse HE neutrino flux. By analyzing the data within three years of operation, they singled out 37 events ranging from 60 TeV to 3 PeV [69]. However, the sources of these neutrinos are unknown, and there is no cluster of the arrival directions and times. It is generally believed that the HE hadronic interactions between CRs and matter/photons within or surrounding the CR sources are responsible for the creation of the astrophysical neutrinos. The same processes, based on fundamental particle physics, should also produce gamma rays through the decay of neutral pions. At production, the flux of TeV-PeV astrophysical neutrinos should be associated with a flux of gamma-rays of similar spectral characteristics. The search for neutrino sources will benefit from the combination of gamma-ray and neutrino observations. Studies of the spatial and temporal correlations between gamma rays and neutrinos rely on searching for neutrinos from known gamma ray sources which are expected to be CR sources, or on searching for gamma rays at detected neutrino positions. While the first approach can help LHAASO pin down the origin of future possibly detected VHE gamma-rays, we focus more on the second approach in the following.

4.3. Point sources

The temporal correlation can be easily determined given the precise measurement of neutrino arrival time, but the spatial correlation is more difficult to be set up because of the limited angular resolution of neutrino direction measurement. While the neutrinos detected by IceCube in the “track” pattern can be reconstructed to within 1° at energies above 100 TeV, the “cascade” events only have angular resolution of about 15° . Due to the large FOV, LHAASO can well cover the error circles even for the cascade events. According to the effective area of IceCube at energies of ~ 100 TeV ($\sim \text{m}^2$) and the operation time (~ 3 years) and the fact that no neutrino doublet observed, the estimated gamma-ray flux from the sources that produce the 100-TeV neutrinos is $\lesssim 10^{-10} \text{TeV cm}^{-2}\text{s}^{-1}$. A 290TeV neutrino, IceCube-170922A, was found to associate with a blazar, TXS 0506+056. The follow-up search in the archive data of prior 9.5 yrs found a neutrino burst in 2014 in the direction of TXS 0506+056. The neutrino burst lasts about 110 days with a neutrino flux of $1.6 \times 10^{-11} \text{TeV cm}^{-2}\text{s}^{-1}$ at 100 TeV, and the averaged flux over the 9.5 yrs is $0.8 \times 10^{-12} \text{TeV cm}^{-2}\text{s}^{-1}$ at 100 TeV. The accompanying 100TeV gamma-ray flux without absorption should be comparable to the neutrino flux. The LHAASO differential sensitivity at 100 TeV, $\sim 2 \times 10^{-13} \text{TeV cm}^{-2}\text{s}^{-1}$ for 1-yr measurement, suggests that the neutrino sources may be observable if

the gamma-ray absorption is not important, although it should be noted that the VHE gamma rays from distance beyond tens of Mpc suffer from absorption by the extragalactic background light (EBL). With the high sensitivity, LHAASO will provide unprecedented constraint of neutrino sources at energies above 100 TeV.

4.3.1. Diffuse emission

Although it is expected that the major sources of the diffuse HE neutrinos detected by IceCube are extragalactic, part of them could be Galactic origin. Moreover it may happen that the Galactic and extragalactic originated neutrinos dominate at different energies. The latest IceCube results of the diffuse neutrino emission seem to show an “excess” in the spectrum at about $E_\nu = 30$ TeV, with a flux of $E_\nu^2 dI_\nu/dE_\nu \sim 10^{-7} \text{ erg cm}^{-2} \text{s}^{-1} \text{sr}^{-1}$ [326]. If they are extragalactic origin and produced by hadronic interactions, the associated gamma rays may result in a gamma-ray cascade emission at sub-TeV energies of comparable flux, which seems to violate the extragalactic gamma-ray background measured by Fermi-LAT [327, 328]. An attractive solution is that the 30-TeV neutrino excess is Galactic origin, i.e., produced by the CR propagation within or surrounding the Galaxy. The associated diffuse gamma-ray flux at $E_\gamma = 60$ TeV will be at the level of $E_\gamma^2 dI_\gamma/dE_\gamma \approx 2E_\nu^2 dI_\nu/dE_\nu$ with $E_\nu = 30$ TeV. The flux should be even larger than this level towards the directions of the Galactic plane, where CRs and medium interactions are expected to be more frequent. The flux level is within reach of the LHAASO sensitivity, thus LHAASO can help to prove or rule out the Galactic origin of the neutrino 30-TeV excess.

4.3.2. UHECR origin

The origin of the observed ultra high energy CRs (UHECRs), $> 10^{19.5} \text{ eV}$, are still unknown. They are expected to be originated from sources within 100 Mpc because of the Greisen-Zatsepin-Kuzmin (GZK) energy-loss mechanism. CRs are deflected by magnetic field during propagation, but UHECRs are expected to be deflected by only a few degrees, assuming UHECRs are protons. Thus their arrival directions may trace back to the sources. The study of spatial correlation of gamma ray positions with UHECRs will enhance the chance of finding the UHECR sources. Within 100 Mpc the EBL absorption may not be very important for TeV gamma rays.

The IceCube-detected PeV neutrino flux comparable to the Waxman-Bahcall bound, derived from UHECR flux, may indicate that the PeV neutrinos origin may be related to the origin of UHECRs. If so a PeV gamma-ray flux comparable to the PeV neutrino flux could be produced by the sources that produce UHECRs. We can use LHAASO to search the HE gamma ray signals from the UHECR positions. Derived from the IceCube detection, the gamma-ray emissivity, i.e., the energy production rate density in the universe, at 100 TeV should be order of $\dot{\rho} \sim 10^{43} \text{ erg Mpc}^{-3} \text{yr}^{-1}$. Given the LHAASO sensitivity for 100-TeV gamma-rays, S_1 (in unit of $\sim 2 \times 10^{-13} \text{ TeV cm}^{-2} \text{s}^{-1}$, for 1-yr measurement), the number of gamma-ray sources that will be observed to be associated with UHECR sources should be $N \sim 0.6S_1^{-3/2}L_{40}^{1/2}$, where $L = 10^{40}L_{40} \text{ erg s}^{-1}$ is the gamma-ray luminosity of the source at 100 TeV. With the sensitivity decreasing with measurement time after a few years, we may expect to detect a few sources from the UHECR positions, or make strong constraint on the gamma-ray luminosity of the sources. The limited horizon due to the LHAASO sensitivity is dependent of the gamma-ray luminosity, $D_h \sim 16S_1^{-1/2}L_{40}^{1/2} \text{ Mpc}$, within which the gamma-gamma absorption by EBL may be not significant for 100-TeV gamma-rays.

Besides, an hot spot in the UHECR data of Telescope Array (TA) [329] had been reported, which also lies in the northern hemisphere as LHAASO. LHAASO is encouraged to look for extended or point sources from the hot spot, which will help to constrain the UHECR sources.

4.3.3. Transient searches

The FOV is an important parameter in detecting transients: the larger is the FOV, the higher is the probability to catch a transient source in the act. The large FOV LHAASO make it promising in

searching for VHE gamma ray transients.

LIGO has provided a break through in GW detection, but the error regions for the GW event is tens to hundreds of square degrees region of the sky [?]. This is the main challenge in searches of the GW counterparts, but LHAASO can observe $\sim 1/7$ of the sky at each moment with deep sensitivity, which may well cover the error region and search for GW counterparts. The detection horizon of GW detectors is few hundred Mpc, for which the EGL absorption of TeV photons could be weak.

Moreover, with large FOV, high duty cycle, and high sensitivity, LHAASO is perfect at monitoring the VHE transient events. It is promising that LHAASO can detect VHE gamma rays from transients, such as supernovae, gamma-ray bursts, tidal disruption events, fast radio bursts, active galactic nuclei flares, and even unknown VHE transient events.

4.4. Studies of Active Galactic Nuclei with LHAASO

abstract. We review the prospects for studies of active galactic nuclei (AGN) using the future Large High Altitude Air Shower Observatory (LHAASO). This review focuses on blazars, which constitute the vast majority of AGN detected at gamma-ray energies. Future progress will be driven by the planned wide field of view and improved flux sensitivity compared to current-generation Cherenkov Telescope facilities. We argue that LHAASO will enable substantial progress on searching for clear evidence of blazar releasing very high energy cosmic rays through its excellent flux sensitivity. We give two proposals: (a) searching for hard spectra > 10 TeV from the extreme blazars (e.g., 1ES 0229+200) and nearby blazars (e.g., Mrk 421); (b) searching for TeV photons from distant blazars with redshift $z \sim 1$. The surveys of LHAASO enable measurement of cosmic TeV background and construction of luminosity function of TeV blazars. These results will help us to understand the origins of Ultra-high energy cosmic rays (UHECRs) and PeV neutrinos. At last, we discuss the potential of LHAASO as tools for probing new physics like Lorentz Invariance Violation (LIV) and axion-like particles (ALPs). The traditional projects such as relativistic jet physics (including high-energy radiation mechanisms and acceleration of particles) and the extragalactic background light (EBL) determination are not discussed in this paper. However it should be pointed out that all these projects are interrelated.

Introduction. Active galactic nuclei (AGN) are the extragalactic sources of enhanced activity that are powered by the release of gravitational energy from the supermassive central black hole. Energy linked to the black hole spin [330] or rotating accretion disks [331] may be instrumental for forming prominent jets which transport the material with relativistic speed from the innermost region of the AGN to kpc-, sometimes even Mpc-scale distances. Such jets are usually identified through the detection of bright non-thermal radio emission as observed in radio-loud AGN. Only a small percentage ($\sim 10\%$) of all AGN are known to be radio-loud. In the vicinity of the central region of an AGN, matter is accreted from a disk onto the black hole; line-emitting clouds (the so-called broad-line region, BLR, and narrow line region, NLR) form at pc to kpc distances from the central engine; and dusty material surrounding the accretion disk may imprint thermal signatures in the infrared part of the AGN spectrum [332].

The radiation from the material which moves relativistically with speed $\beta_\Gamma c$ (with $\Gamma = 1/\sqrt{1-\beta_\Gamma^2}$ being the bulk Lorentz factor) along the jet axis is beamed into an angle $\sim 1/\Gamma$ around the direction of propagation. Because of this beaming effect, mostly those AGN with jets pointing towards us (i.e., blazars) are favorably detected as gamma-ray sources. However, some mis-aligned AGN (i.e., radio galaxies) can be also detected, if they are sufficiently nearby. Blazars therefore offer an excellent opportunity to study jet physics in massive black hole systems and their evolution over cosmic time through population studies.

Blazar emission is dominated by non-thermal radiation over all frequencies ranging from radio to TeV gamma-rays. Its typical multi-wavelength spectral energy distribution (SED) is characterized by two distinct humps (see Fig. 49). It is accepted that the first hump in the SED is the synchrotron emission radiated by relativistic electrons in the jet. The origin of the emission in the gamma-ray hump is still under debate.

Different classes of blazars are defined according to various properties. BL Lac objects are typically defined if the equivalent width of the strongest optical emission line is $< 5\text{\AA}$. By contrast, flat spectrum radio quasars (FSRQs) have strong optical emission lines indicating the presences of dense BLR material and strong illuminating accretion-disk radiation. Blazars also can be divided into low, intermediate, and high synchrotron-peaked sources (LSPs, ISPs, and HSPs, respectively, defined by whether the peak frequency of the synchrotron component of the SED $\nu_{\text{syn}}^{\text{pk}} < 10^{14}$ Hz, $10^{14} < \nu_{\text{syn}}^{\text{pk}} (\text{Hz}) < 10^{15}$, or $\nu_{\text{syn}}^{\text{pk}} > 10^{15}$ Hz) [333]. Most FSRQs are LSP blazars, whereas BL Lac objects include LSP, ISP, and HSP sources. Based on blazar SED and the light variations, the relativistic jet physics (e.g., emission mechanisms and acceleration processes) can be investigated [e.g., 334], if the gamma-ray emissions are certainly produced in the jet.

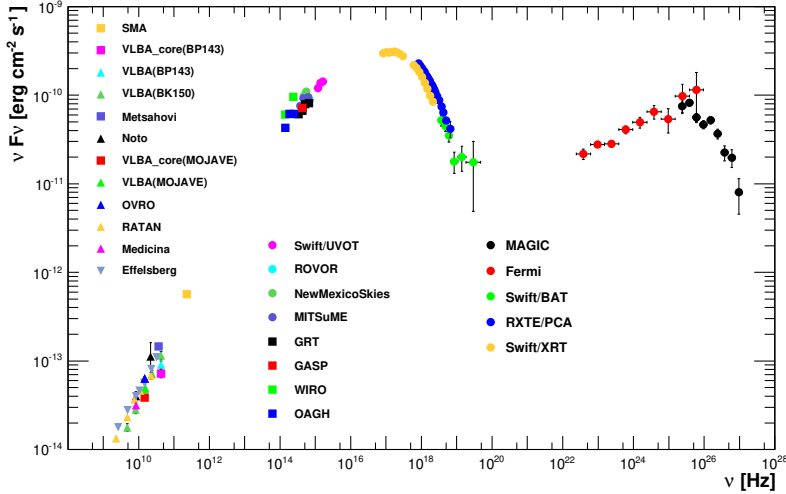


Figure 49: One SED of Mrk 421. [from 30].

In this article, we review the prospects of LHAASO to understand the AGN high-energy phenomenon and its related physics including the origin of ultrahigh energy cosmic rays (UHECRs).

4.4.1. LHAASO and Signatures of UHECRs in Gamma-rays from Blazars

The origin of gamma-ray (GeV - TeV) emission from blazar is not resolved. Three kinds of models have been proposed to resolve this problem. In leptonic models, the gamma-ray emission is supposed to be inverse Compton (IC) emission from relativistic electrons in the jet that up-scatter either low-energy synchrotron photons emitted by the same population of electrons (synchrotron-self-Compton model, SSC), or photons originating from outside the jet (external inverse Compton, EIC). In hadronic models, the gamma-ray emission is attributed to synchrotron radiation of high-energy protons in the jet, or synchrotron radiation of secondary particles created in proton-photon interaction. In the third model, the gamma-ray emission is the secondary cascade gamma-ray photons produced in the propagation of UHECRs emitted by blazar [e.g., 335, 336, 337]. Since the gamma-ray photons in leptonic and hadronic models are produced in the jet, we classify the tow kinds of models as jet model. Moreover, we refer to the model that produces gamma-ray photons in the interactions between the highest-energy cosmic rays and background photons in the Universe as cosmogenic model. The key issue of our attention is to disentangle the jet model and cosmogenic model from observations.

The observations of HESS found the non-variable and extremely hard TeV spectra of several blazars, e.g., 1ES 0229+200 and 1ES 1101-232 [338, 339]. The classical leptonic jet model is difficult to explain such hard TeV spectra⁴. However the hadronic jet models may account for the hard TeV spectra [e.g., 342]. Alternatively, [31] have proposed that the TeV spectrum of 1ES 0229+200 could be from the secondary gamma-ray produced in the propagation of UHECRs in the Universe. With the current TeV observation up to ~ 10 TeV, we cannot disentangle the leptonic, hadronic and cosmogenic models.

In Fig. 50, one can estimate that the energy flux of the UHECR-induced cascade gamma-rays calculated with a low EBL at 30 TeV is $\simeq 2 \times 10^{-13}$ erg cm $^{-2}$ s $^{-1}$. On the other hand, the one-year differential sensitivity of LHAASO at 30 TeV is also $\simeq 2 \times 10^{-13}$ erg cm $^{-2}$ s $^{-1}$. Therefore, LHAASO is capable of detecting the UHECR-induced cascade gamma-rays. By obtaining the good spectra of 1ES 0229+200 above 10 TeV, we could disentangle the jet models and cosmogenic models.

Another interesting object is Mrk 421. The current IACTs observations show that the TeV emissions from Mrk 421 are strongly variable. This suggest that the steady UHECR-induced cascade gamma-rays cannot make a significant contribution to the observed TeV emissions. In Fig. 51, we show the spectrum of UHECR-induced cascade gamma-rays constrained by the current TeV data. In this case, LHAASO

⁴Modified leptonic jet models succeed in explaining the hard TeV spectra [e.g., 340, 341]

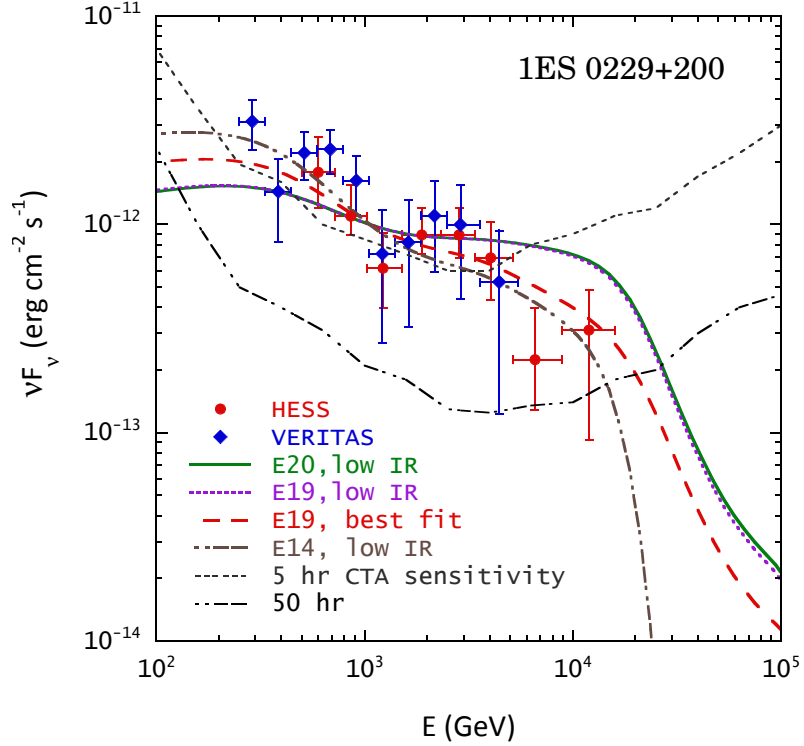


Figure 50: Cosmogenic model of [31] for the non-variable and hard TeV spectrum of 1ES 0229+200. [from 31].

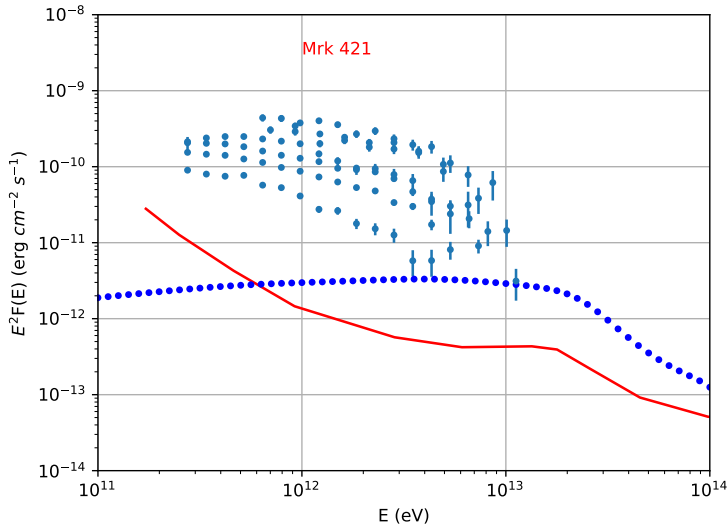


Figure 51: A spectrum of UHECR-induced cascade gamma-rays for Mrk 421 (dotted line) and the historical TeV data of Mrk 421 (points). The data are obtained through the SED Builder of ASDC (<http://tools.asdc.asi.it>). The cascade gamma-rays are calculated by using the TRANSPORTCR code [32]. The injection spectrum of protons is assumed to be a power-law with an exponential cutoff. We take the index of 2.6 and the cutoff energy of 10^{19} eV. The EBL model of [3] is used in the calculation. The solid line is the one-year differential sensitivity of LHAASO.

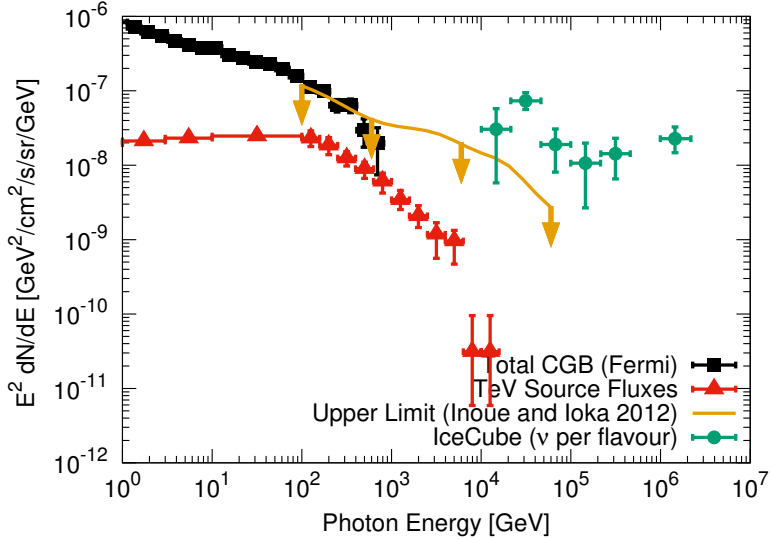


Figure 52: *GeV background radiation measured by Fermi gamma-ray space telescope, and the upper and lower limits on TeV background* [33]. [from 33].

can detect the cascade gamma-rays in one year. LHAASO will detect 100 TeV photons from Mrk 421 if it really emits >1 EeV protons. The observations of LHAASO for these sources could provide strong evidence for UHECR origin.

We also propose another strategy to find the clear evidence of blazar emitting UHECRs. Compared to the jet models, VHE photons produced by cosmogenic models suffer less absorption by extragalactic background light (EBL) because of the long energy-loss distance of UHECRs interactions with background lights. Therefore the VHE photons from the jet in high redshift blazars will suffer strong absorption by EBL. If LHAASO or CTA detect > 1 TeV photons from very distant blazars (with redshift > 1), the observed gamma rays are the secondary photons produced in interactions of high-energy protons originating from the blazar jet and propagating over cosmological distances almost rectilinearly [e.g., 112, 343, 344].

In the two topics mentioned above we do not seek to explain the observed cosmic ray spectrum above 10^{18} eV⁵. We focus on finding the evidence of UHECRs originating from the blazar jet through the observations of VHE gamma rays by the LHAASO.

4.4.2. LHAASO and Cosmic TeV Gamma-Ray Background Radiation

The *Fermi* gamma-ray space telescope has successfully measured the cosmic gamma-ray background (CGB) spectrum at 0.1 - 820 GeV [347]. It also provides an opportunity to explore and decipher the high-energy universe through a multi-messenger approach including the information from cosmic rays (CRs), gamma rays, and neutrinos [e.g., 348, 349]. However, the measurement of the cosmic TeV gamma-ray background radiation is still rare, although its upper and lower limits are given based on the current understandings of TeV sources (see Fig. 52). Based on its good sensitivity and wide field of view, LHAASO will perform an unbiased sky survey of the Northern sky under a detection threshold of a few percent Crab units from sub-TeV/TeV to 100 TeV in one year. The high background rejection capability in the 10 - 100 TeV range will allow LHAASO to measure the cosmic TeV gamma-ray background radiation. This measurement will give stronger constraints on the origins of UHECRs and IceCube neutrinos. It is noted that the cosmogenic model mentioned in Section 4.4.1 predicts a flat spectrum from TeV to a few tens TeV. The signature of the flat spectrum in the cosmic TeV gamma-ray background radiation will be also a key test on the UHECR-induced cascade emission and can help us to

⁵See the studies of [345] and [346] for the constraints on the origin of the observed > 10 EeV cosmic rays with the non-observation of 10 PeV neutrinos by IceCube.

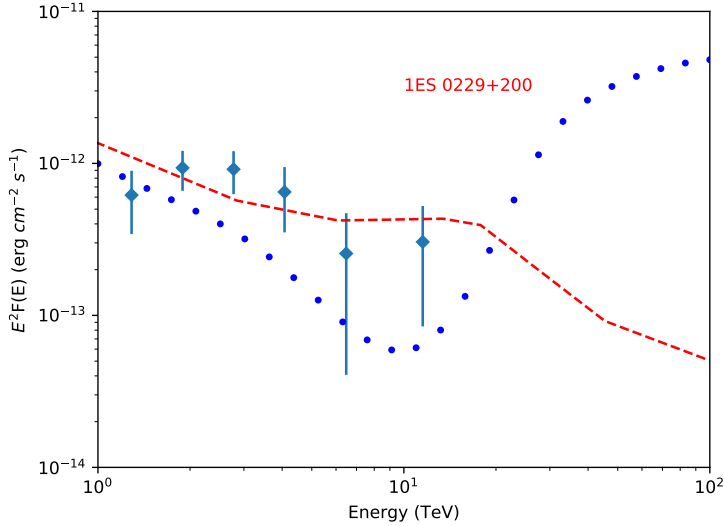


Figure 53: TeV spectrum of 1ES 0229+200 with the consideration of LIV (dotted line). The points are the HESS data of 1ES 0229+200. The EBL model of [34] is used in the calculation. The dashed line is the one-year differential sensitivity of LHAASO.

understand the origin TeV - PeV neutrino [e.g., 348, 349]. In the known 63 TeV blazars and 4 TeV radio galaxies⁶, the highest redshift source detected at >100 GeV is the FSRQ PKS 1441+25 with $z = 0.94$. MAGIC and VERITAS have detected the ~ 200 GeV photons from this source [350, 351], and the variability timescale about ~ 6 days was measured by MAGIC [351], ruling out the UHECR-induced cascade gamma-ray emission. A one-zone leptonic jet model can explain the gamma-ray emissions from PKS 1441+25 [350, 351]. Under LHAASO extragalactic surveys, many high redshift TeV AGNs will be detected to build large and well-defined TeV AGN sample. We can construct the luminosity function of AGN at TeV band to study AGN evolution over cosmic time. An involved interesting project is to assess the effect of gamma-ray emission on the thermal evolution of the intergalactic medium (IGM). Several authors claimed that plasma beam instabilities suppress the inverse-Compton scattering, the electrons and positrons of the UHECRs/TeV photons-induced cascade could provide a novel heating mechanism for the gas of IGM [e.g., 352, 353], changing the thermal history of the diffuse IGM. However the fate of the beam energy :0 is controversial, for instance, [354] claimed that most of the beam energy is still available to power the GeV emission produced by inverse Compton up-scattering of the cosmic microwave background by the beam pairs. Anyway, it is likely that the observations of LHAASO would clarify this issue.

4.4.3. LHAASO and New Physics

Astrophysical observations with gamma-ray experiments have proven to be a powerful tool of searching for physics beyond the Standard Model. For example, observations at gamma-ray energies can be used to search for the traces of axion-like particles (ALPs), in which blazars are abundantly observed sources. The photon-ALP oscillations may lead to two changes in the energy spectra: a) the gamma-ray source flux can be attenuated due to pair production with low energy background photons. ALPs produced in the vicinity of the source would mitigate this attenuation, and if they reconvert to gamma rays, leading to a significant boost of the observed photon flux, and b) the oscillations of the flux should be imprinted in the spectra around E_{crit} ⁷ and E_{max} ⁸ [e.g., 355]. In the analysis of *Fermi*-LAT

⁶ <http://tevcat.uchicago.edu>.

⁷ $E_{\text{crit}} = |m_a^2 - \omega_{\text{pl}}^2|/2g_{a\gamma}B$, where B denotes the field strength transversal to the photon propagation direction, $g_{a\gamma}$ the photon-ALP coupling, and ω_{pl} the plasma frequency of the medium.

⁸ $E_{\text{max}} = 90\pi g_{a\gamma} B_{\text{cr}}^2 / 7\alpha B$, with α the fine structure constant and the critical magnetic field $B_{\text{cr}} \sim 4.4 \times 10^{13}$ G.

and IACT spectra of blazars, no ALP-induced spectral signature, which is a spectral hardening at high optical depths, was found [109, 356]. The LHAASO extragalactic survey with its good sensitivity could be used to search for a spectral hardening correlated with the photon-ALP oscillations.

Lorentz Invariance (LI) is a basic component of Einstein's Special Relativity. It is strictly valid in Quantum Mechanics and has been verified in various accelerator experiments at the electro-weak scale. On the other hand, Lorentz Invariance Violation (LIV) has also been largely predicted in the framework of various classes of Quantum Gravity (QG) models. Tests of LIV with high-energy photons from distant sources have been proposed [e.g., 357, 358]. It is possible to utilize LHAASO for the detection of LIV through anomalies in the multi-TeV gamma-ray spectra of blazars [e.g, 359].

In Fig. 53, we show the predicted TeV spectrum of 1ES 0229+200 under the condition of LIV. One can see that this spectrum becomes harder at 10 TeV, and LHAASO cannot detect the concave shape around 10 TeV. But, it can detect the extremely hard spectrum (the photon index much less than 2) above 20 TeV, which is the evidence of LIV. The observed variability can also be used to probe LIV. Taking advantage of the wide energy-coverage of LHAASO, we can construct the energy-dependent light curves of blazars to search for a possible time lag between low- and high-energy photons, constraining an energy-dependent LIV [e.g., 360], i.e., an energy-dependent speed of light.

4.4.4. Concluding remarks

In this paper, we have proposed several projects for future detector LHAASO. This is surely incomplete in the field of AGN research. The topics on the relativistic jets are not included. Although the EBL and intergalactic magnetic field (IGMF) are not specifically discussed, all the studies mentioned above are related to EBL and IGMF. All these questions are interrelated. To improve upon these constraints, we need a better understanding of the sources and emission mechanisms, including the relativistic jet physics. Actually the key issue is to determine the origin of the observed TeV photons. To better understand these questions, we need an overall emission model, e.g., a self-consistent jet+cosmogenic-propagation emission model [e.g., 344]. Combining the future measurement for the cosmic TeV background radiation and the observations on UHECRs and cosmic neutrinos, it is possible to improve the constraints on their origins. We believe that the observations of LHAASO will improve our understanding of the high-energy universe.

COSMIC RAY PHYSICS WITH LHAASO

5. Cosmic Ray Physics with LHAASO

5.1. Study of the acceleration of cosmic rays in supernova remnants with LHAASO

Executive summary: Considerable progress have been achieved during the last years in understanding the fundamental problem of cosmic rays (CRs) origin. It was shown that the main observed properties of CRs and non-thermal emission generated by them can be explained by acceleration of CRs in supernova remnants up to at least $E \simeq 10^{17}$ eV. The blackbody cutoff in CRs spectrum detected by HiRes, AUGER and Telescope Array experiments indicates that the highest energy CRs are produced in extragalactic sources. The study of transition between the galactic and extragalactic CR components becomes extremely important task.

5.1.1. Introduction

Supernova remnants (SNRs) are considered as a main cosmic ray (CR) source. They are able to support a constant density of the Galactic cosmic ray (GCR) population against loss by escape, nuclear interactions and ionization energy loss. The mechanical energy input to the Galaxy from each supernova (SN) is about 10^{51} erg so that with a rate of about one every 30 years the total mechanical power input from supernovae is of the order 10^{42} erg/s (e.g. [361]). Thus supernovae have enough power to drive the GCR acceleration if there exists a mechanism for channeling about 10% of the mechanical energy into relativistic particles.

An appropriate acceleration mechanism is known since 1977 [362]. This is so called regular or diffusive shock acceleration process. The strong shock produced by high velocity ejecta expanding into the ambient medium pick up a few particles from the plasma flowing into the shock fronts and accelerate them to high energies.

The theory of particle acceleration by the strong shocks associated with SNRs at present is sufficiently well developed and specific to allow quantitative model calculations (e.g. see [363, 364] for reviews). Theoretically progress has been achieved due to the development of the kinetic nonlinear theory of diffusive shock acceleration [365, 366]. The theory consistently includes the most relevant physical factors, essential for SNR evolution and CR acceleration, and it is able to make quantitative predictions of the expected properties of CRs produced in SNRs and their non-thermal radiation.

5.1.2. Maximal energy of CRs accelerated in SNRs

There are strong theoretical and observational reasons, that argue for a significant amplification of the magnetic field as a result of the pressure gradient of the accelerating CRs, exciting instabilities in the precursor of the SNR shock. The most important consequence of magnetic field amplification in SNRs is the substantial increase of the maximal energy of CRs, accelerated by SN shocks, that presumably provides the formation of GCR spectrum inside SNRs up to the energy 10^{17} eV. It is also discussed possibilities of formation GCR spectrum up to significantly higher energies 3×10^{18} eV due to re-acceleration of CRs generated in SNRs [367, 368], or due to contribution of more powerful type IIb supernovae [369].

On Figure 54 the calculated CR intensities of different species accelerated in SNRs are shown together with experimental data. Two different possibilities of maximal energies are shown in thin and thick curves [41]. Both scenarios fit well to the existing data. LHAASO experiment, with expected ability of selection for individual species at 0.1–10 PeV, will provide crucial data to determine the maximal energy of CRs accelerated in SNRs.

5.1.3. Transition from galactic to extragalactic component of CRs

According to the most old idea the intersection of the galactic and extragalactic components takes place at around 4×10^{18} eV. Within this scenario the depression (or dip) of the observed CR spectrum is a result of intersection of relatively steep galactic component with flat extragalactic component (e.g.

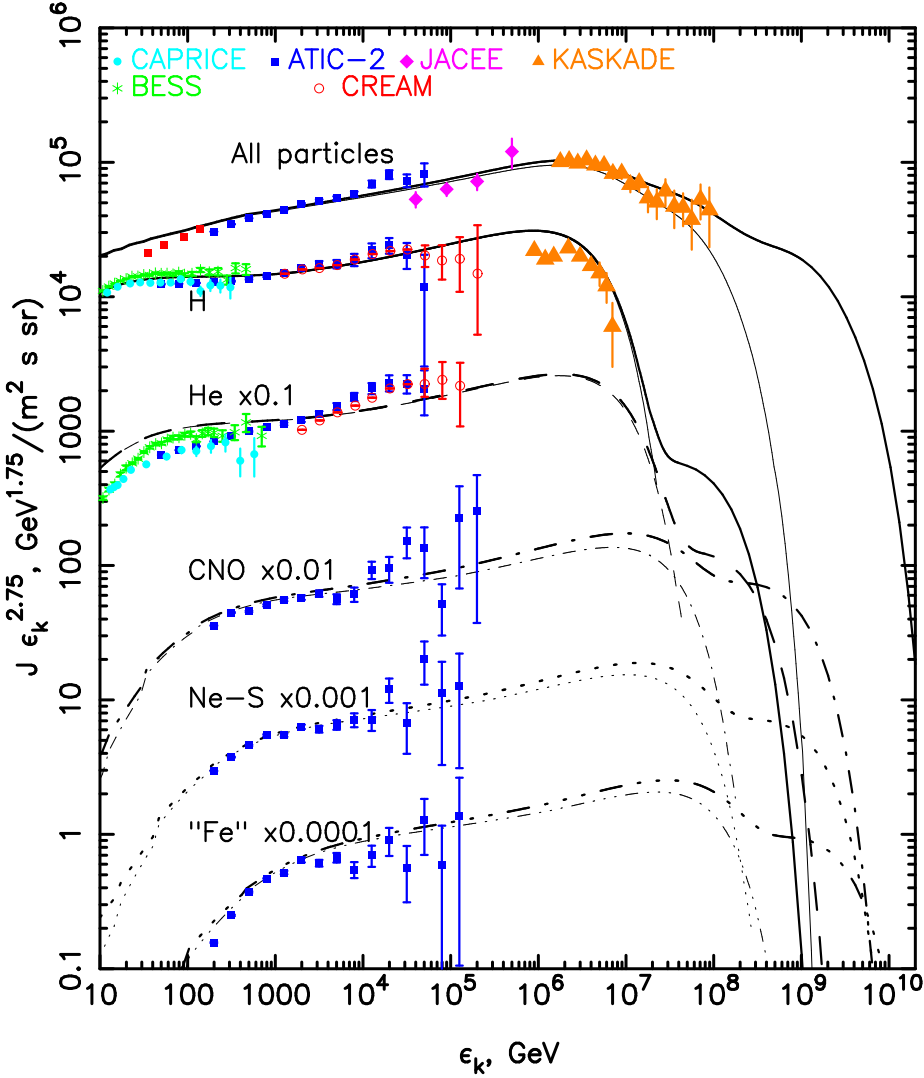


Figure 54: CR intensities at the Solar system as a function of kinetic energy. Experimental data obtained in the CAPRICE [35], BESS [36], ATIC-2 [37], CREAM [38], JACEE [39] and KASCADE [40] experiments are shown as well.

[174]). It is expected that the mass compositions of galactic and extragalactic CRs are significantly differs.

Since within this so called “ankle scenario”, extragalactic CRs dominate only above the energy 10^{19} eV [370] one needs some kind of process which provides the extension of the Galactic CR component produced in SNRs up to about 2×10^{18} eV. The possible solution of this problem is re-acceleration process which picks up the most energetic CRs from SNRs and substantially increases their energy or the second component of Galactic CRs due to supernovae, which explodes into the dense wind of pre-supernova star.

Within the alternative scenario (“dip scenario”) of the overall CR spectrum formation the extragalactic source component dominant at energies above 10^{18} eV. The dip is caused by the e^+e^- pair production in interactions of extragalactic protons with CMB. CR chemical composition is expected to be very different at energies 10^{17} to 10^{19} eV in these two cases.

There are some experimental hint to favor “dip scenario” (see Figure 55) However, discrepancies of data obtained in different experiments does not allow firmly determine the energy of transition between these two components of CRs. Depending on spectrum of extragalactic CRs, the transition energy expected in an energy range $10^{17} - 10^{18}$ eV (soft spectrum of extragalactic component) or in a range $10^{18} - 10^{19}$ eV for hard spectrum of extragalactic component. Therefore the experimental determination

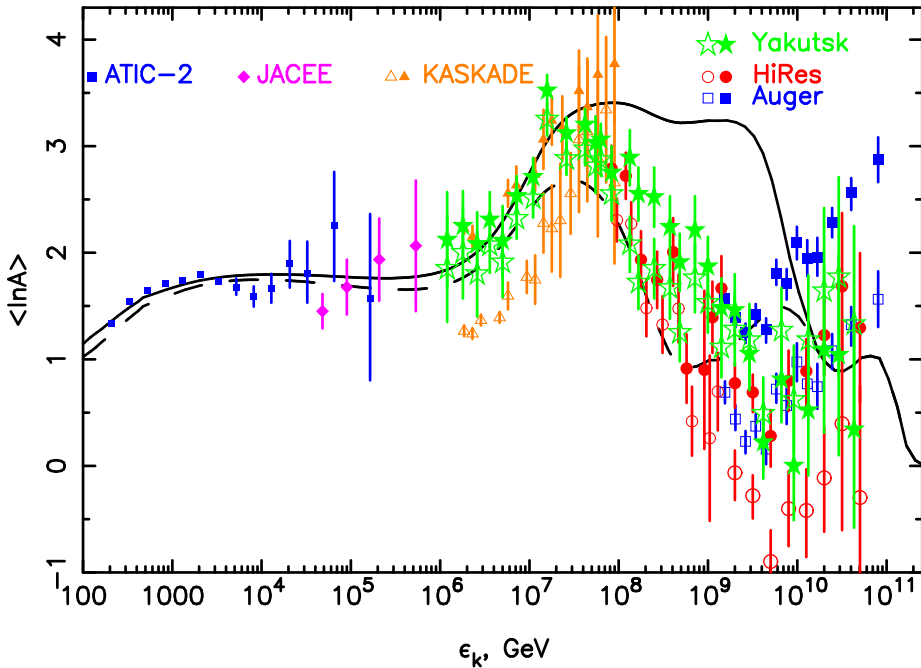


Figure 55: Mean logarithm of the CR nucleus atomic number as a function of energy. Calculations corresponded to ankle and dip scenarios are shown by solid and dashed lines respectively [41]. Experimental data obtained in the ATIC-2 [42], JACEE, KASCADE [43], Auger [44], HiRes at $\epsilon < 10^{18} \text{ eV}$ [45], HiRes at $\epsilon > 10^{18} \text{ eV}$ [46] and Yakutsk [41] experiments are shown. Open and solid symbols corresponds to QGSJET and SIBYLL models respectively.

of CR composition at these energies is very important task for all modern and planned experiments.

5.2. Cosmic rays physics around knee energies

Executive summary: In this paper we present the current understandings of the potential contribution of the LHAASO experiment to the cosmic rays physics around knee energies (i.e. $2 - 4 \times 10^{15}$ eV). To introduce the open problem in the studies of high energy cosmic rays physics, in the first part of the note I will discuss the more recent and relevant experimental results obtained in the $\sim 10^{12} < E < \sim 10^{17}$ eV energy range. Consequently the contribution that a large area, high resolution experiment, located at high altitude (like LHAASO) will bring are presented. Great emphasis is given to the analysis techniques aiming to separate the events into different primary mass groups, whose number must be studied in details by a complete EAS and detector simulation.

5.2.1. Current status of experimental results

Cosmic rays of energies up to about 100 TeV/nucleon can be studied with direct measurements, performed by satellite or balloon experiments that allow (on a event by event basis) a very good element classification, a reliable mass identification and a high resolution measurement of the primary energy (getting worse with increasing primary energy). At higher energies the primary radiation must be studied with indirect experiments detecting the secondary particles generated in the EAS that, mainly because of EAS development fluctuations, have a limited sensitivity to the charge of the primaries. As a consequence, the results are typically displayed as a function of the total energy per particle with the so-called “all-particle” spectrum, i.e. as a function of the total energy per nucleus and not per nucleon.

Last generation experiments, measuring with high resolution different EAS components (mainly the number of electrons, N_e , and the number of muons, N_μ , at observation level), have reached the sensibility to separate two mass groups (light and heavy) with an analysis technique not critically based on EAS simulations or five mass groups (H, He, CNO, MgSi, Fe) with an unfolding technique that is heavily based on EAS simulations. The results obtained by ground-based experiments are still conflicting in the knee energy range. For instance, is still not well defined which is the primary component that is originating the steepening of the all-particle spectrum observed at $2 - 4 \times 10^{15}$ eV (better known as the “knee”). Many results can be interpreted attributing this spectral feature to light elements (but the resolution is not enough to separate between H and He), while others (in particular those obtained by experiments located at high altitudes) seem to indicate heavier primaries as the responsible of the knee.

The actual knowledge about the cosmic rays spectrum around the energy of the knee can thus be summarized [371, 372]:

- (1) the primary H spectrum is steeper than those of other elements (CREAM [373, 374], PAMELA [225], AMS-02 [375]). The CREAM measurements show that, around 10^{20} TeV, He primaries become more abundant than the H ones (~ 100 TeV He/H ~ 1.3) [373, 374].
- (2) Around 200 TeV/nucleon a hardening of the H and He spectra has been observed (PAMELA [225], AMS-02 [375]), the existence of a similar feature in the spectra of heavier elements has not yet been clearly observed.
- (3) The H+He spectra obtained by indirect (ARGO-YBJ [376]) and direct (CREAM [373, 374]) measurements are, in the energy range covered by both experiments, in good agreement; showing the reliability of the hadronic interaction models used for the energy calibration of indirect experiments, at least until 200 TeV.
- (4) All EAS experiments detect a change of slope (known as “knee”) of the primary spectrum (“all-particle”) at about $2 - 4$ PeV.
- (5) The “all-particle” spectrum above the knee cannot be described by a single slope power law (KASCADE-Grande [377], IceTop [378], TUNKA-133 [379], TALE [380]), showing an hardening ($\sim 10^{16}$ eV) and a steepening ($\sim 8 - 9 \times 10^{16}$ eV).
- (6) The knee has been observed in the main EAS components at different atmospheric depths (i.e. observation height and zenith angle): electromagnetic (EAS-TOP [381], KASCADE [382] among the others), muonic (EAS-TOP [383], KASCADE [382]) and hadronic (KASCADE [384]). The results

obtained on every single component at different depths are in agreement with the EAS development models.

- (7) Around knee energies the spectrum of the EAS events with a low value of the N_μ/N_e ratio (representative of light primaries) shows a change of slope, while the one of the events with an high value of the same ratio (representative of heavy primaries) maintains the same spectral index (KASCADE [385]).
- (8) Around 80 PeV primary energy a change of slope, of the event sample having a high N_μ/N_e ratio, has been observed (KASCADE-Grande [386]).
- (9) Crossing the energy of the knee the mean primary chemical composition develops toward heavy elements (EAS-TOP [383], CASA-MIA [387]).
- (10) The spectra of five primary mass groups (represented by H, He, CNO, MgSi, Fe) derived, by unfolding analysis techniques, from two-dimensional (N_e vs N_μ) spectra, show the change of slope at energies increasing with the primary mass (KASCADE [40]). Performing the same analysis at higher energies the spectra of heavier mass groups (MgSi, Fe) show hints of a change of slope (KASCADE-Grande [388]).
- (11) The value of the power law index of the proton spectrum (H) measured by the Tibet-AS γ experiment, operating at high altitude above sea level, in the 1 – 10 PeV energy range is steeper than the one measured at lower energies by direct experiments [389]. This measurement indicates a heavy primary chemical composition already at knee energies.
- (12) Recent results obtained by ARGO-YBJ [390] experiment with different, independent analyses show a knee-like structure in the H spectrum at ~ 700 TeV.
- (13) Large and medium scale anisotropies have been observed, up to tens TeV primary energy, by the Tibet-AS γ [391], MILAGRO [392], ARGO-YBJ [393] and HAWC [394] experiments in the northern hemisphere and by the IceCube [395] experiment in the southern one.
- (14) Higher energy (around 400 TeV) large scale anisotropies (EAS-TOP [396], Ice-Cube [397], Ice-Top [398]) show a sharp variation of the first harmonic phase. The highest energy large scale anisotropy has been published by the IceTop [398] experiment at 2 PeV. The amplitudes of these anisotropies increase with the primary energy.

Results (6), (7), (8) and (12), (13), (14) even if obtained by indirect measurements, are almost independent from hadronic interaction models, while those from (9) to (11) depend on the hadronic interaction model used to simulate the EAS development in atmosphere. Almost all these results are based on interaction models developed before the LHC measurements that cannot correctly describe all different EAS measurements (the main discrepancy being the description of the muonic component and in particular its atmospheric evolution). Revised versions of these models, based on LHC results, have been recently delivered; preliminary analyses based on these models do not significant changes: the main novelty being the indication, respect to previous results, of a lighter chemical composition.

The usual interpretation of these experimental results is based on a scenario describing a galactic origin for the cosmic radiation of energy lower than $10^{17}\text{--}10^{18}$ eV (but the energy of the transition from galactic to extra-galactic cosmic rays has not yet been identified). The knee is attributed to the containment of the radiation inside magnetic fields either in acceleration sites (limiting the maximum attainable energy) or during the propagation: the knee energy is expected to scale with the charge of the elements.

A key-point is the identification of the proton knee. If this feature corresponds to the knee of the all particle spectrum (measured at 2^4 PeV) we expect the iron knee at and energy Z=26 times higher, i.e. from ~ 50 to ~ 100 PeV. While according to the previously discussed results (11) and (12) this energy has to be decreased. Also the measurement mentioned at number (1), i.e. a prevailing He flux respect to the H one, bring into question the H dominance of the spectrum at the knee. It is thus clear that a firm and precise determination of the H knee is the key point to further improve our knowledge about the cosmic rays at these energies.

Direct measurements, operating on balloons or satellite, certainly can reach the accuracy required to separate the H and He spectra, but their acceptance strongly restricts the maximum energies that can be studied (order of magnitude 100 TeV/nucleon). In this sense the more interesting future project is ISS-CREAM, foreseeing the installation on the ISS of a CREAM like device. Moreover moving to energies greater than ~ 100 TeV space based experiments are not only limited by their acceptance but also their mass became a limiting factor, as these calorimetric detectors will not be able to contain and detect the maximum development of the shower generated by the interaction of the primary particle. Thus also space based measurements will only give indirect evaluation of the primary energy and furthermore the absolute energy scale will not be calibrated by beam tests.

Indirect measurements are limited by the EAS development fluctuations that may make the separation of the H and He fluxes very difficult. Such fluctuations can only be minimized locating the arrays at high altitudes where, at knee energies, the EAS reach their maximum development.

5.2.2. Future Prospects and the LHAASO contributions

It is thus clear that the cosmic rays spectrum around knee energies is much more complicated than previously thought and possible, preliminary interpretations of these results have already been proposed (e.g. Gaisser et al. 2013 [372]).

Future experiments willing to improve our knowledge about cosmic rays in this energy range must measure the single element spectra up to the highest attainable energies and the large and small scale anisotropies separating events in, as much as possible, mass groups. As mentioned before the main limitations of EAS experiments are the shower development fluctuations and the detection errors, being the first term the more relevant one. Statistical approaches (like the unfolding) to elemental spectra depend heavily on the hadronic interaction models used in the EAS simulation moreover these analysis techniques do not allow an anisotropy measurement. While the approaches based on an event by event classification can be used for anisotropy studies and show a less pronounced dependence on hadronic interaction models, becoming more and more important as we aim to separate more than two mass groups and measure the absolute elemental fluxes and not only their spectral features. Therefore the best suited projects fulfilling all these requirements are high resolution, large statistics experiments possibly located at atmospheric depths near to shower maximum where development fluctuations are minimized.

The LHAASO experiment covering a km^2 surface and having a very high coverage for the detection of the electromagnetic and muon EAS components that will be located at 4410 m a.s.l. satisfies these needs.

The main role in an event by event classification will be played by the KM2A detector array that will be composed of 5195 1 m^2 unshielded plastic scintillation detector to reveal the electromagnetic EAS component and 1171 $\sim 30 \text{ m}^2$ water Cherenkov detectors (i.e. a total active area of $3.5 \times 10^4 \text{ m}^2$) buried under 2.5 m of soil to measure muons. In table 4 the LHAASO coverage is compared with those of some of the main experiments recently operating in the same energy range. We can see that LHAASO will be an experiment with a coverage (and consequently a resolution) similar to the KASCADE experiment deployed over a much larger effective area. Also the WFCTA and WCDA arrays of the LHAASO experiments have great potentials in this kind of analysis (as already shown by the ARGO-YBJ experiment) their contribution will be explored in detail in the future and will open the possibility of new unexplored ways to separate the event samples.

It is thus clear that it is of main importance to discuss and explore the prospects of the LHAASO experiment to separate as much as possible mass groups samples, once this objective will be reached we will apply it to obtain spectra and anisotropy measurements for all of them. All the main open problems discussed in section 1) will be addressed by such analysis, more precisely:

- (1) A detailed study of the elemental (or at least mass group) spectra in the energy range from 10^{14} to 5×10^{15} eV.

5.2 Cosmic rays physics around knee energies

Table 4: Comparison of the ratio between the active detection area (of the electromagnetic and muonic EAS components) and the effective area of LHAASO experiments with those of some of the more recent experiments operating in the knee energy range. The Ice-Top experiment has no surface muon detectors, high energy muons are measured by the IceCube detector thus limiting the solid angle.

	Altitude [m]	Detection area [m^2]	Effective area [m^2]	ratio
EM Components				
KASCADE	110	5×10^2	4×10^4	1.2×10^{-2}
IceTop	2835	4×10^2	10^6	4×10^{-4}
KASCADE-Grande	110	3.7×10^2	5×10^5	7×10^{-4}
LHAASO	4410	5×10^3	10^6	5×10^{-3}
μ Components				
KASCADE	110	6×10^2	4×10^4	1.5×10^{-2}
LHAASO	4410	3.5×10^4	10^6	3.5×10^{-2}

- (2) A definitive answer to the possible contradiction between the measurements performed at high altitude and at sea level, therefore investigating if the EAS development is correctly described by the current simulation codes.
- (3) Determine the more abundant primary element in the cosmic rays spectrum at the knee.
- (4) Measure the primary anisotropy for different mass groups.

A first preliminary study has been conducted by the Torino group simulating a small sample of fixed primary energy, vertical events to calculate the N_μ/N_e ratio without taking into account an experimental layout, its efficiency and resolution (thus representing the ideal case of a full coverage experiment without errors). Results are shown in figure 56 and indicate that at least up to 10^{17} eV separation in two mass groups is possible with this simple approach (error bars are the RMS of the distributions and not the error on the mean value). Further studies, taking into account also other EAS observables that will be detected in the LHAASO experiment, will be performed to investigate the possibility of separating more than two mass groups. From these studies we must obtain, by mean of a full EAS and detector simulation performed on a power law spectrum and over the full zenith angle range, the mass group selection efficiency and their contamination. The experimental results will have a small dependence from the hadronic interaction models used in the EAS simulation if the selection criteria will be independent from the primary energy.

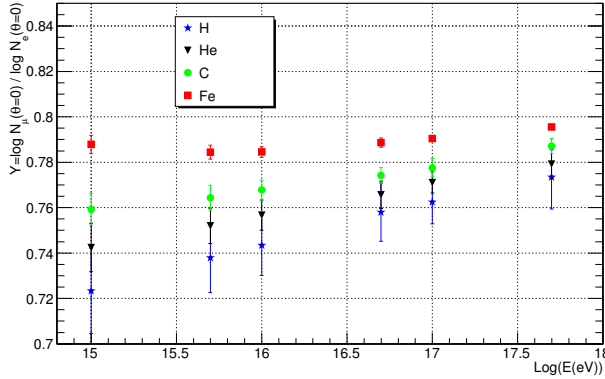


Figure 56: N_μ/N_e calculated for EAS observed at the LHAASO altitude above sea level (4410 m) in the ideal case of a full coverage experiment without detection errors.

The wide energy range covered by the LHAASO experiment allows the possibility to study with the same detector the elemental spectra from energies covered by space born experiments (thus giving

a check of the calibration procedures) to those of the change of slope of the primary spectrum (determining the energy of the knee of each element or mass groups spectra). Being LHAASO the first experiment with high resolution muon and electron detectors covering an effective area of $\text{km} \sim 2$ we will be able, for the first time, to study the mass group anisotropies at the level of $\sim 10^{-3} - 10^{-4}$. This last measurement is the more sensitive one to disentangle the scenarios describing the knee as the lack of containment inside magnetic fields either in the acceleration sites or during propagation.

If the mass group separation will be effective also at energies above 10^{17} eV (since the shower maximum is reached at an atmospheric depth deeper than the experimental site) the LHAASO experiment will also contribute to the study of the transition from galactic to extra-galactic radiation. Again investigating both the spectrum (a spectral hardening at 10^{17} eV was recently claimed by the KASCADE-Grande experiment [399]) and anisotropy (whose amplitude is expected to reduce when the extra-galactic radiation becomes dominant) of light elements. Thus the key point for these studies is again the separation into different mass groups on an event by event basis.

5.3. Cosmic proton spectrum from 30 TeV to 10 PeV measured by hybrid detectors of LHAASO

Executive summary: The measurement of the cosmic single element energy spectrum is an important tool to investigate cosmic ray production and propagation mechanisms. The determination of different species “knees” is believed to be a strong constraint for acceleration and propagation models. Experimental results, the “knees” of the proton is below 1 PeV or above 1 PeV, or two knees, are still unclear. Large High Altitude Air Shower Observatory (LHAASO) which has 18 Wide Field-of-View Cherenkov Telescopes (WFCTA), 1km^2 complex array (KM2A) including 4941 scintillator detectors and 1146 m^2 μ detectors and $78,000\text{ m}^2$ water Cherenkov detector (WCDA), locate at high altitude (4300 m above sea level). Using the number of μ , the number of particles in the shower core, the depth of shower maximum, length to width ratio of Cherenkov image, cosmic protons above 30 TeV have been well separated from other cosmic ray components. A highly uniform energy resolution of about 20% with energy reconstruction bias less than 3% throughout the whole energy range is achieved by the hybrid measurement. In this way, the protons energy spectrum from 30 TeV to 10 PeV is obtained and the “knees” of the proton is measured accurately. This result provides a fundamental input to reevaluate models describing the acceleration and propagation of the Galactic cosmic rays.

5.3.1. LHAASO Experiment

The Large High Altitude Air Shower Observatory (LHAASO) project consists of a 1km^2 EAS array (KM2A), a water Cherenkov detector array (WCDA), a wide field of view Cherenkov/fluorescence telescope array (WFCA). KM2A includes 4941 scintillator detectors, with 15 m spacing, for electromagnetic particle detection and 1146 underground water Cherenkov tanks (36 m^2 per tank), with 30 m spacing, for muon detection. WCDA has two $150\text{ m} \times 150\text{ m}$ water pools plus one $300\text{ m} \times 110\text{ m}$ pool. WCDA has total area of about $78,000\text{ m}^2$ and 3120 cells with an eight inch PMT in each cell. The size of each cell is $5\text{ m} \times 5\text{ m}$. A one-inch PMTs are put close to the eight-inch PMTs in each cell in a $150\text{ m} \times 150\text{ m}$ water pool to enhance the measuring dynamic range. The pool was named pool++. The dynamic range of the eight-inch PMTs is from 1 pe to 4000 pe. The one-inch PMTs will cover the dynamic range from 640 pe to 2×10^7 pe. The working gain of the one-inch PMT is about 2×10^5 . WFCTA has 18 Cherenkov telescopes. Each Cherenkov telescope consists of an array of 32×32 photomultipliers (PMTs) and a 4.7 m^2 spherical aluminized mirror. It has a field of view (FOV) of $14^\circ \times 16^\circ$ with a pixel size of approximately $0.5^\circ \times 0.5^\circ$. The main optical axis of the telescope has an elevation of 60° and observes showers within an angle of about 30° from the zenith. The WCDA is in the center of the 1km^2 EAS array. The distance between the center of WFCTA and the pool++ is about 10 m.

5.3.2. Simulation and quality events selection

(1) Simulation information

A detailed detector simulation is developed to understand the effects due to shower fluctuation and detecting efficiency in order to study reconstruction performance and estimate the systematic uncertainties. Extensive air shower simulations are carried out by a CORSIKA code using the high energy hadronic interaction model QGSJETII-03 and the low energy hadronic interaction model GHEISHA 2002. The primary particles are divided into five groups: protons, helium, CNO (carbon, nitrogen and oxygen) group, MgAlSi (Magnesium, Alumina and Silicon) group and iron.

(2) Criteria for clean images of air showers

Before processing a Cherenkov image, it is necessary to clean the noise pixels in the image. Noise pixels are mainly produced by the night sky background and electronic noise, arriving randomly in time and position, while Cherenkov lights hit the telescope almost simultaneously and produce an image in which the pixels are relatively concentrated. Three procedures are applied for image cleaning. First, the trigger pixels are kept if the signal is greater than 30 pe. Second, all reserved pixels should be within a time window of 240 ns; pixels are rejected if they are out of the time window. Last, the cluster that contains the largest number of pixels in the image is located and is

considered to be the Cherenkov image. Isolated pixels that have no connection to the Cherenkov image are rejected.

- (3) Criteria for well-reconstructed events We selected well-reconstructed showers in the effective aperture of the LHAASO according to the following criteria: 1) well-reconstructed shower core position contained in the pool with small PMTs of WCDA, excluding an outer region by 10 meter, 2) space angle between the incident direction of the shower and the telescope main axis less than 6° , 3) more than six fired pixels in the WFCTA PMT matrix.

5.3.3. Shower Energy Reconstruction

N_{pe} recorded by the telescope is an accumulation of all Cherenkov photons produced in the whole shower development. Since the telescope stands at a certain distance from the shower core, the measured N_{pe} varies dramatically with the impact parameter R_p because of the rapid falling off of the lateral distribution of the Cherenkov light. The shower energy as a two-dimension function of the total N_{pe} and R_p are plotted in Fig.57, where the color represents shower energies in bins with a width of $\Delta \log_{10} E = 0.2$. A look-up table can be established for energy reconstruction. By feeding in the two measured variables N_{pe} and R_p , the shower energy can be interpolated using the pre-generated table. In reality, a minor effect due to the incident direction of the showers relative to the telescope is taken into account in the look-up tables. A specific table for a mixture of protons and helium nuclei are generated with three entries of N_{pe} , R_p and α . First, the table is generated by a Monte Carlo simulation. Then, the shower energy of the observation data can be obtained from the table by using the measurement parameters of total N_{pe} , R_p and α . The energy resolution is about 20% mainly due to the intrinsic fluctuation of shower development. The resolution is quite uniform throughout the energy range and the systematic bias is less than 3% throughout the entire energy range, as shown in Fig.58. This guarantees the ability to estimate the spectral index and scan for any special structures in the spectrum.

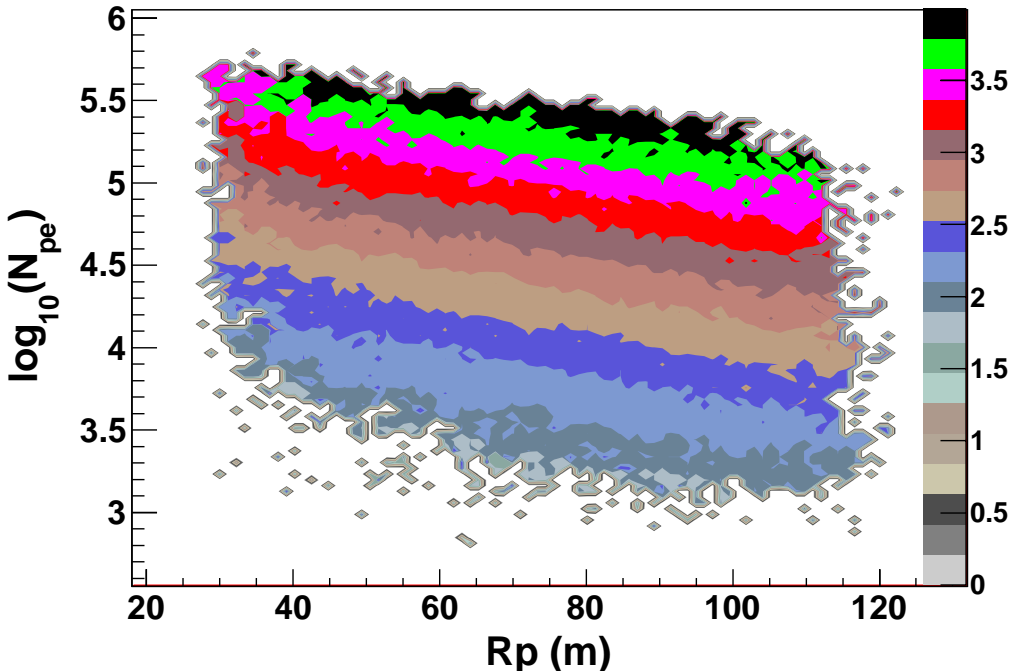


Figure 57: The total number of photoelectrons N_{pe} as a function of the impact parameter R_p for primary protons. The color scale represents the shower energies in bins of $\Delta \log_{10}(E/1\text{TeV}) = 0.2$, covering primary energies from 30 TeV to 10 PeV.

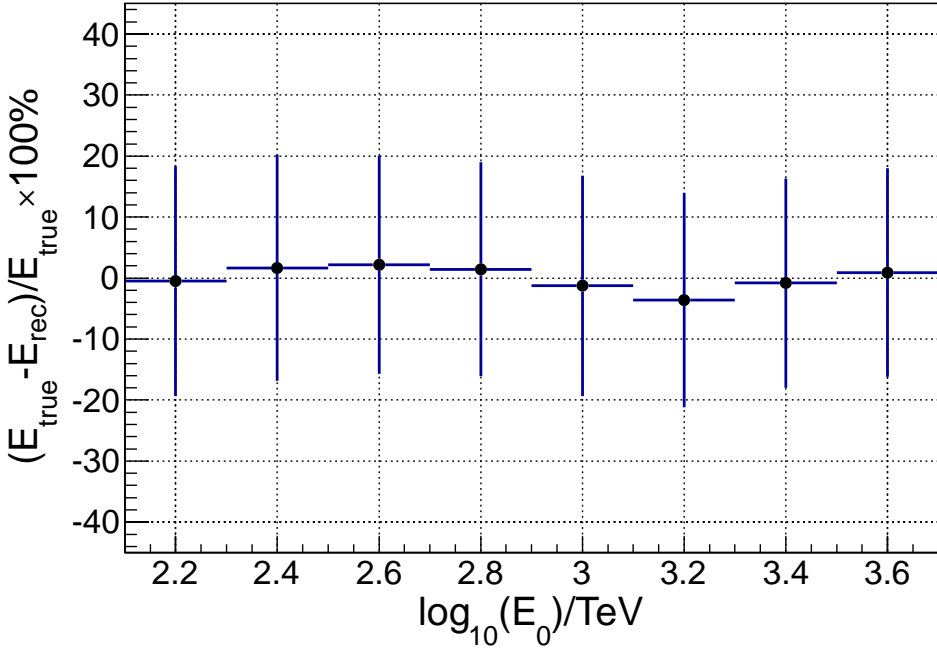


Figure 58: Energy resolution is about 20% and the bias is less than 3% for the light component energy spectrum. E_{rec} is the reconstruction energy from a specific table of a mixture of protons and helium nuclei and E_{true} is the primary energy. The error bars represent the energy resolution.

5.3.4. Mass sensitive parameters

Showers initiated by light nuclei, such as protons and helium, penetrate more deeply into the atmosphere than those from heavier nuclei. The secondary particle densities measured at a certain depth, e.g. 606g/cm² in the pool++ of the WCDA case is not too deep for the maxima of showers initiated by light nuclei above 100 TeV, and are expected to remain in the vicinity of the cores in a shower. In contrast, showers induced by heavier nuclei are farther below the maxima when they reach the pool++ of the WCDA. The secondary particles in showers induced by heavier nuclei are more diffused to the farther area laterally and produce a more uniform distribution due to Coulomb scattering. Therefore, it is clearly seen that there are significant differences between the lateral distributions of showers induced by light and heavy nuclei in the vicinity of cores, while they are very similar at a certain distance, e.g. 30 m, from cores. The pool++ can measures the lateral distribution of secondary particle densities very near the shower cores. This method offers a unique sensitive measure of the cosmic ray composition by simply counting the particles in the cells of the pool++ that are closest to the core. Usually the largest number of particles recorded in the cells in an event, denoted as N_{max} , is in the cell that is closest to the core. N_{max} in cores due to a heavy nucleus must be less than that due to a light nucleus. Obviously, N_{max} is energy dependent; therefore, a normalization procedure is necessary before it can be used for composition determination. According to the simulation, N_{max} is proportional to $(N_0^{pe})^{1.44}$, where N_0^{pe} is the total number of photo-electrons measured by WFCTA normalized to $R_p = 0$ and $\alpha=0^\circ$. The reduced parameter $\log_{10}N_{max} - 1.44\log_{10}N_0^{pe}$, denoted as p_{max} , serves as a good indicator of the shower composition.

The other mass sensitive parameter measured by the pool++ is the total photoelectron measured by the pool++, N_{pool}^{pe} . Obviously, N_{pool}^{pe} is primary energy dependent. The reduced parameter $p_{Npe}^{pool} = \log_{10}N_{pool}^{pe} - 1.18\log_{10}N_0^{pe}$, serves as a good indicator of the shower composition.

A Cherenkov image looks like an ellipse and is described by Hillas parameters [400]; such as the width and length of the image. The width is defined as the root-mean-square (rms) of the angular spread of the Cherenkov photons along the minor axis of the image, which is a measure of the lateral

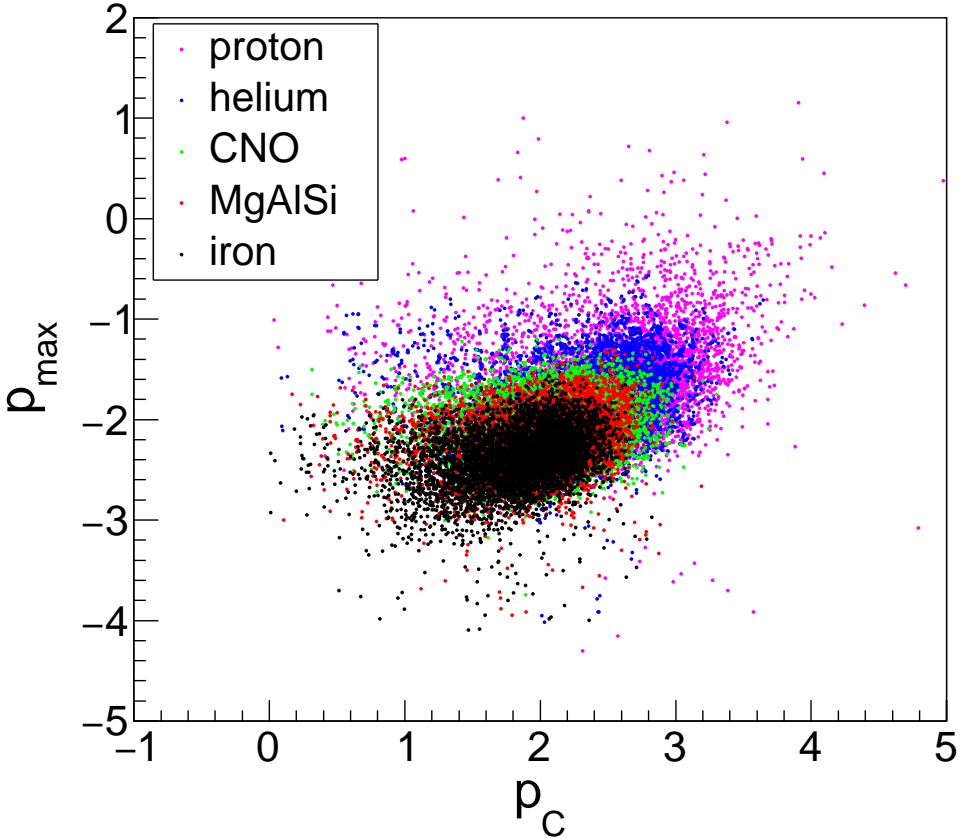


Figure 59: p_{max} - p_C map.

development of the shower. The length is the rms of the angular spread of the Cherenkov photons along the major axis of the image, which is a measure of the longitudinal development of the shower. The images are more stretched, i.e. narrower and longer, for showers that are more deeply developed in the atmosphere. The ratio of the length to the width (L/W) is therefore a good parameter that is sensitive to the primary composition. It is also known that the image is more elongated when the shower is farther away from the telescope, i.e. the image becomes longer and narrower for showers located farther away. Before they are used as indicators of the composition, images must be normalized for showers with different impact parameters, R_p . Furthermore, the images are also more stretched for the more energetic showers. According to simulation, the ratio L/W of images are linearly proportional to R_p and N_0^{pe} . The reduced parameter $L/W - 0.018R_p + 0.28\log_{10}N_0^{pe}$, denoted as p_C , serves as an indicator for the primary components.

The depth of shower maximum X_{max} can be reconstructed by using Cherenkov image, which is mass sensitive parameter too. The resolution of X_{max} is found to about 50 g/cm^2 . Obviously, X_{max} is primary energy dependent. The reduced parameter $p_{Xmax}=X_{max} - k\log_{10}N_0^{pe}$, serves as a good indicator of the shower composition.

There are well known that the total number of muon measured by KM2A, N_μ , is a mass sensitive parameter. Obviously, N_μ is primary energy dependent. The reduced parameter $p_\mu=N_\mu + 0.001R_p - 0.86\log_{10}N_0^{pe}$, serves as a good indicator of the shower composition.

The p_{max} - p_C map is shown in FIG. 59; the p_{max} - p_μ map is shown in FIG. 60; and p_{Xmax} - p_{max} map is shown in FIG. 61. Combining all of the above five composition sensitive parameters, one expects an improvement in the separation between cosmic ray components.

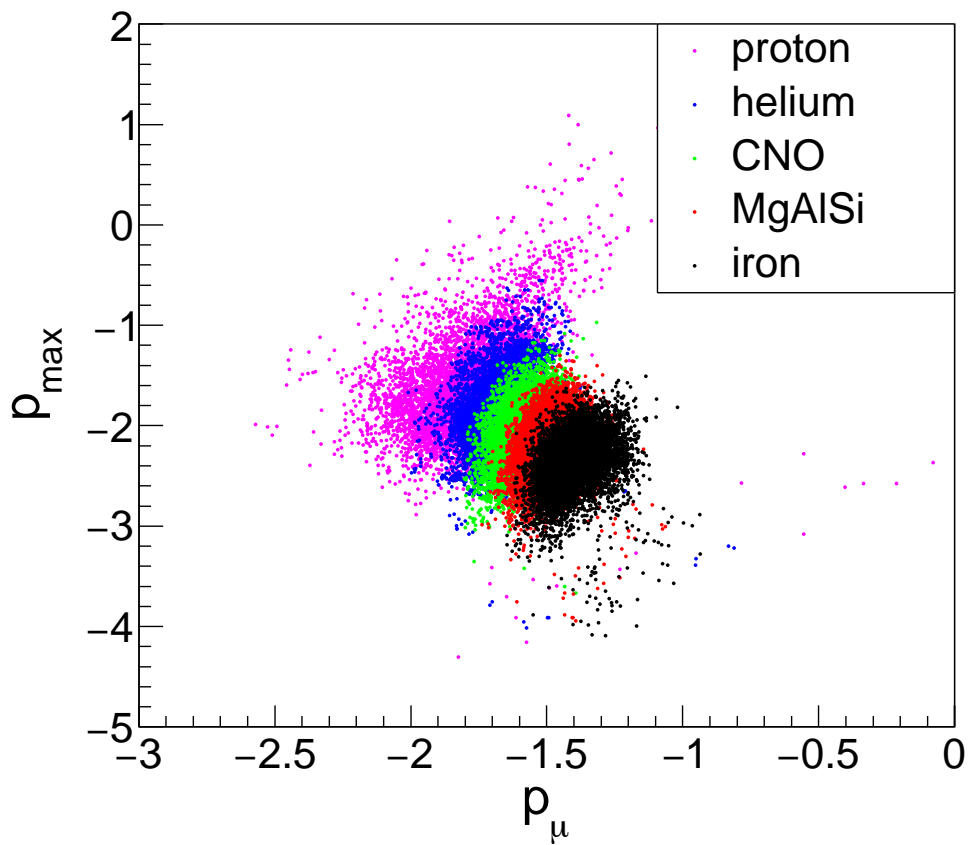


Figure 60: p_{max} - p_μ map.

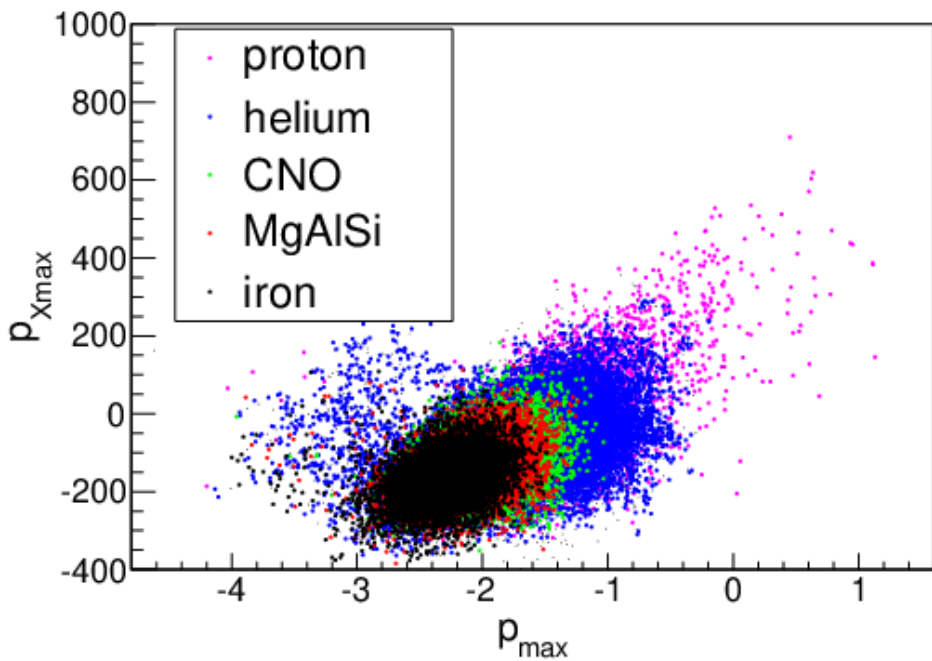


Figure 61: p_{max} - p_μ map.

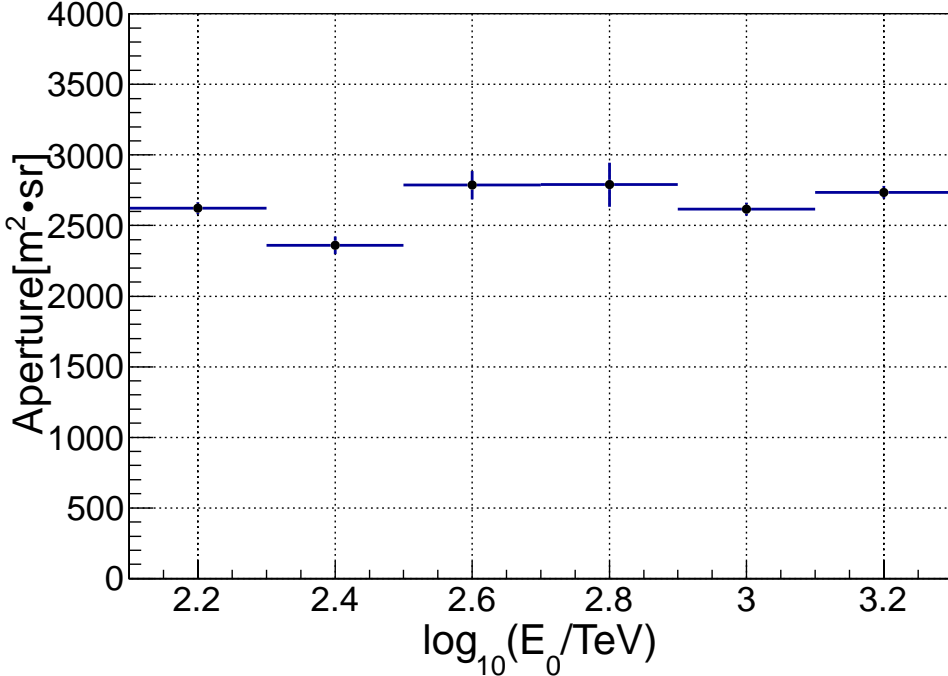


Figure 62: Aperture of the hybrid experiment. Solid circles represent the aperture for the selected H events.

5.3.5. Hydrogen Event Selection

The H sample for this work was selected from the coincident events by combining the two composition-sensitive parameters p_{max} and p_μ as an example. The cuts $p_{max} \geq -1.0$ or $p_\mu \leq -1.9$ result in a selected sample of H showers with a purity of 85% assuming the Hörandel composition models [47]. The aperture, defined as the geometrical aperture times the selection efficiency, gradually increases to $2600 \text{ m}^2 \text{ sr}$ at 100 TeV and remains nearly constant at higher energies (see FIG. 65). The selection efficiency is defined as the ratio of the selected number of H events and the total number of injected H events in the simulation.

In the selected sample, the contamination from the heavy nuclei depends on the composition. Assuming the Hörandel composition [47], the contamination of heavy species is found to be less than 15% at energies range from 100 to 3 PeV, which is shown in FIG. 66. The contamination fraction for different mass groups in FIG. 66 is defined as $N_i/(N_H + N_{He} + N_{CNO} + N_{MgAlSi} + N_{Iron})$ with $N_i = N_{CNO}, N_{MgAlSi}, N_{Iron}$ for $i = 1, 2, 3$.

After the composition selection, H like events from 100 TeV to 10 PeV are selected. The total exposure time of 1×10^6 seconds per year (3.2% duty cycle) is assumed. The number of events in the each energy bins are shown in FIG. 67. There are about 1000 proton like events at around 1 PeV can measured by hybrid experiments of LHAASO per year after the composition selection.

5.3.6. Hydrogen and Helium Event Selection

The $H\&He$ sample for this work was selected from the coincident events by combining the two composition-sensitive parameters p_{max} and p_μ as an example. The cuts $p_{max} \geq -1.3$ or $p_\mu \leq -1.7$ result in a selected sample of $H\&He$ showers with a purity of 96% assuming the Hörandel composition models [47]. The aperture gradually increases to $4500 \text{ m}^2 \text{ sr}$ at 100 TeV and remains nearly constant at higher energies (see FIG. 65).

In the selected sample, the contamination from the heavy nuclei depends on the composition. Assuming the Hörandel composition [47], the contamination of heavy species is found to be less than 5% at energies range from 100 to 3 PeV, which is shown in FIG. 66.

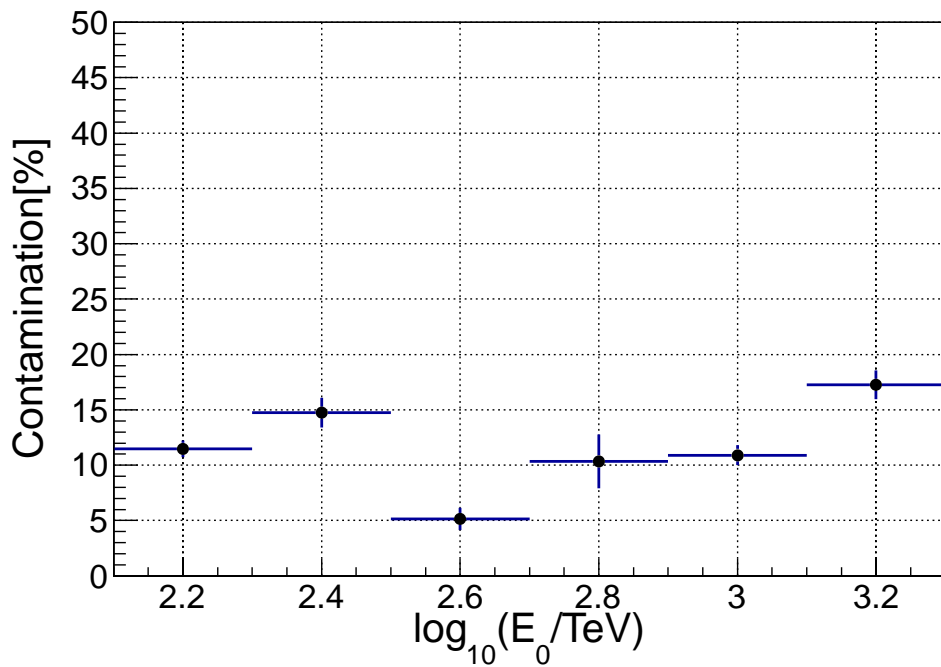


Figure 63: The contamination fraction (%) of events of heavy composition other than protons that survive through the H selection cuts. The Hörandel model is assumed in the simulation.

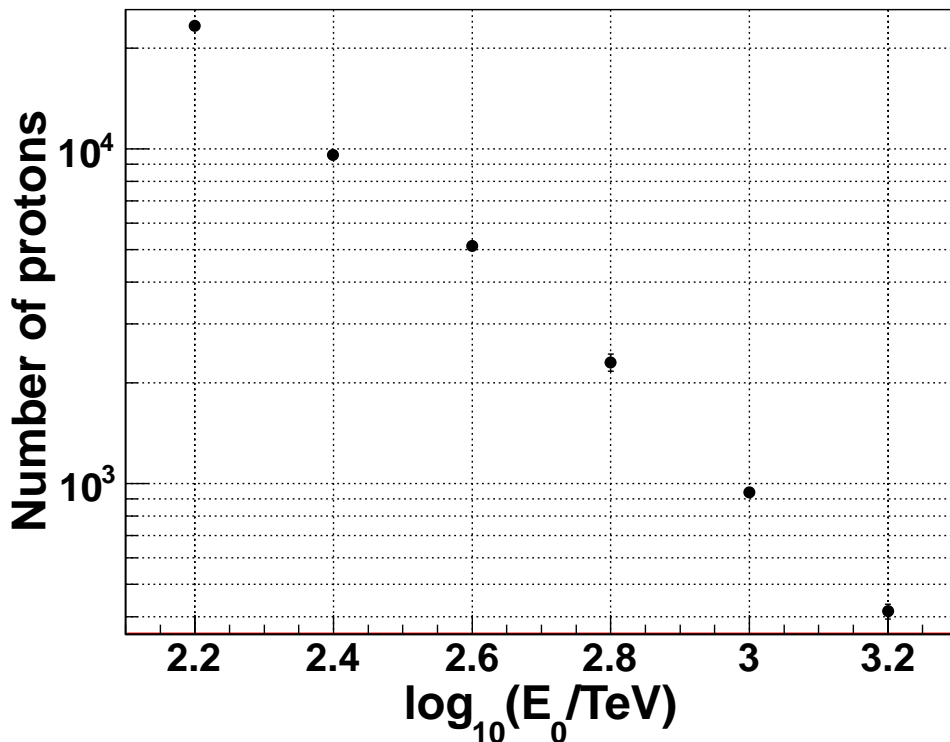


Figure 64: The number of proton like events in each energy bin measured by hybrid experiments of LHAASO per year after the composition selection. The Hörandel model is assumed in the simulation.

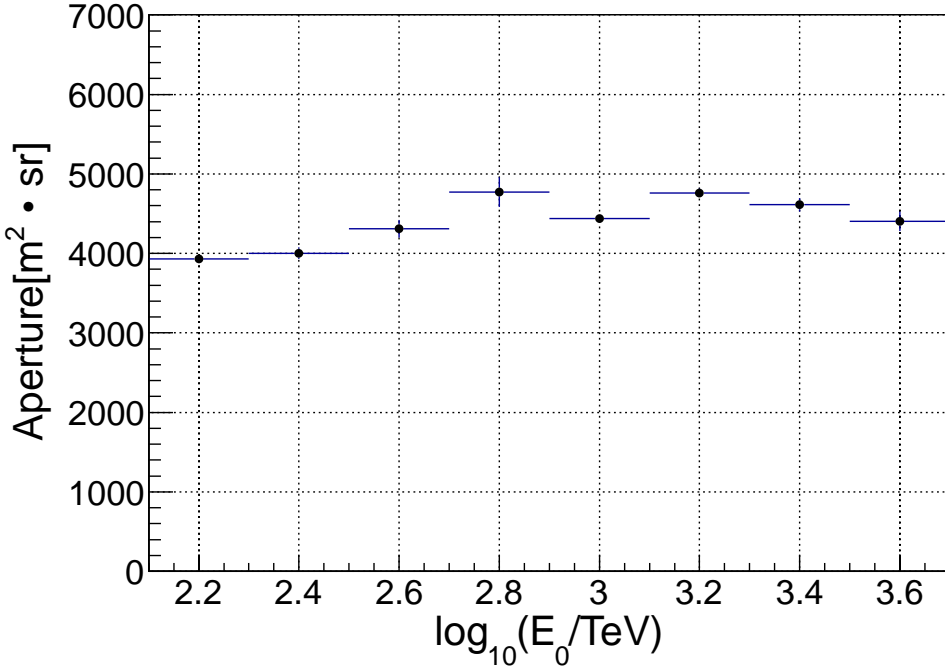


Figure 65: Aperture of the hybrid experiment. Solid circles represent the aperture for the selected H&He events.

After the composition selection, $H\&He$ like events from 100 TeV to 10 PeV are selected. The total exposure time of 1×10^6 seconds per year (3.2% duty cycle) is assumed. The number of events in the each energy bins are shown in FIG. 67. There are about 3000 proton and helium like events at around 1 PeV can measured by hybrid experiments of LHAASO per year after the composition selection.

5.3.7. Conclusion

Cosmic protons are separated from the overall cosmic ray event samples by using two mass sensitive parameters: the number of μ , the number of particles in the shower core. The contamination of heavy nuclei is found about 15% as the worst case. The energy resolution is about 20% with a bias of less than 3% throughout the entire energy range from 100 TeV to 10 PeV. There are more than 1000 proton like events at around 1 PeV can measured by hybrid experiments of LHAASO per year after the composition selection. The purity of proton like events is more than 85%.

Cosmic $H\&He$ are also separated from the overall cosmic ray event samples by using the number of μ and the number of particles in the shower core. The contamination of heavy nuclei is found about 4% as the worst case. The energy resolution is about 20% with a bias of less than 3% throughout the entire energy range from 100 TeV to 10 PeV. There are more than 3000 $H\&He$ like events at around 1 PeV can measured by hybrid experiments of LHAASO per year after the composition selection. The purity of $H\&He$ like events is more than 96%.

The purity will be greatly improved if the multi-parameter technique is used and all of five mass sensitive parameters: the number of μ , the number of particles in the shower core, the depth of shower maximum, length to width ratio of Cherenkov image and the total photoelectron measured by the water Cherenkov detector, are taken into account.

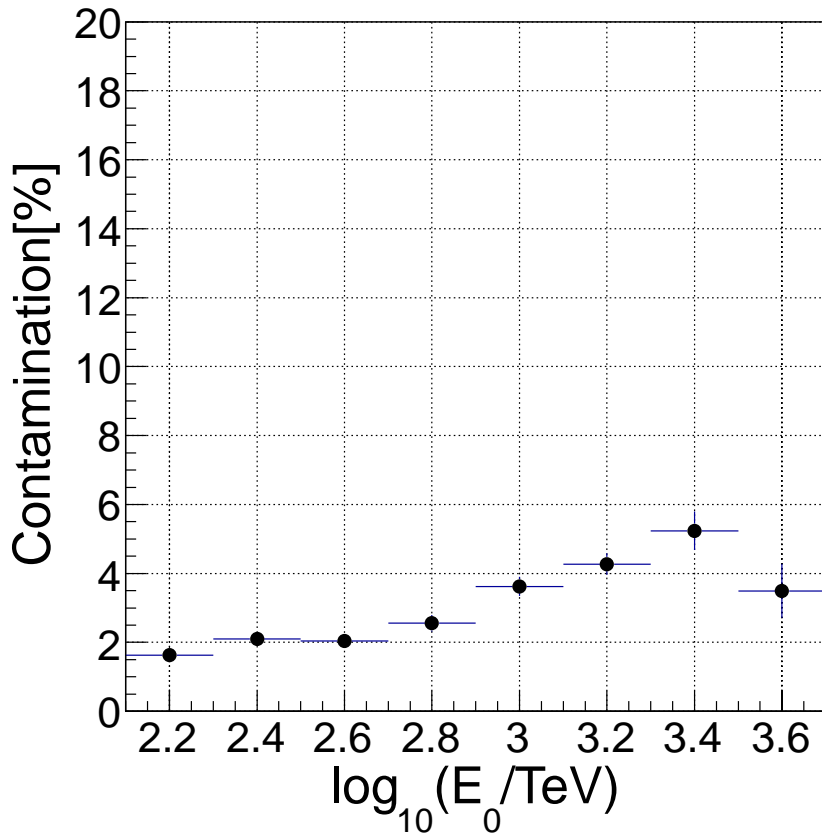


Figure 66: The contamination fraction (%) of events of heavy composition other than H&He that survive through the H&He selection cuts. The Hörandel model is assumed in the simulation.

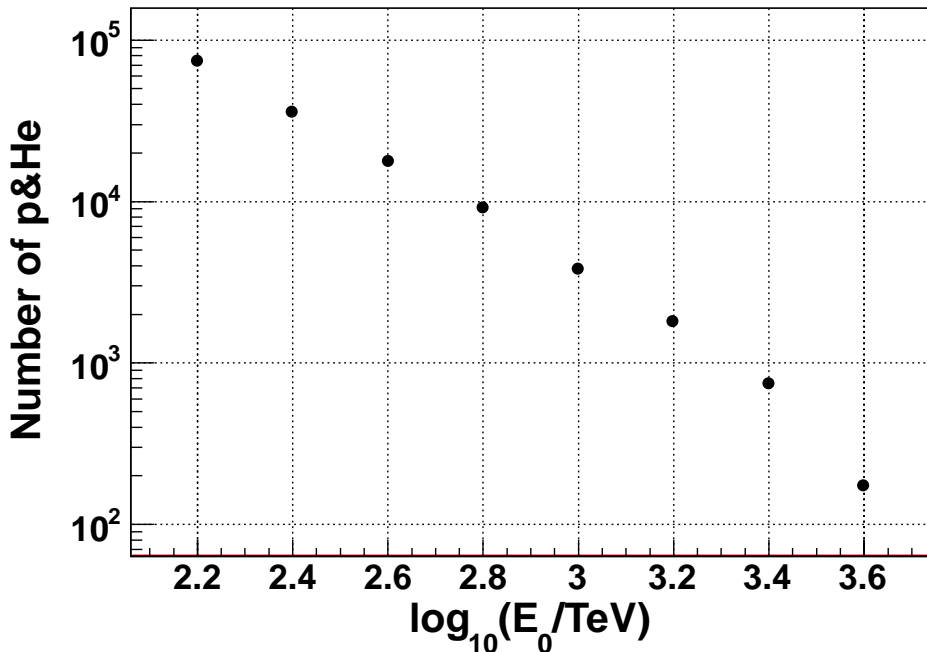


Figure 67: The number of H&He like events in each energy bin measured by hybrid experiments of LHAASO per year after the composition selection. The Hörandel model is assumed in the simulation.

5.4. Measuring Spectrum of heavy component of cosmic rays above 10 PeV Using LHAASO KM2A and WFCTA

Executive summary: Measuring the knees of the CR spectra for individual species is a very important approach to solve the problem of origin of ultra high energy galactic cosmic rays. The knees of the iron spectrum is implied to be above 10 PeV by the previous experiments, such as ARGO-YBJ and LHAASO-WFCTA[401]. LHAASO[62] has a suitable size for the measurements with the required precision. The key is to separate iron nuclei from all CR samples. In this paper, we identify a couple of variables that are sensitive to the composition of showers recorded by the detector arrays in LHAASO. A multi variate analysis is proposed for the separation. The efficiency and the purity of the selection for demanded species are optimized by well configuring the LHAASO array using the LHAASO simulation tools.

5.4.1. Introduction

The most significant feature of the power-law-like spectrum of CRs with all mixed species is the “knee”, i.e. a significant bending of the spectrum from the power-law index of approximately -2.7 to -3.1 around few PeV. The origin of the knee still remains as a mystery since it was discovered. Disclosing the mechanism of the knee would be a significant improvement in understanding of the origin of the galactic cosmic rays. Measuring the knees for every single species will be an significant progress towards the goal. At the altitude of 4300 m above sea level (a.s.l.), the ARGO-YBJ resistive plate chamber (RPC) array and air Cherenkov telescopes were combined to carry out the experiment[402] and resulted a clean measurement of the spectrum of CR protons and α ’s over the range from 100 TeV to 3 PeV and a discovery of the knee of the spectrum at 0.7 PeV, which is well below the knee of the spectrum of all particles[401]. According to plausible assumptions of the bending being either rigidity (Z) or total number of nucleus (A) dependent, the knee of the iron spectrum will be around either 18 PeV or 39 PeV, the precise measurement of the knee of the iron spectrum is obviously very important to understand the mechanism of the knee. However, the composition measurement in the energy range above 10 PeV is really difficult because a rather large detector array is required due to the very low flux. Moreover, a multi-parameter measurement is also required to maintain a high resolution in the shower composition by providing sufficient information about the showers in the identification their composition. A high energy resolution is also essential to find the knee structure and its energy. Therefore, such a measurement has not been achieved so far. Large High Altitude Air Shower Observatory (LHAASO)[62] having many components of detector arrays, may enable the measurement with sizable array to guarantee the required collection of shower samples and the resolutions in both composition and energy of shower detection. In this paper, we plan to describe the LHAASO detector arrays that are relevant to the measurement in the second section, identify the parameters measured by LHAASO that are sensitive to the composition, and the selection of iron samples out of all shower events in third section and report the preliminary results on the expectation of the spectrum measurement using the LHAASO simulation kit in the summary section.

5.4.2. Detector Arrays in LHAASO

1. Scintillator Counter Array and Muon Detector Array The major component of LHAASO is an array of 5195 scintillators counters with a spacing of 15 m between any two counters. Each counter is composed of 1 m^2 of scintillator plates, wave length sifting fibers embedded in the plates and a Photo Multiply Tube (PMT) with a circular photo-cathode of 38 mm in diameter. The scintillating light in the plates induced by particles passing through the counter is collected and guided to the PMT by the fiber bundle. With a timing resolution better than 2 ns[403], the PMT times the arrival moment of the particles as a *hit* with an absolute time stamp distributed from the data center through a fiber network covering the entire array. The White Rabbit protocol (WRP)[404, 405] is running in the network which is connected with the special switches for WRP and synchronizes all clocks at the counters within 200 ps. The total charge of the *hit* proportional to the number of particles passing through the counter is

digitized at the counter with a resolution of 25% at single particle or 5% at 10000 particles, respectively. In order to catch the 90% of shower particles, namely γ 's, a 5 mm sheet of lead is installed on top of the scintillator plate to convert the γ 's into pairs of electrons and positrons. This significantly improves the shower arrival direction and shower core position resolution. Both timing and charge signals are transferred through the network upwards to the data center where a trigger of shower event is formed if any 6 hits in any area with a radius of 100 m are coincident in a window of 300 ns[406].

A shower above 10 PeV typically generates more than 500 hits in the array. They allow a reliable reconstruction of the shower front and result a shower arrival direction with the resolution better than 0.3°. The numbers of particles in counters measure the shower lateral distribution very well and result a shower core location with the resolution of 4 m. The array of 1.0 km² is surrounded by an outskirts ring composed of 294 counters with a spacing of 30 m to identify showers those have their core located outside the array and throw them away in the reconstruction.

Shower muon-content is measured in LHAASO by using the muon detector (MD) array of 1171 water Cherenkov muon counters with the spacing of 30 m and covering an area of 1.0 km². Each MD is a cylinder, with a diameter of 6.8 m and height of 1.2 m, filled up with pure water. The inside layer of the liner in MD is highly reflective material, *i.e.* TYVEK film. An 8" *in* PMT is installed at the center on the top of the liner, looking down into the water in the liner through a transparent window. Muons passing through water generate Cherenkov light which bounces back and forth on the surface of TYVEK until reaches to the cathode of the PMTs. The detecting efficiency of muons that fall inside the area of the counter is around 97% throughout the whole detector, with a threshold of 1/4 height of a single muon pules in the detector[407]. In order to screen the electrons and photons in showers, MDs are covered by dirt with a depth of 2.8 m. This results a very clean measurement of muons above 1 GeV, except one or two counters being hit right on by the shower cores. Those counters could be polluted by the energetic electrons or photons typically in the shower cores and could be saturated as well. Therefore, they will be eliminated in shower reconstruction.

The pulse waveform of a MD is read out by using 500 MHz flash ADC once the signal is over the threshold with linear charge response over a dynamic range from 1 to 10,000 muons. The non-linearity is less than 5%. Each pulse is timed by using the absolute time stamp distributed through the WR network with a resolution of 2 ns. Only integral of the waveform, which is proportional to the total charge from the PMT and the time stamp are collected at the farm in the data center. Using single muon signal, the total charge is calibrated as the number of muons falling into the counter. The resolution is 25% for single muon and 5% for 10,000 muons, respectively. Once a shower event is formed using the scintillator counter array, the numbers of the muons at all MDs within a window of 100 ns are included in the event. Respecting to the shower core determined by the scintillator counter array, the lateral distribution of the muons are well measured. Integrating the distribution over the whole array, the muon content of the shower is calculated.

2. SiPM Staffed Cherenkov Telescope Array and Its Configuration 18 Cherenkov telescopes are arranged as much as possible to the central region of the scintillator counter and MD array to maximize the utilization of the whole area of 1.3 km² as illustrated in Figure 68. For shower energy above 10 PeV, the telescopes are fully efficient in the areas with the shower impact parameter $R_p \leq 400$ m with the trigger criteria of at least 6 registered pixels and each pixel having at least 10 photo-electrons (P.E.'s). The main axes of all telescopes are arranged at elevation of 45°, therefore the field of view (FoV) of the 18 telescopes covers a ring of the sky with the width of 16° in elevation and full circle of 360° in azimuth at the elevation of 37° which is the lower edge of the ring. At the higher edge of the ring, elevation of 53°, there is an overlap of about 13 pixels between the adjacent telescopes. The FoV is also shown in Figure 68, the right panel.

Major upgrade has been made on the design of the telescope, comparing with its prototype[408]. The aluminized spherical reflecting area of 5 m² as the light collector remains as the prototype, but the telescope now can be tilted up and down in elevation from 0° to 90° with an improved support system.

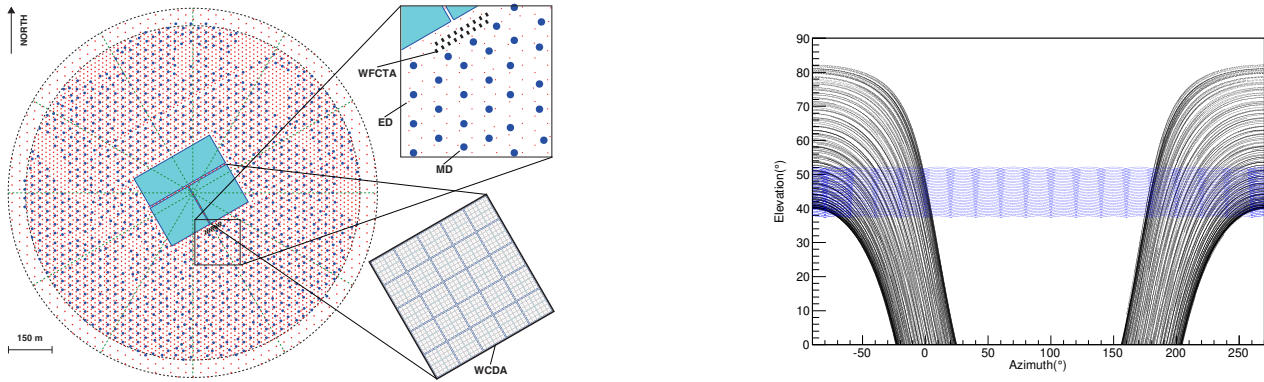


Figure 68: The layout of the scintillator counter (small dots) array, muon counter (big dots) array, water Cherenkov detector (rectangle in the center) array and the location of the wide field of view (FoV) Cherenkov telescope (small squares) array in the LHAASO experiment (left panel). The FoV of the telescopes in the entire northern sky map. The azimuth angle 90° is the north direction. Curves in the sky indicate the trajectories of the moon in one year.

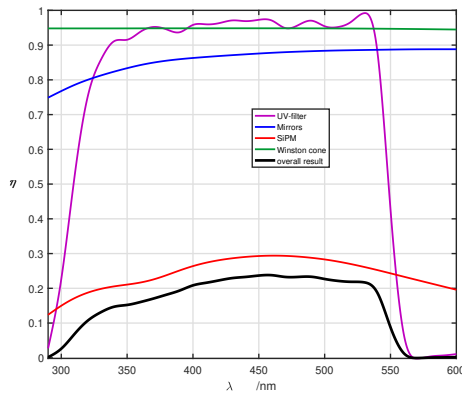


Figure 69: The wavelength response function of relevant components of the telescope including mirrors, filter, Winston cones and the SiPMs. The response of the cones is an average over all incident angles. The overall response function is also shown here.

At the focal plane, 2870 mm away from the mirror center, a camera with 1024 square pixels, instead of 256 hexagonal ones, is redesigned to image the shower in its FoV of $16^\circ \times 16^\circ$. The pixel, with a FoV of $0.5^\circ \times 0.5^\circ$, is formed of $1.5\text{cm} \times 1.5\text{cm}$ SiPM receiving photons reflected by the mirror through a Winston cone. Both entrance and exit pupils of the cone are square shaped with an area ratio of 2.65. The internal reflective surface is aluminized with a reflectivity ranged from 89% to 97% depending on the incident angle. The largest receiving angle is about 35° respect to the normal vector of the SiPM active surface for photons reflected from the edge of the mirror. The overall collecting efficiency of the cone is 93% without counting the blind gaps between the cones due to their thickness. The SiPM is an array of 0.56 million avalanche photo diodes (APD) with a size of $20\ \mu\text{m}$. The diode is working in Geiger mode that allows the whole pixel having a dynamic range from 10 to 40,000 P.E.'s with the non-linearity less than 5%[409]. In front of the cones and SiPMs, a wide-band filter is installed to suppress the incident light above $550\ \text{nm}$ in which bandwidth the night background light (NBL) is mainly distributed. This is the way to enhance the signal to noise ratio. The overall working wavelength range of the telescope is from $300\ \text{nm}$ to $550\ \text{nm}$ including the contribution from the mirrors, filters, Winston cones and SiPMs. The peak at $460\ \text{nm}$ is mainly due to the quantum efficiency of SiPMs, which is about 30% at the peak. The overall response function in wavelength, taking into account the complex angular response of the cones, is shown in Figure 69.

16 pixels form a cluster, which can be removed and replaced easily from the camera, with the front

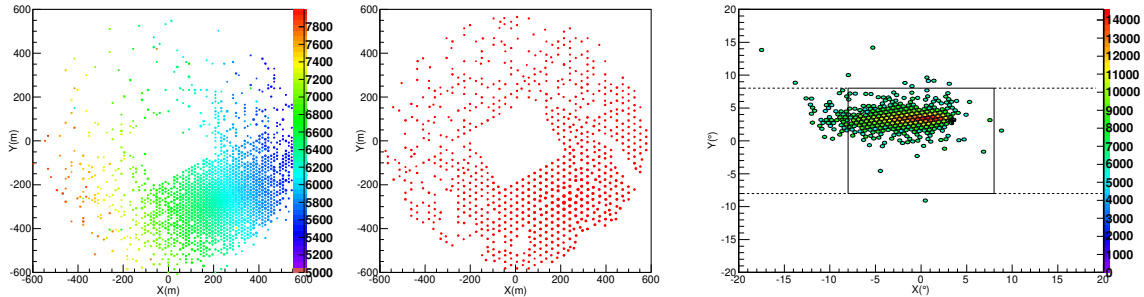


Figure 70: A 20 PeV iron shower event hit in the array with the $R_p \sim 200\text{m}$ to the telescopes. The registered scintillator counter map and muon counter map are shown in the left two panels. The image of the shower taken by the telescopes is shown in right. The ‘cross’ mark in the right panel indicates the arrival direction of the event determined by the scintillator array.

end electronics (FEE) and the digitization of the waveform integrated together. The waveform, typically 120 ns wide, is digitized with a sampling rate of every 20 ns by using two 50 MHz 12-bit flash ADC’s at high gain and low gain channels to cover the whole dynamic range of the SiPM’s. The ratio of gains between the two is 7:1. The high gain channel has its own background fluctuation (σ) measurement and corresponding trigger threshold setting, e.g. 4σ within a window of 240 ns. Once it is triggered, a signal T_0 will be generated and transmitted to the trigger logic that collects all the signals from all 1024 pixels. The trigger logic is installed on the back board of the camera. A pattern recognition algorithm is operated to decide whether or not a shower has been observed and generate a signal T_1 to every channels in all telescopes in the array. The waveform data are read out from each channel and integrated for the total charge measurement. Simultaneously, an average time weighted by the amplitude is calculated for timing measurement in each pixel. Both charge and timing data are transmitted to the data center with the absolute time stamp distributed through the WR network which also allows the data being transmitted upwards to the data center from each telescope.

Figure 70 shows a complete shower event by a 20 PeV iron nucleus as an example by the maps of hits in the scintillator, muon counter array and the Cherenkov image in the cameras from left to right. The spots located at the position of the counters indicate the hit with the radius of the spot proportional to the logarithm of the number of particles, the color (gray degree in black/white version) of the spot indicates the timing of the hit. The shower core is clearly measured in the array. In the right panel, the shower Cherenkov image is recorded by the array of telescopes. The color (or gray degrees) of registered pixels indicate the number of P.E.’s. According to the shower geometry determined by the scintillator counter array, the R_p is 200 m.

In the right panel of Figure 68, which shows the FoV of the telescope arrays in the sky, curves in dashed lines on both sides of the panel indicate the transient trajectories of the moon in the entire year. Since the aging effect of SiPMs is negligible and their operating threshold is higher than the NBL fluctuation even with the full moon, the telescopes are able to be operated in all dark periods except those directly watch into the moon. By timely switching off those telescopes and keeping all others on, one could significantly increases the observational time. In average, 17 telescopes out of 18 have the duty cycle as high as 30%, which is essentially the whole dark period between twilight with or without the moon in the sky. To measure the quite low flux of cosmic rays in such high energy range above 10 PeV, this is very necessary for the hybrid measurement with the 1.3 km² ground array.

5.4.3. Composition sensitive parameters and their measurements

As described above, LHAASO measures the lateral distributions of muons in EAS and ordinary particles, γ ’s and e^+e^- . This allows the calculations of both total number of muons N_μ^A , where A indicates the atomic number of the primary particle of the shower, and the size N_{tot} of the shower. Since the muon content in a shower is a simple power law as a function of the shower energy, so

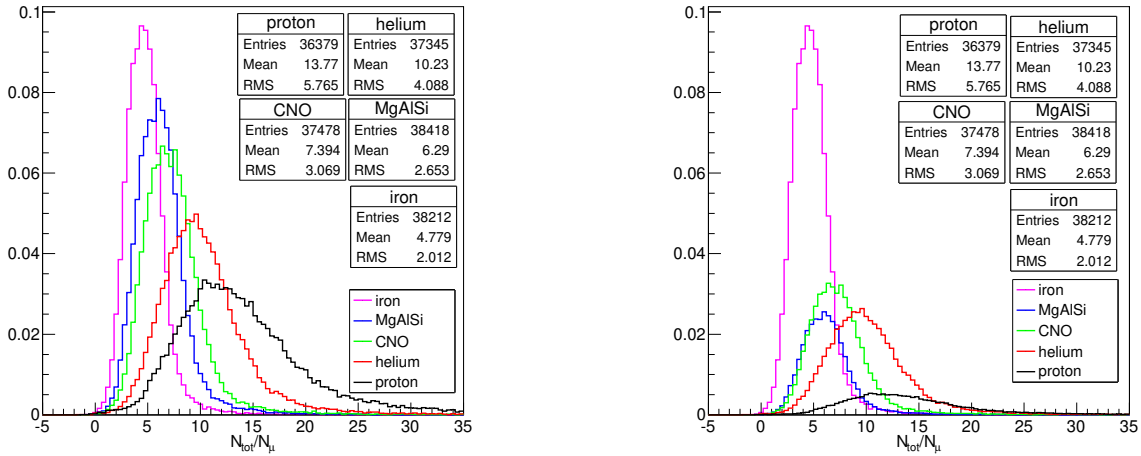


Figure 71: Distributions of inverted muon contents ($1/C_\mu$) in showers with 5 groups of species, *i.e.* iron (in pink), Mg-Al-Si (blue), C-N-O (green), Helium (red) and proton (black). Left, events are evenly distributed among 5 species; Right, with the assumption of composition in[47]

$N_\mu^A/N_\mu^p \approx A^{(1-\eta)}$, where η is the index of the power law and is far away from 1 and p indicate the proton shower, is almost the most sensitive parameter to the shower composition. Usually, the reduced muon content N_μ/N_{tot} , denoted as C_μ , is used in the selection for showers with specific composition. In Figure 71, distributions of the inverted muon content ($1/C_\mu$) for iron showers is plotted to compare with the same distribution of all other showers, with an assumption of every group of species, *i.e.* iron, Mg-Al-Si, C-N-O, Helium and proton are evenly distributed and independent of the shower energy. The separation is quite clear. Also shown in Figure 71, the same comparison between the distributions are plotted for some more realistic assumption about the composition[47].

Telescopes take the Cherenkov images of the showers in their FoV. For 10 PeV and higher energy, the shower image is very bright and the numbers of registered pixels are typically greater than 100 even for showers with $R_p \sim 400$ m. Given the shower distance using the shower geometry reconstructed by the scintillator counter array, the total number of photons in the image measures the shower energy. See below for a detailed discussion on the shower energy reconstruction. The angular offset of the shower image from the arrival direction measures the height of the shower maximum, measured by the vertical atmospheric depth X_{max} with a resolution of ~ 50 g/cm². Figure 72 shows the relationship between X_{max} and the angular offset. The resolution is rather sensitive to how well the shower image is contained in the FoV of the telescopes. In order to achieve a selection for the well imaged showers, the total number of registered pixels, N_{pixel} , and the angular distance from the shower arrival direction to the upper and lower boundary of the FoV, Y , are required to be $N_{pixel} > 100$ and $|Y| > 1^\circ$, hence images with most part falling outside the FoV will be eliminated. Measuring shower X_{max} is the traditional method of primary particle identification in calorimeter detection of showers, such as air fluorescence or Cherenkov light detection of showers. Due to the well known elongation of showers in the air, *i.e.* X_{max} is proportional to $\log E$, where E is the shower energy, $X_{max}^{(p)} - X_{max}^{(A)} \propto \log A$, where A is the atomic number of the primary nucleus and p indicates primary proton. As a comparison, the typical resolution of X_{max} for fluorescence light experiment is about 25 g/cm² if the shower profile is well contained in the FoV of the telescope array. In Figure 73, distributions of the reconstructed X_{max} for iron showers is plotted to compare with the same distribution of all other showers, with an assumption of the 5 groups of species are evenly distributed and independent of the shower energy. The resolution of the Cherenkov telescopes has been taken into account. Also shown in Figure 73, the same comparison between the distributions are plotted for some more realistic assumption about the composition[47].

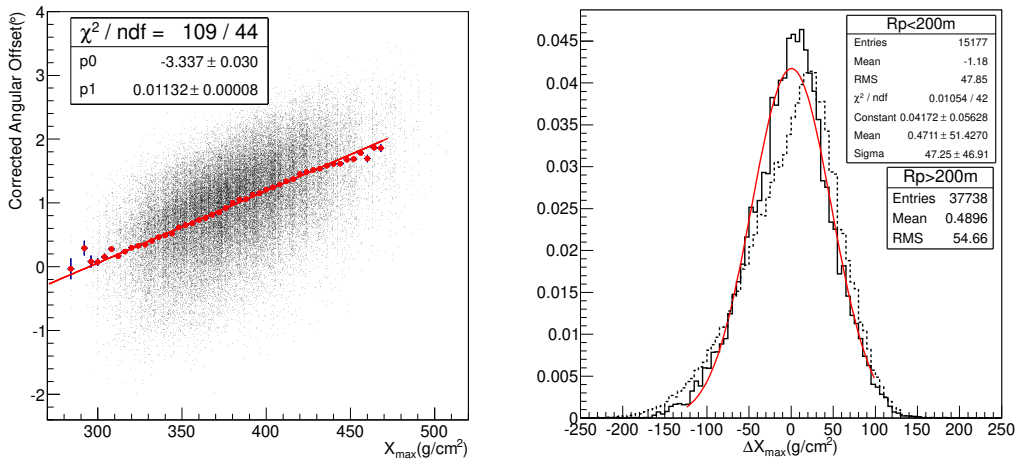


Figure 72: Relationship between vertical X_{\max} and the angular offset of the centroid of the shower image from the arrival direction (left) and corresponding resolution of X_{\max} (right). The solid curve is the resolution function of showers that have impact parameter $R_p < 200\text{m}$ and the dashed curve is for $R_p > 200\text{m}$, respectively

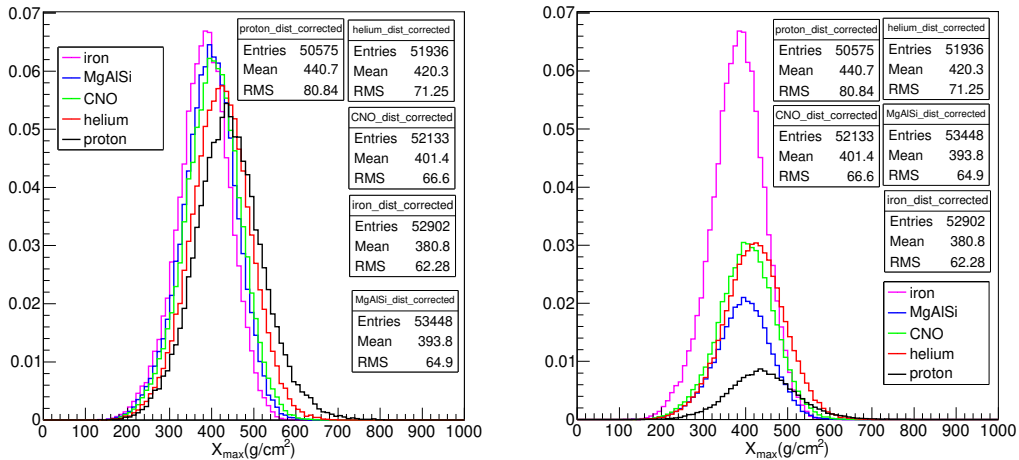


Figure 73: Distributions of vertical X_{\max} of showers with 5 groups of species, i.e. iron (in pink), Mg-Al-Si (blue), C-N-O (green), Helium (red) and proton (black). Left, events are evenly distributed among 5 groups of species; Right, with the assumption of composition in [47].

One-to-one correlation between the parameters, inverted muon content had been checked by plotting them in the scatter map in Figure 74-left and find quite independent between them with the correlation coefficient less than 90%. In this map, 5 group of species are plotted in different colors and the iron showers are clearly outstanding in the lower-left corner from other species. With a simple cut, $1/C_{\mu} < 6$ & $X_{\max} < 460 \text{ g/cm}^2$, one can achieve the selection of the pure iron showers out of all well constructed CR samples with certain purity of 70% at 10 PeV to 85% at 100 PeV. The effective aperture of the detection of the iron showers is about $3.4 \times 10^5 \text{ m}^2 \text{sr}$. This results a collection of about 16,000 iron showers above 10 PeV per year according to an assumption of the spectra of the 5 groups of species with corresponding knees[47] and about 164 iron showers in the last bin near 100 PeV. The expected spectrum is shown in Figure 74-right as the solid squares. The knee, if it is there, will be discovered with high significance in one year operation of the hybrid observation using LHAASO instruments.

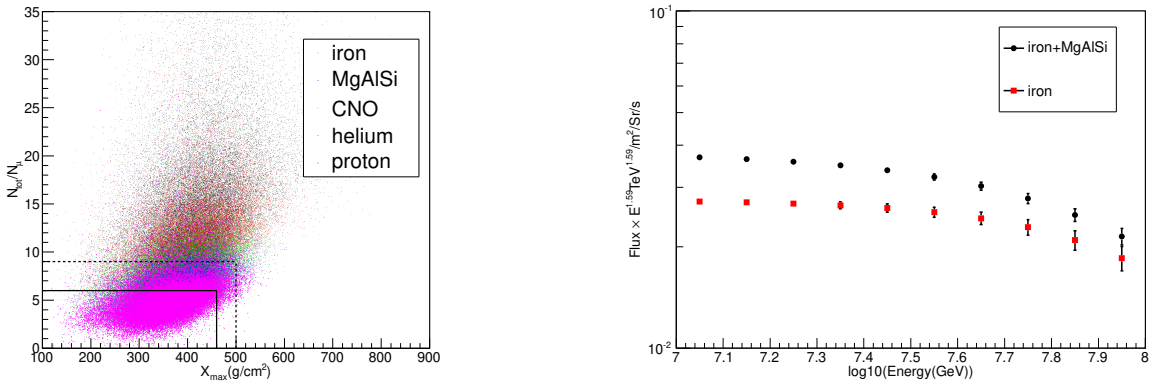


Figure 74: Left: The correlation between $1/C_\mu$ & X_{\max} for 5 groups of species of iron (in pink), Mg-Al-Si (blue), C-N-O (green), Helium (red) and proton (black). The cuts indicated by the two lines can be applied to select the iron samples with a purity about 85% from all measured CR events. Right: The expectation of the pure iron spectrum over an energy range from 10 to 100 PeV with LHAASO in one year observation. The knee structure will be significantly measured if it is as the assumption of model in [47]

Given a single composition sample of CRs with a purity of 75% or better, the energy reconstruction of the shower is rather straightforward by using the total number of Cherenkov photons in the shower image. This minimizes the uncertainty due to the unknown composition. The total number of photons has been proved to be a good energy estimator because the resolution function is symmetric Gaussian with the bias less the 5%. This is a good feature of the Cherenkov technique in the power-law-like spectrum measurement with the minimized distortion. The other good feature of the technique is that the energy resolution is almost a constant of less than 20% over a wide energy range. This is very important in finding the structures of the spectrum if there are, such as the knee. Every part of the spectrum is equally measured with the consistent resolution. Both the resolution and the reconstruction bias as functions of the shower energy are shown in Figure 75.

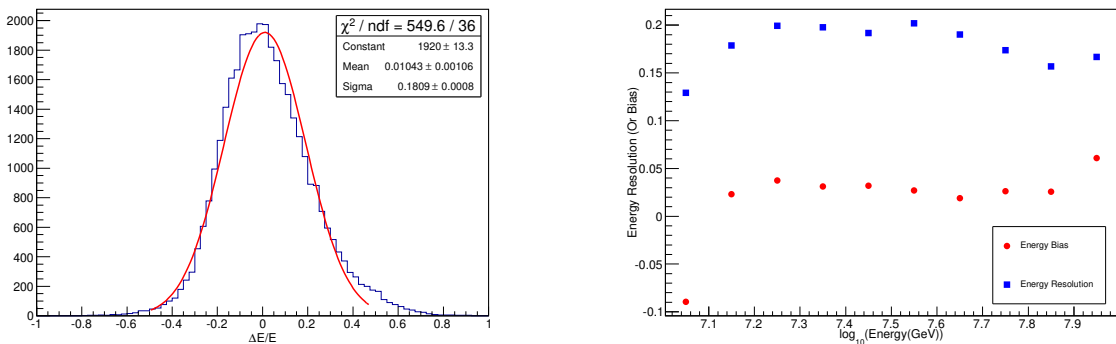


Figure 75: The energy resolution function of the pure iron showers using the total numbers of Cherenkov photons in the shower images (left) which is symmetrical Gaussian function with the mean of 1% and standard deviation of 18% according to the fit indicated by the smooth curve. In the right panel, the systematic offset (spots) and the resolution (squares) of the energy reconstruction for the pure iron events as functions of shower energy are plotted. It is noticed that the resolution is nearly a constant over the energy range.

5.4.4. Summary

In summary, the LHAASO experiment will enable an effective identification of CR primary species by measuring two independent key parameters of the induced air showers, muon content and shower

maximum position in the energy range from 10 to 100 PeV . The selection of pure iron samples with the purity better than 75% has been achieved using the simulation tools developed for LHAASO experiment. With such a pure sample, the CR shower energy measurement using the total number of Cherenkov photons in the shower image is much certain and precise, i.e. the energy bias is under control within 5% and the resolution is maintained to be nearly a constant of below 20% over the energies at which the knee of the iron spectrum is expected. In this paper, we have demonstrated the power of the LHAASO experiment in shower composition analysis with a very simple cut. Together with the observation of the knee of the $P + He$ spectrum[401] and the future observation of pure proton spectrum around 1 PeV in the early stage of the LHAASO experiment[410][411], one would expect the measurement described in this paper to bring us a clear picture of the phenomena associated with the knees or even more detailed structures of the CR spectra over the whole knee region. It will greatly enhance our knowledge on the mechanism of knees, propagation and the production of the galactic CRs.

5.5. Contribution of ENDA to LHAASO

5.5.1. Motivation

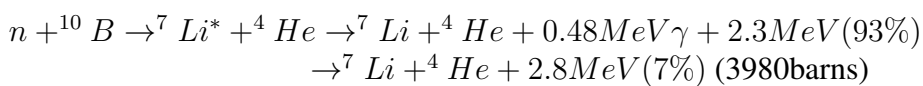
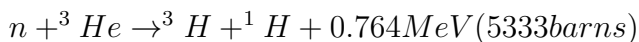
When arriving at Earth, high energy cosmic rays interact with the air nuclei originating extensive air showers (EAS). They consist of a core of high energy hadrons that continuously feed the electromagnetic part of the shower, mainly with photons from neutral pion, kaon and eta particle decays. Nucleons and other high energy hadrons contribute to the hadronic cascade. High energy hadrons, which constitute the EAS skeleton, may carry important information for multi-parameter correlation studies, since some hadronic observables, primarily the hadron number/electron number correlation, depend on the nature of the particle inducing the shower[48][412]. Thus, the detection of high energy hadrons, addressed to improve the discrimination power in these analysis, is highly advisable. A way to deal with this problem avoiding the use of huge and expensive HCALs was brought out in [48, 413]. In these papers the detection of thermal neutrons generated by EAS hadrons is proposed. It is well known that hadrons interacting with ambient matter (air, building, ground, etc.) produce evaporation neutrons due to nuclei disintegration. The neutrons have no charge and lose energy only by scattering. If the medium is a good moderator, i.e., the absorption cross section is much less than the scattering cross section, the neutrons lose energy via scattering down to the thermal ones (moderation process) and then live in the matter until capture. Evaporation neutrons need about 0.5 ms to thermalize in rock (concrete). Neutrons are generated abundantly, up to 2 orders of magnitude more than parent hadrons. The mean number of evaporation neutrons $\langle n \rangle$ produced by hadrons in a 120 cm layer of surrounding soil (about 3 hadron interaction lengths) and/or construction materials can be estimated using the empirical relationship

$$\langle n \rangle \approx 36 \times E_h^{0.56} \quad (8)$$

where E_h is the hadron energy in GeV [414]. A large fraction of the evaporation neutrons thermalize, so that recording thermal neutrons can be exploited to reconstruct the hadron content in the shower (Fig. 76). This approach looks very promising for measurements carried out at high altitude. Indeed, since the hadron content in EAS increases with the altitude, an abundant production of thermal neutrons can be predicted for experiments at 4 (or more) km a.s.l. , about a factor 10 higher than that at sea level [414]. These considerations suggested the development of a simple and cheap thermal neutron detector, to be deployed over a large area, as 'hadron counter' in EAS experiments at mountain level. This idea led to the development of the EN-detector, made of a mixture of the well-known inorganic scintillator ZnS(Ag) with ^6LiF , capable of recording both thermal neutrons and charged particles [415][416].

5.5.2. Detector Principle

Of the isotopes used as neutron capture material, ^3He , ^6Li and ^{10}B are mostly popular. The reactions of neutron capture are:



Of the three isotopes, ^3He has the highest cross section of neutron capture, but it is in shortage seriously, not good in timing and not easy to control due to its gaseous state at room temperature. ^6Li releases the highest energy during the action, but it is the raw material of nuclear fission so that its purchase is strongly limited by government. Although capturing neutron with lower released energy than ^6Li , ^{10}B has larger cross section, and ^{10}B is much easier to be obtained. Moreover, natural Boron

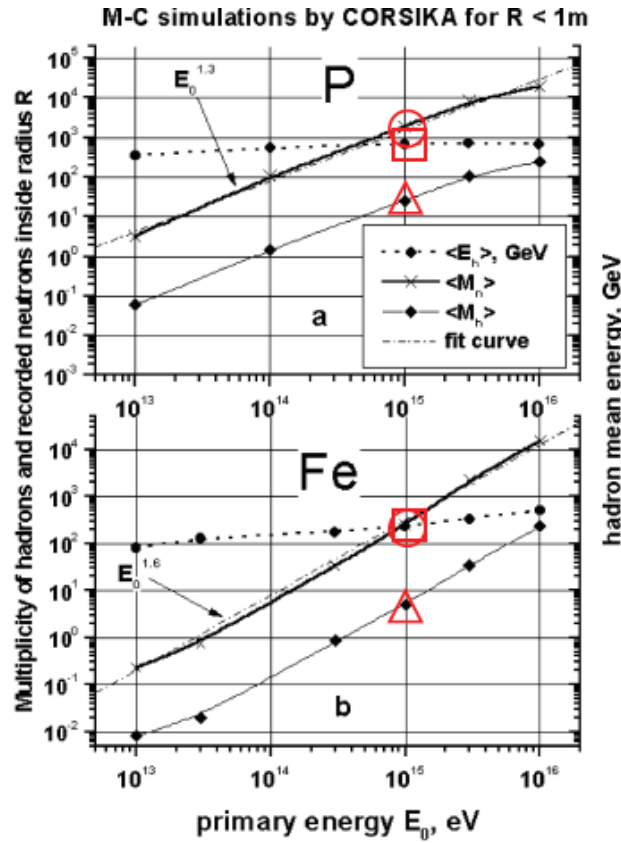


Figure 76: Simulation results: At the same energy, for example, 1PeV, proton has both secondary hadrons M_h and hadron energy E_h and then neutrons M_n about one order higher than ones of Fe [48].

contains 19% versus only 7% of ${}^6\text{Li}$ in natural Lithium and this allowed us to make a natural boron compound compatible with lithium ones enriched with ${}^6\text{Li}$ up to 90%.

A novel type of ZnS(Ag) scintillator alloyed with B_2O_3 with the ${}^{10}\text{B}$ isotope about 20% is developed instead of ZnS(Ag) with ${}^6\text{LiF}$. Powder of ZnS(Ag) and B_2O_3 alloy is not applied on a sheet of plastic or aluminium as convention, but deposited in liquid silicon rubber in the form of a thin one-grain layer. The scintillator is not only easier produced in big size, but also transparent for scintillation lights. The effective thickness of the scintillator layer is 50 mg/cm^2 .

The structure of a typical EN-detector is shown in Fig 77. The scintillator of 0.35 m^2 area is mounted inside a black cylindrical polyethylene (PE) 200-1 tank which is used as the detector housing. The scintillator is supported inside the tank to a distance of 30 cm from the photomultiplier (PMT) photocathode. A 4"-PMT (Beijing Hamamatsu CR-165) is mounted on the tank lid. A light reflecting cone made of foiled PE foam of 5-mm thickness is used to improve the light collection. As a result, ~ 50 photoelectrons per neutron capture are collected. The efficiency for thermal neutron detection in our scintillator was found experimentally by neutron absorption in the scintillator layer to be about 20%. The peculiar characteristics of the EN-detector output, that are weak and fast signals from charged particles compared to high amplitude, slow and delayed signals from thermal neutron capture, make it well suitable for its use in the framework of EAS experiments.

The EN-detector is sensitive to charged particles as well as to thermal neutrons. However, because of existence of several time components in this scintillator, the light output is different for different types of particles. This characteristic makes possible to select neutron signals from those generated by charged particles (or gamma rays) exploiting their different amplitude and pulse shape. Due to the thin layer of the scintillator, charged particles deposit on average only 50 keV against 2.3 - 2.7 MeV deposited

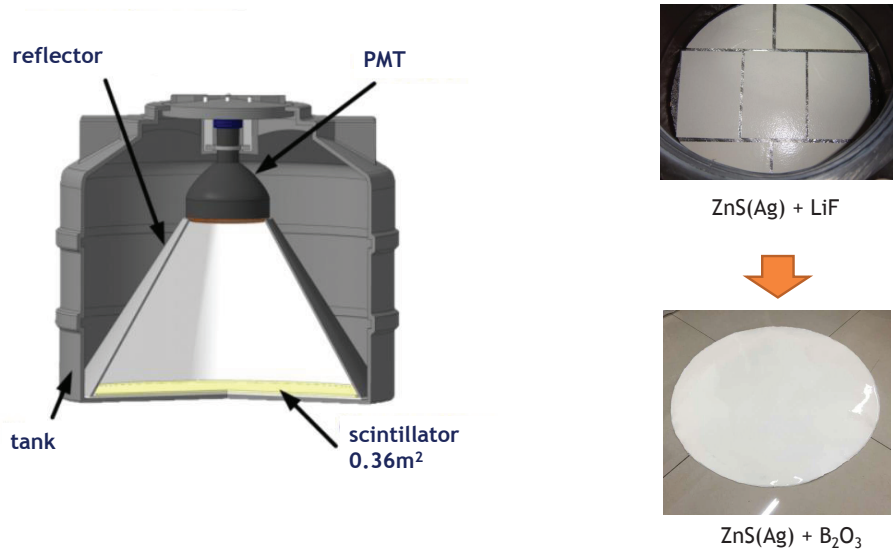


Figure 77: Left: Scheme of the EN-detector. Right top: Photo of the ZnS(Ag)+LiF scintillator used in PRISMA-YBJ. Right bottom: Photo of the ZnS(Ag)+B₂O₃ scintillator used in LHAASO-ENDA.

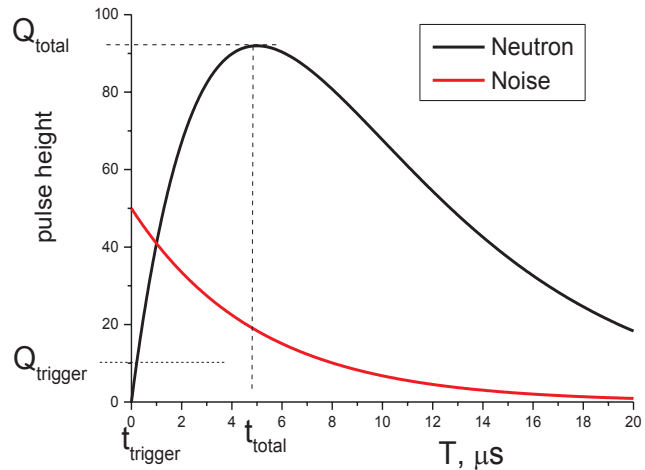


Figure 78: Left: pulse shape of noise and neutron. Right: Separation between noise and neutron in the coordinate system of Q_{trigger} vs Q_{total} .

during the neutron capture. A very high α/e ratio, that is the ratio of the light produced by α particles to the light produced by electrons of the same energy, is the main detector feature. This feature allows to collect enough light using only one PMT viewing 0.35 m^2 scintillator layer. The different pulse shape of the neutron signal with respect to the signal produced by charged particles can be fruitfully exploited to remove this background. Indeed, slowly moving heavy particles (such as α) excite slow components in addition to the emission of fast signals. The charge collection time of a signal due to a neutron capture is $10\text{--}20\text{ }\mu\text{s}$, while the characteristic time of the fast emission induced by charged particles is about 40 ns. We compare in Fig. 78 the pulse shape of the neutron signal with the signal induced by electrons. The remarkable difference in shape allows an efficient use of pulse-shape discrimination to select and record neutron signals in measurements of a neutron flux. Note that all signals are digitized with a FADC whose resolution is equal to 1 V / 1024 ch = 1 mV/ch .

The peculiar characteristics of the EN-detector output, that are weak and fast signals from charged particles compared to high amplitude, slow and delayed signals from thermal neutron capture, make it well suitable for its use in the framework of EAS experiments. In high energy EAS the time thickness

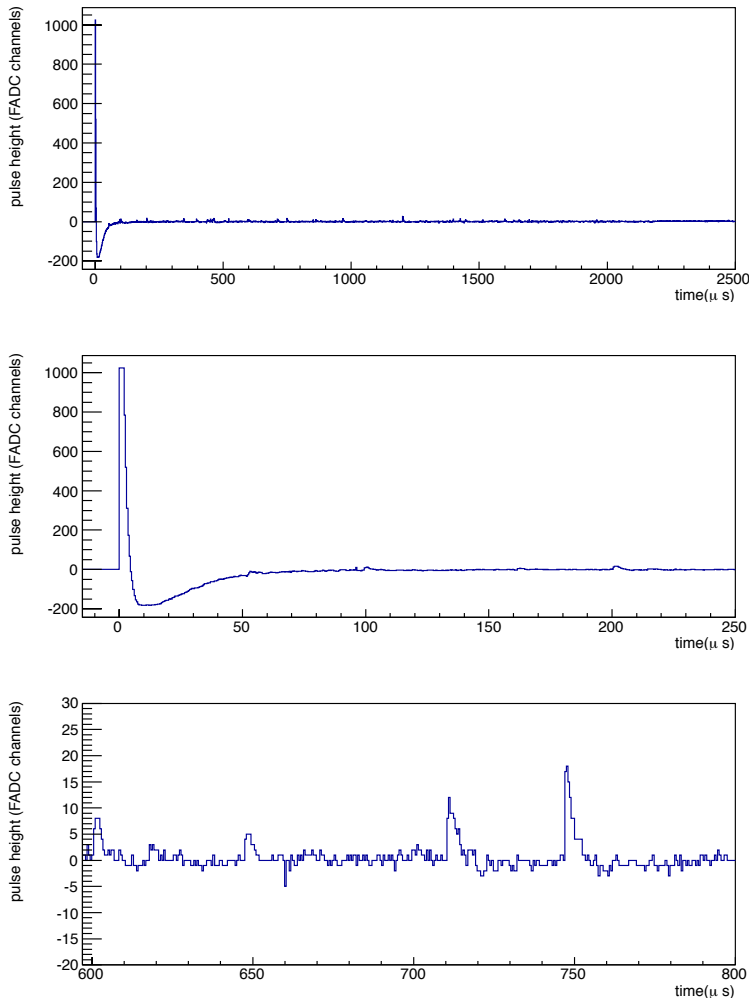


Figure 79: The shape of the signals from the neutron detectors at PRISMA-YBJ. Upper plot: the pulse from 0 to 2.5 ms. The large peak in the first bin is generated by the EAS electrons. Middle plot: the pulse from 0 to 0.25 ms. Lower plot: the pulse from 0.6 to 0.8 ms (note the different scale on the vertical axis). The small peaks following the first peak are generated by thermal neutrons.

of the shower front is about tens of ns, depending on the distance from the core. The individual signals generated by these particles (mainly electrons and positrons) add up to give a signal proportional to their number which can be used also for triggering and timing purposes. Delayed signals from thermal neutron capture follow on a time scale of a few milliseconds. As an example, we show in Fig. 79 the pulses recorded in a high energy EAS event. The first big peak is generated by the large amount of charged particles of the shower front while the smaller delayed signals are generated by thermal neutrons. Thus, the amplitude of the fast signal can be used to measure the charged particle density while the delayed signals measured in a time gate of 10 ms give the number of captured thermal neutrons. The selection of electrons and neutrons is automatically performed by the off-line analysis program.

5.5.3. Progress of ENDA

One prototype array of 32 EN-detectors (PRISMA-32) is now running in Moscow [417][418]. In order to check the performance of this detector at a high altitude site, a small array composed of four EN-detectors (PRISMA-YBJ) has been installed inside the hall hosting the ARGO-YBJ experiment at the Yangbajing Cosmic Ray Observatory (Tibet, China, 4300 m a.s.l. , 606 g/cm²). The two arrays operated together, and coincident events have been analyzed to gather information on the PRISMA-YBJ

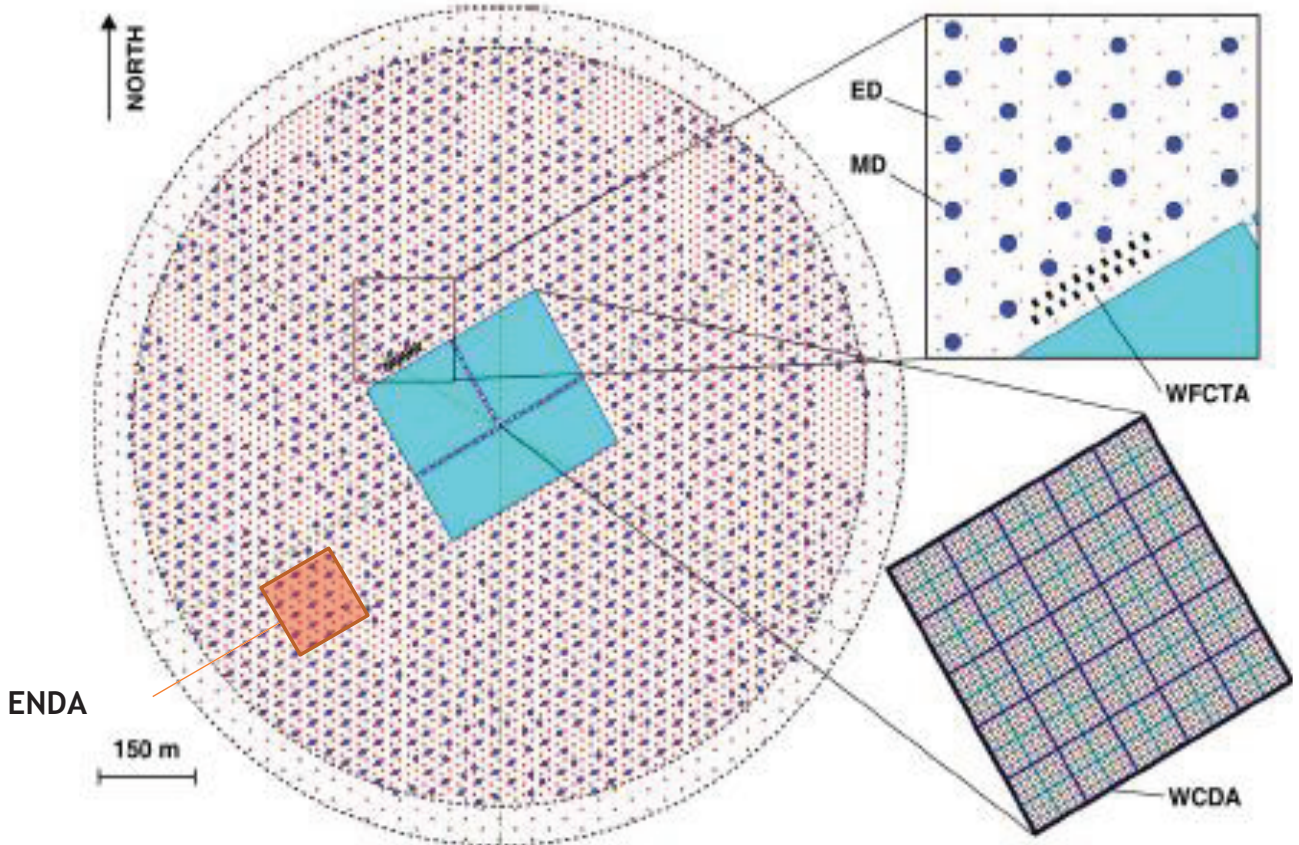


Figure 80: Location of ENDA inside LHAASO.

performance [419]. After more than 3 years running, PRISMA-YBJ was moved to Tibet University to focus on observation of solar activity and earthquakes. In order to check the performance of the new type EN-detectors at a high altitude site, we built an array of 16 ZnS(Ag) with B_2O_3 EN-detectors (LHAASO-ENDA-16) at Tibet University (TU) in Lhasa, Tibet, China (3700 m a.s.l.) In February 2017, and then moved to YBJ at the end of 2018 [420]. Up to now, ENDA has totally 66 detectors (ENDA-64 and the other two as backup), ready for deploying inside LHAASO to make a hybrid detection of cosmic ray spectrum from 100TeV to 2PeV (Fig. 81 left). After achieving good results, ENDA will be extended to 400 detectors with array area of 10000 m^2 (Fig. 81 right), together with LHAASO, to measure energy spectrum at the knee region of iron.

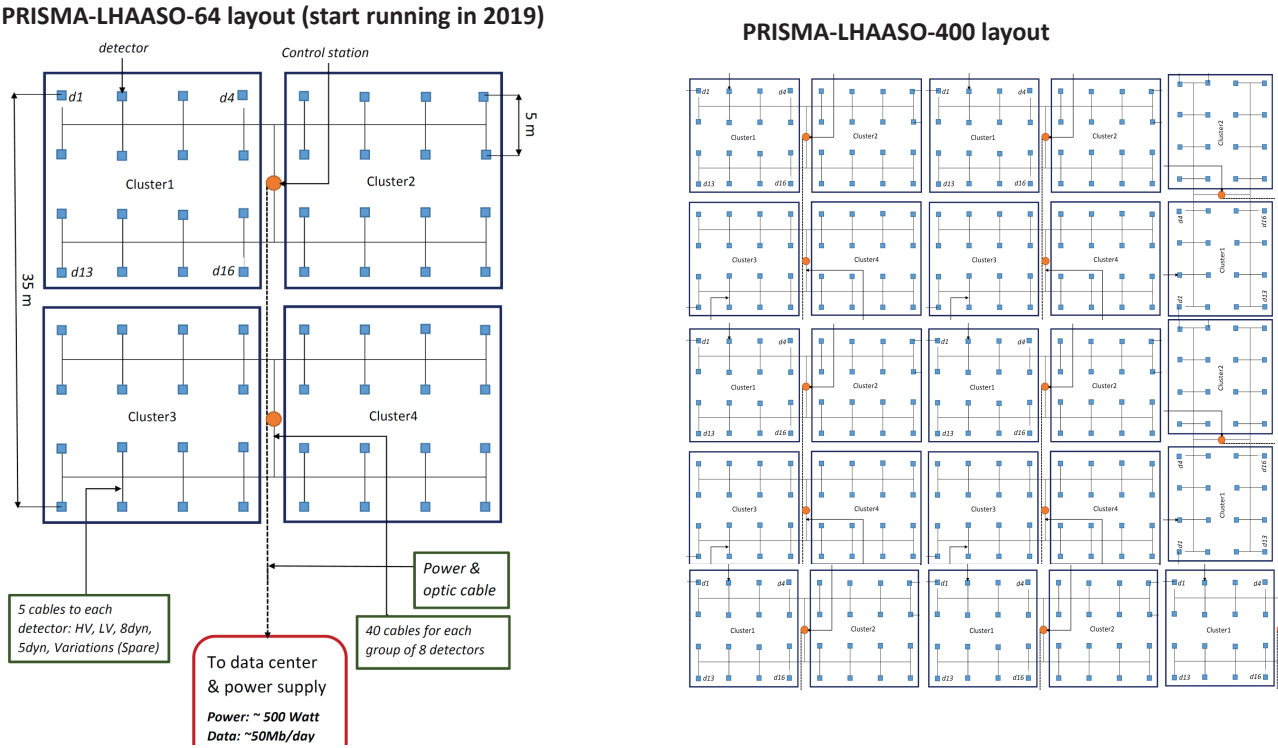


Figure 81: configuration of ENDA-64 (left) and ENDA-400 (right).

5.6. Prospective for radio-detection of air showers at the LHAASO site

5.6.1. Introduction

Here we discuss the opportunity to perform radio-detection of extensive air showers (EAS) in combination with LHAASO measurements. In section 5.6.2 we present a brief status of EAS radio-detection. We then study in section 5.6.3 the possible benefit of radio measurements for LHAASO and finally (section 5.6.4) evaluate how the LHAASO detector could be instrumental in the perspective of the foreseen Giant Radio Array for Neutrino Detection [421].

5.6.2. Status of Extensive Air Shower detection

Creation and acceleration of charges during the development of EAS induced by high energy cosmic rays naturally generates electromagnetic radiations. The dominant effect is the so-called *geomagnetic* effect [422],

corresponding to the drift in opposite directions of positive and negative charges from the shower because of the Lorentz force associated with the Earth magnetic field \mathbf{B}_{geo} . The resulting charge current produces brief flashes (≤ 50 ns) of coherent radio emission in the ~ 10 -200 MHz frequency range, linearly polarized along the $\mathbf{B}_{geo} \times \mathbf{v}$ direction.

Radio emission by EAS was experimentally observed as soon as 1966[423], but it was not before the new millennium that extensive experimental efforts were carried out in order to establish the radio technique as a valid tool for the study of high energy cosmic rays.

- CODALEMA and LOPES were the two pioneering experiments in the early 2000, with radio arrays composed of few tens antennas deployed over areas $\leq 1\text{km}^2$, and triggers provided by ground arrays (the KASKADE-GRANDE experiment in the case of LOPES).
- LOFAR is a radio telescope deployed over several countries in Europe. Among other science goals, LOFAR aims at detecting cosmic rays with the central part of the telescope, composed of ~ 2400 antennas clustered on an area of $\sim 10\text{ km}^2$. This high density of antennas makes LOFAR the perfect tool to study features of the radio emission created by extensive air showers. Air-shower measurements are

conducted based on a trigger received from an array of scintillators (LORA). LOFAR comprises two types of antennas, recording radio emission in low-frequency band from 10 to 90 MHz and also in the high-frequency band (110-190MHz) [424].

- The members of these three collaborations

later joined efforts with others to develop the Auger Engineering Radio Array (AERA), with the explicit goal to test if radio-antenna arrays could eventually replace the standard technics (ground arrays or fluorescence detectors) for future UHECRs detectors. This was motivated by the fact that radio antennas were suspected to be cheaper, easily deployable and would require minimal maintenance and would thus be potentially well suited to the giant detector surfaces required for the detection of UHECRs. AERA is an array of 150 radio antennas working in the 30-80 MHz frequency range and deployed over $\sim 17 \text{ km}^2$ with array step-size between 150 and 350 m. AERA is located in a region with a higher density of water cherenkov detectors (on a 750 m grid) and within the field of view of the HEAT fluorescence telescope, allowing for the calibration of the radio signal using super-hybrid air-shower measurements, i.e., recording simultaneously the fluorescence light, the particles at the ground and the radio emission from extensive air showers [424].

- Tunka-Rex is the radio extension of the Tunka observatory for cosmic-ray air showers. Its main detector, Tunka-133, is an array of non-imaging photomultipliers detecting the Cherenkov light emitted by the air-showers in the atmosphere in the energy range of 10^{16} to 10^{18} eV. Tunka-Rex is composed of 25 antennas deployed over 1 km^2 [50].
- TREND[425] (Tianshan Radio Experiment for Neutrino Detection) is a setup composed of 50 self-triggered antennas running in the 30-100MHz frequency range deployed over 1.5 km^2 on the site of the 21 CMA radio-interferometer in the Tianshan mountains, Xinjiang Autonomous Province, China. Compared to the above-mentioned projects, all triggered by other types of detectors, TREND specifically focuses on autonomous detection and identification of EAS with radio signals only.

A decade of efforts by these various experiments brought some significant results :

- As the geomagnetic effect is the dominant contribution to the radio signal of air showers, its strength strongly depends on its direction of origin, and more precisely on the geomagnetic angle (\mathbf{v} , \mathbf{B}_{geo}). For air showers developing in a direction perpendicular to the geomagnetic field, energies down to few 10^{16} eV could be detected by dense arrays like CODALEMA or LOFAR [426]. An efficiency larger than 80% is reached by CODALEMA for energies above 10^{17} eV [427]. Detection at low energies is limited by the sky background noise, due in particular to Galactic emission, which significantly affects the signal-to-noise ratio. It should be noted however that, to our knowledge, no specific signal treatment was ever applied to identify low amplitude radio pulses in the data. As both noise (from measurements) and air-shower induced radio waveforms (from simulations) can be determined, a dedicated filtering treatment might allow to dig out EAS-induced radio signals from noise for primary energies down to 10^{16} eV.
- LOPES, LOFAR and AERA were able, thanks to their $\sim \text{ns}$ timing resolution, to reconstruct the direction of origin of the incoming cosmic particle from the radio data with a precision of a fraction of a degree typically [428], using a conical parametrization of the shower front [429].
- As the strength of the electromagnetic field is directly related to the number of particles in the shower (coherent radio emission), it is possible to estimate the energy of the primary cosmic particle from the radio signal in a rather straightforward way. A 17% precision was achieved by AERA [49] and 20% by Tunka [50] (see Fig. 82).
- The radio signal pattern at ground depends on the longitudinal development of the shower, and in particular on the position of its maximum of development X_{max} , as can be seen from Fig. 83. It is therefore possible in principle to perform a measurement of X_{max} and hence determine the nature of the primary from the radio data. Various technics were used: LOPES used the information on the shape of the radio waveform (with a smaller curvature radius for showers developing deeper in the atmosphere) to achieve

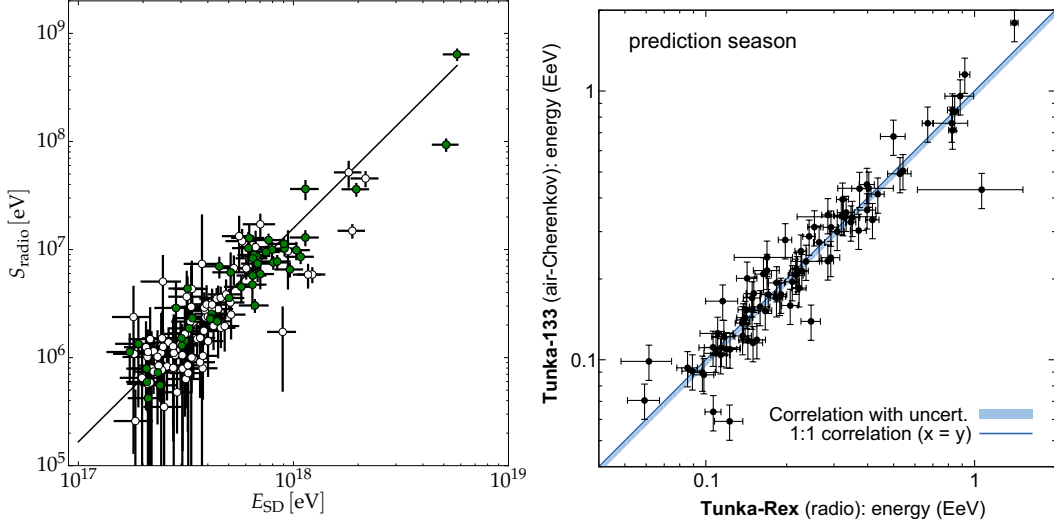


Figure 82: Left: radio-energy estimator S_{radio} as a function of the cosmic-ray energy measured with the Auger surface detector. Green filled circles denote air showers with at least five stations with signal. Open circles denote events with less than five stations with signal and use the surface detector core position. A 17% energy resolution could be achieved for events with 5+ stations triggered. Taken from [49]. Right: correlation of the shower energy reconstructed with Tunka-Rex radio and Tunka-133 air-Cherenkov measurement. Taken from [50].

a 140 g/cm² resolution on X_{max} , while simulation indicate that precisions as good as 30 g/cm² may be achieved for denser and/or more extended arrays deployed in quieter radio environment [428].

Tunka-Rex estimated X_{max} with a \sim 40 g/cm² accuracy by measuring the slope of the lateral intensity profile of radio footprint at ground (steeper for showers developing deeper in the atmosphere) [50]. LOFAR took advantage of its high-density array to reach a 17 g/cm² using a similar technique [51]. AERA developed very recently a method based on the measured frequency spectrum (flatter for showers developing higher in the atmosphere), allowing in principle to measure X_{max} from a single antenna only, and reaching a \sim 20 g/cm² resolution for a subset of AERA events [430].

- The TREND experiment focused on the detection and identification of air showers based on their radio signals only. To achieve this result, TREND developed a DAQ system allowing for a \sim 200Hz trigger rate for each antenna and performed an offline identification of air shower signals based on their specific characteristics, following an algorithm detailed in [431]. TREND could select 465 EAS candidates for 317 live days of data. According to simulations, the distribution of the direction of arrival of these events follows rather well that expected for EAS with energies of 10^{17} eV for zenith angles $\theta \leq 70^\circ$ (see Fig. 84). This result, still to be refined, indicates that it is possible to trigger and identify EAS with a self triggered radio array, with a limited contamination by background events. However TREND detection efficiency was estimated to be around 10% only because of the background rejection cuts applied. Other EAS selection procedures may have to be found to improve the EAS detection efficiency.

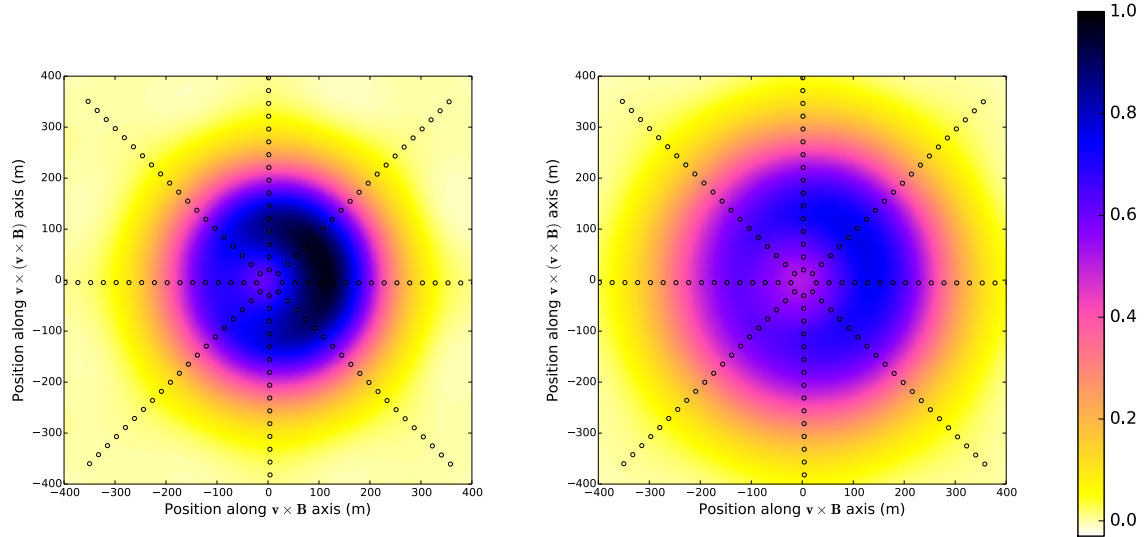


Figure 83: Radio profiles in arbitrary units for a proton shower with $X_{max} = 794 \text{ g/cm}^2$ (left panel) and an iron shower with $X_{max} = 573 \text{ g/cm}^2$ (right panel). Both showers have an energy of $2.3 \cdot 10^{17} \text{ eV}$ and a zenith angle of 49 degrees. Taken from [51].

The experimental developments above detailed allowed a better understanding of EAS radio emission, thus feeding the various simulation codes [432, 433, 434] developed and refined in that period of time, which now fit very well the experimental data. These codes in turn constitute a very valuable tool to further develop the air-shower radio detection technique.

If nice results were achieved by EAS radio detection, some limitations were reached as well. We may stress in particular the fact that the radio emission is very much beamed around the shower axis, with an abrupt exponential drop when moving away from the shower core (signal typically divided by 10 between 100 and 200 m from the shower core for a vertical shower). This feature does not significantly depend on the energy, which implies that arrays of very high density (detector spacing $\sim 50 \text{ m}$) would be necessary to perform EAS radio-detection and reconstruction. This is not realistic for UHECRs detection, which requires huge detection areas. This statement however has to be mitigated by the observation that the EAS radio footprint at ground is much larger for inclined showers [435], as the zone of main electromagnetic emission (mostly around X_{max}) is in that case much more distant from ground, and also because the projection of the radio emission cone on a flat ground is, by construction, more elongated for inclined trajectories. Giant radio arrays might therefore be able to perform a competitive study of UHECRs by selected inclined trajectories. This is presently being studied in the framework of the GRAND project [421].

Another major issue for EAS radio-detection is the high rate of background events. Even in remote areas like the TREND site, background radio sources (trains, planes, cars, but even more frequently HV lines and electric transformers) generate event rates that surpass the EAS flux by orders of magnitudes [431]. The DAQ system of a radio array has to take into account this constraint in order to perform autonomous triggering successfully. GRANDproto should allow to determine the EAS detection efficiency and background rejection potential achievable for an autonomous radio array. GRANDproto [436] is an hybrid setup composed of 35 radio-antennas with a DAQ guaranteeing a 0% dead time for an individual antenna trigger rate up to 5 kHz, running in parallel to a cosmic ray detection array of 21 scintillators. EAS radio-candidates will be selected based on the events polarization information measured by the triggered antennas, while the scintillator array will be used as a cross-check to the EAS nature of the se-

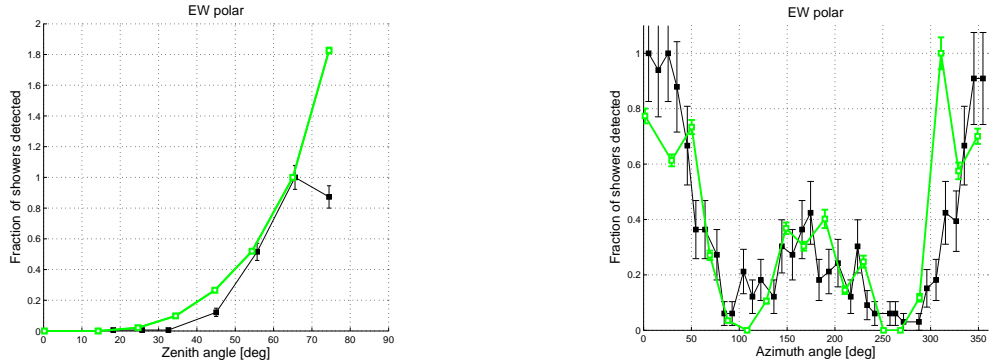


Figure 84: Distribution of reconstructed zenith (left) and azimuth angles for the 465 EAS radio candidates selected in the 317 live days of TREND data (black squares). Also shown are the expected distributions for air showers initiated by protons with $E = 10^{17} \text{ eV}$ (green empty squares).

lected radio candidates, thus allowing a quantitative determination of the background rejection potential of the array. GRANDproto will be fully deployed in summer 2016.

5.6.3. Benefit of radio-measurements for LHAASO

Here we only give some hints on the potential added value of EAS radio measurements for LHAASO, in the light of the status presented in section 5.6.2. We should stress however that a rigorous response to this issue would require a dedicated study based on detailed simulations taking into account the specificities of LHAASO (altitude, magnetic field at the detector location, electromagnetic background, ...) in order to determine what goals and performances would be actually achievable.

In the light of LOPES, Tunka or AERA results for example, it seems realistic to think that a radio array deployed at the LHAASO location could provide an independent measurement of cosmic ray parameters (energy and X_{max} in particular) with good precision, provided the electromagnetic background level is low enough at the LHAASO site, and that other detectors (PMTs in particular) are well shielded. There is no reason to think that performances similar to present arrays (energy resolution of 15-20%, X_{max} resolution in the range of 20 to 40 g/cm²) should not be achievable. An external trigger could be provided by LHAASO detectors to circumvent the challenges of radio autonomous trigger mentioned in the previous section. We shall stress however that the threshold for radio is presently $\sim 10^{17}$ eV for the energy measurement, and even higher for X_{max} . It is possible that a very dense array (~ 50 m detector spacing), and a dedicated signal treatment to improve signal-to-noise ratio could lower this threshold, but this is hard to assess *a priori*. We suggest that a radio array may be interesting as a complement to the high energy end of the KM2A array measurements (X_{max}), or as a complement to WFCTA in order to better constrain the shower geometry through the measurement of the shower core position.

5.6.4. LHAASO and GRAND

GRAND [421] is a proposal to build a giant radio array (total area of 200000 km²) primarily aiming at detecting cosmic neutrinos. The project is still at a very early stage, and many issues have to be studied and solved before the project comes to reality. Preliminary sensitivity studies are however extremely promising, with an expected sensitivity guaranteeing -even for the weakest expected fluxes [437]- the detection of the so-called *cosmogenic neutrinos* produced by the interaction of UHECRs with CMB photons during their cosmic journey [438].

Among the many steps to be completed before GRAND comes to life, an important one will consist in deploying a \sim 1000km² engineering array (GRAND-EA) composed of \sim 1000 antennas in order to validate the technological choices defined for GRAND. This array will obviously be too small to perform a neutrino search, but cosmic rays should be detected above 10^{18} eV. Their reconstructed properties (energy spectrum, directions of arrival, nature of the primaries) will enable us to validate this stage, if found to be compatible with the expectations. Even if the two detectors areas differ a lot, it may be interesting to consider in more details a deployment of GRAND-EA around the LHAASO experimental site. An independent detection by the 2 setups of a statistically significant number of cosmic ray events would indeed be very valuable for the evaluation of GRAND-EA performances. Given the present status of the GRAND proposal, GRAND-EA could not be deployed before 3 or 4 years.

FUNDAMENTAL PHYSICS, HELIOSPHERE PHYSICS AND INTERDISCIPLINARY RESEARCHES WITH LHAASO

6. Fundamental Physics, Heliosphere Physics and Interdisciplinary Researches with LHAASO

6.1. High Energy Emissions of Gamma-Ray Bursts and Constraints on Lorentz Invariance Violation

Executive summary: In this paper we present the current understandings of high-energy emissions from gamma-ray bursts (GRBs), including observation facts and basic theories. We also discuss the applications of GRB high-energy photons observed by LHAASO's WCDA detector to constrain models of GRB high-energy emissions, extragalactic background light, as well as Lorentz invariance violations. With huge detector area, LHAASO may bring forth notable advancements to such areas.

6.1.1. Introduction

Gamma-ray bursts (GRBs for short) are among the most violent explosions in the Universe. Observationally, they show a sudden increase of gamma-ray flux in short time scale (0.01-1000 s). A typical GRB has non-thermal spectrum as well as multi-peak light curves. The GRBs with durations longer than 2s are classified as long bursts [439], and are from deaths of massive stars. While GRBs shorter than 2 s are called short bursts, and are the results of mergers of two compact stars ([440],[441]). Both types of GRBs can give birth to black holes or fast-spinning magnetars.

GRBs provide us a unique opportunity to study the astrophysical relativistic jets. Especially, the high energy emissions from GRBs are of great interest for this purpose, since they are the product of the most extreme physics. By studying GRB high energy emissions we can get insights on the inner works of stellar explosions, as well as high-energy radiation mechanisms. And we can also use high-energy photons from GRBs to probe several key problems in astrophysics and physics, including extragalactic background light, as well as Lorentz invariance violation.

6.1.2. High Energy Emission of Gamma-ray Bursts

The high-energy (> 10 MeV or higher) emission of GRBs were first discovered by Solar Maximum Mission (SMM) satellite in 1985 [442]. Later the EGRET instrument aboard Compton Gamma-Ray Observatory (CGRO) confirmed the existence of GRB high-energy emissions, and detected photons with energies as high as 18 GeV [443]. Since the launch and commissioning of Fermi Gamma-ray Space Telescope (FGST) in 2008, dozens of GRBs with high-energy emissions were discovered with Large Area Telescope (LAT) onboard.

Generally speaking, high energy photons from GRBs are delayed compared with low energy photons [13, 144]. Usually the first LAT peak coincides with the second Gamma-ray Burst Monitor (GBM, low-energy) peak in Fermi light curves (See Figure 1). And high energy emissions usually can last longer (> 1000 s, [13, 144].), with GRB 130427A as the longest (~ 1 day, see ref. [444]). And the spectra of GRBs with high energy emissions can be fitted with three components (See Figure 2), including the blackbody spectrum, the non-thermal Band spectrum of broken power-law, and an extra power-law with possible high-energy cut-off [52]. The latter two can extend to GeV band or higher.

Many theoretical models have been proposed to explain the origin of GRB high energy emissions, including up-scattered cocoon emission [445], electron-positron pair loading [446], hadronic mechanisms [447, 448], as well as afterglow emissions produced by external shocks [315, 449, 450, 451, 452, 453]. All of these models have different predictions on GRB multiband behaviors, and their own advantages and disadvantages. And more high-precision observations are needed to distinguish between them.

With GRB high-energy light-curves and spectra at hand, many crucial parameters of GRBs can be determined. A notable example is the determination of the magnetization parameter of GRB 080916C's ejecta [454]. Since no extra components can be found besides Band spectrum, the photosphere emission of this burst should be oppressed. This can lead to a high magnetization parameter, since in this situation the radiation is though to be dominated by Poynting-flux. Also, any possible high-energy cut-off,

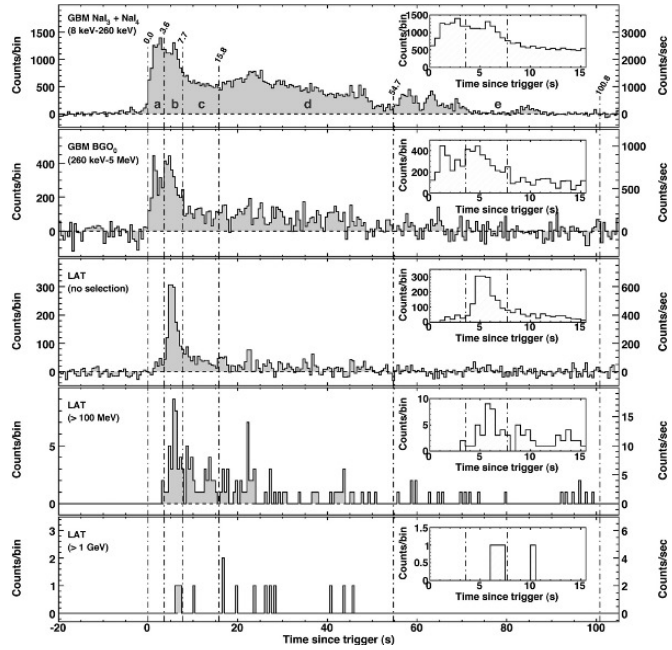


Figure 85: Multiband light curves of GRB 080916C. It can be seen that the light curve in LAT (high-energy) band has a 5 s delay compared with GBM (low-energy) band. The first LAT peak coincides with the second GBM peak. Adopted from Ref. Abdo et al. (2009a).

detected or not, can be used to put limits on the Lorentz factor of GRB outflow [455, 456]. Through this method many high-energy bursts have get the speed of ejecta determined.

However, more high quality multi-band light-curves and spectra are required in order to shed more light on GRB high energy emissions. Fermi/LAT has an effective area of only $9,500 \text{ cm}^2$ (see ref. [457]), which is quite limited for this purpose. Currently it is very difficult to get full light-curves in high energy band. As shown in Figure 1, usually we can only detect very few photons above 10 GeV, which is often insufficient for our studies.

6.1.3. Detecting GRB High Energy Photons with LHAASO

LHAASO is a proposed multi-function detector array, with the ability to detect Cherenkov light from very high energy gamma-ray photons entering Earth's atmosphere. Two LHAASO detectors can be used to make gamma-ray observations. Kilo-Meter Square Array (KM2A) can detect photons with energy higher than 30 TeV. It should be noted that although 100 GeV to $>$ TeV photons from GRBs should be absorbed in the central engine, $>$ PeV photons can have a smaller pair opacity in the emission region, thus get escaped [458]. However, the detection of extragalactic TeV or PeV sources is quite limited, since extragalactic background light (EBL) can strongly absorb very high energy photons via photon-photon reaction $\gamma + \gamma \rightarrow e^- + e^+$ (e.g., see ref. [317]). Only TeV photons within ~ 100 Mpc have optical depth smaller than 1 and can reach Earth, depending on EBL models. The mean free path of a PeV photon is even smaller. Since a typical GRB has a redshift of ~ 2.5 (see ref. [459] and references therein), it is not quite possible to detect many $>$ TeV photons from one GRB with KM2A. Besides, at such high energies, whether GRBs can produce enough photons for detection is quite doubted, since simple extension of GeV spectra gives little flux in PeV range, while synchrotron radiation has a nature upper limit of $\sim 60 \text{ MeV} \times \Gamma$, where Γ is the bulk Lorentz factor, and Klein-Nishina effect may strongly suppress the synchrotron self Compton and external inverse Compton emissions. Of course, KM2A has the possibility to detect some ultra-high energy photons from nearby GRBs with a large bulk Lorentz factor and a high luminosity, and such detections may provide crucial clues and constraints to GRB high-energy emissions.

However, the Water Cherenkov Detector Array (WCDA), which can detect photons with energies

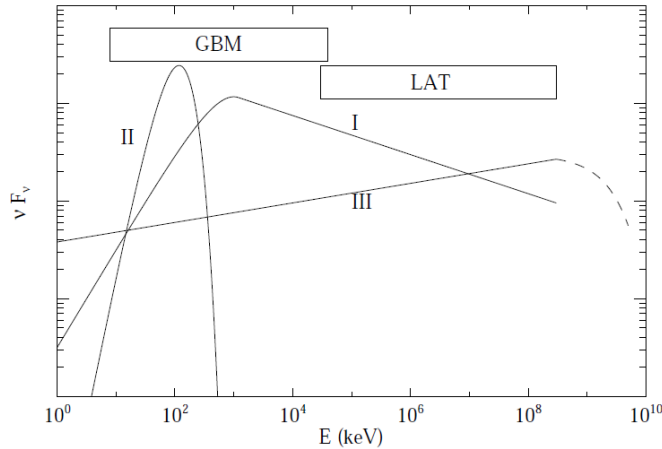


Figure 86: A schematic figure of three spectral components of Fermi GRBs: (I) A Band-type broken power-law component with non-thermal origins; (II) a quasi-blackbody component that is likely from GRB photosphere; and (III) an extra power-law with a possible high-energy cut-off. Adopted from Ref. [52].

higher than ~ 100 GeV, can be more useful for high energy gamma-ray bursts. With an effective area of $9 \times 10^4 \text{ m}^2 \sim 0.1 \text{ km}^2$, that is nearly 10^5 times larger than Fermi/LAT, LHAASO can reach a much higher sensitivity at > 100 GeV band. Currently we have already detected ~ 100 GeV photons from GRBs [444], and such photons are within the reach of LHAASO/WCDA. Assuming GRBs have power-law spectra $dN(E)/dN \propto E^{-\beta}$ with a photon index $\beta \sim 2.3$ at this energy range, we can detect $N(>E) = \int_E^\infty dN(E)/dE \times dE$ photons per unit detector area. From this we can calculate the ratio between photons with energies higher than 100 GeV and the ones with energies higher than 1 GeV:

$$\frac{N_{>100\text{GeV}}}{N_{>1\text{GeV}}} = 100^{1-\beta}$$

Assuming Fermi's LAT can detect ~ 10 photons with energies higher than 1 GeV for one high-energy burst, $10 \times 100^{1-\beta} \approx 10^{-1.6}$ photons with energies higher than 100 GeV should be detected by LAT. Thus the number of > 100 GeV photons detected by LHAASO/WCDA should be $10^5 \times 10 \times 100^{1-\beta} \sim 6 \times 10^3$. Also It should be noted that $\beta \sim 2.3$ is a quite conservative estimate. Many GRBs have high-energy turnoffs overlaying on Band spectrum, and the high-energy spectral indices are often shallower/harder than 2.3. In this case, more high-energy photons can be detected by WCDA. With so many high-energy photons detected by LHAASO/WCDA, high-energy light-curves with high resolution can be constructed, and our understandings of the most extreme process in GRBs should be largely increased. Of course, to estimate the exact detection rate of LHAASO/WCDA, detailed simulations are need. However, although such estimate is only an approximation and very rough, and a large portion of > 100 GeV photons may get absorbed by EBL as well as GRB central engines, the potential of WCDA in GRB high-energy observations is quite promising.

6.1.4. GRB High-Energy Emission Models and Diversities

High-energy emission is the key to understand the inner works of gamma-ray bursts. Such photons are the results of the most extreme processes in burst central engines and outflows. As noted in Section 2, many models have been developed to take account of these extreme radiations. Different models give different predictions of high-energy behaviors of GRBs. For example, up-scattered cocoon emission model [445] predict a double-component radiation spectrum, as well as an early inverse-Compton-scattering-induced low-energy pulse. Electron-positron pair loading model [446] can give rise to bright emissions above 100 GeV originated from inverse-Compton scattering, along with an intense optical flash occurring with GeV peak emission. While external shock model (e.g. [315]) consider GRB high-energy emission as synchrotron origin, and is hard to produce > 100 GeV photons. For the hadronic

models, synchrotron radiation from ultra-high energy protons can give rise to a spectral component starting at much higher energy and later sweeping into the Fermi LAT band [448]. Although photon-pion production model [447] predicts similar high-energy behaviors as leptonic models, it can almost be ruled out by the non-detection of GRB neutrinos by IceCube detector [460], since this model should produce a much higher GRB neutrino flux.

With a large detector area, which means high GRB detection rate and detailed high-energy light curves of GRBs, LHAASO/WCDA can help us to distinguish these models. Currently Fermi/LAT can only detect very few $>$ GeV photons, and is very difficult to show a complete multi-band GRB light-curve, hence leaves a lot of room of theoretical speculations. With high-quality high-energy light-curves provided by WCDA, combining with optical, X-ray and soft gamma-ray observations provided by other instruments, it is possible to pin down GRB high-energy emission models, and many key processes, such as radiation mechanisms and particle accelerations can be determined. Also, with \sim 100 GeV observations, several important parameters, including bulk Lorentz factor and magnetization parameter in GRB central engines can be deduced.

Besides, due to a much higher sensitivity and detector area, LHAASO/WCDA has the possibility to detect more high-energy photons from one gamma-ray burst than Fermi/LAT, making it possible to classify GRBs according to their high-energy behaviors. LHAASO/WCDA may observe high-energy emission from a variety of GRBs, including long and short bursts, X-ray rich bursts and X-ray Flashes, GRBs with low and high luminosities, ultra-long GRBs, supernova-associated GRBS, as well as some other related phenomena, e.g., soft gamma repeaters. Thus a clearer relation between GRB high- and low-energy emissions can be established, and this can shed light to intrinsic GRB mechanisms.

6.1.5. Constraining Extragalactic Background Light

Extragalactic Background Light, or EBL for short, is the second-strongest component of cosmic background light, only after the Cosmic Microwave Background (CMB). EBL covers the infrared to ultraviolet band, and are thought to be originated from star-forming process. Both stellar radiations and re-emission of star light by dust in star-forming regions contribute to the EBL. Also, active galactic nuclei, brown dwarfs, hot intergalactic gas, as well as radiative decay of primordial particles may also be minor contributors of the EBL (see ref. [287] and references therein). However, a direct measurement of EBL is very difficult to conduct, since the Milky Way poses a strong interference. Besides, an absolute sky brightness measurements should be measured to a carefully-calibrated zero flux level in order to get a reliable EBL reading, and this is technically challenging in practice. Thus usually indirect approaches of EBL measurement is preferred.

As noted in Section 3, high-energy photons can get absorbed by EBL via $\gamma + \gamma \rightarrow e^- + e^+$. The threshold of such a reaction is $E\epsilon(1+z)^2 x > 2(m_e c^2)^2$, where E and ϵ are energies of high- and low-energy photons, m_e the mass of electron, z the redshift of the high-energy radiation source, $x = 1 - \cos\theta$, θ the angle between directions of motion of these two photons. If the optical depth of such a reaction is larger than 1, the high-energy spectrum observed on Earth should show a distinct cut-off. Thus the spectrum of EBL can be inferred from the existence of high-energy cut-off in this case, providing the intrinsic spectrum of the high-energy source is already known. Without such a cut-off, the corresponding optical depth should be smaller than 1, and an upper limit of EBL flux can be obtained.

GRBs have much higher instant fluxes than TeV blazars, and they distribute in a wider redshift range. Besides, the intrinsic spectra of GRBs are quite simple, usually in the power-law form. Thus they are ideal tools for EBL studies. Using Fermi/LAT observations of GRBs as well as blazars, a stronger constraint on EBL models has already been proposed, and several models with larger optical depth prediction have been excluded (e.g., see ref. [13, 295, 457]). Even if the GRB spectrum shows an intrinsic cut-off, such constraint on EBL should only become more reliable. Since LHAASO/WCDA should detect more GRBs as well as other sources (e.g., blazars) with $>$ 100 GeV photons than Fermi/LAT, a more stringent constraint can be inferred from WCDA observations. Thus we can learn more on cosmic star forming history using high energy GRB observations provided LHAASO.

6.1.6. Constraining Lorentz Invariance Violation

Lorentz invariance is one of the fundamental principles of special relativity in modern physics. However, many Quantum Gravity (QG) models predict that the non-trivial space-time could lead to the violation of Lorentz invariance. Since it is typically expected for QG to manifest itself fully at the Planck scale, the QG energy scale is approximate to the Planck energy scale, i.e., $E_{\text{QG}} \approx E_{\text{Pl}} = \sqrt{\hbar c^5/G} \simeq 1.22 \times 10^{19} \text{ GeV}$ (e.g., see ref. [461], and references therein). Hence, the Planck energy scale being a natural one at which Lorentz invariance is expected to be broken.

As a result of the Lorentz invariance violation (LIV) effect, the speed of light could becomes energy-dependent in vacuum, instead of a constant speed of light (see ref. [462, 463]). In general, the modified dispersion relation of photons can be approximated by the leading term of the Taylor expansion as (see refs. [464, 465])

$$E^2 \simeq p^2 c^2 \left[1 - s_n \left(\frac{pc}{E_{\text{QG},n}} \right)^n \right], \quad (9)$$

which corresponds to the speed of propagation of photons

$$v = \frac{\partial E}{\partial p} \approx c \left[1 - s_n \frac{n+1}{2} \left(\frac{E}{E_{\text{QG},n}} \right)^n \right], \quad (10)$$

where the n -th order expansion of leading term corresponds to linear ($n = 1$) or quadratic ($n = 2$), E_{QG} is the QG energy scale, and $s_n = \pm 1$ denotes the sign of the LIV correction. For the case of $s_n = +1$ ($s_n = -1$), photons with higher energies travel slower (faster) than those with low energies. The speed of photons have an energy dependence, which means that two photons with different energies emitted simultaneously from the source will arrive at the observer with a time delay Δt , which depends on the distance of the source and the energies of these photons. For a cosmic source, the expansion of the Universe should be taken into account when calculating the traveling time of the photon and one obtains for the LIV induced time delay (see ref. [464, 465, 466])

$$\Delta t = s_n \frac{1+n}{2H_0} \frac{E_{\text{h}}^n - E_{\text{l}}^n}{E_{\text{QG},n}^n} \int_0^z \frac{(1+z')^n dz'}{\sqrt{\Omega_m(1+z')^3 + \Omega_\Lambda}}, \quad (11)$$

where E_{h} and E_{l} ($E_{\text{h}} > E_{\text{l}}$) are the photon energies. For most cases, the energy range considered spreads several orders of magnitude and one can approximate $(E_{\text{h}}^n - E_{\text{l}}^n) \approx E_{\text{h}}^n$. We adopt the cosmological parameters derived from the latest *Planck* data (Ade et al. 2014): $H_0 = 67.3 \text{ km s}^{-1} \text{ Mpc}^{-1}$, $\Omega_{\text{m}} = 0.315$, and $\Omega_\Lambda = 0.685$.

Because of the cosmological distances and high energetic photons, GRBs have been used as a powerful tool for probing the LIV effect (see ref. [462]). The current best limits on both the linear and quadratic term have been set by Fermi/LAT's observation of GRB090510 (see ref. [467]). The limits set are $E_{\text{QG},1} > 9.1 \times 10^{19} \text{ GeV}$ and $E_{\text{QG},2} > 1.3 \times 10^{11} \text{ GeV}$, but such severe constraints have no support from other long GRBs. Generally speaking, a long GRB observed by Fermi/LAT would have an observed time delay $\sim 10 \text{ s}$ (i.e., the time lag between the trigger time of the GRB detected by Fermi/GBM and the arrival time of the highest energy photon), a redshift of $z = 1$. The maximum observed photon energy is $\sim 50 \text{ GeV}$. In this case, it is possible for Fermi/LAT to set a limit of $2.5 \times 10^{18} \text{ GeV}$ for the linear term $E_{\text{QG},1}$ and $1.7 \times 10^{10} \text{ GeV}$ for the quadratic term $E_{\text{QG},2}$.

We use the sources studied by Fermi/LAT to construct reference scenarios for the LHAASO/WCDA and establish its potential to set limits on LIV. The scenario for setting limits on LIV from GRBs is motivated by the excellent detection performance of LHAASO/WCDA. Our reference scenario is a long burst with $\Delta t = 1 \text{ s}$ at a redshift of $z = 1$, with a maximum observed photon energy of $E_{\text{h}} = 500 \text{ GeV}$, within the detecting range of LHAASO/WCDA. Such a burst is certainly detectable by LHAASO/WCDA if it occurs in its field of view. The time delay assumed in this scenario is due to the fact that LHAASO/WCDA has the ability to detect hundreds to thousands of high energy photons

(> 100 GeV) from GRBs and high quality high-energy light-curves will be possible. The assumed redshift is clearly compatible with observed GRBs used to set limits on LIV (see ref. [29, 461]). In this scenario, it is possible for LHAASO/WCDA to set a limit of 2.5×10^{20} GeV for the linear term $E_{\text{QG},1}$ and 5.4×10^{11} GeV for the quadratic term $E_{\text{QG},2}$. Comparing these numbers with the limits by Fermi/LAT shows that LHAASO/WCDA can set much more competitive limits even with very basic analysis techniques.

6.2 Suggestions for Section on Solar-Heliospheric Science

6.2. Suggestions for Section on Solar-Heliospheric Science

Executive summary: The LHAASO team will also perform interesting studies, both for basic science and for applications, of solar and heliospheric effects on the cosmic ray flux. These are basically the effects of the solar wind and solar storms, and as such they are directly related to so-called “space weather” effects of the solar wind and solar storms on human activity. LHAASO will obtain unique information on the magnetic fields between the Sun and the Earth, which are moving toward Earth with the solar wind. Indeed, LHAASO will obtain information on the direction of the interplanetary magnetic field, which is a key determinant of whether a solar wind disturbance or solar storm will result in reconnection with Earth’s magnetic field and trigger a geomagnetic storm. Thus the real-time data from LHAASO will complement other information for space weather forecasting. In addition, LHAASO will be perform numerous other studies of solar, heliospheric, and geomagnetic effects on cosmic rays.

6.2.1. Types of data

Solar storms and the solar wind, as they propagate throughout the heliosphere, have a profound effect on cosmic rays at GeV-range energy, leading to a wide variety of signatures in cosmic ray flux variations with time. These have mostly been studied with detection thresholds up to 10 GeV or slightly higher. With its tremendous count rate at high altitude, LHAASO will obtain sufficient statistics to open the gateway to study many of these phenomena at even higher energy, thus performing new information on these processes. In addition, some phenomena, such as the sun shadow and moon shadow, are more profitably examined at TeV energies, where LHAASO will again provide improved statistical accuracy. In studies of time variations, improved statistics allow the possibility of studies at finer time resolution. As we shall describe, LHAASO can even provide useful real-time data for space weather forecasting.

LHAASO will generate two types of data of interest for solar-heliospheric studies: reconstructed shower rates (as a function of energy, direction, and time) and scalar rates (as a function of threshold energy and time).

One of the design goals of LHAASO is to reconstruct showers for gamma rays and cosmic rays down to tens of GeV in energy. Thus reconstructed showers with information on the arrival direction of primary cosmic rays will allow the study of the sun and moon shadows over a wider energy range, as well as loss-cone anisotropy to provide advance warning of the arrival of some interplanetary shocks, which can lead to various space weather effects. Directional shower data down to tens of GeV will allow a better determination of the diurnal anisotropy as well [468].

LHAASO will also produce scalar rates (also referred to as the single particle technique or SPT), in which the shower is not reconstructed but count rates are collected for various threshold numbers of “hits” in the detectors. The rate for each threshold has a different response as a function of the primary cosmic ray energy. This opens a possibility to obtain higher rates (and better time resolution) and information on lower energies below the shower threshold. (Note, however, that the LHAASO site has a cutoff rigidity of about 13 GeV for protons, so cosmic rays below this energy cannot be examined.) Examples of existing detectors that have examined scalar rates are ARGO-YBJ [309, 310, 469] and Auger [470]. To make proper use of scalar rates, we will need to correct for environmental factors. This will require careful monitoring of the weather, atmospheric conditions, and local temperature at each detector.

6.2.2. Sun shadow and advance warning of the interplanetary magnetic field for space weather forecasting

(1) Information from the sun shadow

The shadow of the Sun in TeV-range cosmic rays directly relates to solar-terrestrial relations, i.e., how solar phenomena affect the Earth and its immediate environment. The solar wind is a radial flow of plasma out from the Sun at supersonic speeds, which comes out at all times and in all directions (Figure 87). The solar wind drags out the complex coronal magnetic field to become

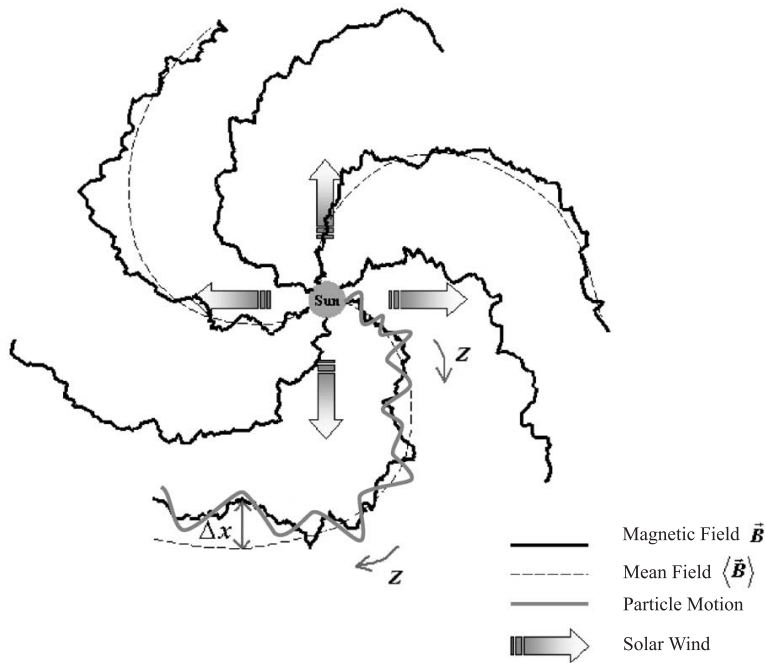


Figure 87: Illustration of the solar wind and interplanetary magnetic field. The solar wind is emitted radially from the Sun in all directions at all times. The spiral magnetic field lines connect plasma that originated from the same location on the rotating solar surface. Note that the turbulent magnetic field lines (solid lines) do not coincide with the mean magnetic field lines (dashed lines). The Earth might be located near the bottom of the figure.

the interplanetary magnetic field. However, both the solar wind plasma flow and the interplanetary magnetic field are highly turbulent, and magnetic fluctuation amplitudes are of the same order as the mean field. Roughly speaking, an interplanetary field line connects parcels of plasma that came from the same region of the solar corona, and because of the solar rotation, its shape is curved into an Archimedean spiral. The solar wind plasma and magnetic field usually take about 4 days to come from the Sun to the Earth.

The arrival direction distribution from shower reconstruction of TeV-range cosmic ray trajectories shows deficits corresponding to the locations of the Sun (and Moon) [471]. The solar, interplanetary, and terrestrial magnetic fields deflect the particle paths and shift the shadow of the Sun from its actual location, as first reported by the Tibet AS experiment [472]. In other words, the measured deflection of cosmic rays is a cumulative effect of magnetic fields along the whole path from the Sun to the Earth.

This experiment also observed the effect of the interplanetary magnetic field (IMF) [473] and a solar cycle variation [474], and evaluated the effects of two coronal magnetic field models [475]: the potential field source surface (PFSS) [476, 477] and current sheet source (CSSS) models [478, 479].

(2) Solar cycle variation of the sun shadow

Solar activity, including the likelihood of solar storms and space weather effects on human activity, is positively associated with the sunspot number, which varies with a cycle of roughly 11 years, known as the “sunspot cycle” or “solar cycle” (see Figure 88). The ARGO-YBJ collaboration also found that the deficit of cosmic ray flux in the sun shadow is reduced with increasing solar activity [480], as shown in Figure 89. To understand the shadow effect, it is useful to imagine trajectories of antiparticles traveling backward from Earth to intersect the Sun’s surface, which are equivalent to the forward trajectories that are blocked by the Sun, causing the shadow. One possible explanation of weaker Sun shadow with increasing solar activity is that if the solar coronal magnetic fields are very irregularly distributed, the cosmic ray deflections could be so randomized that backwards trajectories over a wider range of angles can intersect the Sun. Ref. [480] considers another

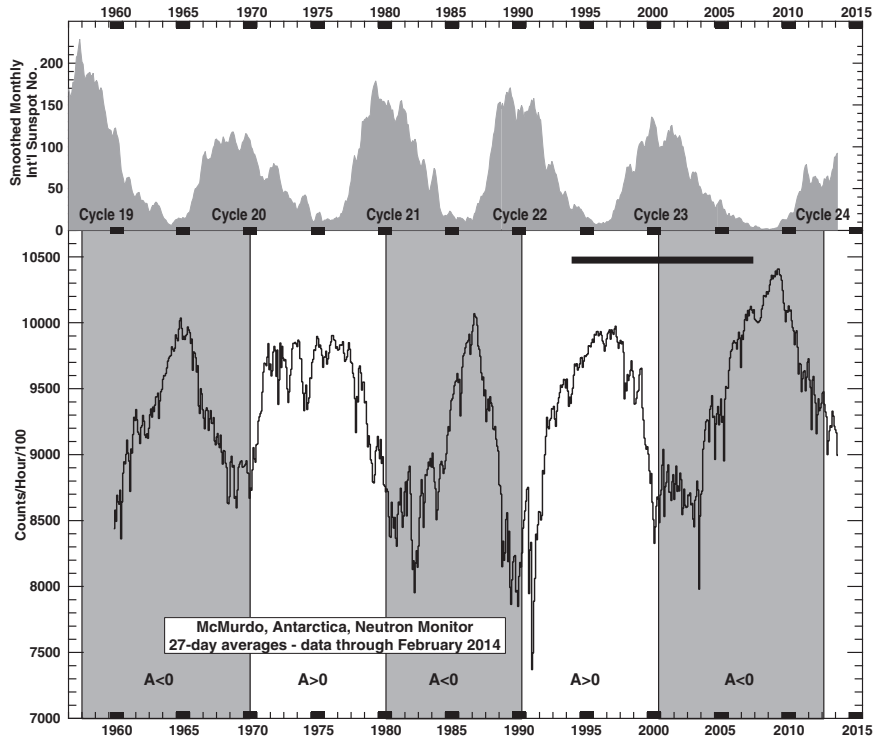


Figure 88: Smoothed monthly international sunspot number (using 5-month boxcar smoothing) and McMurdo neutron monitor count rate as a function of time. The long-term drift at McMurdo has been corrected following [53]. A neutron monitor count rate indicates the Galactic cosmic ray flux, which undergoes “solar modulation” in association with solar activity. Solar modulation includes dramatic 11-year variations with the sunspot cycle, and a 22-year variation with the solar magnetic cycle, seen here in changes in the solar modulation pattern between positive ($A > 0$) and negative ($A < 0$) magnetic polarity. [54].

mechanism: variation and frequent reversals of the IMF during each three-month observation period causes a superposition of Sun shadows with different shifts and leads to an observed shadow that is wider and weaker.

(3) Relevance to space weather forecasting

The Sun produces energetic particles due to occasional sudden explosions at its surface, called solar storms, which can accelerate particles to relativistic energies (ions up to tens of GeV, electrons up to tens of MeV) for durations up to about an hour. Furthermore, a type of storm called a coronal mass ejection (CME) can drive an interplanetary shock that accelerates ions up to tens of MeV (called “energetic storm particles”) over several days. The particles due to solar storms, collectively called solar energetic particles (SEPs), pose a radiation hazard to astronauts and high-altitude passenger aircraft for short but unpredictable time periods, as well as damaging expensive satellites and spacecraft (at least fifteen have been disabled by solar storms to date). Strong UV and X-ray fluxes lead to increased ionospheric ionization and disturb human communications and navigation signals. The shock and CME carry particularly strong magnetic fields, and they can significantly disturb the Earth’s magnetosphere. In particular, a strong southward magnetic field can lead to magnetic reconnection and a strong inflow of solar wind plasma and energetic particles into the Earth’s magnetosphere, which can also damage satellites. A disturbed magnetosphere can lead to geomagnetically induced currents and power outages. All these effects on human activity can collectively be called “space weather” effects.

There is great practical interest in space weather prediction, but current prediction capabilities are very limited. The situation is analogous to long-term weather forecasting some decades ago, when the best results were based on prior experience and qualitative concepts. For modern space weather

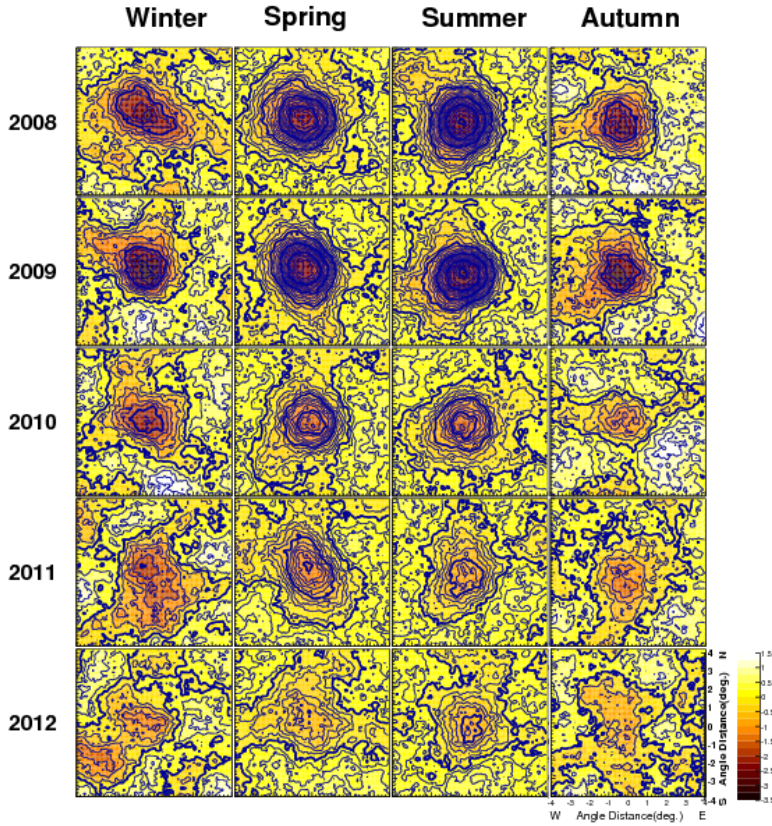


Figure 89: Seasonal variation in the sun shadow observed by the ARGO-YBJ experiment in cosmic rays at median energy 5 TeV. The observation period for each map is one astronomical season in the Northern Hemisphere. The smoothing radius is 1.2° and the pixels are $0.1^\circ \times 0.1^\circ$. Each map shows the fractional change in the cosmic ray flux (color scale) and the statistical significance of the change (contours). Each contour represents an integral value of the significance (in units of the standard deviation), with darker contours every 5 units. Maps for the Spring and Summer seasons show stronger significance because the Sun was higher in the sky at the ARGO-YBJ site in Tibet. The fractional change suddenly weakened in Spring 2010, in association with a sudden increase in IMF variability, whereas the sunspot number and some other generic indicators of solar activity started to increase rapidly only in Spring 2011.

forecasting, even after a CME has been observed at the Sun, it remains difficult to predict when an interplanetary shock and CME will arrive at Earth (which can be $\sim 1\text{-}4$ days, depending on the CME speed), and very difficult to measure or infer the orientation of the magnetic field of the CME; a southward field would result in particularly strong space weather effects.

The ARGO-YBJ experiment first used the Sun shadow displacement in the south-north direction to measure the intensity of the magnetic field between the solar wind from the Sun to the Earth, during the recent period of minimum solar activity [481]. This capability could also be used to determine the mean magnetic field orientation between the Sun and Earth, before the field arrives at Earth. At present, the best reported time resolution for sun shadows - that of the ARGO-YBJ group [480] - is three months, which is not of practical use for space weather forecasting. However, because of its much greater size, LHAASO is expected to produce a statistically meaningful sun shadow every 1-2 days. This is then directly useful for space weather forecasting. For example, a sun shadow determined for time t can be compared with the previous sun shadow, observed 1-2 days earlier, and the difference is due to new magnetic fields that have emerged from the sun minus old fields

that have passed the Earth. When making use of *in situ* spacecraft observations of the interplanetary magnetic field, we can determine the new magnetic field that emerged from the Sun during that time interval. Then we can infer the orientation of the magnetic field that will pass by Earth in the next few days, including whether the field will have a strong southward component. This will be important information to complement existing data for space weather forecasting.

6.2.3. *Loss-cone anisotropy and advance warning of shock arrival for space weather forecasting*

The loss cone anisotropy is another type of measurement of Galactic cosmic rays that is directly relevant to space weather forecasting because could provide advance warning of the arrival of an interplanetary shock, and could also indicate an expected time of arrival. This would be useful because a shock arrival often coincides with a sudden storm commencement as determined by ground-based geomagnetic observatories, i.e., it marks the start of a geomagnetic storm and the associated space weather effects.

The loss cone anisotropy is a decrease in GeV-range cosmic ray density in only a narrow range of directions, found 1-2 days before the arrival of an interplanetary shock at Earth. Note that after the shock arrives, there is a decreases in the cosmic ray flux from all directions, known as a Forbush decrease [482], because the high plasma speed and strong magnetic fields inhibit access of cosmic rays to the region downstream of the shock. Now the Forbush decrease itself is not directly useful for space weather forecasting because it arrives after the shock, i.e., after the geomagnetic storm commencement. However, the “loss cone” is a range of angles close to the interplanetary magnetic field direction toward the shock, and particles from these directions came from downstream of the shock where the particle flux is lower. Hence a loss cone anisotropy is an indicator of the approach of an interplanetary shock.

A loss cone anisotropy was first reported in data from neutron monitors, in 1992 [483]. Later there were numerous other reports of loss cone decreases in neutron monitor data, as well as an enhancement of cosmic ray flux in a ring of directions surrounding the loss cone, which was attributed to reflection from the shock. The first theoretical description of the anisotropy and its spatial distribution was provided by [484]. Further computer simulations [485] provided a basis for comparison, so that an observed loss cone angle can be used to infer the shock-field angle. That work has been used to parameterize more recent determinations of loss cone shock precursors by the Global Muon Detector Network (GMDN) with fine directional resolution [486, 487].

LHAASO’s reconstructed showers will have excellent directional precision and a huge count rate, over a cosmic ray energy range similar to that of GMDN, so LHAASO will provide improved measurements of the loss cone anisotropy, including a possible discovery of fine directional structure beyond the axisymmetric fits performed with presently available data. This could be used in real time to provide advance warning of impending shock arrivals and geomagnetic storm onsets. According to [485], in this energy range the loss cone feature can provide warning up to 12 hours in advance. With a single detector facility, loss cone precursors can be seen when the interplanetary magnetic field direction rotates into view, which will often but not always occur during that 12-hour window. Therefore, a more comprehensive warning system could be obtained by teaming up with GMDN, other air shower arrays, or neutron monitors worldwide to continuously monitor loss cone features along the interplanetary magnetic field direction.

6.2.4. *Forbush decreases due to solar storms*

There are also transient cosmic ray flux and anisotropy variations due to major solar storms. The main effect is the so-called Forbush decrease [482]. The first stage of the decrease occurs at a shock driven by a CME. There may be a second stage associated with the arrival of the CME ejecta, with a further decrease that lasts while the ejecta pass the observer [488]. After that, the flux returns to normal over the next few days. It is common to observe interesting anisotropy patterns during a Forbush decrease, often indicating interesting directional distributions of particles following the magnetic struc-

6.2 Suggestions for Section on Solar-Heliospheric Science

tures of the CME. The mechanism for the Forbush decrease is not clear, and the energy distribution of the decrease could provide important clues.

Air shower arrays can play a role by determining the Forbush decrease at high energies, where the energy and time dependence have not been systematically studied. For example, the ARGO-YBJ Collaboration reported the detection of a Forbush decrease on 2005 Jan 18 [489]. LHAASO could provide a great increase in statistics, though it will be necessary to understand and correct for environmental effects on the count rate as a function of time.

6.2.5. Modulation of the cosmic ray flux with the solar cycle

The longest-period cosmic ray variations that are directly measured are related to the 11-year sunspot cycle and the 22-year solar magnetic cycle. The number of sunspots typically varies over 11 years. There were sunspot maxima in 1989, 2000, and 2014, and sunspot minima in 1996 and 2008. Although the Sun is currently in solar maximum conditions, the sunspot number is substantially lower than during the 2000 maximum. Because magnetic fields and solar storms are concentrated near sunspots, numerous solar phenomena vary with the solar cycle. They do not precisely depend on the sunspot number, so we tend to speak of “solar maximum” as a period of several years around solar maximum, and “solar minimum” as a period of several years with very few sunspots. Because of the higher solar wind speed (on average) and stronger magnetic fields during solar maximum, the transport of cosmic rays to the inner heliosphere is inhibited. Thus the flux of cosmic rays is observed to have an inverse association with the sunspot number, with the most cosmic rays during solar minimum, and the fewest during solar maximum [490]. The amplitude of variation is $\sim 30\%$ at an energy of 1 GeV. This roughly 11-year variation is called the solar modulation of cosmic rays (Figure 88).

The Sun’s magnetic field is much more complex than the Earth’s, and magnetic fields are highly concentrated at the sunspots, typically directed outward at one and inward at another. Nevertheless, there is an overall preponderance of one polarity on one hemisphere and the opposite polarity on the other. Every 11 years or so, at solar maximum, there is a magnetic reversal in which the preponderance reverses sign. Therefore, a complete magnetic cycle requires 2 sunspot cycles, i.e., about 22 years. Charged particle orbits undergo drift motions that depend on the charge sign and the sign of the magnetic field. The drifts therefore reverse every 11 years and repeat every 22 years. The same holds for the effect of magnetic helicity on the particle scattering. Therefore, there is also a roughly 22-year cosmic ray flux variation corresponding to the solar magnetic cycle [491]. In other words, 11-year periods with opposite magnetic polarity exhibit distinct cosmic ray variations. These effects are associated with a variety of interesting phenomena, such as guiding center drifts, cosmic ray gradients with helio-latitude, particle charge sign dependence, and changing diffusion coefficients [492, 493, 494]. These phenomena depend on the sign of qA , where q is the particle charge and A is the solar magnetic polarity.

With stable, long-term operation, LHAASO will provide important information to further explore solar modulation as a function of energy and time. There may even be sufficient compositional information to discern the individual modulation of protons and alpha particles as a function of energy throughout the solar cycle. This is information that is not available from traditional ground-based observatories of GeV-range cosmic rays, such as neutron monitors and muon detectors.

6.2.6. 27-day variations

Roughly speaking, a faster solar wind speed can inhibit the entry of cosmic rays to the inner heliosphere, and is typically associated with a reduced cosmic ray flux. Thus co-rotational variations in solar wind speed (which rotate with the Sun) are associated with well-known “synodic” or “27 day variations” in the cosmic ray flux [495], which have sometimes been called “recurrent Forbush decreases.” It frequently happens that a region of the solar corona that produces fast solar wind, e.g., a coronal hole, lies eastward of a region that produces slow solar wind. Then as the Sun rotates, the source region of fast solar wind moves underneath the region where slow solar wind came out previously, and the fast solar wind will collide with the slow solar wind that lies in front of it. Such a collision region is called

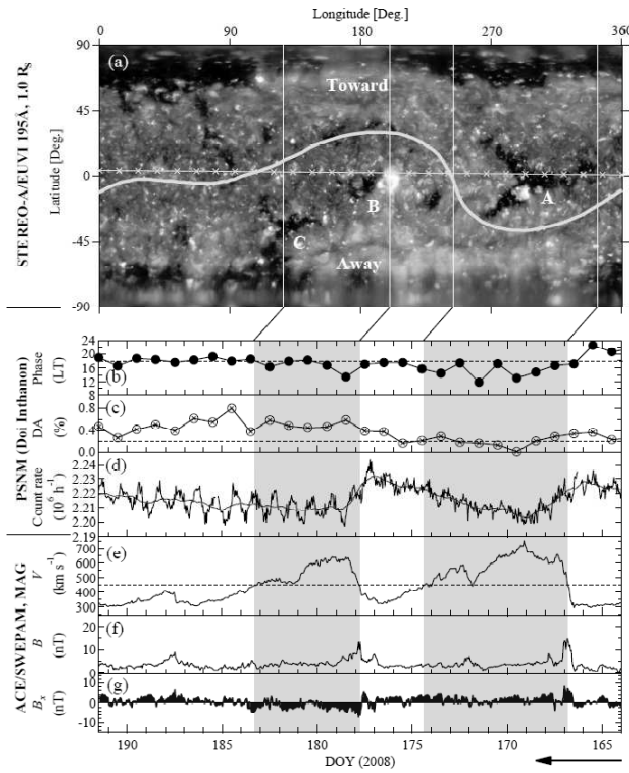


Figure 90: Reversed time plots in day of year (DOY) for Carrington (solar) rotation 2071 (between 2008 June 12 and 2008 July 10). Top panel: Synoptic map of the solar corona as observed by the EUVI-A imager in the Fe II 195 bandpass. Upper three graphs: Data of the diurnal anisotropy and flux of Galactic cosmic rays (GCRs) as measured by PSNM at Doi Inthanon. Lower graphs: Hourly interplanetary plasma parameters from the ACE and OMNIWeb databases in GSE coordinates. When the high speed solar wind streams pass the Earth they reduce the cosmic ray flux. Each dotted-dashed line represents a boundary between magnetic polarities of the streams. After the rapid solar wind speed increase of DOY 177, there was a strong, long-lasting enhancement in the diurnal anisotropy of GCRs. This is attributed to an extra $\mathbf{B} \times \nabla n$ anisotropy with a latitudinal gradient in association with the coronal hole (dark region) morphology [55].

a co-rotating interaction region (CIR). The CIR also has a spiral shape, and it represents a region where solar wind is suddenly compressed by the collision. An observer near Earth sees the solar wind speed suddenly increase when the faster solar wind arrives.

It is common to see the cosmic ray flux suddenly decrease at the time of the CIR, either as part of the inverse relationship with solar wind speed or because the compressed plasma and increased magnetic field serve as a barrier to hinder access to cosmic rays (see Figure 90, and note the reversed time axis). These jumps are a key component of the 27-day variations in cosmic ray flux with solar rotation. Note that CIRs also cause geomagnetic storms and space weather effects, so there is some practical interest in what cosmic rays can tell us about the physical properties of CIRs. LHAASO data will provide further insight, especially with regard to the energy dependence, which may allow us to clarify and quantify the association between solar wind parameters and the cosmic ray flux.

6.2.7. Sidereal anisotropy

The sidereal anisotropy (also called the sidereal diurnal anisotropy) refers to the difference in cosmic ray flux from different directions in space, ideally averaged over the Earth's yearly orbit of the Sun. For scalar rates from a ground-based detector rotating with Earth, the sidereal anisotropy is related to the

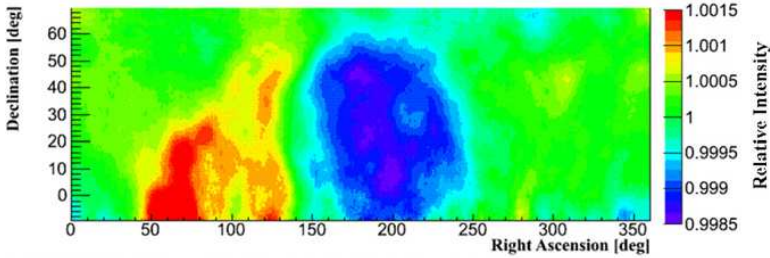


Figure 91: Relative intensity map of TeV cosmic rays as measured by ARGO-YBJ, showing the sidereal anisotropy [56].

data organized as a function of sidereal time, as opposed to solar time. The sidereal anisotropy of TeV-range cosmic rays has been a very exciting topic of study, since the initial discoveries of the “loss-cone” deficit from a direction close to the Galactic center and a “tail-in” enhancement from the direction of an assumed heliotail [496]. Further measurements have produced sky maps of the large-scale anisotropy, e.g., [497, 56] (see Figure 91). With better statistics and detector sensitivity, more and more structures have been found at medium and small scales [392, 393]. The possible explanations include large-scale flows in the galaxy, nearby sources of cosmic rays, and/or the fingerprint of interstellar turbulence [498]. For more details, see the section on Cosmic Ray Measurement and Physics.

To some extent, the cosmic ray anisotropy pattern must be affected and distorted by heliospheric magnetic fields [499], so solar and heliospheric phenomena are relevant. Because these magnetic fields vary strongly with the (roughly) 11-year solar cycle, various air shower experiments are looking for such a time dependence in the anisotropy pattern. Other possible types of time variation are a difference between patterns for opposite polarities of the interplanetary magnetic field, and a dependence on the location of the Sun in the sky. Results published to date are consistent with a time-independent anisotropy, but when LHAASO takes data with improved statistics over a substantial portion of a solar cycle, the imprint of heliospheric magnetic fields should be found.

The first impact of such a ground-breaking measurement would be to help determine the heliospheric magnetic field, and indeed the shape of the heliosphere itself. The large-scale structure of the heliosphere, and the shape of its boundary, the heliopause, are still hotly debated. The traditional view is that the interstellar medium (ISM), which moves relative to the heliosphere, pushes past the heliosphere to create a bullet-shaped nose to the heliopause on its upstream side and an extended tail on its downstream side. Others contend that there is no heliotail and that the solar wind instead flows as jets along the poles of solar rotation, with the jets bent downstream by the ISM [500].

The sidereal anisotropy in GeV-range cosmic rays is also of substantial scientific interest. The anisotropy decreases in amplitude with decreasing energy [56], presumably due to solar modulation. However, in data from the Matsushiro underground muon detector at ~ 0.6 TeV, there was at most a minor solar cycle dependence [501]. This is surprising, because solar modulation had apparently reduced the amplitude by a factor of 3 at that energy. With greater statistics and improved resolution of time variations, LHAASO data may help shed light on this mystery.

6.2.8. Diurnal anisotropy

The diurnal anisotropy (also called the solar diurnal anisotropy) refers to the difference in cosmic ray flux from different directions in space relative to the Sun, e.g., as expressed in geocentric solar ecliptic (GSE) coordinates. This is an anisotropy related to solar phenomena, or the Earth’s orbit around the Sun. For scalar rates from a ground-based detector rotating with Earth, the diurnal anisotropy is related to the data organized as a function of local solar time. For GeV-range cosmic rays, it is also necessary to account for significant deflection of the cosmic ray direction by Earth’s magnetic field.

The basic physical explanation of the diurnal anisotropy is very different for TeV-range and GeV-range cosmic rays. In the TeV range, the cosmic ray distribution is almost isotropic in an inertial frame,

so the diurnal anisotropy is dominated by the Compton-Getting effect from Earth's orbital motion. The greatest flux arrives at \sim 0600 local time. In contrast, cosmic rays of energy up to \sim 100 GeV are affected by the Sun and the interplanetary magnetic field (IMF), which introduces an energy-dependent anisotropy [502]. The average diurnal anisotropy (DA) vector has been explained as a consequence of the equilibrium established between the radial convection of the cosmic ray particles by solar wind and the inward diffusion of GCR particles along the IMF. In a reference frame co-rotating with the Sun, convection and parallel diffusion (i.e., diffusion parallel to the large-scale magnetic field) can nearly cancel and the GCR distribution has almost no net flow. Then in Earth's reference frame, there is a net flow as the co-rotating GCR distribution impinges on Earth from the dusk sector, i.e., \sim 1800 local time. Transient variations are superimposed on the steady state co-rotational anisotropy, and they sometimes form "trains" of enhanced diurnal variation that persist for several consecutive days (see Figure 90). Thus the long-term variation in GeV-range diurnal anisotropy provides information on solar modulation and cosmic ray gradients [494, 468], while the changes on shorter time scales tell us about the changing structure of the heliosphere [55].

LHAASO will examine the diurnal anisotropy of cosmic rays over a wide range of energies, using both scalar data and shower data. Consistency between those two data sets, and also with previous reports, will provide a demanding test that the flux data are properly corrected for environmental effects. Even in the TeV range, previous experiments apparently disagree about whether there is a strong deviation from the expected Compton-Getting effect [56, 503]. Then there is an interesting transition in the TeV range from Compton-Getting to mostly co-rotational anisotropy. Finally, in the GeV range, LHAASO results can be compared with results from neutron monitors (\sim 10-35 GeV median energy) and muon detectors (\sim 60-110 GeV median energy for surface detectors, and higher for underground detectors), and we expect to find interesting structure in the diurnal anisotropy as a function of energy and time.

6.2.9. Short-time variations

Clearly there are sharp decreases in cosmic ray flux associated with discrete structures that accompany an interplanetary coronal mass ejection (ICME) and accompanying shock, as discussed in the section on Forbush decreases. Here we consider the slightly different issue of variations in cosmic ray flux, over times shorter than one day, due to fluctuations in the IMF, the solar wind, or possibly the magnetosphere. It has become clear from observational and theoretical work that apparently homogeneous regions of the solar wind are really permeated by flux-tube like structures that can guide the motion of energetic particles, leading to non-uniform spatial distributions [504, 505, 506, 507, 508, 509, 510], including clear observational confirmation at MeV energies or lower. For decades, there has been a notion in the cosmic ray community that there should be local fluctuations in the GeV-range cosmic ray rate in concert with small-scale turbulent fluctuations or coherent structures in the IMF [511]. However, the correlations obtained are somewhat weak, and instrumental and environmental fluctuations could be important. Furthermore, for a ground-based detector with no directional information for individual cosmic rays, and a directional acceptance that rotates with Earth, it is often unclear whether short-term variations in the cosmic ray flux are due to temporal changes in the IMF or due to the cosmic ray directional distribution, i.e., structure in the diurnal anisotropy.

LHAASO data from shower reconstruction at tens of GeV could be a game-changer for this type of study, providing an ability to distinguish between temporal effects and changes in the directional distribution over its wide field of view. There is some reason to expect temporal changes in the Galactic cosmic ray flux in association with interplanetary structures, based on successful observations at MeV energies [512, 513]. Furthermore, neutron monitors in Antarctica had a rare opportunity to observe minute-scale fluctuations in GeV-range solar particles during the giant solar event of 2005 Jan 20 [514] (the Galactic cosmic ray flux does not provide sufficient statistics to study minute-scale fluctuations in such detectors). That study found huge variations in flux with periods of 2 to 4 minutes, which they attributed to fluctuations in the beaming direction of the particle distribution. Thus LHAASO data, with

excellent statistics and direction information, will provide a means to seriously search for short-term variations in Galactic cosmic rays at tens of GeV and above and to identify their nature and origin. Environmental stability of the LHAASO detectors will be crucial for this work.

6.2.10. Moon shadow and geomagnetic field variations

The moon shadow in TeV cosmic rays is a very important tool for calibrating the resolution and absolute energy scale of an air shower array [471], because the Moon has a known size and the observed shadow has an energy-dependent deflection due to the known geomagnetic field; see also the section on Cosmic Ray Measurement and Physics. Usually time variations in the moon shadow are not expected, and indeed the constancy of the moon shadow is an important test of an air shower detector's stability. However, there has been a suggestion of a possible so-called day/night effect, because the solar wind continually impinges upon Earth's magnetosphere and compresses the dayside magnetosphere, while the nightside magnetosphere is elongated into the magnetotail. Thus the moon shadow deflection due to the geomagnetic field could be different during different phases of the Moon's orbit, depending on whether it is on Earth's dayside or nightside. There have been previous reports of no day/night effect [471, 515], and also a claim of such an effect [516]. LHAASO should be able to check for this possible effect with better statistics and over a wider energy range. If successfully detected, this could provide a valuable magnetospheric database of measurements of the integrated geomagnetic field along the line of sight to the Moon as it orbits the Earth.

6.3. LHAASO research topics about CME shock and SNR shock

Executive summary: We will apply the probable Sun and coronal mass ejection (CME) shadows from LHAASO to study CME's magnetic field evolution temporally in the interplanetary space. Observations from multiple spacecraft show that CME-driven shock exhibits an energy spectral "break" at 1-10MeV. So we expect to apply the possible detections of CME's shadow from LHAASO at TeV cosmic rays to study the turbulent magnetic field driven by CME shock. On the other hand, observations of old supernova remnants (SNRs) IC443 and W44 from Fermi Large Area Telescope (Fermi-LAT) also give evidences of γ -ray spectral bumps between the energy spectrum range from ~ 250 MeV to a few GeV. In addition, analytic model suggest that these energy spectral bumps can be traced to the parent proton spectral "breaks" at ~ 239 GeV and ~ 22 GeV for IC443 and W44, respectively. Currently the proton energy spectral "break" is estimated to be related to the interactions between SNRs and dense gas clumps. We propose WCDA of LHAASO could provide a survey of γ -ray at energy range from GeV to TeV for measuring SNRs IC443 and W44. Simultaneously, we still coordinately perform a numerical model to study the mechanism of the energy spectral "breaks".

6.3.1. Topic-1: CME's shadow

Here is one idea regarding shadows of Sun and coronal mass ejection (CME) in TeV cosmic rays (see Figure 92). Note that they require that the telescope be able to produce "snapshots" of the TeV cosmic-ray intensity at high time and space resolution.

If it is possible to measure the flux of TeV-energy galactic cosmic rays (GCR) coming from the direction of the Sun with high enough temporal cadence and high-enough spatial resolution, then it might be possible to measure effects of interplanetary magnetic field (IMF) associated with CME as they propagate outward from the Sun. The Sun's shadow seen in maps of TeV cosmic rays is known to be offset from the actual location of the Sun, which is caused by the deflection of TeV cosmic rays crossing through the Sun's magnetic field [517, 518, 519]. If the telescope sensitivity is sufficient, one also could see shadows of CME, which carry very strong magnetic fields with them on such images. Since the magnetic field in a CME falls off with distance, again if the sensitivity of CR's flux is sufficient, one might be able to measure the variation of IMF with the distance and time according to CME's shadow on the large field of view (FOV) in LHAASO [517]. This would be extremely valuable for studying the formation of the energy spectral "break" in the propagation of the shock. Note that large and fast

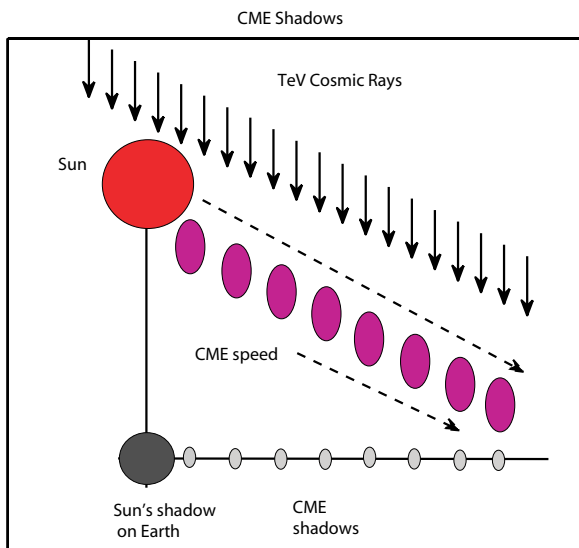


Figure 92: The schematic diagram of the CME's shadow.

CMEs can move with the order of 2000 km/s, or even more, so that a CME can move a distance with

the order of the solar radius in about 5 minutes. This would have to be the time resolution of the cosmic ray snapshots. Is this possible at all? A very rough calculation we just did, based on the known GCR spectrum at Earth, yields that at 1-TeV, the flux of GCR's at Earth is about 0.5 particles per square meter per second. So, in 5 minutes, there are about 150 particles at 1-TeV cosmic rays arriving at Earth in a square meter. We are not sure how many secondary particles arrive at Earth's surface. But, we will leave it to the telescope builders to decide whether it is possible to measure TeV cosmic rays on such a high time cadence. It would be great if the LHAASO team could do. We hope this proposal would be helpful to understand the IMF as a CME propagates on it and interacts with nearby planet.

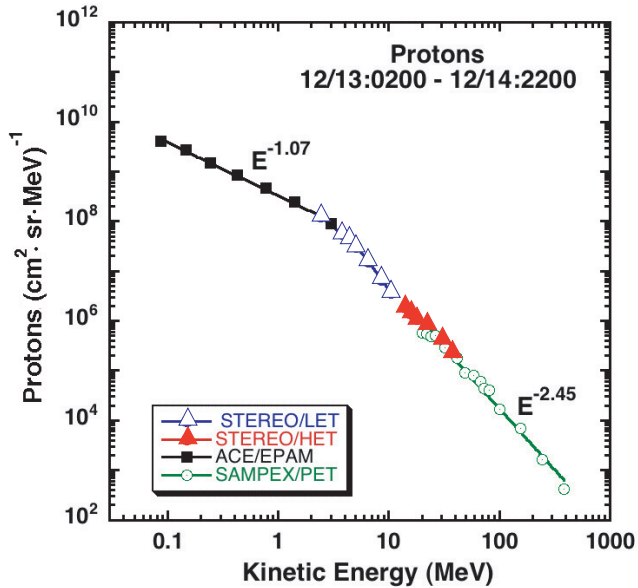


Figure 93: The observation from the spacecraft. The energy distribution shows a double power law with a “break” at $\sim 2\text{-}5\text{ MeV}$ [57]

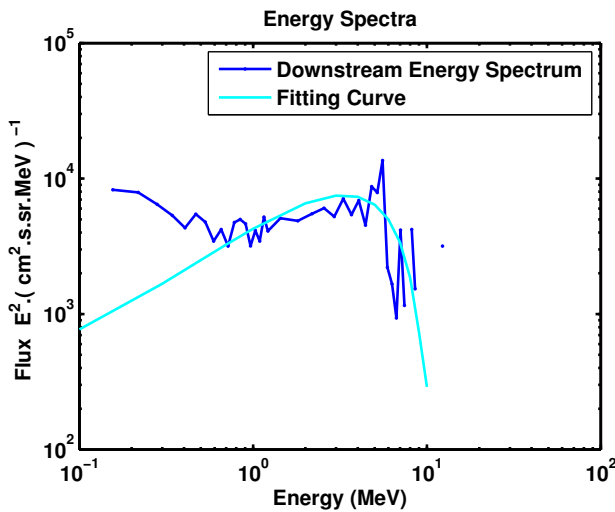


Figure 94: Simulated energy spectrum of 13,Dec,2006 shock event shows a “break” occurred at $\sim 5\text{ MeV}$ in the $E^2 \cdot F(E)$ representation [58].

In the interplanetary (IP) space, observations from the spacecraft such as ACE, Wind, STEREO, RHESSI, SOHO, SAMPEX show proton energy spectral “break” occurred on the IP shocks. There are six events with hard energy spectra occurred on 1997 Nov 6, 2001 Feb 15, 2005 Jan 20, 2005 Sep 7, 2006 Dec 5, and 2006 Dec 13. These six large events all have spectral “breaks” at the energy range of

1~10MeV [57]. Figure 93 shows the 2006 Dec 13 event, which energy distribution of proton exhibits a ‘‘break’’ at 1~10MeV.

Although a number of in situ observations exhibit the CR’s proton spectral ‘‘breaks’’ associated with either galaxy source or solar source, there is still no reliable prediction of ‘‘breaks’’ by numerical methods. In addition, numerical simulation usually builds a simple DSA model with a short size of the diffusive region ahead of shock. If the energy spectral ‘‘break’’ associated with a large diffusive size, the simple numerical model would hardly include this energy spectral ‘‘break’’ in its simulation result. Since Monte Carlo (MC) method can easily treat thermal ion injection [520, 451], the scattering mean free path is assumed to be a function of the particle rigidity, this treatment allow to follow individual ions for a long time until the appearance of the highest energy tail. However, the acceleration efficiency, as well as the maximum particle energy, are depended on the size of the precursor region, which is parameterized by the size of free escape boundary (FEB) in MC numerical model. In ref. [521] is presented an ion spectra with a maximum particle energy less than 1MeV by applying a fixed FEB size ahead of the bow shock. In ref. [522] and [523] are improved the simulated result for the maximum particle energy up to \sim 4MeV using a moving FEB ahead of the shock. In ref. [524], it is investigated that the maximum particle energy in MC model could climb to a saturation at \sim 5.5MeV within the same size of FEB by using different scattering mean free path. Wang [58] also obtained the maximum particle energy up to 10MeV in a converged two shocks model, and the simulated results in Figure 94 showed that the energy spectrum of 2006 Dec 13 event appeared a ‘‘break’’ at \sim 5.5MeV in the $E^2 \cdot F(E)$ representation.

In this proposal, we will analyze the data of TeV GCR from LHAASO project to study the evolution of CME’s shadows . We will use the possible shadows of CME to measure the variation of IMF when a CME propagates on it and interacts with planets. This would be great to investigate the energy spectral ‘‘break’’ formation in the observed CME shocks.

6.3.2. Topic-2: Particles acceleration in SNR shock

Since cosmic rays are important both dynamically and diagnostically, it is essential that we understand their acceleration, transport, radiative emissions, and interaction with nearby environments. In particular, the CRs spectrum shape is usually referred to as a knee-ankle structure with the ‘‘knee’’ at a few PeV and the ‘‘ankle’’ at a few EeV. There are some debated understandings for the energy spectral ‘‘break’’. The first understanding has proposed that the ‘‘break’’ determined by the Larmor radius for ions. A heavy nucleus with charge Z has maximum energies Z times of proton with the same Larmor radius. This leads the heavier ions would not escape easier than protons and a ‘‘break’’ is formed at a certain energy range [525]. The second understanding is that the ‘‘break’’ would probably be associated with the leakage mechanism. It means that CRs can drive Alfvén waves efficiently to build a transport barrier that strongly reduces the leakage of particles leading to an energy spectral ‘‘break’’ [59]. The third understanding is that the ‘‘break’’ would be formed in site of drifting shock interacted with surroundings media. For example, if a SNR approaches a molecular clouds (MCs) or a pre-supernova swept-up shell with a significant amount of neutrals, the confinement of accelerated particles will deteriorate and would lead to an energy spectral ‘‘break’’ [526]. Also a multiple shocks model, which assumed that the medium is highly turbulent and that the number of shocks are propagating through it, would produce the particle spectral features such as ‘‘breaks’’ [527, 528]. Besides, we propose that a collided shocks model could probably inform the energy spectral ‘‘break’’ by converged two shocks. We hope it will be investigated by the measurement of LHAASO in gamma-ray energies of GeV-TeV.

SNRs, as the major contributors to the galactic CRs, are believed to maintain an average CR spectrum by diffusive shock acceleration (DSA) regardless of the way they release CRs into the interstellar medium (ISM) as showed in Figure 95. However, the interaction of the CRs with nearby gas clouds crucially depends on the release mechanism. The generation of CRs in SNR shocks by DSA mechanism is understood reasonably well up to the point of their escape into SNR surroundings. But making this mechanism responsible for the most of galactic CRs requires understanding all stages of the CR production including their escape from the accelerators. In fact, the best markers for CR-proton factories are

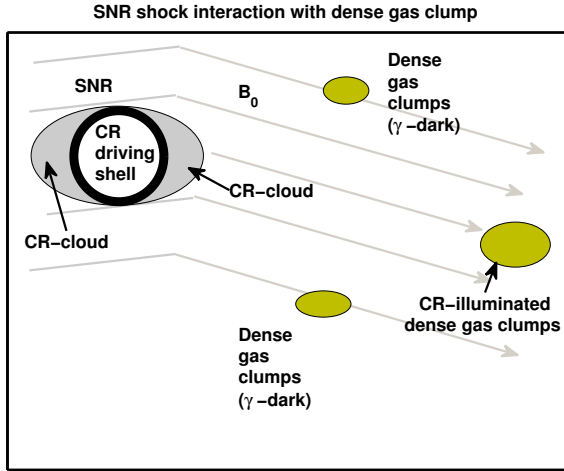


Figure 95: The schematic diagram of the SNRs shock interacted with nearby MCs [59]

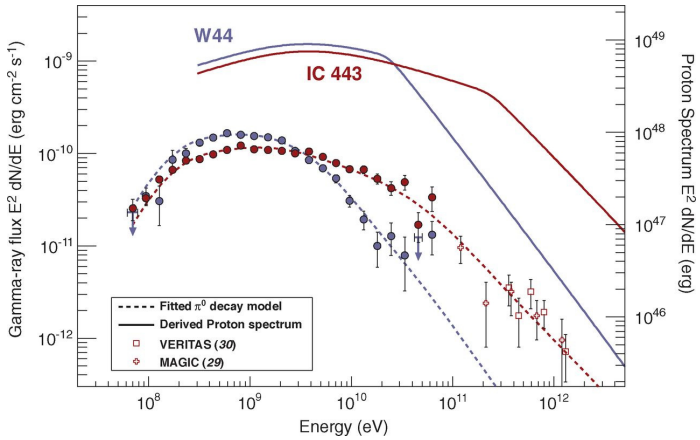


Figure 96: The spectral energy distribution obtained for IC 443 and W44 at different energy range from multiple spacecraft [60].

nearby MCs illuminated by protons leaking from SNRs. CRs will be visible in gamma rays generated by collisions with protons in the cloud.

In recent years several in situ observations indicate SNRs are the essential candidates for the sources of the CR's proton spectrum up to the "knee" at a few PeV. Since the TeV γ -ray from Crab Nebula were first clearly detected by imaging air Cherenkov telescope (IACT) in 1989, IACTs have been extensively constructed and are operating around the world. There are about 160 of TeV γ -ray sources are identified up to now [529]. In addition, with the development of the observed technology on spacecraft, more than 3,000 sources below TeV γ -ray are identified in the second Fermi-LAT list. The old SNRs IC443 and W44 are the highest-significance sources for detailed studies in their γ -ray spectra. SNRs IC443 and W44 are located at distances of 1.5kpc and 2.9kpc, respectively. Figure 96 shows the spectral energy distribution obtained for IC 443 and W44 at energy range from 60 MeV to 100 GeV. In both two sources, the spectra below \sim 200 MeV steeply rise and clearly exhibit bumps at \sim 200-250 MeV, which can be interpreted by the effect of pion decay caused by the interaction processes between SNRs and the MCs [60]. The energy distributions of the high-energy protons, with "breaks" p_{br} at higher energies, were derived from the gamma-ray spectra. These parameters for the underlying proton spectrum are as follows:

6.3 LHAASO research topics about CME shock and SNR shock

$= 2.36 \pm 0.02$, $s2 = 3.1 \pm 0.1$, and $p_{br} = 239 \pm 74 \text{ GeV c}^{-1}$ for IC 443, and $s1 = 2.36 \pm 0.05$, $s2 = 3.5 \pm 0.3$, and $p_{br} = 22 \text{ GeV c}^{-1}$ for W44.

The recent surge in measurements of gamma-bright SNR suggests that the sensitivity threshold have already been surpassed for at least several galactic SNRs and it is increasing timely to improve our understanding of the CR leakage mechanism nearby remnant sites. Without such improvement, it is also difficult to resolve the ongoing debates about the primary origin of gamma emission from some of the gamma-active remnants in complicated environs. In arguing for hadronic or leptonic origin, one needs to know exactly how far the CRs are spread from the source at a given time and with what spectrum [59]. We expect LHAASO project to present exactly measurement at 0.3-30TeV γ -rays in WCDA and up to 10PeV γ -ray survey in KM2A to calm down these disputes.

Simultaneously, we will use a numerical model to simulate the γ -ray spectrum and testify the measurements of the γ -ray spectrum at 0.3-30TeV in WCDA and γ -ray map up to 10PeV in KM2A of LHAASO. Our numerical shock model will focus on two shocks interaction and possibly produce the energy spectral “break”. Our numerical model is based on the interaction between the SNR shock and the MC shock. With two shock precursors moving together temporally, we can obtain an enough higher energy “tail” with an appearance of power-law structure. Finally, we would verify the energy spectral shapes such as “breaks”.

6.4. Investigating a possible link between cosmic ray flux and Earth's climate

Earth's climate change, including global warming, is one of the most important scientific issues of our time. It has been suggested that solar activity has historically played an important role in governing Earth's temperature [530], and one possible mechanism for such a connection involves cosmic rays. In this scenario, increased solar activity leads to decreased cosmic ray flux (see Figure 88), cosmic ray showers are the main cause of atmospheric ionization a few kilometers above ground level, and decreased atmospheric ionization leads to decreased cloud formation, stronger sunlight at Earth's surface, and an increased surface temperature.

The controversy is whether cosmic ray variations really lead to significant changes in cloud cover. Some researchers have claimed a correlation between temporary Forbush decreases and cloud cover [531, 532], while others claim there is no significant effect of cosmic ray variations on cloud cover or on Earth's temperature [533, 534]. It should be possible to improve upon the methodology used by [531]. For example, they model the effect of a Forbush decrease on the GCR spectrum using a function that gives a non-sensical decrease of $> 100\%$ at a rigidity of 1 GV, and they treat each detection rate as a differential flux at the median rigidity rather than an integral flux. With LHAASO data, we can estimate the GCR spectrum with greater accuracy, and we can also use Monte Carlo simulations based on the inferred spectrum to estimate atmospheric ionization and its dependence on geomagnetic cutoff rigidity (or roughly speaking, on geomagnetic latitude), altitude, and time. We should be able to address the issue of a possible effect of cosmic ray variations on cloud cover variations with much greater accuracy.

In the big picture, the world's experts on climate change, through the Intergovernmental Panel on Climate Change, have reached a consensus that solar and volcanic variations account for Earth's surface temperature changes before 1960 and that anthropogenic effects have dominated thereafter.⁹ We do not intend to challenge that expert consensus. We will address the specific question of whether (and how) cloud cover changes are associated with cosmic ray variations, but we would not interpret a positive association as indicating the dominance of solar effects over anthropogenic effects.

6.5. Detection of MeV-range γ -rays from thundershowers

The scalar rates at LHAASO may be able to detect MeV-range γ -rays from thunderstorms, which have previously been detected by ground-based γ -ray detectors [535] and the solar neutron telescope and neutron monitor at Yangbajing, China [536]. The latter reference contends that the signals in neutron detectors were due to γ -rays. For this purpose, it will be useful to have electric field measurements at the LHAASO site, to corroborate an association with lightning activity. Measurements of the time profile of γ -ray emission, as indicated by increased scalar rates in LHAASO's electromagnetic detectors, in conjunction with the electric field data, may help clarify the physical mechanism causing this mysterious emission from thunderstorms.

⁹http://www.grida.no/publications/other/ipcc_tar/?src=/climate/ipcc_tar/wg1/fig12-7.htm

6.6. Geophysical researches with environmental neutrons flux

Environmental neutrons are produced by two natural sources: by cosmic rays in air and in upper layers of soil and by natural radioactivity (mostly due to (α, n) -reactions on light nuclei) throughout the Earth's crust. Being produced as fast the neutrons are moderated by media up to thermal energy and live there up to nuclear capture. Neutron lifetime depends on media chemical composition, temperature and water (or any hydrogenous material). Natural radioactivity chain daughter product inert gas radon-222 having 3.8d lifetime can migrate in air and in soil (rock, concrete, etc.) to a long distance and even accumulate in some places thus changing the neutron flux in underground locations. It is also sensitive to a local seismic activity. Therefore, the flux (or concentration) of thermal neutrons in the media is sensitive to the media parameters such as its temperature, humidity, porosity (seismic activity), etc. Measuring of neutron flux time variations for a long time could thus be used to control the above media parameters.

We plan to use the en-detectors of ENDA-LHAASO array for continuous environmental thermal neutron flux monitoring and its variation study needed not only for EAS experiment background estimation but also for some geophysical applications. We have already some results [537, 538, 539] of this study and it has promising future. Following geophysical items will be investigated through thermal neutrons study:

- Neutrons during thunderstorms (surface)
- Earth's crust Moon tidal effects (surface and underground)
- Seasonal radon-neutron waves at high altitude (surface)
- Free Earth oscillations (underground)
- Forbush effect and Sun-Earth interconnections (surface and underground)
- Ground Level Enhancement (GLE) effect (surface)

The additional geophysical studies on the Earth's surface could be performed cost free using PRISMA-LHAASO detectors. The items needed underground detector location could use existing underground or basement rooms to decrease the cosmic ray source and to emphasize the radon-neutron source. Otherwise, it will needs additional investments.

1. Developing and constructing of a prototype array (PRISMA-YBJ) at high altitude in Tibet in January of 2013. It consists of 4 en-detectors in ARGO hall and is running continuously since August 30, 2013. Some results are already published and some are in preparation.

2. Coincidence run of PRISMA-YBJ and ARGO in 2013. The results are partially published.

3. Autonomous running accumulated up to date 2 years of data taking. Results on thermal neutrons lateral and temporal distributions in EAS were published at 33ICRC, 34ICRC and TAUP2015 conferences.

4. Monte-Carlo simulations based on CORSIKA and GEANT were performed to simulate PRISMA-YBJ experiment configuration. Now we have very good agreement between the simulations and experiment and we need not make any normalization. The program code is ready now to simulate LHAASO-ENDA configuration.

5. Search for new cheap scintillator for thermal neutron detection has been done. As a result we found scintillator producer in Russia and have developed together a novel technology for scintillator compound based on ZnS(Ag) with natural boron as a target for neutron capture. Resulting thermal neutron recording efficiency of the compound is close to 20% at the compound thickness of 50 mg/cm². The price for the compound is now by a factor of 5 lower than that for lithium one (⁶Li enriched compound).

6. Data acquisition system has been developed and it has been tested at an expanded up to 16 en-detector prototype in YangBaJing

6.7. Effects of the near-earth thunderstorms electric field on intensity of the ground cosmic ray electron at YBJ

Executive summary: It has been found that most of the near-earth thunderstorms electric field strength at YBJ (4300 m a.s.l., Tibet, China) is within the range of 1000 V/cm according to the ARGO-YBJ experiment. In this work, Monte Carlo simulations were performed by using CORSIKA to study the intensity change of the ground cosmic rays in near-earth thunderstorms electric field. We found that the number of electrons in secondary particles at YBJ was changed with the strength and polarity of the electric field. In the negative field, the number increases with the increasing electric field. Nevertheless, it increases, or does not change obviously or even declines with different energies of primary particles in the different positive fields. Our results are consistent with the observations obtained from ARGO-YBJ experiment during thunderstorms. What is more, these preliminary results provide important information in understanding the acceleration mechanism of secondary charged particles caused by electric field.

6.7.1. Introduction

It was first mentioned by Wilson that the secondary electrons in cosmic rays can be influenced by the electric field in thunderstorms [540]. Gurevich et al. put forward the relativistic runaway electron avalanche (RREA) in 1992 [541], that air showers of sufficient energy can start an avalanche of runaway electrons in thunderstorms electric field. Ionization electrons that are produced in collisions of shower particles with air molecules are accelerated. Under the right conditions, they can gain enough energy to ionize further molecules, which makes the electron number increase exponentially.

Over the years, it caught much attention that the cosmic rays will suddenly increase during a thunderstorm. Many scientists have carried out lots of ground-based experiments to detect the thunderstorm ground enhancements (TGEs), trying to find high-energy electrons accelerated by the thunderstorms electric field. In 1985, Alexeenko et al. [542] found that the intensity of ground cosmic rays changed during a thunderstorm by using Baksan data for the first time. These changes have nothing to do with air pressure, temperature, but are associated with electric field. Through analyzing the data of the Norikura experiment, Tsuchiya et al. [543] found that the counting rates of photons and electrons were related to the electric field. Several TGE events were detected through analyzing ASEC experimental data by Chilingarian et al. [544, 545]. It seems that these ground experimental observations are consistent with RREA mechanism. In 2010, Buitink et al. [546] performed Monte Carlo simulations to calculate the effects of electric field configurations on more than 10^{16} eV proton shower development. Their results show that the RREA maybe occurs at high altitudes.

A short duration increase of the single particle counting rate occurs accompanied with thunderstorms electric field, while some cases decrease happens in ARGO-YBJ experiment (located at YBJ, Tibet, China) [547, 548]. In this paper, Monte Carlo simulations were performed to study the effects of near-earth thunderstorms electric field on intensity of the ground cosmic ray electron at YBJ.

6.7.2. Simulation Parameters

CORSIKA (COsmic Ray SImulations for KAscade) is a detailed Monte Carlo program to study the evolution and properties of extensive air showers in the atmosphere [318]. The CORSIKA7.3700, which includes the electron transport in the electric and magnetic fields proposed by Bielajew [549], was used in our simulations. The high energy hadronic interaction model is QGSJETII-04; the low energy hadronic interaction model is GHEISHA.

Studies have shown that the atmospheric electric field roughly distributed within the altitude scope of 4–12 km during a thunderstorm [550]. The effect on the total number of electrons and positions can be neglected in the electric field which is far from detectors [546]. It has been found that the near-earth thunderstorms electric field changes dramatically and the strength is mostly within 1000 V/cm from ARGO-YBJ data in 2012. In our simulations, the range of atmospheric electric field is -1000–1000

V/cm at altitudes from 6300 m to 4300 m (corresponding to the atmospheric depth 484–606 g/cm²). Here, we defined the positive electric field was downward.

According to the energy threshold of ARGO-YBJ (a few tens of GeV in scalar mode and a few hundred of GeV in shower mode), the primary particles are chosen as vertical protons with energies 30 GeV, 100 GeV and 770 GeV. In view of the acceleration of the field, we set the energy cutoff below which electrons and positrons are discarded at 0.1 MeV in the simulation.

6.7.3. Simulation Results

Firstly, the number of electrons and positrons as a function of electric field was simulated with primary proton of 30 GeV. Fig.1 shows the percent change of the particle number for 30 GeV proton shower at YBJ in different electric fields. The black cross data points correspond to the percent change of the sum of electrons and positrons. The red solid circle and blue solid square points correspond to positron and electron, respectively. When the field strength increases, the effect on the percent change of particle number becomes different.

As shown in Fig.1, when the electric field is negative (accelerating the electrons), the number of electrons increases, while the positrons reduces, and the total number of electrons and positrons increases with the increasing strength of electric field.

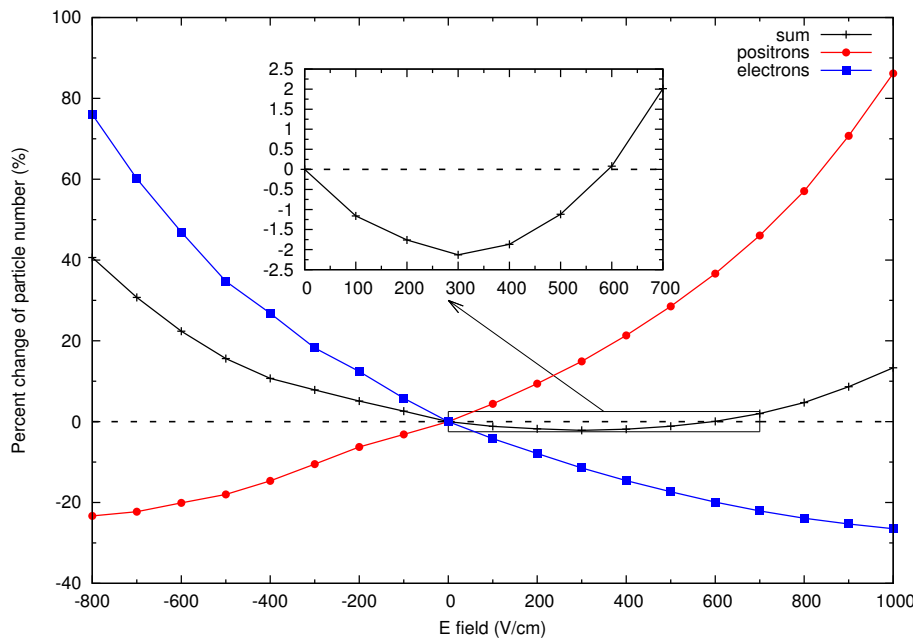


Fig. 97: Percent change of particle number as a function of electric field at YBJ (The illustration is the enlarged view of the total number in reducing range)

When the field is positive (accelerating the positrons), the number of electrons reduces, while the number of positrons increases. In the range 0–600 V/cm, the total number declines and the decrease is about 2.5%. In the positive field greater than 600 V/cm, the total number increases with the increasing strength of electric field.

In the series papers of ARGO-YBJ, they reported that the change of ground cosmic ray intensity is also associated with the primary energy. In this work, different primary energies (30, 100, 770 GeV) were stimulated in different positive fields. Fig.2 shows the percent change of total number of particles as a function of electric field strength for different primary energies at YBJ.

The black solid square data points correspond to primary energy of 30 GeV and the red solid circle and blue solid triangle points to energy of 100 GeV and 770 GeV, respectively. As we can see from Fig.2, the variation tendencies of these three different primary energies are almost the same. In 0–600 V/cm field, an obvious decline of the total number can be seen. The degree of decline is about 3% at YBJ.

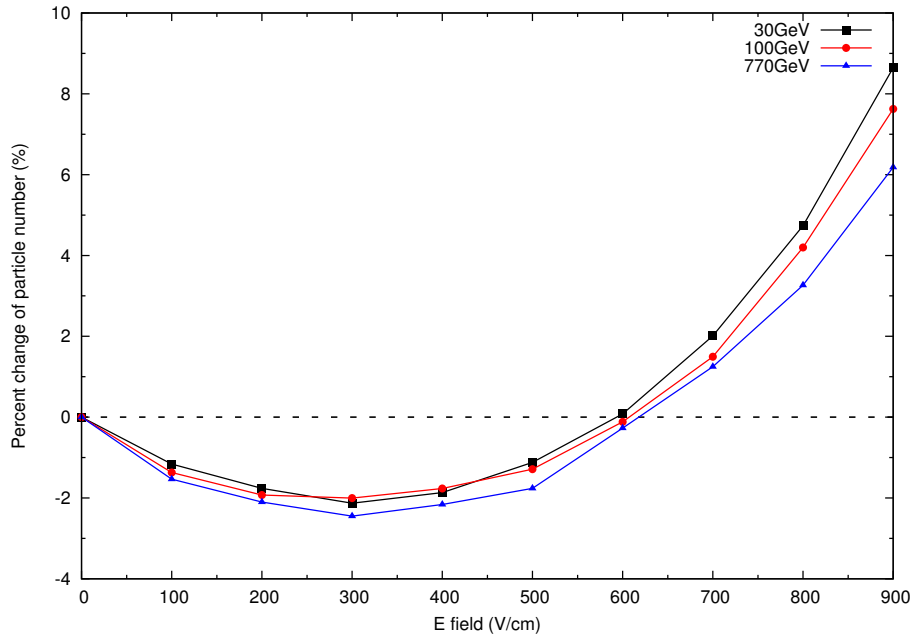


Fig. 98: Percent change of the total number of electrons and positrons as a function of positive electric field strength for different primary energies at YBJ.

Fig.3 shows the percent change of the total number of electrons and positrons as a function of atmospheric depth for different primary energies in 400, 500, 600 and 700 V/cm.

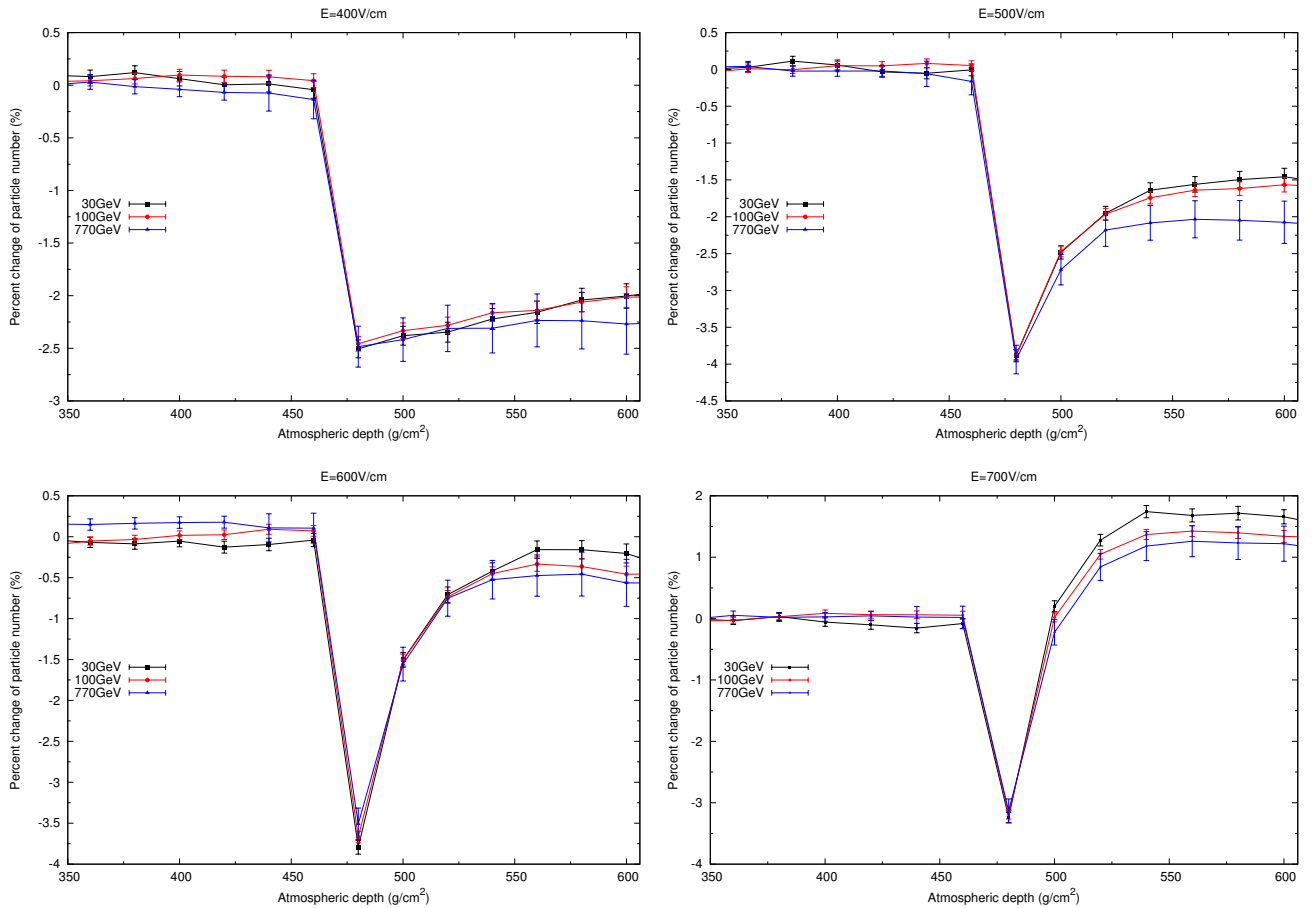


Fig. 99: Percent change of electrons and positrons as a function of atmospheric depth for different primary energies shower in different positive fields.

As we can see from the figure, the number drops quickly, then it increases with increasing atmospheric depth. The black solid square data points correspond to the primary energy of 30 GeV and the red solid circle and blue solid triangle points to 100 GeV and 770 GeV, respectively. At YBJ, the total number declines in 400 V/cm and 500 V/cm, and it is no significant change in 600 V/cm. However, the increase occurs in 700 V/cm. The degree of decrease or increase is related to the primary energy to some extent.

6.7.4. Discussion

The total number of electrons and positrons in cosmic rays declines in thunderstorms electric field is probably related to several factors such as the polarity of electric field, the strength of electric field, the proportion of electron and positron, the energy of primary particle and so on. Here we take the primary proton of 30 GeV as an example to discuss it in detail.

Fig.4 shows that the percentage of positron (electron) in the total number at different atmospheric depth in absence electric field. It shows that the percentage of electron increases with the increasing atmospheric depth, while the positron decreases. At YBJ, the number of electrons is about 1.8 times of that of positrons. The phenomenon that the number of positrons is less than the number of electrons is mostly caused by Compton scattering effect [551].

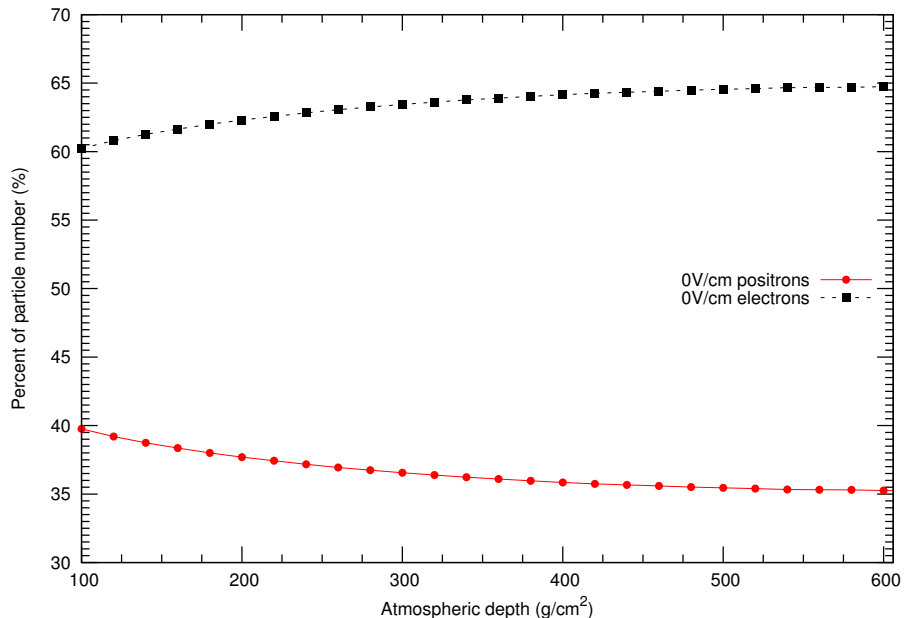


Fig. 100: Percent of electrons and positrons number as a function of atmospheric depth in absence electric field.

Fig.5 shows that, in the negative electric field, the percentage of electrons keeps increasing with the increasing atmospheric depth, while the percentage of positrons keeps declining. At YBJ, the percentage of electrons is about 4.0 times of that of positrons in -800 V/cm.

As shown in Fig.6, the situation becomes somewhat complicated when a positive electric field is switched on. The electron-positron ratio decreased with the increasing atmospheric depth. When the strength of electric field is less than 600 V/cm, the number of electrons is still greater than positrons. For example, the number of electrons is 1.2 times of that of positrons in electric field of 500 V/cm at YBJ. While the electric field is greater than 600 V/cm, the number of electrons is less than the positrons. For instance, the number of electrons is about 89% of that of positrons in electric field of 800 V/cm at YBJ.

The number of electrons is greater than positrons, which is caused by Compton scattering effect. Meanwhile electrons are more easily affected by electric field than positrons in the same strength field [546]. So the total number of electrons and positrons may decline in a certain positive electric

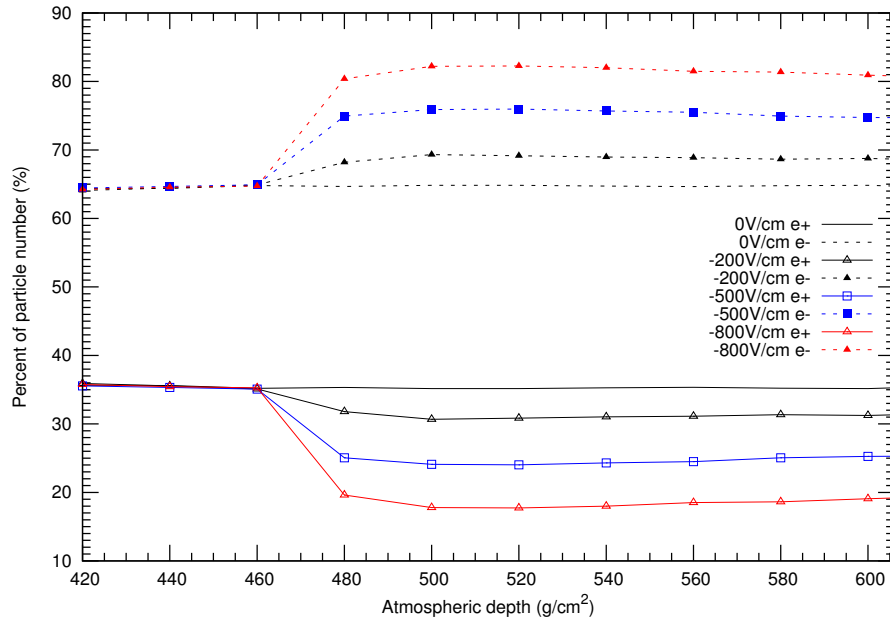


Fig. 101: Percent of electrons and positrons number as a function of atmospheric depth in different negative fields.

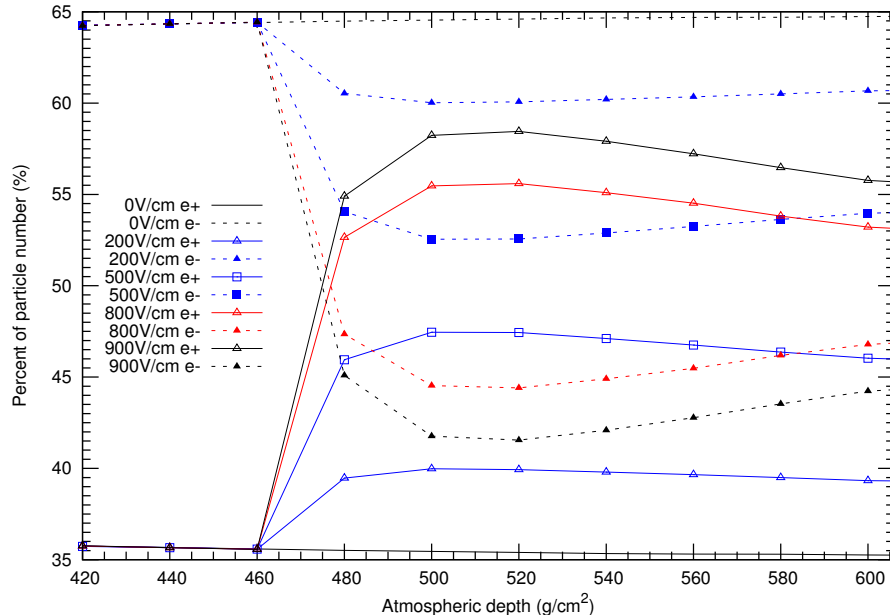


Fig. 102: Percent of electrons and positrons number as a function of atmospheric depth in different positive fields

field. In our simulations, the decline phenomenon occurs in the positive electric field less than 600 V/cm.

6.7.5. Conclusion

In this paper, Monte Carlo simulations were performed with CORSIKA7.3700 packages to study the intensity change of ground cosmic rays in near-earth thunderstorms electric field. The total number of electrons and positrons increases with the strength of the field in the negative field or in the positive field greater than 600 V/cm, while a certain degree of decline ($\sim 3\%$) occurs in the positive field less than 600 V/cm. Our simulation results are consistent with the experimental observations of ARGO-YBJ.

6.8. Effects of thunderstorms electric field on the energy of cosmic ray electron

Executive summary: Studies on energy changes of cosmic ray electron in thunderstorms electric field are very important to understand the acceleration mechanism of secondary charged particles caused by electric field. In this paper, Monte Carlo simulations were performed with CORSIKA to study the energy of cosmic ray electron in two typical electric fields. One is upper than the threshold field strength resulting in a runaway breakdown process (i.e. the order of 1 kV/cm), the other is lower than that (i.e. the order of 0.1 kV/cm). The energy spectra of electrons and positrons were obtained in different fields at different altitudes, especially above YBJ (4300 m a.s.l., Tibet, China). The decrease of the ground cosmic ray in intensity during thunderstorms observed in ARGO-YBJ was discussed by using the simulation results.

6.8.1. Introduction

The atmospheric electric field can change the intensity of the extensive air shower (EAS) by accelerating or decelerating the charged particles. Especially during thunderstorms, the electric field with strength of the order up to 1 kV/cm may appear [540]. In 1925, Wilson [552] suggested that the strong electric field in the thunderstorms can cause observable effects on electron which has very tiny mass in the secondary cosmic ray. When the electron gains more energy from the electric field than it loses in various interactions with air, the energy of the electron will increase and lead to the occurrence of "runaway" electron. However, the conventional critical electric field strength to start this process is quite high (~ 10 kV/cm) and was never measured in thunderclouds [553]. Gurevich et al. [541] proposed a new breakdown mechanism based on a relativistic runaway electron avalanche (RREA) in 1992. Marshall et al.[554] and Dwyer [555] pointed out that this threshold field is of the order ~ 1 kV/cm, about an order of magnitude lower than that needed for a conventional breakdown. The knocked-out electrons from the collisions of shower particles with air molecules or atoms are accelerated in the thunderstorms electric field. Under optimal conditions [546], they can gain enough energy, then the free electrons may become runaway and ionize further molecules, which results in avalanche process. The RREA process is believed to be the reasonable explanation of the initiation of lightning.

For years, scientists have carried out lots of ground-based experiments to detect the thunderstorm ground enhancements (TGEs) [545] and masses of satellite-borne experiments to investigate the terrestrial gamma flashes (TGFs) [556, 557], trying to find the high-energy electrons accelerated by the thunderstorms electric field or the high-energy rays radiated by bremsstrahlung.

Buitink et al.[546] found that the particle count rates increased in the field of 1 kV/cm by simulating the primary proton with energy higher than 10^{16} eV. They also obtained the energy spectra of electrons and positrons at different altitudes. Vanyan et al.[556] discussed the energy spectra of the electrons and photons in the uniform electric fields 1.7-2.0 kV/cm by simulating the RREA process. Chilingarian et al.[558] introduced two component models of the TGE origin by recovering the energy spectra of electrons and gamma rays from the thunderclouds, the RREA process and the modification of energy spectra (MOS) process. Recently, an analytical approach for calculating energy spectra of relativistic runaway electron avalanches in air has been proposed by Cramer et al.[559]. In their work, the energy spectra of the runaway electron population and the dependence of electron avalanche development on properties were discussed in detail. They found that the diffusion in energy space helped maintain an exponential energy spectrum for electric field that approaches the runaway electron threshold field.

Several detection researches on correlations between the intensity of the ground cosmic ray and the thunderstorms electric field were carried out at YBJ (4300 m a.s.l., Tibet, China) [560, 547]. They found that the particle count rates were not always increase in the field, in some cases it would decline. In this work, Monte Carlo simulations were performed with CORSIKA to study the effects of thunderstorms electric field on the energy of electrons and positrons in secondary particles at altitudes from 6400 to 4400 m.

6.8.2. Simulation setup

CORSIKA is a detailed Monte Carlo program to study the evolution and properties of extensive air showers in the atmosphere [318]. In this work, we simulated the energy spectra of the electrons in different fields by using CORSIKA 7.3700. The primary particle is a vertical 770 GeV proton. QGSJETII-04 was used for the high-energy hadronic interactions while GHEISHA for the low energy ones. Since electrons and positrons predominate in the secondary charged particles of the cosmic rays, and the apparent acceleration (or deceleration) of electric field on electrons (or positrons) is more obvious, the effects of electric field on electrons (or positrons) were properly taken into account in this work.

It has been found that the strength of the thunderstorms electric field can be high up to 1 kV/cm or even higher at YBJ. In our simulations, the electric field distributes from 6400 to 4400 m. It can be calculated the threshold field of the RREA process at 4400 m is higher than 1.6 kV/cm by using the formula proposed by Symbalisty et al. [561].

6.8.3. Simulation results

In order to get clues in the mechanism of electron acceleration in the thunderclouds, we chose two typical electric fields to discuss the accelerating mechanism by analyzing the longitudinal development and energy distribution of secondary charged particles. One is above the critical field of the RREA process (i.e. ± 1.7 kV/cm) and the other is the field below this threshold (i.e. ± 0.4 kV/cm). In view of the acceleration of the field, we set the energy cutoff below which electrons and positrons are discarded at 0.1 MeV in the simulation.

(1) The longitudinal development of secondary particles

In our work, we took for granted the positive field was downward.

In the positive field, the positrons (or electrons) are accelerated (or decelerated) downward, and dependent on the strength of the field, the fluxes of electrons and positrons reaching earth surface may exhibit significant amplification.

(a) The longitudinal development of particles in electric field strength of 1.7 kV/cm

Figs. 103 show the simulation results in electric field strength of 1.7 kV/cm, which is above the threshold field of the RREA process. The number of electrons (or positrons) is plotted as a function of atmospheric depth. The blue and red lines represent the development of electrons and positrons, respectively. The dashed lines correspond to the absence of an electric field and the solid lines correspond to the presence of a field. As shown in Fig.1, the number of positrons exceeds the number of electrons in the positive field (accelerating the positrons), causing a positive charge excess. The sum of electrons and positrons increases obviously. In Fig.2, we can apparently see an explosive increase in the number of electrons when the negative field is switched on. High up in the atmosphere, the number of electrons increases exponentially, and reaching a maximum at an atmospheric depth ~ 560 g/cm². The energy cutoff at 0.1 MeV in our simulations may be of influence to the location of the maximum. These results are consistent with the theory of relativistic runaway electron avalanche (RREA).

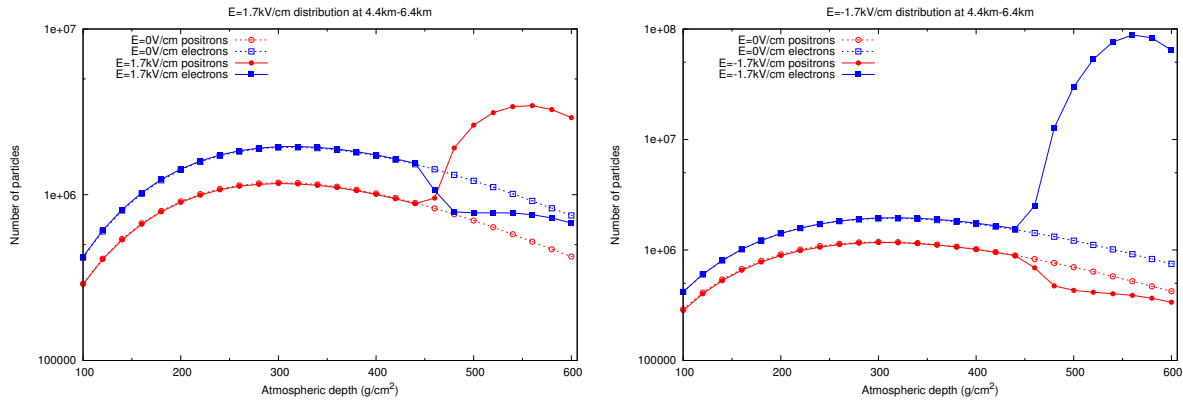


Figure 103: Number of electrons and positrons as a function of atmospheric depth in an electric field of 1.7 kV/cm (left) and -1.7 kV/cm (right). [Electric field area: 457-599 g/cm²]

- (b) The longitudinal development of particles in electric field strength of 0.4 kV/cm

In Fig.3, the total number of electrons and positrons is plotted as a function of atmospheric depth in electric field strength of 0.4 kV/cm, which is far below the threshold field of the RREA process. The black dashed line is the evolution of electrons and positrons in absence of an electric field. The red and blue lines represent that in 0.4 kV/cm and -0.4 kV/cm, respectively. As we can see from Fig.3, the total population of electrons and positrons increases in negative electric field. While in the positive field, a certain degree decline occurs. Our simulations have the similar phenomenon with the experimental observations of ARGO-YBJ.

- (2) The energy spectra of electrons and positrons

It is well known that the slowing-down force of an electron in the air varies with its energy [562]. As low energetic electrons propagate through air, they lose their energies predominately from ionization losses. The drag force decreases with an increase of the energy. Electrons with initial kinetic energies larger than the threshold value, ε_{th} (~ 1 MeV, suggested by Gurevich [563]), may run away. Conversely, high energetic electrons loose energies mostly due to radiative losses such as bremsstrahlung. While the energy exceeds the maximum value ε_{max} (described by Buitink et al. [546]), the energy radiation losses dominate. Namely, electrons with initial kinetic energy ranging from ε_{th} to ε_{max} , may be accelerated in applied field. Beyond this energy value, electrons lose energy rapidly.

In order to understand the acceleration mechanism of secondary charged particles caused by electric field inside the thunderclouds, Monte Carlo simulations were performed with CORSIKA to study the energy spectra of cosmic ray particles in two typical electric fields, as described in the following.

- (a) The energy spectra of electrons and positrons in strong electric field

At first, we compared the energy distribution of electrons with positrons at the altitude of 4400 m in the absence of a field. As shown in Fig.4, in low energy range (~ 1 -7 MeV), the ratio of electrons is larger than the ratio of positrons of the same energies. But the situation is reversed in higher energy range. That is to say that the ratio of positrons with energies above 7 MeV becomes more dominant. Based on the analysis above, it is easy to understand why the electric field alters the intensity of electrons more significantly than the intensity of the positrons.

Fig.5 shows the energy distribution of electrons and positrons at the altitude of 4400 m in the electric field of -1.7 kV/cm. The same shower in absence of a field is plotted for reference. The two vertical lines represent special energies. The solid line is the maximum energy ε_{max} , the main effect of the particle acceleration is expected to occur below this energy, and no significant change is expected above this energy. We can see in Fig.5 that $\varepsilon_{max} \sim 60$ MeV at the altitude of 4400 m in -1.7 kV/cm. The dashed line represents the critical energy $\varepsilon_c \sim 25$ MeV. When the energy is below ε_c , the particle multiplication comes from RREA process. In the range 1-25

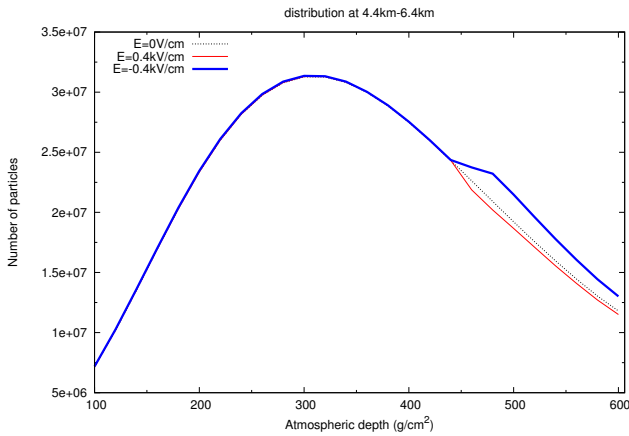


Fig. 104: Total number of electrons and positrons as a function of atmospheric depth in electric field strength of 0.4 kV/cm. (electric field area: 457-599 g/cm²)

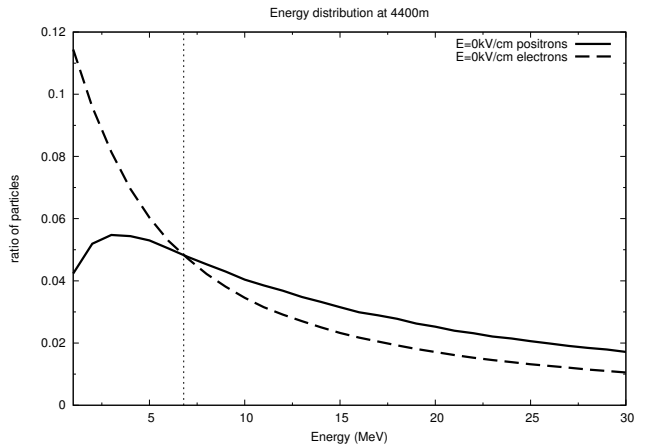


Fig. 105: The ratio distribution of electrons and positrons in energy range 1-30 MeV as a function of energy in absence of a field at the altitude of 4400 m

MeV, the energy spectrum can be fitted by exponential function. While the energy is above ε_c , the particle experiences a normal accelerating process. At 25-60 MeV, the spectrum becomes power law. It means that there are two modes of particle generation. Seen from Fig.5, the RREA mode with maximal energy of electrons is ~ 25 MeV and the normal mode accelerates electrons up to ~ 60 MeV. The normal accelerating mode regime is fast fading after 60 MeV. As for positrons, the number of the same energy declines due to the deceleration of the negative field.

Fig.6 shows energy distribution of electrons in different fields at the altitude of 4400 m. The spectrum shapes of the electron in -1.7 kV/cm and -1.8 kV/cm are similar, but the flux and the maximum energy ε_{max} increase with the increasing field. It is in agreement with previous results [546]. We also notice that the spectrum shape in -1.5 kV/cm is different from the others. Because the field strength of 1.5 kV/cm is smaller than the threshold electric field, the particles in this field do not undergo the RREA process.

Fig.7 indicates the variation of the energy distribution of electrons at different altitudes. The electric field is switched on from the altitude of 6400 m. From the figure, we can see the flux increases with the increasing electric field length and the maximum energy ε_{max} becomes greater as well. The acceleration effects of the field length on particles are quite obvious.

- (b) The energy spectra of electrons and positrons in an electric field of 0.4 kV/cm

As shown in Fig.8, the positrons are accelerated and the electrons are decelerated in the positive field. The red bold line corresponds to the change number of the positrons, and the dashed blue line to the change of the electrons and the continuous thin line to the change of total particles. We can see in Fig.8 that the increased number of positrons is apparently smaller than the decreased number of electrons of the same energies especially when the energy is below 20 MeV. There are two main factors may be taking into consideration. One is that the electric field has more obvious effects on the electrons which have smaller energy than the positrons. The other is that the number of positrons is less than the number of electrons due to Compton scattering effect. As a result, the change of the total number of positrons and electrons is negative in the energy range 1-20 MeV. While the energy is above 20 MeV, the effect of the electric field on electrons (or positrons) is very small. That is, the total number will decline in positive field of 0.4 kV/cm. The simulation results support the experimental observations of ARGO-YBJ.

Fig.9 shows the variation of the energy distribution of positrons in an electric field of 0.4 kV/cm

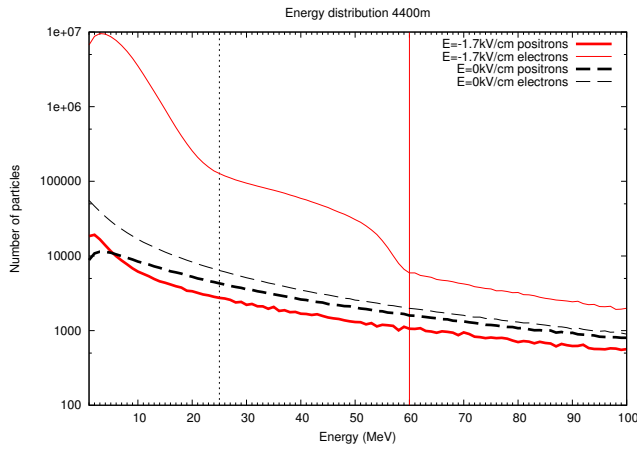


Fig. 106: Energy distribution of electrons and positrons in electric field of -1.7 kV/cm and the same in absence of a field at the altitude of 4400 m

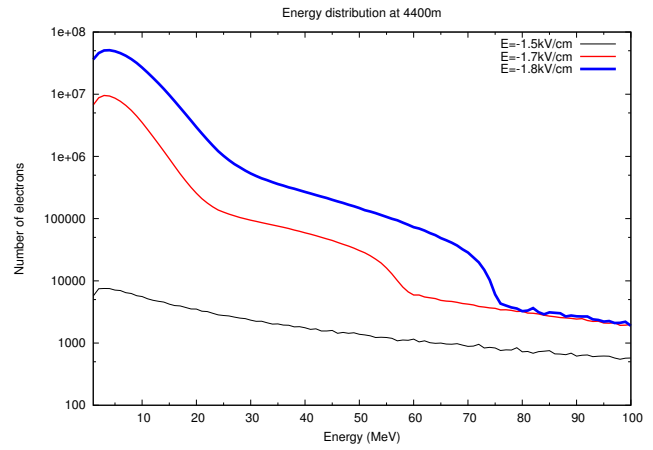


Fig. 107: Electron energy spectra at 4400 m altitude in different fields

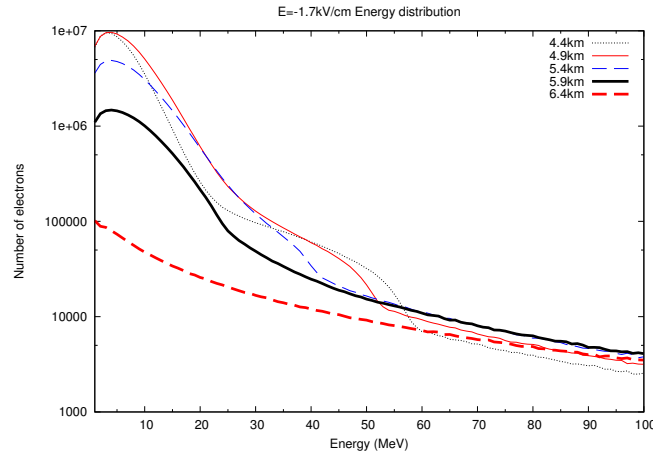


Fig. 108: Electron energy spectra at different altitudes in an electric field of -1.7 kV/cm

at different altitudes. The electric field is switched on from the altitude of 6400 m . The flux of the positrons does not vary obviously; it decreases with the increasing electric field length. This result seems to be in contradiction to the result in strong field which is upper than the threshold field of the RREA process. It is reasonable because the energy gains from the small field are too weak to compensate the energy losses due to ionization in air with the decreasing altitude. However, when the applied field is strong enough, as shown in Fig.7, the energy gains become bigger and bigger with the increasing electric field length, leading to the enhancement of the particle flux.

6.8.4. Conclusion

In this paper, Monte Carlo simulations were performed with CORSIKA to study the effects of thunderstorms electric field on electrons and positrons in secondary particles. We chose two typical electric fields to analyze the accelerating mechanism of secondary charged particles at altitudes from 6400 m to 4400 m . One is above the critical field of the RREA process ($\pm 1.7 \text{ kV/cm}$) and the other is the field below this threshold ($\pm 0.4 \text{ kV/cm}$).

The intensity of electrons increases exponentially in an electric field of -1.7 kV/cm , which is consistent with the theory of relativistic runaway electron avalanche (RREA). Through analyzing the energy distribution of the electrons, we can see there are two modes of the acceleration in strong field. The

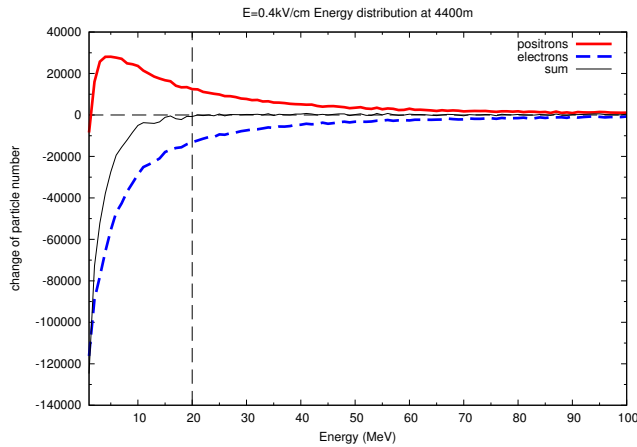


Fig. 109: The change of particle number as a function of energy in an electric field of 0.4 kV/cm at the altitude of 4400 m

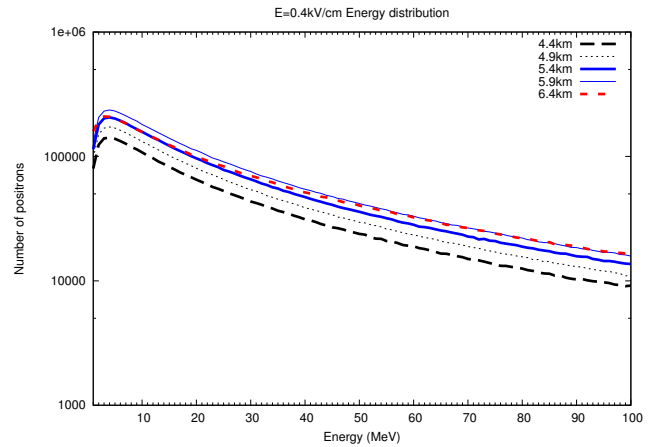


Fig. 110: Positron energy spectra at different altitudes in an electric field of 0.4 kV/cm

RREA mode with maximal energy of electrons is \sim 25 MeV and the normal mode accelerates electrons up to \sim 60 MeV. The normal accelerating mode regime is fast fading after 60 MeV. We also discussed energy distribution of electrons in different negative fields at the altitude of 4400 m and the same in negative field of 1.7 kV/cm at different altitudes.

In a positive electric field strength of 0.4 kV/cm, the total number of electrons and positrons declines to some extent. Seen from the energy distribution, the total number of the electrons and positrons will decline in energy range of 20 MeV. Here may be two main reasons for this. One is that the electric field has more obvious effects on the electrons which have smaller energy than the positrons, the other is that the number of positrons is less than the number of electrons due to Compton scattering effect. These simulation results support the experimental observations of ARGO-YBJ.

In this work, we just simulated the case of uniform electric field and the primary proton of 770 GeV. Combined with the ambient electric field within thunderclouds, more cases (such as the different primary particle types, energies, incidence directions etc.) will be taken into account in further study.

References

- [1] H. He, Lhaaso Collaboration. “Design highlights and status of the LHAASO project”. In “34th International Cosmic Ray Conference (ICRC2015)”, , vol. 34 (2015), p. 1010.
- [2] B. Bartoli, P. Bernardini, *et al.* “CRAB NEBULA: FIVE-YEAR OBSERVATION WITH ARGO-YBJ”. The Astrophysical Journal, **798**(2), (2015) p. 119.
URL <http://dx.doi.org/10.1088/0004-637x/798/2/119>
- [3] Franceschini, A., Rodighiero, G., Vaccari, M. “Extragalactic optical-infrared background radiation, its time evolution and the cosmic photon-photon opacity”. *A&A*, **487**(3), (2008) pp. 837–852.
URL <http://dx.doi.org/10.1051/0004-6361:200809691>
- [4] Y. Liu, Z. Cao, *et al.* “Expectation on Observation of Supernova Remnants with the LHAASO Project”. *Astrophys. J.*, **826**(1), (2016) p. 63. [1605.05472](https://arxiv.org/abs/1605.05472).
URL <http://dx.doi.org/10.3847/0004-637X/826/1/63>
- [5] F. Acero, M. Ackermann, *et al.* “Fermi Large Area Telescope Third Source Catalog”. *ApJS*, **218**, 23. [1501.02003](https://arxiv.org/abs/1501.02003).
URL <http://dx.doi.org/10.1088/0067-0049/218/2/23>
- [6] H. Li, Y. Chen. “ γ -rays from molecular clouds illuminated by accumulated diffusive protons from supernova remnant W28”. *Monthly Notices of the Royal Astronomical Society: Letters*, **409**(1), (2010) pp. L35–L38. ISSN 1745-3925. <http://oup.prod.sis.lan/mnrasl/article-pdf/409/1/L35/3231385/409-1-L35.pdf>.
URL <http://dx.doi.org/10.1111/j.1745-3933.2010.00944.x>
- [7] —. “ γ -rays from molecular clouds illuminated by accumulated diffusive protons – II. Interacting supernova remnants”. *Monthly Notices of the Royal Astronomical Society*, **421**(2), (2012) pp. 935–942. ISSN 0035-8711. <http://oup.prod.sis.lan/mnras/article-pdf/421/2/935/3909156/mnras0421-0935.pdf>.
URL <http://dx.doi.org/10.1111/j.1365-2966.2012.20270.x>
- [8] M. Ackermann, M. Ajello, *et al.* “A cocoon of freshly accelerated cosmic rays detected by fermi in the cygnus superbubble”. *Science*, **334**(6059), (2011) pp. 1103–1107. ISSN 0036-8075. <http://science.sciencemag.org/content/334/6059/1103.full.pdf>.
URL <http://dx.doi.org/10.1126/science.1210311>
- [9] B. Bartoli, P. Bernardini, *et al.* “IDENTIFICATION OF THE TeV GAMMA-RAY SOURCE ARGO j2031+4157 WITH THE CYGNUS COCOON”. *The Astrophysical Journal*, **790**(2), (2014) p. 152.
URL <http://dx.doi.org/10.1088/0004-637x/790/2/152>
- [10] A. A. Abdo, B. Allen, *et al.* “Discovery of TeV gamma-ray emission from the cygnus region of the galaxy”. *The Astrophysical Journal*, **658**(1), (2007) pp. L33–L36.
URL <http://dx.doi.org/10.1086/513696>
- [11] —. “TeV gamma-ray sources from a survey of the galactic plane with milagro”. *The Astrophysical Journal*, **664**(2), (2007) pp. L91–L94.
URL <http://dx.doi.org/10.1086/520717>
- [12] Yang, Rui-zhi, Aharonian, Felix. “Diffuse emission near the young massive cluster ngc 3603”. *A&A*, **600**, (2017) p. A107.
URL <http://dx.doi.org/10.1051/0004-6361/201630213>
- [13] A. A. Abdo, B. T. Allen, *et al.* “MILAGRO OBSERVATIONS OF MULTI-TeV EMISSION FROM GALACTIC SOURCES IN THE FERMIBRIGHT SOURCE LIST”. *The Astrophysical Journal*, **700**(2), (2009) pp. L127–L131.
URL <http://dx.doi.org/10.1088/0004-637x/700/2/1127>
- [14] A. U. Abeysekara, A. Albert, *et al.* “Extended gamma-ray sources around pulsars constrain the origin of the positron flux at earth”. *Science*, **358**(6365), (2017) pp. 911–914. ISSN 0036-8075. <http://science.sciencemag.org/content/358/6365/911.full.pdf>.
URL <http://dx.doi.org/10.1126/science.aan4880>
- [15] Ahnen, M. L., Ansoldi, S., *et al.* “Search for vhe gamma-ray emission from geminga pulsar and nebula with the magic telescopes”. *A&A*, **591**, (2016) p. A138.
URL <http://dx.doi.org/10.1051/0004-6361/201527722>
- [16] A. O’Faolain de Bhroithe, VERITAS collaboration. “VERITAS observations of exceptionally bright TeV flares from LS I +61° 303”. arXiv e-prints. [1508.06800](https://arxiv.org/abs/1508.06800).
- [17] HESS Collaboration, A. Abramowski, *et al.* “Acceleration of petaelectronvolt protons in the Galactic Centre”. *Nature*, **531**, (2016) pp. 476–479. [1603.07730](https://arxiv.org/abs/1603.07730).
URL <http://dx.doi.org/10.1038/nature17147>
- [18] M. Ackermann, A. Albert, *et al.* “The Spectrum and Morphology of the Fermi Bubbles”. *ApJ*, **793**, 64. [1407.1407](https://arxiv.org/abs/1407.1407).

7905.
URL <http://dx.doi.org/10.1088/0004-637X/793/1/64>
- [19] R. M. Crocker, F. Aharonian. “Fermi Bubbles: Giant, Multibillion-Year-Old Reservoirs of Galactic Center Cosmic Rays”. *Phys. Rev. Lett.*, **vol. 106**, 101102. [1008.2658](#).
URL <http://dx.doi.org/10.1103/PhysRevLett.106.101102>
- [20] Y. Q. Guo, H. B. Hu, *et al.*. “Pinpointing the Knee of Cosmic Rays with Diffuse PeV γ -Rays and Neutrinos”. *ApJ*, **vol. 795**, 100. [1312.7616](#).
URL <http://dx.doi.org/10.1088/0004-637X/795/1/100>
- [21] Z. Cao. “Status of LHAASO updates from ARGO-YBJ”. *Nuclear Instruments and Methods in Physics Research A*, **vol. 742**, (2014) pp. 95–98.
URL <http://dx.doi.org/10.1016/j.nima.2013.12.012>
- [22] “Ska1 system baseline design”.
URL <https://www.skatelescope.org/key-documents/>
- [23] J. Vink, J. Bleeker, *et al.*. “The X-ray synchrotron emission of RCW 86 and the implications for its age”. *Astrophys. J.*, **vol. 648**, (2006) pp. L33–L38. [astro-ph/0607307](#).
URL <http://dx.doi.org/10.1086/507628>
- [24] M. Aartsen, M. Ackermann, *et al.*. “Multimessenger observations of a flaring blazar coincident with high-energy neutrino icecube-170922a”. *Science*, **vol. 361**(6398). ISSN 0036-8075. <https://science.sciencemag.org/content/361/6398/eaat1378.full.pdf>.
URL <http://dx.doi.org/10.1126/science.aat1378>
- [25] B. Bartoli, P. Bernardini, *et al.*. “Long-term monitoring of MRK 501 for its very high energy γ emission and a flare in 2011 october”. *The Astrophysical Journal*, **vol. 758**(1), (2012) p. 2.
URL <http://dx.doi.org/10.1088/0004-637X/758/1/2>
- [26] A. Dominguez, *et al.*. “Extragalactic Background Light Inferred from AEGIS Galaxy SED-type Fractions”. *Mon. Not. Roy. Astron. Soc.*, **vol. 410**, (2011) p. 2556. [1007.1459](#).
URL <http://dx.doi.org/10.1111/j.1365-2966.2010.17631.x>
- [27] Q. Yuan, H.-L. Huang, X.-J. Bi, H.-H. Zhang. “Measuring the extragalactic background light from very high energy gamma-ray observations of blazars”, **2012**. [1212.5866](#).
- [28] M. Ackermann, K. Asano, *et al.*. “Fermi Observations of GRB 090510: A Short-Hard Gamma-ray Burst with an Additional, Hard Power-law Component from 10 keV TO GeV Energies”. *ApJ*, **vol. 716**, (2010) pp. 1178–1190. [1005.2141](#).
URL <http://dx.doi.org/10.1088/0004-637X/716/2/1178>
- [29] A. A. Abdo, M. Ackermann, *et al.*. “Fermi LAT Discovery of Extended Gamma-Ray Emission in the Direction of Supernova Remnant W51C”. *ApJL*, **vol. 706**, (2009) pp. L1–L6. [0910.0908](#).
URL <http://dx.doi.org/10.1088/0004-637X/706/1/L1>
- [30] —. “Fermi Large Area Telescope Observations of Markarian 421: The Missing Piece of its Spectral Energy Distribution”. *ApJ*, **vol. 736**, 131. [1106.1348](#).
URL <http://dx.doi.org/10.1088/0004-637X/736/2/131>
- [31] K. Murase, C. D. Dermer, H. Takami, G. Migliori. “Blazars as Ultra-high-energy Cosmic-ray Sources: Implications for TeV Gamma-Ray Observations”. *ApJ*, **vol. 749**, 63. [1107.5576](#).
URL <http://dx.doi.org/10.1088/0004-637X/749/1/63>
- [32] Kalashev, O. E. and Kido, E. “Simulations of ultra-high-energy cosmic rays propagation”. *Journal of Experimental and Theoretical Physics*, **vol. 120**(5), (2015) pp. 790–797. ISSN 1090-6509.
URL <http://dx.doi.org/10.1134/S1063776115040056>
- [33] Y. Inoue, Y. T. Tanaka. “LOWER BOUND ON THE COSMIC TeV GAMMA-RAY BACKGROUND RADIATION”. *The Astrophysical Journal*, **vol. 818**(2), (2016) p. 187.
URL <http://dx.doi.org/10.3847/0004-637X/818/2/187>
- [34] J. D. Finke, S. Razzaque, C. D. Dermer. “Modeling the Extragalactic Background Light from Stars and Dust”. *ApJ*, **vol. 712**(1), (2010) pp. 238–249. [0905.1115](#).
URL <http://dx.doi.org/10.1088/0004-637X/712/1/238>
- [35] M. Boezio, V. Bonvicini, *et al.*. “The cosmic-ray proton and helium spectra measured with the CAPRICE98 balloon experiment”. *Astroparticle Physics*, **vol. 19**, (2003) pp. 583–604. [astro-ph/0212253](#).
URL [http://dx.doi.org/10.1016/S0927-6505\(02\)00267-0](http://dx.doi.org/10.1016/S0927-6505(02)00267-0)
- [36] S. Haino, T. Sanuki, *et al.*. “Measurements of primary and atmospheric cosmic-ray spectra with the bess-tev spectrometer”. *Physics Letters B*, **vol. 594**(1), (2004) pp. 35 – 46. ISSN 0370-2693.
URL <http://dx.doi.org/https://doi.org/10.1016/j.physletb.2004.05.019>
- [37] A. D. Panov, *et al.*. “Elemental Energy Spectra of Cosmic Rays from the Data of the ATIC-2 Experiment”. *Bull. Russ. Acad. Sci. Phys.*, **vol. 71**, (2007) pp. 494–497. [Izv. Ross. Akad. Nauk Ser. Fiz.71,512(2007)], [astro-ph/0612377](#).

- URL <http://dx.doi.org/10.3103/S1062873807040168>
- [38] Y. S. Yoon, H. S. Ahn, *et al.* “COSMIC-RAY PROTON AND HELIUM SPECTRA FROM THE FIRST CREAM FLIGHT”. *The Astrophysical Journal*, **vol. 728**(2), (2011) p. 122.
URL <http://dx.doi.org/10.1088/0004-637x/728/2/122>
- [39] K. Asakimori, T. H. Burnett, *et al.* “Cosmic-ray proton and helium spectra: Results from the JACEE experiment”. *The Astrophysical Journal*, **vol. 502**(1), (1998) pp. 278–283.
URL <http://dx.doi.org/10.1086/305882>
- [40] T. Antoni, *et al.* “KASCADE measurements of energy spectra for elemental groups of cosmic rays: Results and open problems”. *Astropart. Phys.*, **vol. 24**, (2005) pp. 1–25. [astro-ph/0505413](http://arxiv.org/abs/astro-ph/0505413).
URL <http://dx.doi.org/10.1016/j.astropartphys.2005.04.001>
- [41] E. Berezhko, S. Knurenko, L. Ksenofontov. “Composition of cosmic rays at ultra high energies”. *Astroparticle Physics*, **vol. 36**(1), (2012) pp. 31 – 36. ISSN 0927-6505.
URL <http://dx.doi.org/https://doi.org/10.1016/j.astropartphys.2012.04.014>
- [42] A. D. Panov, J. H. Adams, *et al.* “Energy spectra of abundant nuclei of primary cosmic rays from the data of atic-2 experiment: Final results”. *Bulletin of the Russian Academy of Sciences: Physics*, **vol. 73**(5), (2009) pp. 564–567. ISSN 1934-9432.
URL <http://dx.doi.org/10.3103/S1062873809050098>
- [43] J. R. Hörandel. “A review of experimental results at the knee”. *Journal of Physics: Conference Series*, **vol. 47**, (2006) pp. 41–50.
URL <http://dx.doi.org/10.1088/1742-6596/47/1/005>
- [44] J. Abraham, P. Abreu, *et al.* “Measurement of the depth of maximum of extensive air showers above 10^{18} eV”. *Phys. Rev. Lett.*, **vol. 104**, (2010) p. 091101.
URL <http://dx.doi.org/10.1103/PhysRevLett.104.091101>
- [45] R. Abbasi, M. Abe, *et al.* “Study of ultra-high energy cosmic ray composition using telescope array’s middle drum detector and surface array in hybrid mode”. *Astroparticle Physics*, **vol. 64**, (2015) pp. 49 – 62. ISSN 0927-6505.
URL <http://dx.doi.org/https://doi.org/10.1016/j.astropartphys.2014.11.004>
- [46] R. U. Abbasi, T. Abu-Zayyad, *et al.* “Indications of proton-dominated cosmic-ray composition above 1.6 eev”. *Phys. Rev. Lett.*, **vol. 104**, (2010) p. 161101.
URL <http://dx.doi.org/10.1103/PhysRevLett.104.161101>
- [47] J. R. Hoerandel. “On the knee in the energy spectrum of cosmic rays”. *Astropart. Phys.*, **vol. 19**, (2003) pp. 193–220. [astro-ph/0210453](http://arxiv.org/abs/astro-ph/0210453).
URL [http://dx.doi.org/10.1016/S0927-6505\(02\)00198-6](http://dx.doi.org/10.1016/S0927-6505(02)00198-6)
- [48] Y. V. Stenkin, J. F. Valdés-Galicia. “On the Neutron Bursts Origin”. *Modern Physics Letters A*, **vol. 17**(26), (2002) pp. 1745–1751.
URL <http://dx.doi.org/10.1142/S0217732302008137>
- [49] A. Aab, *et al.* “Energy Estimation of Cosmic Rays with the Engineering Radio Array of the Pierre Auger Observatory”. Submitted to: *Phys. Rev. D*. [1508.04267](https://arxiv.org/abs/1508.04267).
- [50] P. A. Bezyazeekov, *et al.* “Radio measurements of the energy and the depth of the shower maximum of cosmic-ray air showers by Tunka-Rex”. *JCAP*, **vol. 1601**(01), (2016) p. 052. [1509.05652](https://arxiv.org/abs/1509.05652).
URL <http://dx.doi.org/10.1088/1475-7516/2016/01/052>
- [51] S. Buitink, A. Corstanje, *et al.* “Method for high precision reconstruction of air shower X_{\max} using two-dimensional radio intensity profiles”. *Phys. Rev. D*, **vol. 90**, (2014) p. 082003.
URL <http://dx.doi.org/10.1103/PhysRevD.90.082003>
- [52] B.-B. Zhang, B. Zhang, *et al.* “A Comprehensive Analysis of Fermi Gamma-ray Burst Data. I. Spectral Components and the Possible Physical Origins of LAT/GBM GRBs”. *ApJ*, **vol. 730**(2), 141. [1009.3338](https://arxiv.org/abs/1009.3338).
URL <http://dx.doi.org/10.1088/0004-637X/730/2/141>
- [53] S. Oh, J. W. Bieber, *et al.* “Record neutron monitor counting rates from galactic cosmic rays”. *Journal of Geophysical Research: Space Physics*, **vol. 118**(9), (2013) pp. 5431–5436. <https://agupubs.onlinelibrary.wiley.com/doi/10.1002/jgra.50544>.
URL <http://dx.doi.org/10.1002/jgra.50544>
- [54] W. Nuntiyakul, P. Evenson, *et al.* “LATITUDE SURVEY INVESTIGATION OF GALACTIC COSMIC RAY SOLAR MODULATION DURING 1994-2007”. *The Astrophysical Journal*, **vol. 795**(1), (2014) p. 11.
URL <http://dx.doi.org/10.1088/0004-637x/795/1/11>
- [55] T. Yeeram, D. Ruffolo, *et al.* “COROTATING SOLAR WIND STRUCTURES AND RECURRENT TRAINS OF ENHANCED DIURNAL VARIATION IN GALACTIC COSMIC RAYS”. *The Astrophysical Journal*, **vol. 784**(2), (2014) p. 136.
URL <http://dx.doi.org/10.1088/0004-637x/784/2/136>
- [56] B. Bartoli, P. Bernardini, *et al.* “ARGO-YBJ Observation of the Large-scale Cosmic Ray Anisotropy During the Solar Minimum between Cycles 23 and 24”. *ApJ*, **vol. 809**, 90.

- URL <http://dx.doi.org/10.1088/0004-637X/809/1/90>
- [57] R. A. Mewaldt, C. M. S. Cohen, *et al.* “Observations of the December 2006 solar energetic particle events with the Low Energy Telescope (LET) on STEREO”. International Cosmic Ray Conference, **vol. 1**, (2008) pp. 107–110.
- [58] X. Wang, J. Giacalone, *et al.* “Particles Acceleration in Converged Two Shocks”, **2015**. [1509.07934](https://arxiv.org/abs/1509.07934).
- [59] M. A. Malkov, P. H. Diamond, *et al.* “Analytic Solution for Self-regulated Collective Escape of Cosmic Rays from Their Acceleration Sites”. *ApJ*, **vol. 768**, 73. [1207.4728](https://arxiv.org/abs/1207.4728).
- URL <http://dx.doi.org/10.1088/0004-637X/768/1/73>
- [60] M. Ackermann, M. Ajello, *et al.* “THE FIRSTFERMI-LAT GAMMA-RAY BURST CATALOG”. *The Astrophysical Journal Supplement Series*, **vol. 209**(1), (2013) p. 11.
- URL <http://dx.doi.org/10.1088/0067-0049/209/1/11>
- [61] Yang, Rui-zhi, de Oña Wilhelmi, Emma, Aharonian, Felix. “Probing cosmic rays in nearby giant molecular clouds with the fermi large area telescope”. *A&A*, **vol. 566**, (2014) p. A142.
- URL <http://dx.doi.org/10.1051/0004-6361/201321044>
- [62] Z. Cao. “A future project at tibet: the large high altitude air shower observatory (LHAASO)”. *Chinese Physics C*, **vol. 34**, (2010) pp. 249–252.
- URL <http://dx.doi.org/10.1088/1674-1137/34/2/018>
- [63] “Fermi background models”.
- URL <http://fermi.gsfc.nasa.gov/ssc/data/access/lat/BackgroundModels.html>
- [64] B. Acharya, M. Actis, *et al.* “Introducing the cta concept”. *Astroparticle Physics*, **vol. 43**, (2013) pp. 3 – 18. ISSN 0927-6505. Seeing the High-Energy Universe with the Cherenkov Telescope Array - The Science Explored with the CTA.
- URL <http://dx.doi.org/https://doi.org/10.1016/j.astropartphys.2013.01.007>
- [65] A. Abeysekara, R. Alfaro, *et al.* “Sensitivity of the high altitude water cherenkov detector to sources of multi-tev gamma rays”. *Astroparticle Physics*, **vol. 50-52**, (2013) pp. 26 – 32. ISSN 0927-6505.
- URL <http://dx.doi.org/https://doi.org/10.1016/j.astropartphys.2013.08.002>
- [66] M. Tluczykont, D. Hampf, *et al.* “The hiscore concept for gamma-ray and cosmic-ray astrophysics beyond 10tev”. *Astroparticle Physics*, **vol. 56**, (2014) pp. 42 – 53. ISSN 0927-6505.
- URL <http://dx.doi.org/https://doi.org/10.1016/j.astropartphys.2014.03.004>
- [67] F. A. Aharonian. “Gamma rays from supernova remnants”. *Astroparticle Physics*, **vol. 43**, (2013) pp. 71 – 80. ISSN 0927-6505. Seeing the High-Energy Universe with the Cherenkov Telescope Array - The Science Explored with the CTA.
- URL <http://dx.doi.org/https://doi.org/10.1016/j.astropartphys.2012.08.007>
- [68] M. Ackermann, M. Ajello, *et al.* “Detection of the characteristic pion-decay signature in supernova remnants”. *Science*, **vol. 339**(6121), (2013) pp. 807–811. ISSN 0036-8075. <http://science.sciencemag.org/content/339/6121/807.full.pdf>.
- URL <http://dx.doi.org/10.1126/science.1231160>
- [69] M. G. Aartsen, M. Ackermann, *et al.* “Observation of High-Energy Astrophysical Neutrinos in Three Years of IceCube Data”. *Phys. Rev. Lett.*, **vol. 113**, 101101. [1405.5303](https://arxiv.org/abs/1405.5303).
- URL <http://dx.doi.org/10.1103/PhysRevLett.113.101101>
- [70] S. Cui, Y. Liu, Y. Liu, X. Ma. “Simulation on gamma ray astronomy research with LHAASO-KM2A”. *Astroparticle Physics*, **vol. 54**, (2014) pp. 86–92.
- URL <http://dx.doi.org/10.1016/j.astropartphys.2013.11.003>
- [71] I. Collaboration, M. G. Aartsen, *et al.* “Search for galactic pev gamma rays with the icecube neutrino observatory”. *Phys. Rev. D*, **vol. 87**, (2013) p. 062002.
- URL <http://dx.doi.org/10.1103/PhysRevD.87.062002>
- [72] B. Bartoli, P. Bernardini, *et al.* “TeV GAMMA-RAY SURVEY OF THE NORTHERN SKY USING THE ARGO-YBJ DETECTOR”. *The Astrophysical Journal*, **vol. 779**(1), (2013) p. 27.
- URL <http://dx.doi.org/10.1088/0004-637x/779/1/27>
- [73] R. Atkins, W. Benbow, *et al.* “TeV gamma-ray survey of the northern hemisphere sky using the milagro observatory”. *The Astrophysical Journal*, **vol. 608**(2), (2004) pp. 680–685.
- URL <http://dx.doi.org/10.1086/420880>
- [74] F. Aharonian, A. G. Akhperjanian, *et al.* “The h.e.s.s. survey of the inner galaxy in very high energy gamma rays”. *The Astrophysical Journal*, **vol. 636**(2), (2006) pp. 777–797.
- URL <http://dx.doi.org/10.1086/498013>
- [75] R. A. Ong. “Recent Results on Galactic Sources in Cygnus by VERITAS”. In “Proceedings, 33rd International Cosmic Ray Conference (ICRC2013): Rio de Janeiro, Brazil, July 2-9, 2013”, **(2013)**, p. 0243. [1307.5003](https://arxiv.org/abs/1307.5003).
- URL <http://www.cbpf.br/%7Eicrc2013/papers/icrc2013-0243.pdf>
- [76] “Tevcat catalogue”.
- URL <http://tevcat.uchicago.edu>

- [77] F. A. Aharonian, A. G. Akhperjanian, *et al.*. “The energy spectrum of TeV gamma rays from the crab nebula as measured by the HEGRA system of imaging air cerenkov telescopes”. *The Astrophysical Journal*, **vol. 539**(1), (2000) pp. 317–324.
URL <http://dx.doi.org/10.1086/309225>
- [78] Aharonian, F., Akhperjanian, A. G., *et al.*. “Observations of the crab nebula with hess”. *A&A*, **vol. 457**(3), (2006) pp. 899–915.
URL <http://dx.doi.org/10.1051/0004-6361:20065351>
- [79] J. Aleksić, *et al.*. “Measurement of the Crab Nebula spectrum over three decades in energy with the MAGIC telescopes”. *JHEA*, **vol. 5-6**, (2015) pp. 30–38. [1406.6892](https://arxiv.org/abs/1406.6892).
URL <http://dx.doi.org/10.1016/j.jheap.2015.01.002>
- [80] A. A. Abdo, B. T. Allen, *et al.*. “OBSERVATION AND SPECTRAL MEASUREMENTS OF THE CRAB NEBULA WITH MILAGRO”. *The Astrophysical Journal*, **vol. 750**(1), (2012) p. 63.
URL <http://dx.doi.org/10.1088/0004-637x/750/1/63>
- [81] M. Tavani, A. Bulgarelli, *et al.*. “Discovery of powerful gamma-ray flares from the crab nebula”. *Science*, **vol. 331**(6018), (2011) pp. 736–739. ISSN 0036-8075. <http://science.sciencemag.org/content/331/6018/736.full.pdf>.
URL <http://dx.doi.org/10.1126/science.1200083>
- [82] A. A. Abdo, M. Ackermann, *et al.*. “Gamma-ray flares from the crab nebula”. *Science*, **vol. 331**(6018), (2011) pp. 739–742. ISSN 0036-8075. <http://science.sciencemag.org/content/331/6018/739.full.pdf>.
URL <http://dx.doi.org/10.1126/science.1199705>
- [83] r. buehler, j. d. scargle, *et al.*. “Gamma-Ray Activity in the Crab Nebula: The Exceptional Flare of 2011 April”. *ApJ*, **vol. 749**, 26. [1112.1979](https://arxiv.org/abs/1112.1979).
URL <http://dx.doi.org/10.1088/0004-637X/749/1/26>
- [84] E. Striani, M. Tavani, *et al.*. “Variable Gamma-Ray Emission from the Crab Nebula: Short Flares and Long ”Waves””. *ApJ*, **vol. 765**, 52. [1302.4342](https://arxiv.org/abs/1302.4342).
URL <http://dx.doi.org/10.1088/0004-637X/765/1/52>
- [85] S. Vernetto. “Gamma ray sources observed with argo-ybj”. *Nuclear Physics B - Proceedings Supplements*, **vol. 239-240**, (2013) pp. 98 – 103. ISSN 0920-5632. Proceedings of the 9th workshop on Science with the New Generation of High Energy Gamma-ray Experiments: From high energy gamma sources to cosmic rays, one century after their discovery.
URL <http://dx.doi.org/https://doi.org/10.1016/j.nuclphysbps.2013.05.016>
- [86] E. Aliu, *et al.*. “A Search for Enhanced Very High Energy Gamma-Ray Emission from the 2013 March Crab Nebula Flare”. *Astrophys. J.*, **vol. 781**(1), (2014) p. L11. [1309.5949](https://arxiv.org/abs/1309.5949).
URL <http://dx.doi.org/10.1088/2041-8205/781/1/L11>
- [87] H.E.S.S. Collaboration, Abramowski, A., *et al.*. “H.e.s.s. observations of the crab during its march 2013 gev gamma-ray flare”. *A&A*, **vol. 562**, (2014) p. L4.
URL <http://dx.doi.org/10.1051/0004-6361/201323013>
- [88] Aharonian, F., Akhperjanian, A. G., *et al.*. “Primary particle acceleration above 100 tev in the shell-type supernova remnant rx j1713.7 - 3946 with deep h.e.s.s. observations (corrigendum)”. *A&A*, **vol. 531**, (2011) p. C1.
URL <http://dx.doi.org/10.1051/0004-6361/20066381e>
- [89] A. A. Abdo, M. Ackermann, *et al.*. “OBSERVATIONS OF THE YOUNG SUPERNOVA REMNANT RX j1713.7-3946 WITH THEFERMILARGE AREA TELESCOPE”. *The Astrophysical Journal*, **vol. 734**(1), (2011) p. 28.
URL <http://dx.doi.org/10.1088/0004-637x/734/1/28>
- [90] H. E. S. S. Collaboration, H. Abdalla, *et al.*. “H.E.S.S. observations of RX J1713.7-3946 with improved angular and spectral resolution: Evidence for gamma-ray emission extending beyond the X-ray emitting shell”. *Astron. Astrophys.*, **vol. 612**, A6. [1609.08671](https://arxiv.org/abs/1609.08671).
URL <http://dx.doi.org/10.1051/0004-6361/201629790>
- [91] M. L. Ahnen, S. Ansoldi, *et al.*. “A cut-off in the TeV gamma-ray spectrum of the SNR Cassiopeia A”. *Mon. Not. R. Astron. Soc.*, **vol. 472**, (2017) pp. 2956–2962. [1707.01583](https://arxiv.org/abs/1707.01583).
URL <http://dx.doi.org/10.1093/mnras/stx2079>
- [92] H.E.S.S. Collaboration, Abramowski, A., *et al.*. “Detailed spectral and morphological analysis of the shell type supernova remnant rcw 86”. *A&A*, **vol. 612**, (2018) p. A4.
URL <http://dx.doi.org/10.1051/0004-6361/201526545>
- [93] V. A. Acciari, E. Aliu, *et al.*. “DISCOVERY OF TeV GAMMA-RAY EMISSION FROMTYCHO’s SUPERNOVA REMNANT”. *The Astrophysical Journal*, **vol. 730**(2), (2011) p. L20.
URL <http://dx.doi.org/10.1088/2041-8205/730/2/120>
- [94] Albert, J., Aliu, E., *et al.*. “Observation of vhe s from cassiopeia a with the magic telescope”. *A&A*, **vol. 474**(3), (2007) pp. 937–940.

- URL <http://dx.doi.org/10.1051/0004-6361:20078168>
- [95] Aleksić, J., Alvarez, E. A., *et al.* “Morphological and spectral properties of the w51 region measured with the magic telescopes”. *A&A*, **vol. 541**, (2012) p. A13.
URL <http://dx.doi.org/10.1051/0004-6361/201218846>
- [96] V. A. Acciari, E. Aliu, *et al.* “OBSERVATION OF EXTENDED VERY HIGH ENERGY EMISSION FROM THE SUPERNOVA REMNANT IC 443 WITH VERITAS”. *The Astrophysical Journal*, **vol. 698**(2), (2009) pp. L133–L137.
URL <http://dx.doi.org/10.1088/0004-637x/698/2/1133>
- [97] F. Brun, M. de Naurois, *et al.* “Discovery of VHE gamma-ray emission from the W49 region with H.E.S.S.” In “25th Texas Symposium on Relativistic Astrophysics”, (2010), p. 201. [1104.5003](https://arxiv.org/abs/1104.5003)
- [98] V. A. Acciari, E. Aliu, *et al.* “DETECTION OF EXTENDED VHE GAMMA RAY EMISSION FROM g106.3+2.7 WITH VERITAS”. *The Astrophysical Journal*, **vol. 703**(1), (2009) pp. L6–L9.
URL <http://dx.doi.org/10.1088/0004-637x/703/1/16>
- [99] S. Archambault, A. Archer, *et al.* “Gamma-ray observations of tycho’s supernova remnant with VERITAS and Fermi”. *The Astrophysical Journal*, **vol. 836**(1), (2017) p. 23.
URL <http://dx.doi.org/10.3847/1538-4357/836/1/23>
- [100] B. Bartoli, P. Bernardini, *et al.* “Study of the Diffuse Gamma-Ray Emission from the Galactic Plane with ARGO-YBJ”. *ApJ*, **vol. 806**, 20. [1507.06758](https://arxiv.org/abs/1507.06758).
URL <http://dx.doi.org/10.1088/0004-637X/806/1/20>
- [101] A. Borione, M. A. Catanese, *et al.* “Constraints on gamma-ray emission from the galactic plane at 300 TeV”. *The Astrophysical Journal*, **vol. 493**(1), (1998) pp. 175–179.
URL <http://dx.doi.org/10.1086/305096>
- [102] I. V. Moskalenko, T. A. Porter, A. W. Strong. “Attenuation of very high energy gamma rays by the milky way interstellar radiation field”. *The Astrophysical Journal*, **vol. 640**(2), (2006) pp. L155–L158.
URL <http://dx.doi.org/10.1086/503524>
- [103] E. Dwek, F. Krennrich. “The extragalactic background light and the gamma-ray opacity of the universe”. *Astroparticle Physics*, **vol. 43**, (2013) pp. 112–133. [1209.4661](https://arxiv.org/abs/1209.4661).
URL <http://dx.doi.org/10.1016/j.astropartphys.2012.09.003>
- [104] T. V. Collaboration, V. A. Acciari, *et al.* “A connection between star formation activity and cosmic rays in the starburst galaxy m82”. *Nature*, **vol. 462**, (2009) p. 770.
URL <https://doi.org/10.1038/nature08557>
- [105] L. Costamante. “Gamma-rays from Blazars and the Extragalactic Background Light”. *Int. J. Mod. Phys.*, **vol. D22**(13), (2013) p. 1330025. [1309.0612](https://arxiv.org/abs/1309.0612).
URL <http://dx.doi.org/10.1142/S0218271813300255>
- [106] F. Aharonian, A. G. Akhperjanian, *et al.* “A low level of extragalactic background light as revealed by g-rays from blazars”. *Nature*, **vol. 440**, (2006) pp. 1018 EP –.
URL <https://doi.org/10.1038/nature04680>
- [107] M. Ackermann, M. Ajello, *et al.* “The imprint of the extragalactic background light in the gamma-ray spectra of blazars”. *Science*, **vol. 338**(6111), (2012) pp. 1190–1192. ISSN 0036-8075. <http://science.sciencemag.org/content/338/6111/1190.full.pdf>.
URL <http://dx.doi.org/10.1126/science.1227160>
- [108] H.E.S.S. Collaboration, Abramowski, A., *et al.* “Measurement of the extragalactic background light imprint on the spectra of the brightest blazars observed with h.e.s.s.” *A&A*, **vol. 550**, (2013) p. A4.
URL <http://dx.doi.org/10.1051/0004-6361/201220355>
- [109] J. Biteau, D. A. Williams. “The Extragalactic Background Light, the Hubble Constant, and Anomalies: Conclusions from 20 Years of TeV Gamma-ray Observations”. *ApJ*, **vol. 812**, 60. [1502.04166](https://arxiv.org/abs/1502.04166).
URL <http://dx.doi.org/10.1088/0004-637X/812/1/60>
- [110] J. Sitarek, J. Becerra Gonzalez, *et al.* “Detection of very-high-energy gamma rays from the most distant and gravitationally lensed blazar QSO B0218+35 using the MAGIC telescope system”. *PoS*, **vol. ICRC2015**, (2016) p. 825. [34,825(2015)], [1508.04580](https://arxiv.org/abs/1508.04580).
URL <http://dx.doi.org/10.22323/1.236.0825>
- [111] R. Mirzoyan. “Atel (2015), article #7416”, **2015**.
- [112] F. Aharonian, W. Essey, A. Kusenko, A. Prosekin. “Tev gamma rays from blazars beyond $z = 1$?” *Phys. Rev. D*, **vol. 87**, (2013) p. 063002.
URL <http://dx.doi.org/10.1103/PhysRevD.87.063002>
- [113] M. Meyer, D. Horns, M. Raue. “First lower limits on the photon-axion-like particle coupling from very high energy gamma-ray observations”. *Phys. Rev. D*, **vol. 87**, (2013) p. 035027.
URL <http://dx.doi.org/10.1103/PhysRevD.87.035027>
- [114] J. Biteau, D. A. Williams. “Gamma-ray cosmology and fundamental physics with TeV blazars: results from 20 years

- of observations”. PoS, **vol. ICRC2015**, (2016) p. 748. [34,748(2015)], [1508.06248](https://arxiv.org/abs/1508.06248).
URL <http://dx.doi.org/10.22323/1.236.0748>
- [115] C. L. Bhat, M. R. Issa, C. J. Mayer, A. W. Wolfendale. “Acceleration of cosmic rays in the loop i ’supernova remnant?’” *Nature*, **vol. 314**(6011), (1985) pp. 515–517. ISSN 1476-4687.
URL <http://dx.doi.org/10.1038/314515a0>
- [116] A. M. Hillas. “Can diffusive shock acceleration in supernova remnants account for high-energy galactic cosmic rays?” *Journal of Physics G: Nuclear and Particle Physics*, **vol. 31**(5), (2005) pp. R95–R131.
URL <http://dx.doi.org/10.1088/0954-3899/31/5/r02>
- [117] B. Katz, E. Waxman. “In which shell-type SNRs should we look for gamma-rays and neutrinos from p–p collisions?” *Journal of Cosmology and Astroparticle Physics*, **vol. 2008**(01), (2008) p. 018.
URL <http://dx.doi.org/10.1088/1475-7516/2008/01/018>
- [118] Z. Mao, Y.-W. Yu. “A statistical classification of the unassociated gamma-ray sources in the second fermi large area telescope catalog”. *Research in Astronomy and Astrophysics*, **vol. 13**(8), (2013) pp. 952–960.
URL <http://dx.doi.org/10.1088/1674-4527/13/8/007>
- [119] G. Joncas, L. A. Higgs. “The DRAO galactic-plane survey. II - Field at L = 105 deg”. *Astronomy and Astrophysics Suppl. Series*, **vol. 82**, (1990) pp. 113–144.
- [120] S. Pineault, G. Joncas. “G106.3+2.7: A supernova remnant in a late stage of evolution”. *The Astronomical Journal*, **vol. 120**(6), (2000) pp. 3218–3225.
URL <http://dx.doi.org/10.1086/316863>
- [121] R. C. Hartman, D. L. Bertsch, *et al.* “The Third EGRET Catalog of High-Energy Gamma-Ray Sources”. *ApJS*, **vol. 123**, (1999) pp. 79–202.
URL <http://dx.doi.org/10.1086/313231>
- [122] Q. Yuan, S. Liu, *et al.* “MODELING THE MULTI-WAVELENGTH EMISSION OF THE SHELL-TYPE SUPER-NOVA REMNANT RX J1713.7–3946”. *The Astrophysical Journal*, **vol. 735**(2), (2011) p. 120.
URL <http://dx.doi.org/10.1088/0004-637x/735/2/120>
- [123] Q. Yuan, S. Liu, X. Bi. “AN ATTEMPT AT a UNIFIED MODEL FOR THE GAMMA-RAY EMISSION OF SUPERNOVA REMNANTS”. *The Astrophysical Journal*, **vol. 761**(2), (2012) p. 133.
URL <http://dx.doi.org/10.1088/0004-637x/761/2/133>
- [124] Y. Uchiyama, F. A. Aharonian, *et al.* “Extremely fast acceleration of cosmic rays in a supernova remnant”. *Nature*, **vol. 449**, (2007) pp. 576 EP –.
URL <https://doi.org/10.1038/nature06210>
- [125] A. A. Abdo, M. Ackermann, *et al.* “Fermi Large Area Telescope Observations of the Crab Pulsar And Nebula”. *ApJ*, **vol. 708**, (2010) pp. 1254–1267. [0911.2412](https://arxiv.org/abs/0911.2412).
URL <http://dx.doi.org/10.1088/0004-637X/708/2/1254>
- [126] A. A. Abdo, M. Ackermann, *et al.* “Gamma-ray emission from the shell of supernova remnant w44 revealed by the fermi lat”. *Science*, **vol. 327**(5969), (2010) pp. 1103–1106. ISSN 0036-8075. <http://science.sciencemag.org/content/327/5969/1103.full.pdf>.
URL <http://dx.doi.org/10.1126/science.1182787>
- [127] H.E.S.S. Collaboration, Abramowski, A., *et al.* “A new snr with tev shell-type morphology: Hess j1731-347”. *A&A*, **vol. 531**, (2011) p. A81.
URL <http://dx.doi.org/10.1051/0004-6361/201016425>
- [128] L. Saha, T. Ergin, *et al.* “Origin of gamma-ray emission in the shell of Cassiopeia A”. *Astron. Astrophys.*, **vol. 563**, (2014) p. A88. [1401.5626](https://arxiv.org/abs/1401.5626).
URL <http://dx.doi.org/10.1051/0004-6361/201323218>
- [129] R. Hanbury Brown, C. Hazard. “A survey of 23 localized radio sources in the northern hemisphere”. *Mon. Not. R. Astron. Soc.*, **vol. 113**, (1953) p. 123.
URL <http://dx.doi.org/10.1093/mnras/113.2.123>
- [130] J. R. Dickel, W. J. M. van Breugel, R. G. Strom. “Radio Structure of the Remnant of Tycho’s Supernova (SN1572)”. *Astronomical Journal*, **vol. 101**, (1991) p. 2151.
URL <http://dx.doi.org/10.1086/115837>
- [131] U. Hwang, R. Petre, A. E. Szymkowiak, S. S. Holt. “Chandra Observations of Tycho’s Supernova Remnant”. *Journal of Astrophysics and Astronomy*, **vol. 23**, (2002) p. 81.
URL <http://dx.doi.org/10.1007/BF02702469>
- [132] A. Bamba, R. Yamazaki, J. S. Hiraga. “Chandra Observations of Galactic Supernova Remnant Vela Jr.: A New Sample of Thin Filaments Emitting Synchrotron X-Rays”. *ApJ*, **vol. 632**, (2005) pp. 294–301. [astro-ph/0506331](https://arxiv.org/abs/astro-ph/0506331).
URL <http://dx.doi.org/10.1086/432711>
- [133] W. Stroman, M. Pohl. “Radio Polarimetry Signatures of Strong Magnetic Turbulence in Supernova Remnants”. *ApJ*, **vol. 696**, (2009) pp. 1864–1870. [0902.1701](https://arxiv.org/abs/0902.1701).
URL <http://dx.doi.org/10.1088/0004-637X/696/2/1864>

- [134] S. Katsuda, R. Petre, *et al.* “X-RAY MEASURED DYNAMICS OF TYCHO's SUPERNOVA REMNANT”. The Astrophysical Journal, **vol. 709**(2), (2010) pp. 1387–1395.
URL <http://dx.doi.org/10.1088/0004-637x/709/2/1387>
- [135] F. Giordano, M. Naumann-Godo, *et al.* “FERMILARGE AREA TELESCOPE DETECTION OF THE YOUNG SUPERNOVA REMNANT TYCHO”. The Astrophysical Journal, **vol. 744**(1), (2011) p. L2.
URL <http://dx.doi.org/10.1088/2041-8205/744/1/12>
- [136] S. R. Kelner, F. A. Aharonian, V. V. Bugayov. “Energy spectra of gamma rays, electrons, and neutrinos produced at proton-proton interactions in the very high energy regime”. Phys. Rev. D, **vol. 74**, (2006) p. 034018.
URL <http://dx.doi.org/10.1103/PhysRevD.74.034018>
- [137] V. A. Acciari, E. Aliu, *et al.* “Discovery of Variability in the Very High Energy γ -Ray Emission of 1ES 1218+304 with VERITAS”. ApJ, **vol. 709**, (2010) pp. L163–L167. [1001.2590](https://arxiv.org/abs/1001.2590).
URL <http://dx.doi.org/10.1088/2041-8205/709/2/L163>
- [138] Aharonian, F., Akhperjanian, A., *et al.* “Evidence for tev gamma ray emission from cassiopeia a”. A&A, **vol. 370**(1), (2001) pp. 112–120.
URL <http://dx.doi.org/10.1051/0004-6361:20010243>
- [139] Y. Yuan, S. Funk, *et al.* “FERMILARGE AREA TELESCOPE DETECTION OF a BREAK IN THE GAMMA-RAY SPECTRUM OF THE SUPERNOVA REMNANT CASSIOPEIA a”. The Astrophysical Journal, **vol. 779**(2), (2013) p. 117.
URL <http://dx.doi.org/10.1088/0004-637x/779/2/117>
- [140] A. A. Abdo, M. Ackermann, *et al.* “OBSERVATION OF SUPERNOVA REMNANT IC 443 WITH THEFERMILARGE AREA TELESCOPE”. The Astrophysical Journal, **vol. 712**(1), (2010) pp. 459–468.
URL <http://dx.doi.org/10.1088/0004-637x/712/1/459>
- [141] J. Albert, E. Aliu, *et al.* “Discovery of VHE Gamma Radiation from IC443 with the MAGIC Telescope”. Astrophys. J., **vol. 664**, (2007) pp. L87–L90. [0705.3119](https://arxiv.org/abs/0705.3119).
URL <http://dx.doi.org/10.1086/520957>
- [142] B.-C. Koo, K.-T. Kim, F. D. Seward. “ROSAT Observations of the Supernova Remnant W51C”. ApJ, **vol. 447**, (1995) p. 211.
URL <http://dx.doi.org/10.1086/175867>
- [143] I. Reichardt, E. Carmona, J. Krause, MAGIC Collaboration. “Probing proton acceleration in W51C with MAGIC ”. Memorie della Società Astronomica Italiana, **vol. 82**, (2011) p. 735.
- [144] A. A. Abdo, M. Ackermann, *et al.* “A limit on the variation of the speed of light arising from quantum gravity effects”. Nature, **vol. 462**, (2009) pp. 331 EP –.
URL <https://doi.org/10.1038/nature08574>
- [145] A. Fiasson, V. Marandon, R. Chaves, O. Tibolla. “Discovery of a vhe gamma-ray source in the w51 region”. In “31st International Cosmic Ray Conference (ICRC 2009), Lodz, poland”, , vol. 1 (**2009**), p. 1.
URL <http://hal.in2p3.fr/in2p3-00432338>
- [146] X. Zhang, S. Liu. “Is supernova remnant cassiopeia a a PeVatron?” The Astrophysical Journal, **vol. 874**(1), (2019) p. 98.
URL <http://dx.doi.org/10.3847/1538-4357/ab09fe>
- [147] Y. Zhang, S. Liu, Q. Yuan. “Anomalous distributions of primary cosmic rays as evidence for time-dependent particle acceleration in supernova remnants”. The Astrophysical Journal, **vol. 844**(1), (2017) p. L3.
URL <http://dx.doi.org/10.3847/2041-8213/aa7de1>
- [148] W. R. Binns, M. H. Israel, *et al.* “Observation of the 60fe nucleosynthesis-clock isotope in galactic cosmic rays”. Science, **vol. 352**(6286), (2016) pp. 677–680. ISSN 0036-8075. <http://science/sciencemag.org/content/352/6286/677.full.pdf>.
URL <http://dx.doi.org/10.1126/science.aad6004>
- [149] F. Acero, M. Ackermann, *et al.* “DEVELOPMENT OF THE MODEL OF GALACTIC INTERSTELLAR EMISSION FOR STANDARD POINT-SOURCE ANALYSIS OFFERMILARGE AREA TELESCOPE DATA”. The Astrophysical Journal Supplement Series, **vol. 223**(2), (2016) p. 26.
URL <http://dx.doi.org/10.3847/0067-0049/223/2/26>
- [150] R. Yang, F. Aharonian, C. Evoli. “Radial distribution of the diffuse γ -ray emissivity in the galactic disk”. Phys. Rev. D, **vol. 93**, (2016) p. 123007.
URL <http://dx.doi.org/10.1103/PhysRevD.93.123007>
- [151] Parizot, E., Marcowith, A., *et al.* “Superbubbles and energetic particles in the galaxy - i. collective effects of particle acceleration”. A&A, **vol. 424**(3), (2004) pp. 747–760.
URL <http://dx.doi.org/10.1051/0004-6361:20041269>
- [152] P. L. Nolan, A. A. Abdo, *et al.* “FERMILARGE AREA TELESCOPE SECOND SOURCE CATALOG”. The Astrophysical Journal Supplement Series, **vol. 199**(2), (2012) p. 31.
URL <http://dx.doi.org/10.1088/0067-0049/199/2/31>

- [153] P. G. Mezger, J. Schraml, Y. Terzian. “Galactic H II Regions. III. The Nature of the Radio Source W49”. *ApJ*, **vol. 150**, (1967) p. 807.
URL <http://dx.doi.org/10.1086/149384>
- [154] A. W. Sievers, P. G. Mezger, *et al.*. “Dust emission from star forming regions. I - The W49A and W51A complexes”. *Astron. Astrophys.*, **vol. 251**, (1991) pp. 231–244.
- [155] R. Simon, J. M. Jackson, *et al.*. “The structure of four molecular cloud complexes in the BU-FCRAO milky way galactic ring survey”. *The Astrophysical Journal*, **vol. 551**(2), (2001) pp. 747–763.
URL <http://dx.doi.org/10.1086/320230>
- [156] C. G. D. Pree, D. M. Mehringer, W. M. Goss. “Multifrequency, high-resolution radio recombination line observations of the massive star-forming region w49a”. *The Astrophysical Journal*, **vol. 482**(1), (1997) pp. 307–333.
URL <http://dx.doi.org/10.1086/304119>
- [157] R. Genzel, D. Downes, *et al.*. “Structure and kinematics of H₂O sources in clusters of newly-formed OB stars”. *Astron. Astrophys.*, **vol. 66**, (1978) pp. 13–29.
- [158] C. R. Gwinn, J. M. Moran, M. J. Reid. “Distance and kinematics of the W49N H₂O maser outflow”. *ApJ*, **vol. 393**, (1992) pp. 149–164.
URL <http://dx.doi.org/10.1086/171493>
- [159] Peng, T.-C., Wyrowski, F., *et al.*. “W49a: a starburst triggered by expanding shells”. *A&A*, **vol. 520**, (2010) p. A84.
URL <http://dx.doi.org/10.1051/0004-6361/201014975>
- [160] A. G. Muslimov, A. K. Harding. “High-Altitude Particle Acceleration and Radiation in Pulsar Slot Gaps”. *ApJ*, **vol. 606**, (2004) pp. 1143–1153. [astro-ph/0402462](http://arxiv.org/abs/astro-ph/0402462).
URL <http://dx.doi.org/10.1086/383079>
- [161] A. McCann. “Detection of the Crab Pulsar with VERITAS above 100 GeV”. *International Cosmic Ray Conference*, **vol. 7**, (2011) p. 208. [1110.4352](https://arxiv.org/abs/1110.4352).
URL <http://dx.doi.org/10.7529/ICRC2011/V07/1090>
- [162] Ansoldi, S., Antonelli, L. A., *et al.*. “Teraelectronvolt pulsed emission from the crab pulsar detected by magic”. *A&A*, **vol. 585**, (2016) p. A133.
URL <http://dx.doi.org/10.1051/0004-6361/201526853>
- [163] G. C. K. Leung, J. Takata, *et al.*. “Fermi-LAT Detection of Pulsed Gamma-Rays above 50 GeV from the Vela Pulsar”. *ApJ*, **vol. 797**, L13. [1410.5208](https://arxiv.org/abs/1410.5208).
URL <http://dx.doi.org/10.1088/2041-8205/797/2/L13>
- [164] Y. Xing, Z. Wang. “Fermi Study of γ -ray Millisecond Pulsars: the Spectral Shape and Pulsed Emission from J0614-3329 up to GeV”. *Astrophys. J.*, **vol. 831**(2), (2016) p. 143. [1604.08710](https://arxiv.org/abs/1604.08710).
URL <http://dx.doi.org/10.3847/0004-637X/831/2/143>
- [165] M. Lyutikov. “Inverse compton origin of pulsar γ -ray emission and the reconnection model of crab nebula flares”. *Astronomische Nachrichten*, **vol. 335**(3), (2014) pp. 227–233. <https://onlinelibrary.wiley.com/doi/10.1002/asna.201312023>.
URL <http://dx.doi.org/10.1002/asna.201312023>
- [166] A. K. Harding, C. Kalapotharakos. “Synchrotron Self-Compton Emission from the Crab and Other Pulsars”. *Astrophys. J.*, **vol. 811**(1), (2015) p. 63. [1508.06251](https://arxiv.org/abs/1508.06251).
URL <http://dx.doi.org/10.1088/0004-637X/811/1/63>
- [167] J. Takata, C. W. Ng, K. S. Cheng. “Probing gamma-ray emissions of Fermi-LAT pulsars with a non-stationary outer gap model”. *Mon. Not. R. Astron. Soc.*, **vol. 455**, (2016) pp. 4249–4266. [1511.06542](https://arxiv.org/abs/1511.06542).
URL <http://dx.doi.org/10.1093/mnras/stv2612>
- [168] M. Ackermann, M. Ajello, *et al.*. “The First Fermi-LAT Gamma-Ray Burst Catalog”. *ApJS*, **vol. 209**, 11. [1303.2908](https://arxiv.org/abs/1303.2908).
URL <http://dx.doi.org/10.1088/0067-0049/209/1/11>
- [169] B. M. Gaensler, P. O. Slane. “The evolution and structure of pulsar wind nebulae”. *Annual Review of Astronomy and Astrophysics*, **vol. 44**(1), (2006) pp. 17–47. <https://doi.org/10.1146/annurev.astro.44.051905.092528>.
URL <http://dx.doi.org/10.1146/annurev.astro.44.051905.092528>
- [170] A. Lemiere, P. Slane, B. M. Gaensler, S. Murray. “High-resolution X-ray Observations of the Pulsar Wind Nebula Associated with the Gamma-ray Source HESS J1640-465”. *ApJ*, **vol. 706**, (2009) pp. 1269–1276. [0910.2652](https://arxiv.org/abs/0910.2652).
URL <http://dx.doi.org/10.1088/0004-637X/706/2/1269>
- [171] J. Fang, L. Zhang. “Multiband emission from pulsar wind nebulae: a possible injection spectrum”. *Astron. Astrophys.*, **vol. 515**, A20. [1003.1656](https://arxiv.org/abs/1003.1656).
URL <http://dx.doi.org/10.1051/0004-6361/200913615>
- [172] D. F. Torres, N. Rea, J. Martín. “Time-dependent modelling of pulsar wind nebulae: study on the impact of the diffusion-loss approximations”. *Monthly Notices of the Royal Astronomical Society*, **vol. 427**(1), (2012) pp. 415–427. ISSN 0035-8711. <http://oup.prod.sis.lan/mnras/article-pdf/427/1/415/18235481/>

- 427-1-415.pdf.
URL <http://dx.doi.org/10.1111/j.1365-2966.2012.22014.x>
- [173] F. Acero, M. Ackermann, *et al.*. “CONSTRAINTS ON THE GALACTIC POPULATION OF TeV PULSAR WIND NEBULAE USING FERMILARGE AREA TELESCOPE OBSERVATIONS”. *The Astrophysical Journal*, **vol. 773**(1), (2013) p. 77.
URL <http://dx.doi.org/10.1088/0004-637x/773/1/77>
- [174] A. M. Hillas. “The origin of ultra-high-energy cosmic rays”. *Annual Review of Astronomy and Astrophysics*, **vol. 22**(1), (1984) pp. 425–444. <https://doi.org/10.1146/annurev.aa.22.090184.002233>.
URL <http://dx.doi.org/10.1146/annurev.aa.22.090184.002233>
- [175] K. S. Cheng, T. Cheung, *et al.*. “Could very high energy gamma rays from the Crab Nebula result from p-p collision?” *Journal of Physics G Nuclear Physics*, **vol. 16**, (1990) pp. 1115–1121.
URL <http://dx.doi.org/10.1088/0954-3899/16/7/022>
- [176] Y. Ohira, S. Kisaka, R. Yamazaki. “Pulsar Wind Nebulae inside Supernova Remnants as Cosmic-Ray PeVatrons”. *Mon. Not. Roy. Astron. Soc.*, **vol. 478**(1), (2018) pp. 926–931. [1702.05866](https://doi.org/10.1093/mnras/sty1159).
URL <http://dx.doi.org/10.1093/mnras/sty1159>
- [177] H. Bartko, W. Bednarek. “ γ -ray emission from PWNe interacting with molecular clouds”. *Monthly Notices of the Royal Astronomical Society*, **vol. 385**(3), (2008) pp. 1105–1109. ISSN 0035-8711. <http://oup.prod.sis.lan/mnras/article-pdf/385/3/1105/3274080/mnras0385-1105.pdf>.
URL <http://dx.doi.org/10.1111/j.1365-2966.2008.12870.x>
- [178] L. Zhang, X. C. Yang. “TeV GAMMA-RAY EMISSION FROM VELA x: LEPTONIC OR HADRONIC?” *The Astrophysical Journal*, **vol. 699**(2), (2009) pp. L153–L156.
URL <http://dx.doi.org/10.1088/0004-637x/699/2/1153>
- [179] H. Li, Y. Chen, L. Zhang. “Lepto-hadronic origin of γ -rays from the G54.1+0.3 pulsar wind nebula”. *Monthly Notices of the Royal Astronomical Society: Letters*, **vol. 408**(1), (2010) pp. L80–L84. ISSN 1745-3925. <http://oup.prod.sis.lan/mnrasl/article-pdf/408/1/L80/3269897/408-1-L80.pdf>.
URL <http://dx.doi.org/10.1111/j.1745-3933.2010.00934.x>
- [180] O. Adriani, G. C. Barbarino, *et al.*. “An anomalous positron abundance in cosmic rays with energies 1.5–100 GeV”. *Nature*, **vol. 458**, (2009) pp. 607–609. [0810.4995](https://doi.org/10.1038/nature07942).
URL <http://dx.doi.org/10.1038/nature07942>
- [181] M. Ackermann, *et al.*. “Measurement of separate cosmic-ray electron and positron spectra with the Fermi Large Area Telescope”. *Phys. Rev. Lett.*, **vol. 108**, (2012) p. 011103. [1109.0521](https://doi.org/10.1103/PhysRevLett.108.011103).
URL <http://dx.doi.org/10.1103/PhysRevLett.108.011103>
- [182] M. Aguilar, *et al.*. “First Result from the Alpha Magnetic Spectrometer on the International Space Station: Precision Measurement of the Positron Fraction in Primary Cosmic Rays of 0.5–350 GeV”. *Phys. Rev. Lett.*, **vol. 110**, (2013) p. 141102.
URL <http://dx.doi.org/10.1103/PhysRevLett.110.141102>
- [183] D. Hooper, P. Blasi, P. D. Serpico. “Pulsars as the sources of high energy cosmic ray positrons”. *Journal of Cosmology and Astroparticle Physics*, **vol. 2009**(01), (2009) pp. 025–025.
URL <http://dx.doi.org/10.1088/1475-7516/2009/01/025>
- [184] D. Malyshev, I. Cholis, J. Gelfand. “Pulsars versus dark matter interpretation of atic/pamela”. *Phys. Rev. D*, **vol. 80**, (2009) p. 063005.
URL <http://dx.doi.org/10.1103/PhysRevD.80.063005>
- [185] H. Yüksel, M. D. Kistler, T. Stanev. “Tev gamma rays from geminga and the origin of the gev positron excess”. *Phys. Rev. Lett.*, **vol. 103**, (2009) p. 051101.
URL <http://dx.doi.org/10.1103/PhysRevLett.103.051101>
- [186] T. Linden, S. Profumo. “Probing the Pulsar Origin of the Anomalous Positron Fraction with AMS-02 and Atmospheric Cherenkov Telescopes”. *Astrophys. J.*, **vol. 772**, (2013) p. 18. [1304.1791](https://doi.org/10.1088/0004-637X/772/1/18).
URL <http://dx.doi.org/10.1088/0004-637X/772/1/18>
- [187] D. Hooper, I. Cholis, T. Linden, K. Fang. “HAWC Observations Strongly Favor Pulsar Interpretations of the Cosmic-Ray Positron Excess”. *Phys. Rev.*, **vol. D96**(10), (2017) p. 103013. [1702.08436](https://doi.org/10.1103/PhysRevD.96.103013).
URL <http://dx.doi.org/10.1103/PhysRevD.96.103013>
- [188] J. P. W. Verbiest, J. M. Weisberg, *et al.*. “On Pulsar Distance Measurements and Their Uncertainties”. *ApJ*, **vol. 755**, 39. [1206.0428](https://doi.org/10.1088/0004-637X/755/1/39).
URL <http://dx.doi.org/10.1088/0004-637X/755/1/39>
- [189] G. Dubus. “Gamma-ray binaries and related systems”. *The Astronomy and Astrophysics Review*, **vol. 21**(1), (2013) p. 64. ISSN 1432-0754.
URL <http://dx.doi.org/10.1007/s00159-013-0064-5>
- [190] A. G. Lyne, B. W. Stappers, *et al.*. “The binary nature of PSR J2032+4127”. *Mon. Not. R. Astron. Soc.*, **vol. 451**, (2015) pp. 581–587. [1502.01465](https://doi.org/10.1093/mnras/stv100).

- URL <http://dx.doi.org/10.1093/mnras/stv236>
- [191] R. Zanin, A. Fernández-Barral, *et al.*. “Gamma rays detected from Cygnus X-1 with likely jet origin”. *Astron. Astrophys.*, **vol. 596**, A55. [1605.05914](https://arxiv.org/abs/1605.05914).
URL <http://dx.doi.org/10.1051/0004-6361/201628917>
- [192] M. Tavani, A. Bulgarelli, *et al.*. “Extreme particle acceleration in the microquasar CygnusX-3”. *Nature*, **vol. 462**, (2009) pp. 620–623. [0910.5344](https://arxiv.org/abs/0910.5344).
URL <http://dx.doi.org/10.1038/nature08578>
- [193] A. Loh, S. Corbel, *et al.*. “High-energy gamma-ray observations of the accreting black hole V404 Cygni during its 2015 June outburst”. *Mon. Not. R. Astron. Soc.*, **vol. 462**, (2016) pp. L111–L115. [1607.06239](https://arxiv.org/abs/1607.06239).
URL <http://dx.doi.org/10.1093/mnrasl/slw142>
- [194] A. A. Abdo, M. Ackermann, *et al.*. “Fermi Large Area Telescope Observation of a Gamma-ray Source at the Position of Eta Carinae”. *ApJ*, **vol. 723**, (2010) pp. 649–657. [1008.3235](https://arxiv.org/abs/1008.3235).
URL <http://dx.doi.org/10.1088/0004-637X/723/1/649>
- [195] P. H. T. Tam, R. H. H. Huang, *et al.*. “DISCOVERY OF GeV γ -RAY EMISSION FROM PSR b1259–63/LS 2883”. *The Astrophysical Journal*, **vol. 736**(1), (2011) p. L10.
URL <http://dx.doi.org/10.1088/2041-8205/736/1/110>
- [196] A. A. Abdo, M. Ackermann, *et al.*. “DISCOVERY OF HIGH-ENERGY GAMMA-RAY EMISSION FROM THE BINARY SYSTEM PSR b1259–63/LS 2883 AROUND PERIASTRON WITHFERMI”. *The Astrophysical Journal*, **vol. 736**(1), (2011) p. L11.
URL <http://dx.doi.org/10.1088/2041-8205/736/1/111>
- [197] M. G. Aartsen, M. Ackermann, *et al.*. “SEARCHES FOR TIME-DEPENDENT NEUTRINO SOURCES WITH ICECUBE DATA FROM 2008 TO 2012”. *The Astrophysical Journal*, **vol. 807**(1), (2015) p. 46.
URL <http://dx.doi.org/10.1088/0004-637X/807/1/46>
- [198] J. M. Paredes, W. Bednarek, *et al.*. “Binaries with the eyes of CTA”. *Astroparticle Physics*, **vol. 43**, (2013) pp. 301–316. [1210.3215](https://arxiv.org/abs/1210.3215).
URL <http://dx.doi.org/10.1016/j.astropartphys.2012.09.004>
- [199] M. Clavel, R. Terrier, *et al.*. “Echoes of multiple outbursts of Sagittarius A* revealed by Chandra”. *Astron. Astrophys.*, **vol. 558**, A32. [1307.3954](https://arxiv.org/abs/1307.3954).
URL <http://dx.doi.org/10.1051/0004-6361/201321667>
- [200] M. Su, T. R. Slatyer, D. P. Finkbeiner. “Giant Gamma-ray Bubbles from Fermi-LAT: Active Galactic Nucleus Activity or Bipolar Galactic Wind?” *ApJ*, **vol. 724**, (2010) pp. 1044–1082. [1005.5480](https://arxiv.org/abs/1005.5480).
URL <http://dx.doi.org/10.1088/0004-637X/724/2/1044>
- [201] F. Aharonian, A. Neronov. “High-Energy Gamma Rays from the Massive Black Hole in the Galactic Center”. *ApJ*, **vol. 619**, (2005) pp. 306–313. [astro-ph/0408303](https://arxiv.org/abs/astro-ph/0408303).
URL <http://dx.doi.org/10.1086/426426>
- [202] K. Dodds-Eden, D. Porquet, *et al.*. “Evidence for X-Ray Synchrotron Emission from Simultaneous Mid-Infrared to X-Ray Observations of a Strong Sgr A* Flare”. *ApJ*, **vol. 698**, (2009) pp. 676–692. [0903.3416](https://arxiv.org/abs/0903.3416).
URL <http://dx.doi.org/10.1088/0004-637X/698/1/676>
- [203] S. Markoff, H. Falcke, F. Yuan, P. L. Biermann. “The Nature of the 10 kilosecond X-ray flare in Sgr A*”. *Astron. Astrophys.*, **vol. 379**, (2001) pp. L13–L16. [astro-ph/0109081](https://arxiv.org/abs/astro-ph/0109081).
URL <http://dx.doi.org/10.1051/0004-6361:20011346>
- [204] R. P. Eatough, H. Falcke, *et al.*. “A strong magnetic field around the supermassive black hole at the centre of the Galaxy”. *Nature*, **vol. 501**, (2013) pp. 391–394. [1308.3147](https://arxiv.org/abs/1308.3147).
URL <http://dx.doi.org/10.1038/nature12499>
- [205] K. Tsuchiya, R. Enomoto, *et al.*. “Detection of Sub-TeV Gamma Rays from the Galactic Center Direction by CANGAROO-II”. *ApJL*, **vol. 606**, (2004) pp. L115–L118. [astro-ph/0403592](https://arxiv.org/abs/astro-ph/0403592).
URL <http://dx.doi.org/10.1086/421292>
- [206] K. Kosack, H. M. Badran, *et al.*. “TeV Gamma-Ray Observations of the Galactic Center”. *ApJL*, **vol. 608**, (2004) pp. L97–L100. [astro-ph/0403422](https://arxiv.org/abs/astro-ph/0403422).
URL <http://dx.doi.org/10.1086/422469>
- [207] A. W. Smith, for the VERITAS Collaboration. “VERITAS Observations of The Galactic Center Ridge”. *arXiv e-prints*. [1508.06311](https://arxiv.org/abs/1508.06311).
- [208] F. Aharonian, A. G. Akhperjanian, *et al.*. “Very high energy gamma rays from the direction of Sagittarius A*”. *Astron. Astrophys.*, **vol. 425**, (2004) pp. L13–L17. [astro-ph/0406658](https://arxiv.org/abs/astro-ph/0406658).
URL <http://dx.doi.org/10.1051/0004-6361:200400055>
- [209] —. “Discovery of very-high-energy γ -rays from the Galactic Centre ridge”. *Nature*, **vol. 439**, (2006) pp. 695–698. [astro-ph/0603021](https://arxiv.org/abs/astro-ph/0603021).
URL <http://dx.doi.org/10.1038/nature04467>
- [210] —. “HESS Observations of the Galactic Center Region and Their Possible Dark Matter Interpretation”. *Physical*

- Review Letters, **vol. 97**(22), 221102. [astro-ph/0610509](http://arxiv.org/abs/astro-ph/0610509).
URL <http://dx.doi.org/10.1103/PhysRevLett.97.221102>
- [211] —. “Simultaneous HESS and Chandra observations of Sagittarius A^{star} during an X-ray flare”. Astron. Astrophys., **vol. 492**, (2008) pp. L25–L28. [0812.3762](http://arxiv.org/abs/0812.3762).
URL <http://dx.doi.org/10.1051/0004-6361:200810912>
- [212] J. Albert, E. Aliu, *et al.* “Observation of Gamma Rays from the Galactic Center with the MAGIC Telescope”. ApJL, **vol. 638**, (2006) pp. L101–L104. [astro-ph/0512469](http://arxiv.org/abs/astro-ph/0512469).
URL <http://dx.doi.org/10.1086/501164>
- [213] F. Aharonian, A. G. Akhperjanian, *et al.* “Spectrum and variability of the Galactic center VHE γ -ray source HESS J1745-290”. Astron. Astrophys., **vol. 503**, (2009) pp. 817–825. [0906.1247](http://arxiv.org/abs/0906.1247).
URL <http://dx.doi.org/10.1051/0004-6361/200811569>
- [214] S. Gabici, F. A. Aharonian, P. Blasi. “Gamma rays from molecular clouds”. Astrophysics and Space Science, **vol. 309**(1), (2007) pp. 365–371. ISSN 1572-946X.
URL <http://dx.doi.org/10.1007/s10509-007-9427-6>
- [215] F. Aharonian, A. G. Akhperjanian, *et al.* “Energy spectrum of cosmic-ray electrons at tev energies”. Phys. Rev. Lett., **vol. 101**, (2008) p. 261104.
URL <http://dx.doi.org/10.1103/PhysRevLett.101.261104>
- [216] A. W. Strong, I. V. Moskalenko, V. S. Ptuskin. “Cosmic-ray propagation and interactions in the galaxy”. Annual Review of Nuclear and Particle Science, **vol. 57**(1), (2007) pp. 285–327. <https://doi.org/10.1146/annurev.nucl.57.090506.123011>.
URL <http://dx.doi.org/10.1146/annurev.nucl.57.090506.123011>
- [217] F. A. Aharonian. “Gamma Rays From Molecular Clouds”. Space Science Reviews, **vol. 99**, (2001) pp. 187–196. [arXiv:astro-ph/0012290](http://arxiv.org/abs/astro-ph/0012290).
- [218] S. Casanova, F. A. Aharonian, *et al.* “Molecular Clouds as Cosmic-Ray Barometers”. PASJ, **vol. 62**, (2010) pp. 769–. [0904.2887](http://arxiv.org/abs/0904.2887).
- [219] G. Pedaletti, D. F. Torres, *et al.* “On the potential of the Cherenkov Telescope Array for the study of cosmic-ray diffusion in molecular clouds”. Astron. Astrophys., **vol. 550**, A123. [1301.5240](http://arxiv.org/abs/1301.5240).
URL <http://dx.doi.org/10.1051/0004-6361/201220583>
- [220] M. Ackermann, M. Ajello, *et al.* “FERMILARGE AREA TELESCOPE STUDY OF COSMIC RAYS AND THE INTERSTELLAR MEDIUM IN NEARBY MOLECULAR CLOUDS”. The Astrophysical Journal, **vol. 755**(1), (2012) p. 22.
URL <http://dx.doi.org/10.1088/0004-637x/755/1/22>
- [221] —. “GAMMA-RAY OBSERVATIONS OF THE ORION MOLECULAR CLOUDS WITH THE FERMILARGE AREA TELESCOPE”. The Astrophysical Journal, **vol. 756**(1), (2012) p. 4.
URL <http://dx.doi.org/10.1088/0004-637x/756/1/4>
- [222] A. Neronov, D. V. Semikoz, A. M. Taylor. “Low-energy break in the spectrum of galactic cosmic rays”. Phys. Rev. Lett., **vol. 108**, (2012) p. 051105.
URL <http://dx.doi.org/10.1103/PhysRevLett.108.051105>
- [223] Yang, Rui-zhi, Jones, David I., Aharonian, Felix. “Fermi-lat observations of the sagittarius b complex”. A&A, **vol. 580**, (2015) p. A90.
URL <http://dx.doi.org/10.1051/0004-6361/201425233>
- [224] M. Aguilar, D. Aisa, B. Alpat, *et al.* “Precision Measurement of the Proton Flux in Primary Cosmic Rays from Rigidity 1 GV to 1.8 TV with the Alpha Magnetic Spectrometer on the International Space Station”. Physical Review Letters, **vol. 114**(17), 171103.
URL <http://dx.doi.org/10.1103/PhysRevLett.114.171103>
- [225] O. Adriani, G. C. Barbarino, *et al.* “Pamela measurements of cosmic-ray proton and helium spectra”. Science, **vol. 332**(6025), (2011) pp. 69–72. ISSN 0036-8075. <http://science.sciencemag.org/content/332/6025/69.full.pdf>.
URL <http://dx.doi.org/10.1126/science.1199172>
- [226] W. R. Binns, M. H. Israel, *et al.* “Observation of the ^{60}Fe nucleosynthesis-clock isotope in galactic cosmic rays”. Science, **vol. 352**, (2016) pp. 677–680.
URL <http://dx.doi.org/10.1126/science.aad6004>
- [227] W. R. Binns, M. E. Wiedenbeck, *et al.* “Cosmic-Ray Neon, Wolf-Rayet Stars, and the Superbubble Origin of Galactic Cosmic Rays”. ApJ, **vol. 634**, (2005) pp. 351–364. [astro-ph/0508398](http://arxiv.org/abs/astro-ph/0508398).
URL <http://dx.doi.org/10.1086/496959>
- [228] J. Bally. “Overview of the orion complex”. In B. Reipurth (Ed.) “Handbook of Star Forming Regions, Volume I”, , (Astronomical Society of the Pacific Monograph Publications2008). ISBN 978-1-58381-670-7, p. 459.
- [229] A. Abramowski, F. Aharonian, *et al.* “DISCOVERY OF THE HARD SPECTRUM VHE γ -RAY SOURCE HESS j1641–463”. The Astrophysical Journal, **vol. 794**(1), (2014) p. L1.

- URL <http://dx.doi.org/10.1088/2041-8205/794/1/11>
- [230] —. “DISCOVERY OF THE HARD SPECTRUM VHE γ -RAY SOURCE HESS j1641–463”. *The Astrophysical Journal*, **vol. 794**(1), (2014) p. L1.
URL <http://dx.doi.org/10.1088/2041-8205/794/1/11>
- [231] R. C. G. Chaves, M. Renaud, M. Lemoine-Goumard, P. Goret. “HESS J1848-018: Discovery Of VHE γ -ray Emission From The Direction Of W 43”. In F. A. Aharonian, W. Hofmann, F. Rieger (Eds.) “American Institute of Physics Conference Series”,, *American Institute of Physics Conference Series*, vol. 1085 (2008), pp. 372–375.
URL <http://dx.doi.org/10.1063/1.3076684>
- [232] A. U. Abeysekara, R. Alfaro, *et al.*. “Search for TeV Gamma-Ray Emission from Point-like Sources in the Inner Galactic Plane with a Partial Configuration of the HAWC Observatory”. *The Astrophysical Journal*, **vol. 817**(1), (2016) p. 3.
URL <http://dx.doi.org/10.3847/0004-637x/817/1/3>
- [233] M. S. Longair. *High Energy Astrophysics*, (Cambridge University Press2011). ISBN 978-0521-7561-8.
- [234] W. L. Kraushaar, G. W. Clark, *et al.*. “High-Energy Cosmic Gamma-Ray Observations from the OSO-3 Satellite”. *ApJ*, **vol. 177**, (1972) p. 341.
URL <http://dx.doi.org/10.1086/151713>
- [235] C. E. Fichtel, R. C. Hartman, *et al.*. “High-energy gamma-ray results from the second Small Astronomy Satellite.” *ApJ*, **vol. 198**, (1975) pp. 163–182.
URL <http://dx.doi.org/10.1086/153590>
- [236] G. F. Bignami, G. Boella, *et al.*. “The COS-B experiment for gamma-ray astronomy.” *Space Science Instrumentation*, **vol. 1**, (1975) pp. 245–268.
- [237] A. W. Strong, K. Bennett, *et al.*. “Diffuse continuum gamma rays from the Galaxy observed by COMPTEL.” *Astron. Astrophys.*, **vol. 292**, (1994) pp. 82–91.
- [238] S. C. Kappadath, J. Ryan, *et al.*. “The preliminary cosmic diffuse γ -ray spectrum from 800keV to 30MeV measured with COMPTEL.” *Astronomy and Astrophysics Supplement Series*, **vol. 120**, (1996) pp. 619–622.
- [239] R. L. Kinzer, G. V. Jung, *et al.*. “Diffuse Cosmic Gamma Radiation Measured by HEAO 1”. *ApJ*, **vol. 475**, (1997) pp. 361–372.
URL <http://dx.doi.org/10.1086/303507>
- [240] S. D. Hunter, D. L. Bertsch, *et al.*. “EGRET Observations of the Diffuse Gamma-Ray Emission from the Galactic Plane”. *ApJ*, **vol. 481**, (1997) pp. 205–240.
URL <http://dx.doi.org/10.1086/304012>
- [241] M. Ackermann, M. Ajello, *et al.*. “Fermi-LAT Observations of the Diffuse γ -Ray Emission: Implications for Cosmic Rays and the Interstellar Medium”. *ApJ*, **vol. 750**, 3. [1202.4039](https://arxiv.org/abs/1202.4039).
URL <http://dx.doi.org/10.1088/0004-637X/750/1/3>
- [242] M. Ajello, A. Albert, *et al.*. “Fermi-LAT Observations of High-Energy Gamma-Ray Emission toward the Galactic Center”. *ApJ*, **vol. 819**, 44. [1511.02938](https://arxiv.org/abs/1511.02938).
URL <http://dx.doi.org/10.3847/0004-637X/819/1/44>
- [243] L. Bouchet, E. Jourdain, *et al.*. “INTEGRAL SPI All-Sky View in Soft Gamma Rays: A Study of Point-Source and Galactic Diffuse Emission”. *ApJ*, **vol. 679**, (2008) pp. 1315–1326. [0801.2086](https://arxiv.org/abs/0801.2086).
URL <http://dx.doi.org/10.1086/529489>
- [244] L. Bouchet, A. W. Strong, *et al.*. “Diffuse Emission Measurement with the SPectrometer on INTEGRAL as an Indirect Probe of Cosmic-Ray Electrons and Positrons”. *ApJ*, **vol. 739**, 29. [1107.0200](https://arxiv.org/abs/1107.0200).
URL <http://dx.doi.org/10.1088/0004-637X/739/1/29>
- [245] S. LeBohec, I. H. Bond, *et al.*. “Gamma-Ray Observations of the Galactic Plane at Energies $E > 500$ GEV”. *ApJ*, **vol. 539**, (2000) pp. 209–215. [astro-ph/0003265](https://arxiv.org/abs/astro-ph/0003265).
URL <http://dx.doi.org/10.1086/309227>
- [246] F. A. Aharonian, A. G. Akhperjanian, *et al.*. “A search for gamma-ray emission from the Galactic plane in the longitude range between 37° and 43° ”. *Astron. Astrophys.*, **vol. 375**, (2001) pp. 1008–1017.
URL <http://dx.doi.org/10.1051/0004-6361:20010898>
- [247] A. Abramowski, F. Aharonian, *et al.*. “Diffuse Galactic gamma-ray emission with H.E.S.S.” *Phys. Rev. D*, **vol. 90**, 122007. [1411.7568](https://arxiv.org/abs/1411.7568).
URL <http://dx.doi.org/10.1103/PhysRevD.90.122007>
- [248] A. W. Strong, I. V. Moskalenko, O. Reimer. “Diffuse Galactic Continuum Gamma Rays: A Model Compatible with EGRET Data and Cosmic-Ray Measurements”. *ApJ*, **vol. 613**, (2004) pp. 962–976. [astro-ph/0406254](https://arxiv.org/abs/astro-ph/0406254).
URL <http://dx.doi.org/10.1086/423193>
- [249] A. W. Strong, I. V. Moskalenko, *et al.*. “The distribution of cosmic-ray sources in the Galaxy, γ -rays and the gradient in the CO-to-H₂ relation”. *Astron. Astrophys.*, **vol. 422**, (2004) pp. L47–L50. [astro-ph/0405275](https://arxiv.org/abs/astro-ph/0405275).
URL <http://dx.doi.org/10.1051/0004-6361:20040172>
- [250] T. Delahaye, A. Fiasson, M. Pohl, P. Salati. “The GeV-TeV Galactic gamma-ray diffuse emission. I. Uncertainties in

- the predictions of the hadronic component”. Astron. Astrophys., **vol. 531**, A37. [1102.0744](https://arxiv.org/abs/1102.0744).
URL <http://dx.doi.org/10.1051/0004-6361/201116647>
- [251] A. A. Abdo, M. Ackermann, *et al.* “Fermi Large Area Telescope Measurements of the Diffuse Gamma-Ray Emission at Intermediate Galactic Latitudes”. Phys. Rev. Lett., **vol. 103**, 251101. [0912.0973](https://arxiv.org/abs/0912.0973).
URL <http://dx.doi.org/10.1103/PhysRevLett.103.251101>
- [252] X.-J. Bi, J. Zhang, *et al.* “The diffuse Galactic γ -rays from dark matter annihilation”. Physics Letters B, **vol. 668**, (2008) pp. 87–92. [astro-ph/0611783](https://arxiv.org/abs/0611783).
URL <http://dx.doi.org/10.1016/j.physletb.2008.08.041>
- [253] J. Zhang, Q. Yuan, X.-J. Bi. “Galactic Diffuse Gamma Rays—Recalculation Based on New Measurements of the Cosmic Electron Spectrum”. ApJ, **vol. 720**, (2010) pp. 9–19. [0908.1236](https://arxiv.org/abs/0908.1236).
URL <http://dx.doi.org/10.1088/0004-637X/720/1/9>
- [254] Y.-Q. Guo, H.-B. Hu, Z. Tian. “On the contribution of a hard galactic plane component to the excesses of secondary particles”. Chinese Physics C, **vol. 40**, 115001. [1412.8590](https://arxiv.org/abs/1412.8590).
URL <http://dx.doi.org/10.1088/1674-1137/40/11/115001>
- [255] R. Atkins, W. Benbow, *et al.* “Evidence for TeV Gamma-Ray Emission from a Region of the Galactic Plane”. Phys. Rev. Lett., **vol. 95**, 251103. [astro-ph/0502303](https://arxiv.org/abs/0502303).
URL <http://dx.doi.org/10.1103/PhysRevLett.95.251103>
- [256] F. Aharonian, J. Buckley, T. Kifune, G. Sinnis. “High energy astrophysics with ground-based gamma ray detectors”. Reports on Progress in Physics, **vol. 71**, 096901.
URL <http://dx.doi.org/10.1088/0034-4885/71/9/096901>
- [257] I. A. Grenier, J. H. Black, A. W. Strong. “The Nine Lives of Cosmic Rays in Galaxies”. Annual Review of Astronomy and Astrophysics, **vol. 53**, (2015) pp. 199–246.
URL <http://dx.doi.org/10.1146/annurev-astro-082214-122457>
- [258] G. Di Sciaccio, LHAASO Collaboration. “The LHAASO experiment: From Gamma-Ray Astronomy to Cosmic Rays”. Nuclear and Particle Physics Proceedings, **vol. 279**, (2016) pp. 166–173. [1602.07600](https://arxiv.org/abs/1602.07600).
URL <http://dx.doi.org/10.1016/j.nuclphysbps.2016.10.024>
- [259] M. G. Aartsen, R. Abbasi, *et al.* “First Observation of PeV-Energy Neutrinos with IceCube”. Phys. Rev. Lett., **vol. 111**, 021103. [1304.5356](https://arxiv.org/abs/1304.5356).
URL <http://dx.doi.org/10.1103/PhysRevLett.111.021103>
- [260] S. Razzaque. “Galactic Center origin of a subset of IceCube neutrino events”. Phys. Rev. D, **vol. 88**, 081302. [1309.2756](https://arxiv.org/abs/1309.2756).
URL <http://dx.doi.org/10.1103/PhysRevD.88.081302>
- [261] M. Ahlers, K. Murase. “Probing the Galactic origin of the IceCube excess with gamma rays”. Phys. Rev. D, **vol. 90**, 023010. [1309.4077](https://arxiv.org/abs/1309.4077).
URL <http://dx.doi.org/10.1103/PhysRevD.90.023010>
- [262] A. Neronov, D. Semikoz, C. Tchernin. “PeV neutrinos from interactions of cosmic rays with the interstellar medium in the Galaxy”. Phys. Rev. D, **vol. 89**, 103002. [1307.2158](https://arxiv.org/abs/1307.2158).
URL <http://dx.doi.org/10.1103/PhysRevD.89.103002>
- [263] D. Gaggero, D. Grasso, *et al.* “The Gamma-Ray and Neutrino Sky: A Consistent Picture of Fermi-LAT, Milagro, and IceCube Results”. ApJ, **vol. 815**, L25. [1504.00227](https://arxiv.org/abs/1504.00227).
URL <http://dx.doi.org/10.1088/2041-8205/815/2/L25>
- [264] Y. Fukuda, *et al.* “Evidence for oscillation of atmospheric neutrinos”. Phys. Rev. Lett., **vol. 81**, (1998) pp. 1562–1567. [hep-ex/9807003](https://arxiv.org/abs/hep-ex/9807003).
URL <http://dx.doi.org/10.1103/PhysRevLett.81.1562>
- [265] M. D. Weinberg. “The dynamics of the galactic bar”. International Astronomical Union Colloquium, **vol. 157**, (1996) p. 516–528.
URL <http://dx.doi.org/10.1017/S0252921100050363>
- [266] P. Blasi. “The Origin of Galactic Cosmic Rays”. Astron. Astrophys. Rev., **vol. 21**, (2013) p. 70. [1311.7346](https://arxiv.org/abs/1311.7346).
URL <http://dx.doi.org/10.1007/s00159-013-0070-7>
- [267] J. Vink. “Supernova remnants: the x-ray perspective”. The Astronomy and Astrophysics Review, **vol. 20**(1), (2011) p. 49. ISSN 1432-0754.
URL <http://dx.doi.org/10.1007/s00159-011-0049-1>
- [268] T. K. Gaisser, R. J. Protheroe, T. Stanev. “Gamma-ray production in supernova remnants”. The Astrophysical Journal, **vol. 492**(1), (1998) pp. 219–227.
URL <http://dx.doi.org/10.1086/305011>
- [269] X. Wu, M. Su, *et al.* “PANGU: A High Resolution Gamma-ray Space Telescope”. Proc. SPIE Int. Soc. Opt. Eng., **vol. 9144**, (2014) p. 91440F. [1407.0710](https://arxiv.org/abs/1407.0710).
URL <http://dx.doi.org/10.1117/12.2057251>
- [270] G. Park, B. C. Koo, *et al.* “H I Shells and Supershells in the I-GALFA H I 21 cm Line Survey. I. Fast-expanding H I

- Shells Associated with Supernova Remnants”. *ApJ*, **vol. 777**, 14. [1306.6699](https://doi.org/10.1088/0004-637X/777/1/14).
URL <http://dx.doi.org/10.1088/0004-637X/777/1/14>
- [271] A. A. Abdo, M. Ackermann, *et al.* “Fermi-Lat Discovery of GeV Gamma-Ray Emission from the Young Supernova Remnant Cassiopeia A”. *ApJ*, **vol. 710**, (2010) pp. L92–L97. [1001.1419](https://doi.org/10.1088/2041-8205/710/1/L92).
URL <http://dx.doi.org/10.1088/2041-8205/710/1/L92>
- [272] W. W. Tian, D. A. Leahy, M. Havercorn, B. Jiang. “Discovery of the radio and x-ray counterpart of TeV γ -ray source HESS j1731-347”. *The Astrophysical Journal*, **vol. 679**(2), (2008) pp. L85–L88.
URL <http://dx.doi.org/10.1086/589506>
- [273] T. Wenwu, Z. Jianli. “Exploration of Galactic γ -Ray Supernova Remnants”, **2013**. [1301.6824](https://doi.org/10.1301/6824).
- [274] Y. Uchiyama, S. Funk, *et al.* “Fermi Large Area Telescope Discovmry of GeV Gamma-Ray Emission from the Vicinity of SNR W44”. *ApJ*, **vol. 749**, L35. [1203.3234](https://doi.org/10.1088/2041-8205/749/2/L35).
URL <http://dx.doi.org/10.1088/2041-8205/749/2/L35>
- [275] B. P. Abbott, R. Abbott, *et al.* “Gw170814: A three-detector observation of gravitational waves from a binary black hole coalescence”. *Phys. Rev. Lett.*, **vol. 119**, (2017) p. 141101.
URL <http://dx.doi.org/10.1103/PhysRevLett.119.141101>
- [276] Y. Zhao, Q. Yuan, *et al.* “Perspective of detecting very high energy gamma-ray emission from active galactic nuclei with large high altitude air shower observatory (lhaaso)”. *International Journal of Modern Physics D*, **vol. 25**(01), (2016) p. 1650006. <https://doi.org/10.1142/S0218271816500061>.
URL <http://dx.doi.org/10.1142/S0218271816500061>
- [277] A. U. Abeysekara, A. Albert, *et al.* “Observation of the crab nebula with the HAWC gamma-ray observatory”. *The Astrophysical Journal*, **vol. 843**(1), (2017) p. 39.
URL <http://dx.doi.org/10.3847/1538-4357/aa7555>
- [278] B. Bartoli, P. Bernardini, *et al.* “CRAB NEBULA: FIVE-YEAR OBSERVATION WITH ARGO-YBJ”. *The Astrophysical Journal*, **vol. 798**(2), (2015) p. 119.
URL <http://dx.doi.org/10.1088/0004-637x/798/2/119>
- [279] F. Acero, F. Aharonian, *et al.* “Detection of gamma rays from a starburst galaxy”. *Science*, **vol. 326**(5956), (2009) pp. 1080–1082. ISSN 0036-8075. <http://science.sciencemag.org/content/326/5956/1080.full.pdf>.
URL <http://dx.doi.org/10.1126/science.1178826>
- [280] Q.-W. Tang, X.-Y. Wang, P.-H. T. Tam. “Discovery of GeV Emission from the Direction of the Luminous Infrared Galaxy NGC 2146”. *ApJ*, **vol. 794**(1), 26. [1407.3391](https://doi.org/10.1088/0004-637X/794/1/26).
URL <http://dx.doi.org/10.1088/0004-637X/794/1/26>
- [281] A. Loeb, E. Waxman. “The cumulative background of high energy neutrinos from starburst galaxies”. *Journal of Cosmology and Astro-Particle Physics*, **vol. 2006**(5), 003. [astro-ph/0601695](https://arxiv.org/abs/astro-ph/0601695).
URL <http://dx.doi.org/10.1088/1475-7516/2006/05/003>
- [282] X.-C. Chang, R.-Y. Liu, X.-Y. Wang. “Star-forming Galaxies as the Origin of the IceCube PeV Neutrinos”. *ApJ*, **vol. 805**(2), 95. [1412.8361](https://doi.org/10.1088/0004-637X/805/2/95).
URL <http://dx.doi.org/10.1088/0004-637X/805/2/95>
- [283] K. Murase, M. Ahlers, B. C. Lacki. “Testing the hadronuclear origin of PeV neutrinos observed with IceCube”. *Phys. Rev. D*, **vol. 88**(12), 121301. [1306.3417](https://doi.org/10.1103/PhysRevD.88.121301).
URL <http://dx.doi.org/10.1103/PhysRevD.88.121301>
- [284] R.-Y. Liu, X.-Y. Wang, *et al.* “Diffuse PeV neutrinos from EeV cosmic ray sources: Semirelativistic hypernova remnants in star-forming galaxies”. *Phys. Rev. D*, **vol. 89**(8), 083004. [1310.1263](https://doi.org/10.1103/PhysRevD.89.083004).
URL <http://dx.doi.org/10.1103/PhysRevD.89.083004>
- [285] X.-Y. Wang, S. Razzaque, P. Mészáros, Z.-G. Dai. “High-energy cosmic rays and neutrinos from semirelativistic hypernovae”. *Phys. Rev. D*, **vol. 76**(8), 083009. [0705.0027](https://doi.org/10.1103/PhysRevD.76.083009).
URL <http://dx.doi.org/10.1103/PhysRevD.76.083009>
- [286] A. Kashlinsky. “Cosmic infrared background and early galaxy evolution”. *Phys. Rept.*, **vol. 409**, (2005) pp. 361–438. [astro-ph/0412235](https://arxiv.org/abs/astro-ph/0412235).
URL <http://dx.doi.org/10.1016/j.physrep.2004.12.005>
- [287] M. G. Hauser, E. Dwek. “The cosmic infrared background: measurements and implications”. *Ann. Rev. Astron. Astrophys.*, **vol. 39**, (2001) pp. 249–307. [astro-ph/0105539](https://arxiv.org/abs/astro-ph/0105539).
URL <http://dx.doi.org/10.1146/annurev.astro.39.1.249>
- [288] P. Madau, L. Pozzetti. “Deep galaxy counts, extragalactic background light, and the stellar baryon budget”. *Mon. Not. Roy. Astron. Soc.*, **vol. 312**, (2000) p. L9. [astro-ph/9907315](https://arxiv.org/abs/astro-ph/9907315).
URL <http://dx.doi.org/10.1046/j.1365-8711.2000.03268.x>
- [289] G. G. Fazio, *et al.* “Number counts at $3 < \lambda < 10$ μm from the Spitzer Space Telescope”. *Astrophys. J. Suppl.*, **vol. 154**, (2004) pp. 39–43. [astro-ph/0405595](https://arxiv.org/abs/astro-ph/0405595).
URL <http://dx.doi.org/10.1086/422585>

- [290] A. I. Nikishov. “Absorption of High-Energy Photons in the Universe.”. *Journal of Experimental and Theoretical Physics*, **vol. 14**, (1962) p. 393.
- [291] F. W. Stecker, O. C. de Jager, M. H. Salamon. “TeV gamma rays from 3C 279 - A possible probe of origin and intergalactic infrared radiation fields”. *ApJL*, **vol. 390**, (1992) pp. L49–L52.
URL <http://dx.doi.org/10.1086/186369>
- [292] E. Aliu, *et al.*. “Very-High-Energy Gamma Rays from a Distant Quasar: How Transparent Is the Universe?” *Science*, **vol. 320**(5884), (2008) p. 1752. [0807.2822](http://dx.doi.org/10.1126/science.1157087).
URL <http://dx.doi.org/10.1126/science.1157087>
- [293] D. Mazin, M. Raue. “New limits on the density of the extragalactic background light in the optical to the far-infrared from the spectra of all known TeV blazars”. *Astron. Astrophys.*, **vol. 471**, (2007) pp. 439–452. [astro-ph/0701694](#).
URL <http://dx.doi.org/10.1051/0004-6361:20077158>
- [294] J. D. Finke, S. Razzaque. “Constraints on the Extragalactic Background Light from very High Energy Gamma-Ray Observations of Blazars”. *ApJ*, **vol. 698**, (2009) pp. 1761–1766. [0904.2583](#).
URL <http://dx.doi.org/10.1088/0004-637X/698/2/1761>
- [295] A. A. Abdo, M. Ackermann, *et al.*. “Fermi Large Area Telescope Constraints on the Gamma-ray Opacity of the Universe”. *ApJ*, **vol. 723**, (2010) pp. 1082–1096. [1005.0996](#).
URL <http://dx.doi.org/10.1088/0004-637X/723/2/1082>
- [296] M. R. Orr, F. Krennrich, E. Dwek. “Strong New Constraints on the Extragalactic Background Light in the Near- to Mid-infrared”. *ApJ*, **vol. 733**, 77. [1101.3498](#).
URL <http://dx.doi.org/10.1088/0004-637X/733/2/77>
- [297] M. Meyer, M. Raue, D. Mazin, D. Horns. “Limits on the extragalactic background light in the Fermi era”. *Astron. Astrophys.*, **vol. 542**, A59. [1202.2867](#).
URL <http://dx.doi.org/10.1051/0004-6361/201118284>
- [298] Y. Gong, A. Cooray. “The extragalactic background light from the measurements of the attenuation of high-energy gamma-ray spectrum”. *Astrophys. J.*, **vol. 772**, (2013) p. L12. [1305.5249](#).
URL <http://dx.doi.org/10.1088/2041-8205/772/1/L12>
- [299] R. J. Gould, G. P. Schreder. “Pair Production in Photon-Photon Collisions”. *Phys. Rev.*, **vol. 155**, (1967) pp. 1404–1407.
URL <http://dx.doi.org/10.1103/PhysRev.155.1404>
- [300] J. Guy, C. Renault, *et al.*. “Constraints on the cosmic infrared background based on BeppoSAX and CAT spectra of Mkn-501”. *Astron. Astrophys.*, **vol. 359**, (2000) p. 419. [astro-ph/0004355](#).
- [301] E. Komatsu, *et al.*. “Five-Year Wilkinson Microwave Anisotropy Probe (WMAP) Observations: Cosmological Interpretation”. *Astrophys. J. Suppl.*, **vol. 180**, (2009) pp. 330–376. [0803.0547](#).
URL <http://dx.doi.org/10.1088/0067-0049/180/2/330>
- [302] J. Albert, *et al.*. “Observations of mkn 421 with the magic telescope”. *Astrophys. J.*, **vol. 663**, (2007) pp. 125–138. [astro-ph/0603478](#).
URL <http://dx.doi.org/10.1086/518221>
- [303] Y. Zhao, Q. Yuan, *et al.*. “Perspective of detecting very high energy gamma-ray emission from active galactic nuclei with large high altitude air shower observatory (lhaaso)”. *International Journal of Modern Physics D*, **vol. 25**(01), (2016) p. 1650006. <https://doi.org/10.1142/S0218271816500061>.
URL <http://dx.doi.org/10.1142/S0218271816500061>
- [304] M. Ackermann, *et al.*. “The Third Catalog of Active Galactic Nuclei Detected by the Fermi Large Area Telescope”. *Astrophys. J.*, **vol. 810**(1), (2015) p. 14. [1501.06054](#).
URL <http://dx.doi.org/10.1088/0004-637X/810/1/14>
- [305] B. Zhang. “Gamma-Ray Burst Prompt Emission”. *Int. J. Mod. Phys.*, **vol. D23**, (2014) p. 1430002. [1402.7022](#).
URL <http://dx.doi.org/10.1142/S021827181430002X>
- [306] P. Meszaros, M. J. Rees. “Gamma-Ray Bursts”, **2014**. [1401.3012](#).
- [307] R. C. Gilmore, A. Bouvier, *et al.*. “IACT observations of gamma-ray bursts: prospects for the Cherenkov Telescope Array”. *Experimental Astronomy*, **vol. 35**, (2013) pp. 413–457. [1201.0010](#).
URL <http://dx.doi.org/10.1007/s10686-012-9316-z>
- [308] S. Vernetto. “Detection of gamma-ray bursts in the 1 gev–1 tev energy range by ground-based experiments”. *Astroparticle Physics*, **vol. 13**(1), (2000) pp. 75 – 86. ISSN 0927-6505.
URL [http://dx.doi.org/https://doi.org/10.1016/S0927-6505\(99\)00114-0](http://dx.doi.org/https://doi.org/10.1016/S0927-6505(99)00114-0)
- [309] G. Aielli, C. Bacci, *et al.*. “Scaler mode technique for the ARGO-YBJ detector”. *Astroparticle Physics*, **vol. 30**, (2008) pp. 85–95. [0807.2139](#).
URL <http://dx.doi.org/10.1016/j.astropartphys.2008.07.002>
- [310] G. Aielli, C. Bacci, *et al.*. “SEARCH FOR GAMMA RAY BURSTS WITH THE ARGO-YBJ DETECTOR IN SCALER MODE”. *The Astrophysical Journal*, **vol. 699**(2), (2009) pp. 1281–1287.

- URL <http://dx.doi.org/10.1088/0004-637X/699/2/1281>
- [311] A. U. Abeysekara, J. A. Aguilar, *et al.* “On the sensitivity of the HAWC observatory to gamma-ray bursts”. *Astroparticle Physics*, **vol. 35**, (2012) pp. 641–650. [1108.6034](https://arxiv.org/abs/1108.6034).
URL <http://dx.doi.org/10.1016/j.astropartphys.2012.02.001>
- [312] A. Tepe, I. Taboada. “Prospects for grb detection with hawc scalers”. *Advances in Space Research*, **vol. 49**(1), (2012) pp. 103 – 107. ISSN 0273-1177.
URL <http://dx.doi.org/https://doi.org/10.1016/j.asr.2011.09.002>
- [313] H.-C. Li, M.-J. Chen, *et al.* “Study on the optimization of the water cherenkov detector array of the LHAASO project for surveying VHE gamma ray sources”. *Chinese Physics C*, **vol. 38**(1), (2014) p. 016002.
URL <http://dx.doi.org/10.1088/1674-1137/38/1/016002>
- [314] I. Taboada, R. C. Gilmore. “Prospects for the detection of grbs with hawc”. *Nuclear Instruments and Methods in Physics Research Section A: Accelerators, Spectrometers, Detectors and Associated Equipment*, **vol. 742**, (2014) pp. 276 – 277. ISSN 0168-9002. 4th Roma International Conference on Astroparticle Physics.
URL <http://dx.doi.org/https://doi.org/10.1016/j.nima.2013.09.013>
- [315] G. Ghisellini, G. Ghirlanda, L. Nava, A. Celotti. “GeV emission from gamma-ray bursts: a radiative fireball?” *Mon. Not. R. Astron. Soc.*, **vol. 403**(2), (2010) pp. 926–937. [0910.2459](https://arxiv.org/abs/0910.2459).
URL <http://dx.doi.org/10.1111/j.1365-2966.2009.16171.x>
- [316] G. I. Rubtsov, S. V. Troitsky. “Breaks in gamma-ray spectra of distant blazars and transparency of the Universe”. *JETP Lett.*, **vol. 100**(6), (2014) pp. 355–359. [Pisma Zh. Eksp. Teor. Fiz. 100,no.6,397(2014)], [1406.0239](https://arxiv.org/abs/1406.0239).
URL <http://dx.doi.org/10.7868/S0370274X14180015,10.1134/S0021364014180088>
- [317] T. M. Kneiske, T. Bretz, K. Mannheim, D. H. Hartmann. “Implications of cosmological gamma-ray absorption. II. Modification of gamma-ray spectra”. *Astron. Astrophys.*, **vol. 413**, (2004) pp. 807–815. [astro-ph/0309141](https://arxiv.org/abs/astro-ph/0309141).
URL <http://dx.doi.org/10.1051/0004-6361:20031542>
- [318] D. Heck, J. Knapp, *et al.* “CORSIKA: A Monte Carlo code to simulate extensive air showers”, **1998**.
- [319] T.-P. Li, Y.-Q. Ma. “Analysis methods for results in gamma-ray astronomy”. *ApJ*, **vol. 272**, (1983) pp. 317–324.
URL <http://dx.doi.org/10.1086/161295>
- [320] A. von Kienlin, *et al.* “The Second Fermi GBM Gamma-Ray Burst Catalog: The First Four Years”. *Astrophys. J. Suppl.*, **vol. 211**, (2014) p. 13. [1401.5080](https://arxiv.org/abs/1401.5080).
URL <http://dx.doi.org/10.1088/0067-0049/211/1/13>
- [321] S. Zhu, J. Racusin, *et al.* “Grb 130427a: Fermi-lat detection of a burst gcn circular # 14471”.
- [322] A. A. Abdo, M. Ackermann, *et al.* “Fermi observations of high-energy gamma-ray emission from grb 080916c”. *Science*, **vol. 323**(5922), (2009) pp. 1688–1693. ISSN 0036-8075. <http://science.scienmag.org/content/323/5922/1688.full.pdf>.
URL <http://dx.doi.org/10.1126/science.1169101>
- [323] M. Ackermann, M. Ajello, *et al.* “Detection of a Spectral Break in the Extra Hard Component of GRB 090926A”. *ApJ*, **vol. 729**, 114. [1101.2082](https://arxiv.org/abs/1101.2082).
URL <http://dx.doi.org/10.1088/0004-637X/729/2/114>
- [324] F. Aharonian, *et al.* “The Crab nebula and pulsar between 500-GeV and 80-TeV. Observations with the HEGRA stereoscopic air Cerenkov telescopes”. *Astrophys. J.*, **vol. 614**, (2004) pp. 897–913. [astro-ph/0407118](https://arxiv.org/abs/astro-ph/0407118).
URL <http://dx.doi.org/10.1086/423931>
- [325] B. P. Abbott, R. Abbott, *et al.* “Observation of gravitational waves from a binary black hole merger”. *Phys. Rev. Lett.*, **vol. 116**, (2016) p. 061102.
URL <http://dx.doi.org/10.1103/PhysRevLett.116.061102>
- [326] M. G. Aartsen, M. Ackermann, *et al.* “Atmospheric and astrophysical neutrinos above 1 tev interacting in icecube”. *Phys. Rev. D*, **vol. 91**, (2015) p. 022001.
URL <http://dx.doi.org/10.1103/PhysRevD.91.022001>
- [327] Z. Berezhiani, A. D. Dolgov, I. I. Tkachev. “Reconciling Planck results with low redshift astronomical measurements”. *Phys. Rev.*, **vol. D92**(6), (2015) p. 061303. [1505.03644](https://arxiv.org/abs/1505.03644).
URL <http://dx.doi.org/10.1103/PhysRevD.92.061303>
- [328] K. Murase, D. Guetta, M. Ahlers. “Hidden Cosmic-Ray Accelerators as an Origin of TeV-PeV Cosmic Neutrinos”. *Phys. Rev. Lett.*, **vol. 116**(7), (2016) p. 071101. [1509.00805](https://arxiv.org/abs/1509.00805).
URL <http://dx.doi.org/10.1103/PhysRevLett.116.071101>
- [329] R. U. Abbasi, M. Abe, *et al.* “Indications of intermediate-scale anisotropy of cosmic rays with energy greater than 57 EeV in the Northern sky measured with the surface detector of the Telescope Array experiment”. *The Astrophysical Journal*, **vol. 790**(2), (2014) p. L21.
URL <http://dx.doi.org/10.1088/2041-8205/790/2/121>
- [330] R. D. Blandford, R. L. Znajek. “Electromagnetic extraction of energy from Kerr black holes”. *Mon. Not. R. Astron. Soc.*, **vol. 179**, (1977) pp. 433–456.
URL <http://dx.doi.org/10.1093/mnras/179.3.433>

- [331] R. D. Blandford, D. G. Payne. “Hydromagnetic flows from accretion discs and the production of radio jets”. *Mon. Not. R. Astron. Soc.* , **vol. 199**, (1982) pp. 883–903.
URL <http://dx.doi.org/10.1093/mnras/199.4.883>
- [332] C. M. Urry, P. Padovani. “Unified Schemes for Radio-Loud Active Galactic Nuclei”. *Publ. Astron. Soc. Pac.* , **vol. 107**, (1995) p. 803. [astro-ph/9506063](http://arxiv.org/abs/astro-ph/9506063).
URL <http://dx.doi.org/10.1086/133630>
- [333] A. A. Abdo, M. Ackermann, *et al.*. “The Spectral Energy Distribution of Fermi Bright Blazars”. *ApJ*, **vol. 716**, (2010) pp. 30–70. [0912.2040](http://arxiv.org/abs/0912.2040).
URL <http://dx.doi.org/10.1088/0004-637X/716/1/30>
- [334] G. Ghisellini, F. Tavecchio, *et al.*. “The power of relativistic jets is larger than the luminosity of their accretion disks”. *Nature*, **vol. 515**, (2014) p. 376. [1411.5368](http://arxiv.org/abs/1411.5368).
URL <http://dx.doi.org/10.1038/nature13856>
- [335] W. Essey, O. E. Kalashev, A. Kusenko, J. F. Beacom. “Secondary photons and neutrinos from cosmic rays produced by distant blazars”. *Phys. Rev. Lett.*, **vol. 104**, (2010) p. 141102.
URL <http://dx.doi.org/10.1103/PhysRevLett.104.141102>
- [336] W. Essey, A. Kusenko. “A new interpretation of the gamma-ray observations of distant active galactic nuclei”. *Astroparticle Physics*, **vol. 33**(2), (2010) pp. 81 – 85. ISSN 0927-6505.
URL <http://dx.doi.org/https://doi.org/10.1016/j.astropartphys.2009.11.007>
- [337] W. Essey, O. Kalashev, A. Kusenko, J. F. Beacom. “ROLE OF LINE-OF-SIGHT COSMIC-RAY INTERACTIONS IN FORMING THE SPECTRA OF DISTANT BLAZARS IN TeV GAMMA RAYS AND HIGH-ENERGY NEUTRINOS”. *The Astrophysical Journal*, **vol. 731**(1), (2011) p. 51.
URL <http://dx.doi.org/10.1088/0004-637X/731/1/51>
- [338] F. Aharonian, A. G. Akhperjanian, *et al.*. “New constraints on the mid-IR EBL from the HESS discovery of VHE γ -rays from 1ES 0229+200”. *Astron. Astrophys.*, **vol. 475**, (2007) pp. L9–L13. [0709.4584](http://arxiv.org/abs/0709.4584).
URL <http://dx.doi.org/10.1051/0004-6361:20078462>
- [339] —. “Detection of VHE gamma-ray emission from the distant blazar 1ES 1101-232 with HESS and broadband characterisation”. *Astron. Astrophys.*, **vol. 470**, (2007) pp. 475–489. [0705.2946](http://arxiv.org/abs/0705.2946).
URL <http://dx.doi.org/10.1051/0004-6361:20077057>
- [340] M. Böttcher, C. D. Dermer, J. D. Finke. “The hard VHE γ -ray emission in high-redshift TeV blazars: Comptonization of cosmic microwave background radiation in an extended jet?” *The Astrophysical Journal*, **vol. 679**(1), (2008) pp. L9–L12.
URL <http://dx.doi.org/10.1086/588780>
- [341] D. Yan, H. Zeng, L. Zhang. “Non-variable tev emission from the extended jet of a blazar in the stochastic acceleration scenario: the case of the hard tev emission of 1es 1101–232”. *Monthly Notices of the Royal Astronomical Society*, **vol. 424**(3), (2012) pp. 2173–2179. <https://onlinelibrary.wiley.com/doi/pdf/10.1111/j.1365-2966.2012.21376.x>.
URL <http://dx.doi.org/10.1111/j.1365-2966.2012.21376.x>
- [342] M. Cerruti, A. Zech, C. Boisson, S. Inoue. “A hadronic origin for ultra-high-frequency-peaked BL Lac objects”. *Monthly Notices of the Royal Astronomical Society*, **vol. 448**(1), (2015) pp. 910–927. ISSN 0035-8711. <http://oup.prod.sis.lan/mnras/article-pdf/448/1/910/9379400/stu2691.pdf>.
URL <http://dx.doi.org/10.1093/mnras/stu2691>
- [343] H. Takami, K. Murase, C. D. Dermer. “Disentangling Hadronic and Leptonic Cascade Scenarios from the Very-high-energy Gamma-Ray Emission of Distant Hard-spectrum Blazars”. *ApJL*, **vol. 771**, L32. [1305.2138](http://arxiv.org/abs/1305.2138).
URL <http://dx.doi.org/10.1088/2041-8205/771/2/L32>
- [344] D. Yan, O. Kalashev, L. Zhang, S.-N. Zhang. “A self-consistent interpretation of the GeV-TeV emission from a distant blazar PKS 1424+240”. *Mon. Not. R. Astron. Soc.* , **vol. 449**, (2015) pp. 1018–1023. [1412.4894](http://arxiv.org/abs/1412.4894).
URL <http://dx.doi.org/10.1093/mnras/stv363>
- [345] J. Heinze, D. Boncioli, M. Bustamante, W. Winter. “Cosmogenic Neutrinos Challenge the Cosmic-Ray proton DIP Model”. *The Astrophysical Journal*, **vol. 825**(2), (2016) p. 122.
URL <http://dx.doi.org/10.3847/0004-637X/825/2/122>
- [346] M. G. Aartsen, K. Abraham, *et al.*. “Constraints on ultrahigh-energy cosmic-ray sources from a search for neutrinos above 10 pev with icecube”. *Phys. Rev. Lett.*, **vol. 117**, (2016) p. 241101.
URL <http://dx.doi.org/10.1103/PhysRevLett.117.241101>
- [347] M. Ackermann, M. Ajello, *et al.*. “The Spectrum of Isotropic Diffuse Gamma-Ray Emission between 100 MeV and 820 GeV”. *ApJ*, **vol. 799**, 86. [1410.3696](http://arxiv.org/abs/1410.3696).
URL <http://dx.doi.org/10.1088/0004-637X/799/1/86>
- [348] K. Murase, J. F. Beacom, H. Takami. “Gamma-ray and neutrino backgrounds as probes of the high-energy universe: hints of cascades, general constraints, and implications for TeV searches”. *Journal of Cosmology and Astroparticle Physics*, **vol. 2012**(08), (2012) pp. 030–030.

- URL <http://dx.doi.org/10.1088/1475-7516/2012/08/030>
- [349] O. E. Kalashev, A. Kusenko, W. Essey. “PeV Neutrinos from Intergalactic Interactions of Cosmic Rays Emitted by Active Galactic Nuclei”. Physical Review Letters, **vol. 111**(4), 041103. [1303.0300](https://arxiv.org/abs/1303.0300).
URL <http://dx.doi.org/10.1103/PhysRevLett.111.041103>
- [350] A. U. Abeysekara, S. Archambault, *et al.* “Gamma-Rays from the Quasar PKS 1441+25: Story of an Escape”. ApJ, **vol. 815**, L22. [1512.04434](https://arxiv.org/abs/1512.04434).
URL <http://dx.doi.org/10.1088/2041-8205/815/2/L22>
- [351] M. L. Ahnen, S. Ansoldi, *et al.* “Very High Energy γ -Rays from the Universe’s Middle Age: Detection of the $z = 0.940$ Blazar PKS 1441+25 with MAGIC”. ApJ, **vol. 815**, L23. [1512.04435](https://arxiv.org/abs/1512.04435).
URL <http://dx.doi.org/10.1088/2041-8205/815/2/L23>
- [352] A. E. Broderick, P. Chang, C. Pfrommer. “The Cosmological Impact of Luminous TeV Blazars. I. Implications of Plasma Instabilities for the Intergalactic Magnetic Field and Extragalactic Gamma-Ray Background”. ApJ, **vol. 752**, 22. [1106.5494](https://arxiv.org/abs/1106.5494).
URL <http://dx.doi.org/10.1088/0004-637X/752/1/22>
- [353] P. Chang, A. E. Broderick, C. Pfrommer. “THE COSMOLOGICAL IMPACT OF LUMINOUS TeV BLAZARS. II. REWRITING THE THERMAL HISTORY OF THE INTERGALACTIC MEDIUM”. The Astrophysical Journal, **vol. 752**(1), (2012) p. 23.
URL <http://dx.doi.org/10.1088/0004-637X/752/1/23>
- [354] L. Sironi, D. Giannios. “Relativistic pair beams from TeV blazars: a source of reprocessed GeV emission rather than intergalactic heating”. The Astrophysical Journal, **vol. 787**(1), (2014) p. 49.
URL <http://dx.doi.org/10.1088/0004-637X/787/1/49>
- [355] M. Meyer. “Searches for Axionlike Particles Using γ -Ray Observations”. In “Proceedings, 12th Patras Workshop on Axions, WIMPs and WISPs (PATRAS 2016): Jeju Island, South Korea, June 20-24, 2016”, (2017), pp. 102–111. [1611.07784](https://arxiv.org/abs/1611.07784).
URL http://dx.doi.org/10.3204/DESY-PROC-2009-03/Meyer_Manuel
- [356] A. Domínguez, M. Ajello. “SPECTRAL ANALYSIS OFFERMI-LAT BLAZARS ABOVE 50 GEV”. The Astrophysical Journal, **vol. 813**(2), (2015) p. L34.
URL <http://dx.doi.org/10.1088/2041-8205/813/2/134>
- [357] J. R. Ellis, N. E. Mavromatos, D. V. Nanopoulos. “Derivation of a Vacuum Refractive Index in a Stringy Space-Time Foam Model”. Phys. Lett., **vol. B665**, (2008) pp. 412–417. [0804.3566](https://arxiv.org/abs/0804.3566).
URL <http://dx.doi.org/10.1016/j.physletb.2008.06.029>
- [358] G. Amelino-Camelia, L. Smolin. “Prospects for constraining quantum gravity dispersion with near term observations”. Phys. Rev., **vol. D80**, (2009) p. 084017. [0906.3731](https://arxiv.org/abs/0906.3731).
URL <http://dx.doi.org/10.1103/PhysRevD.80.084017>
- [359] Tavecchio, F., Bonnoli, G. “On the detectability of lorentz invariance violation through anomalies in the multi-tev spectra of blazars”. A&A, **vol. 585**, (2016) p. A25.
URL <http://dx.doi.org/10.1051/0004-6361/201526071>
- [360] A. Abramowski, F. Acero, *et al.* “Search for lorentz invariance breaking with a likelihood fit of the pks 2155-304 flare data taken on mjd 53944”. Astroparticle Physics, **vol. 34**(9), (2011) pp. 738 – 747. ISSN 0927-6505.
URL <http://dx.doi.org/https://doi.org/10.1016/j.astropartphys.2011.01.007>
- [361] V. Ginzburg. “The origin of cosmic rays”. In V. GINZBURG, S. SYROVATSKII (Eds.) “The Origin of Cosmic Rays”, , (Pergamon1964). ISBN 978-0-08-013526-7, p. 444.
URL <http://dx.doi.org/https://doi.org/10.1016/C2013-0-05547-8>
- [362] G. F. Krymskii. “A regular mechanism for the acceleration of charged particles on the front of a shock wave”. Akademiiia Nauk SSSR Doklady, **vol. 234**, (1977) pp. 1306–1308.
- [363] L. O. Drury. “An introduction to the theory of diffusive shock acceleration of energetic particles in tenuous plasmas”. Reports on Progress in Physics, **vol. 46**(8), (1983) pp. 973–1027.
URL <http://dx.doi.org/10.1088/0034-4885/46/8/002>
- [364] M. A. Malkov, L. O. Drury. “Nonlinear theory of diffusive acceleration of particles by shock waves”. Reports on Progress in Physics, **vol. 64**, (2001) pp. 429–481.
URL <http://dx.doi.org/10.1088/0034-4885/64/4/201>
- [365] E. G. Berezhko, V. K. Elshin, L. T. Ksenofontov. “Cosmic ray acceleration in supernova remnants”. Soviet Journal of Experimental and Theoretical Physics, **vol. 82**, (1996) pp. 1–21.
- [366] E. Berezhko. “Origin of galactic cosmic rays from supernova remnants”. Nuclear Physics B - Proceedings Supplements, **vol. 256-257**, (2014) pp. 23 – 35. ISSN 0920-5632. Cosmic Ray Origin – Beyond the Standard Models.
URL <http://dx.doi.org/https://doi.org/10.1016/j.nuclphysbps.2014.10.003>
- [367] Völk, H. J., Zirakashvili, V. N. “Cosmic ray acceleration by spiral shocks in the galactic wind”. A&A, **vol. 417**(3), (2004) pp. 807–817.
URL <http://dx.doi.org/10.1051/0004-6361:20040018>

- [368] E. G. Berezhko. “COMPOSITION OF COSMIC RAYS ACCELERATED IN ACTIVE GALACTIC NUCLEI”. *The Astrophysical Journal*, **vol. 698**(2), (2009) pp. L138–L141.
URL <http://dx.doi.org/10.1088/0004-637x/698/2/1138>
- [369] V. Ptuskin, V. Zirakashvili, E.-S. Seo. “SPECTRUM OF GALACTIC COSMIC RAYS ACCELERATED IN SUPER-NOVA REMNANTS”. *The Astrophysical Journal*, **vol. 718**(1), (2010) pp. 31–36.
URL <http://dx.doi.org/10.1088/0004-637x/718/1/31>
- [370] V. Berezinsky, A. Gazizov, S. Grigorieva. “On astrophysical solution to ultrahigh energy cosmic rays”. *Phys. Rev. D*, **vol. 74**, (2006) p. 043005.
URL <http://dx.doi.org/10.1103/PhysRevD.74.043005>
- [371] J. Blümner, R. Engel, J. R. Hörandel. “Cosmic rays from the knee to the highest energies”. *Progress in Particle and Nuclear Physics*, **vol. 63**(2), (2009) pp. 293 – 338. ISSN 0146-6410.
URL <http://dx.doi.org/https://doi.org/10.1016/j.ppnp.2009.05.002>
- [372] T. K. Gaisser, T. Stanev, S. Tilav. “Cosmic ray energy spectrum from measurements of air showers”. *Frontiers of Physics*, **vol. 8**(6), (2013) pp. 748–758. ISSN 2095-0470.
URL <http://dx.doi.org/10.1007/s11467-013-0319-7>
- [373] H. S. Ahn, P. Allison, *et al.*. “Discrepant Hardening Observed in Cosmic-ray Elemental Spectra”. *ApJ*, **vol. 714**, (2010) pp. L89–L93. [1004.1123](https://doi.org/10.1088/2041-8205/714/1/L89).
URL <http://dx.doi.org/10.1088/2041-8205/714/1/L89>
- [374] Y. S. Yoon, H. S. Ahn, *et al.*. “COSMIC-RAY PROTON AND HELIUM SPECTRA FROM THE FIRST CREAM FLIGHT”. *The Astrophysical Journal*, **vol. 728**(2), (2011) p. 122.
URL <http://dx.doi.org/10.1088/0004-637x/728/2/122>
- [375] V. Choutko. “Precision Measurement of the Proton Flux in Primary Cosmic Rays from 1 GV to 1.8 TV with the Alpha Magnetic Spectrometer on the International Space Station”. In “34th International Cosmic Ray Conference (ICRC2015)”, , vol. 34 (**2015**), p. 260.
- [376] B. Bartoli, P. Bernardini, *et al.*. “Knee of the cosmic hydrogen and helium spectrum below 1 pev measured by argo-ybj and a cherenkov telescope of lhaaso”. *Phys. Rev. D*, **vol. 92**, (2015) p. 092005.
URL <http://dx.doi.org/10.1103/PhysRevD.92.092005>
- [377] W. Apel, J. Arteaga-Velázquez, *et al.*. “The spectrum of high-energy cosmic rays measured with kascade-grande”. *Astroparticle Physics*, **vol. 36**(1), (2012) pp. 183 – 194. ISSN 0927-6505.
URL <http://dx.doi.org/https://doi.org/10.1016/j.astropartphys.2012.05.023>
- [378] M. G. Aartsen, R. Abbasi, *et al.*. “Measurement of the cosmic ray energy spectrum with icetop-73”. *Phys. Rev. D*, **vol. 88**, (2013) p. 042004.
URL <http://dx.doi.org/10.1103/PhysRevD.88.042004>
- [379] V. Prosin, S. Berezhnev, *et al.*. “Tunka-133: Results of 3 year operation”. *Nuclear Instruments and Methods in Physics Research Section A: Accelerators, Spectrometers, Detectors and Associated Equipment*, **vol. 756**, (2014) pp. 94 – 101. ISSN 0168-9002.
URL <http://dx.doi.org/https://doi.org/10.1016/j.nima.2013.09.018>
- [380] D. Ivanov. “TA Spectrum Summary”. *PoS*, **vol. ICRC2015**, (2016) p. 349.
URL <http://dx.doi.org/10.22323/1.236.0349>
- [381] M. Aglietta, B. Alessandro, *et al.*. “The eas size spectrum and the cosmic ray energy spectrum in the region 1015–1016 ev”. *Astroparticle Physics*, **vol. 10**(1), (1999) pp. 1 – 9. ISSN 0927-6505.
URL [http://dx.doi.org/https://doi.org/10.1016/S0927-6505\(98\)00035-8](http://dx.doi.org/https://doi.org/10.1016/S0927-6505(98)00035-8)
- [382] R. Glasstetter. “Analysis of Electron and Muon Size Spectra of EAS”. *International Cosmic Ray Conference*, **vol. 1**, (1999) p. 222.
- [383] M. Aglietta, B. Alessandro, *et al.*. “The cosmic ray primary composition in the “knee” region through the eas electromagnetic and muon measurements at eas-top”. *Astroparticle Physics*, **vol. 21**(6), (2004) pp. 583 – 596. ISSN 0927-6505.
URL <http://dx.doi.org/https://doi.org/10.1016/j.astropartphys.2004.04.005>
- [384] J. R. Horandel, *et al.*. “First measurement of the knee in the hadronic component of EAS”. In “Proceedings, 26th International Cosmic Ray Conference (ICRC), August 17-25, 1999, Salt Lake City: Invited, Rapporteur, and Highlight Papers”, (**1999**), pp. 337–340.
URL http://krusty.physics.utah.edu/~icrc1999/root/vol1/h2_2_41.pdf
- [385] T. Antoni, W. Apel, *et al.*. “A non-parametric approach to infer the energy spectrum and the mass composition of cosmic rays”. *Astroparticle Physics*, **vol. 16**(3), (2002) pp. 245 – 263. ISSN 0927-6505.
URL [http://dx.doi.org/https://doi.org/10.1016/S0927-6505\(01\)00111-6](http://dx.doi.org/https://doi.org/10.1016/S0927-6505(01)00111-6)
- [386] W. D. Apel, J. C. Arteaga-Velázquez, *et al.*. “Kneelike structure in the spectrum of the heavy component of cosmic rays observed with kascade-grande”. *Phys. Rev. Lett.*, **vol. 107**, (2011) p. 171104.
URL <http://dx.doi.org/10.1103/PhysRevLett.107.171104>
- [387] M. Glasmacher, M. Catanese, *et al.*. “The cosmic ray composition between 1014 and 1016 ev”. *Astroparticle Physics*,

- vol. **12**(1), (1999) pp. 1 – 17. ISSN 0927-6505.
URL [http://dx.doi.org/https://doi.org/10.1016/S0927-6505\(99\)00076-6](http://dx.doi.org/https://doi.org/10.1016/S0927-6505(99)00076-6)
- [388] W. D. Apel, *et al.*. “KASCADE-Grande measurements of energy spectra for elemental groups of cosmic rays”. *Astropart. Phys.*, **vol. 47**, (2013) pp. 54–66. [1306.6283](https://doi.org/10.1016/j.astropartphys.2013.06.004).
URL <http://dx.doi.org/10.1016/j.astropartphys.2013.06.004>
- [389] M. Amenomori, S. Ayabe, *et al.*. “Are protons still dominant at the knee of the cosmic-ray energy spectrum?” *Physics Letters B*, **vol. 632**(1), (2006) pp. 58 – 64. ISSN 0370-2693.
URL <http://dx.doi.org/https://doi.org/10.1016/j.physletb.2005.10.048>
- [390] G. Di Sciasco. “Measurement of the Cosmic Ray Energy Spectrum with ARGO-YBJ”. In “Proceedings, Vulcano Workshop 2014: Frontier Objects in Astrophysics and Particle Physics: Vulcano, Italy, May 18-24, 2014”, **(2014)**, p. 2. [1408.6739](https://doi.org/10.21468/SciPostPhys.1408.6739).
- [391] M. Amenomori, S. Ayabe, *et al.*. “Implication of the sidereal anisotropy of 5 tev cosmic ray intensity observed with the tibet iii air shower array”. *AIP Conference Proceedings*, **vol. 932**(1), (2007) pp. 283–289. <https://doi.org/10.1063/1.2778976>.
URL <http://dx.doi.org/10.1063/1.2778976>
- [392] A. A. Abdo, B. Allen, *et al.*. “Discovery of localized regions of excess 10-tev cosmic rays”. *Phys. Rev. Lett.*, **vol. 101**, (2008) p. 221101.
URL <http://dx.doi.org/10.1103/PhysRevLett.101.221101>
- [393] B. Bartoli, P. Bernardini, *et al.*. “Medium scale anisotropy in the tev cosmic ray flux observed by argo-ybj”. *Phys. Rev. D*, **vol. 88**, (2013) p. 082001.
URL <http://dx.doi.org/10.1103/PhysRevD.88.082001>
- [394] S. BenZvi, D. W. Fiorino, S. Westerhoff. “Observation of Anisotropy in the Arrival Direction Distribution of TeV Cosmic Rays with HAWC”. *PoS*, **vol. ICRC2015**, (2016) p. 241. [34,241(2015)], [1508.04781](https://doi.org/10.22323/1.236.0241).
URL <http://dx.doi.org/10.22323/1.236.0241>
- [395] R. Abbasi, Y. Abdou, *et al.*. “Observation of Anisotropy in the Arrival Directions of Galactic Cosmic Rays at Multiple Angular Scales with IceCube”. *ApJ*, **vol. 740**, 16. [1105.2326](https://doi.org/10.1088/0004-637X/740/1/16).
URL <http://dx.doi.org/10.1088/0004-637X/740/1/16>
- [396] M. Aglietta, V. V. Alekseenko, *et al.*. “EVOLUTION OF THE COSMIC-RAY ANISOTROPY ABOVE 1014ev”. *The Astrophysical Journal*, **vol. 692**(2), (2009) pp. L130–L133.
URL <http://dx.doi.org/10.1088/0004-637X/692/2/1130>
- [397] R. Abbasi, Y. Abdou, *et al.*. “OBSERVATION OF ANISOTROPY IN THE GALACTIC COSMIC-RAY ARRIVAL DIRECTIONS AT 400 TeV WITH ICECUBE”. *The Astrophysical Journal*, **vol. 746**(1), (2012) p. 33.
URL <http://dx.doi.org/10.1088/0004-637X/746/1/33>
- [398] M. G. Aartsen, R. Abbasi, *et al.*. “OBSERVATION OF COSMIC-RAY ANISOTROPY WITH THE ICETOP AIR SHOWER ARRAY”. *The Astrophysical Journal*, **vol. 765**(1), (2013) p. 55.
URL <http://dx.doi.org/10.1088/0004-637X/765/1/55>
- [399] W. D. Apel, J. C. Arteaga-Velàzquez, *et al.*. “Ankle-like feature in the energy spectrum of light elements of cosmic rays observed with kascade-grande”. *Phys. Rev. D*, **vol. 87**, (2013) p. 081101.
URL <http://dx.doi.org/10.1103/PhysRevD.87.081101>
- [400] A. M. Hillas. “Cherenkov light emission of extensive air showers produced by primary γ rays and by nuclei”. In “Proceedings, 19th International Cosmic Ray Conference (ICRC1985) La Jolla;”, , vol. 4 **(1985)**, p. 445.
- [401] B. Bartoli, P. Bernardini, *et al.*. “Cosmic ray proton plus helium energy spectrum measured by the ARGO-YBJ experiment in the energy range 3-300 TeV”. *Phys. Rev. D*, **vol. 91**, 112017. [1503.07136](https://doi.org/10.1103/PhysRevD.91.112017).
URL <http://dx.doi.org/10.1103/PhysRevD.91.112017>
- [402] —. “Energy spectrum of cosmic protons and helium nuclei by a hybrid measurement at 4300 m a.s.l.” *Chinese Physics C*, **vol. 38**, 045001. [1401.6987](https://doi.org/10.1088/1674-1137/38/4/045001).
URL <http://dx.doi.org/10.1088/1674-1137/38/4/045001>
- [403] Z. Zhang, C. Hou, *et al.*. “Study on the performance of electromagnetic particle detectors of lhaaso-km2a”. *Nuclear Instruments and Methods in Physics Research Section A: Accelerators, Spectrometers, Detectors and Associated Equipment*, **vol. 845**, (2017) pp. 429 – 433. ISSN 0168-9002. *Proceedings of the Vienna Conference on Instrumentation 2016*.
URL <http://dx.doi.org/https://doi.org/10.1016/j.nima.2016.04.079>
- [404] H. Li, G. Gong, *et al.*. “Temperature effect on white rabbit timing link”. *IEEE Transactions on Nuclear Science*, **vol. 62**(3), (2015) pp. 1021–1026. ISSN 0018-9499.
URL <http://dx.doi.org/10.1109/TNS.2015.2425659>
- [405] H. Li, G. Gong, J. Li. “Portable calibration node for lhaaso-km2a detector array”. *IEEE Transactions on Nuclear Science*, **vol. 64**(6), (2017) pp. 1363–1366. ISSN 0018-9499.
URL <http://dx.doi.org/10.1109/TNS.2017.2654491>
- [406] S. Wu, L. Chen, *et al.*. “Study of the trigger mode of lhaaso-km2a”. *Astroparticle Physics*, **vol. 103**, (2018) pp. 41 –

48. ISSN 0927-6505.
URL <http://dx.doi.org/https://doi.org/10.1016/j.astropartphys.2018.07.002>
- [407] X. Zuo, G. Xiao, *et al.* “Design and performances of prototype muon detectors of lhaaso-km2a”. Nuclear Instruments and Methods in Physics Research Section A: Accelerators, Spectrometers, Detectors and Associated Equipment, **vol. 789**, (2015) pp. 143 – 149. ISSN 0168-9002.
URL <http://dx.doi.org/https://doi.org/10.1016/j.nima.2015.04.010>
- [408] S. Zhang, Y. Bai, *et al.* “Properties and performance of two wide field of view cherenkov/fluorescence telescope array prototypes”. Nuclear Instruments and Methods in Physics Research Section A: Accelerators, Spectrometers, Detectors and Associated Equipment, **vol. 629**(1), (2011) pp. 57 – 65. ISSN 0168-9002.
URL <http://dx.doi.org/https://doi.org/10.1016/j.nima.2010.11.120>
- [409] B. Bi, S. Zhang, *et al.* “Performance of sipms and pre-amplifier for the wide field of view cherenkov telescope array of lhaaso”. Nuclear Instruments and Methods in Physics Research Section A: Accelerators, Spectrometers, Detectors and Associated Equipment, **vol. 899**, (2018) pp. 94 – 100. ISSN 0168-9002.
URL <http://dx.doi.org/https://doi.org/10.1016/j.nima.2018.05.019>
- [410] Cao, Z. and LHAASO Collaboration. “Prospects of spectrum measurements for individual species 85 of comic ray particles above 100 TeV using LHAASO array”. Frascati Phys. Ser., **vol. 64**, (2017) pp. 85–95.
- [411] —. “Measurement of the knees of proton and H&He spectra below 1 PeV”. In “15th International Conference on Topics in Astroparticle and Underground Physics (TAUP 2017) Sudbury, Ontario, Canada, July 24-28, 2017”, (2018), p. 5.
- [412] Y. V. Stenkin. “On the PRISMA Project”. Nuclear Physics B Proceedings Supplements, **vol. 196**, (2009) pp. 293–296. [0902.0138](https://doi.org/10.1016/j.nuclphysbps.2009.09.056).
URL <http://dx.doi.org/10.1016/j.nuclphysbps.2009.09.056>
- [413] Y. V. Stenkin, J. F. Valdés-Galicia. “Neutron bursts in EAS: new physics or nuclear physics?” International Cosmic Ray Conference, **vol. 4**, (2001) p. 1453.
- [414] V. Y. Stenkin, V. V. Alekseenko, *et al.* “Thermal neutron flux produced by EAS at various altitudes”. Chinese Physics C, **vol. 37**(1), 015001.
URL <http://dx.doi.org/10.1088/1674-1137/37/1/015001>
- [415] Y. V. Stenkin, D. D. Djappuev, J. F. Valdés-Galicia. “Neutrons in extensive air showers”. Physics of Atomic Nuclei, **vol. 70**(6), (2007) pp. 1088–1099.
URL <http://dx.doi.org/10.1134/S1063778807060117>
- [416] Y. V. Stenkin. “Thermal neutrons in EAS: a new dimension in EAS study”. Nuclear Physics B Proceedings Supplements, **vol. 175**, (2008) pp. 326–329. [hep-ex/0702048](https://arxiv.org/abs/hep-ex/0702048).
URL <http://dx.doi.org/10.1016/j.nuclphysbps.2007.11.023>
- [417] Y. Stenkin. “The ProtoPRISMA array for EAS study”. International Cosmic Ray Conference, **vol. 3**, (2011) p. 263.
URL <http://dx.doi.org/10.7529/ICRC2011/V03/1136>
- [418] D. Gromushkin, V. Alekseenko, *et al.* “The array for EAS neutron component detection”. Journal of Instrumentation, **vol. 9**(8), C08028.
URL <http://dx.doi.org/10.1088/1748-0221/9/08/C08028>
- [419] B. Bartoli, P. Bernardini, *et al.* “Detection of thermal neutrons with the PRISMA-YBJ array in extensive air showers selected by the ARGO-YBJ experiment”. Astroparticle Physics, **vol. 81**, (2016) pp. 49–60. [1512.01326](https://arxiv.org/abs/1512.01326).
URL <http://dx.doi.org/10.1016/j.astropartphys.2016.04.007>
- [420] B.-B. Li, V. Alekseenko, *et al.* “EAS thermal neutron detection with the PRISMA-LHAASO-16 experiment”. Journal of Instrumentation, **vol. 12**(12), (2017) pp. P12028–P12028.
URL <http://dx.doi.org/10.1088/1748-0221/12/12/p12028>
- [421] O. Martineau-Huynh, *et al.* “The Giant Radio Array for Neutrino Detection”. EPJ Web Conf., **vol. 116**, (2016) p. 03005. [1508.01919](https://arxiv.org/abs/1508.01919).
URL <http://dx.doi.org/10.1051/epjconf/201611603005>
- [422] K. F. Daniel, L. I., L. A. C. Bernard. “Radiation from cosmic ray air showers”. Proceedings of the Royal Society of London. Series A. Mathematical and Physical Sciences, **vol. 289**(1417), (1966) pp. 206–213.
URL <http://dx.doi.org/10.1098/rspa.1966.0007>
- [423] H. R. Allan, R. W. Clay, J. K. Jones. “Radio pulses from extensive air showers”. Nature, **vol. 227**(5263), (1970) pp. 1116–1118. ISSN 1476-4687.
URL <http://dx.doi.org/10.1038/2271116a0>
- [424] J. R. Hörandel. “Radio detection of air showers with LOFAR and AERA”. JPS Conf. Proc., **vol. 9**, (2016) p. 010004. [1509.04960](https://arxiv.org/abs/1509.04960).
URL <http://dx.doi.org/10.7566/JPSCP.9.010004>
- [425] O. Martineau-Huynh, D. Ardouin, *et al.* “First results of the tianshan radio experiment for neutrino detection”. Nuclear Instruments and Methods in Physics Research Section A: Accelerators, Spectrometers, Detectors and Associated Equipment, **vol. 662**, (2012) pp. S29 – S31. ISSN 0168-9002. 4th International workshop on Acoustic and Radio

- EeV Neutrino detection Activities.
URL <http://dx.doi.org/https://doi.org/10.1016/j.nima.2010.11.143>
- [426] A. Nelles, *et al.*. “The radio emission pattern of air showers as measured with LOFAR—a tool for the reconstruction of the energy and the shower maximum”. *JCAP*, **vol. 1505**(05), (2015) p. 018. [1411.7868](https://doi.org/10.1088/1475-7516/2015/05/018).
URL <http://dx.doi.org/10.1088/1475-7516/2015/05/018>
- [427] D. Ardouin, *et al.*. “Geomagnetic origin of the radio emission from cosmic ray induced air showers observed by CODALEMA”. *Astropart. Phys.*, **vol. 31**, (2009) pp. 192–200. [0901.4502](https://doi.org/10.1016/j.astropartphys.2009.01.001).
URL <http://dx.doi.org/10.1016/j.astropartphys.2009.01.001>
- [428] W. Apel, J. Arteaga-Velázquez, *et al.*. “The waveform of the radio signal emitted by cosmic ray air showers”. *Journal of Cosmology and Astroparticle Physics*, **vol. 2014**(09), (2014) pp. 025–025.
URL <http://dx.doi.org/10.1088/1475-7516/2014/09/025>
- [429] A. Corstanje, P. Schellart, *et al.*. “The shape of the radio waveform of extensive air showers as measured with lofar”. *Astroparticle Physics*, **vol. 61**, (2015) pp. 22 – 31. ISSN 0927-6505.
URL <http://dx.doi.org/https://doi.org/10.1016/j.astropartphys.2014.06.001>
- [430] S. Jansen. *Radio for the masses*. Ph.D. thesis, Nijmegen U., **2016**.
- [431] D. Ardouin, C. Cârloganu, *et al.*. “First detection of extensive air showers by the trend self-triggering radio experiment”. *Astroparticle Physics*, **vol. 34**(9), (2011) pp. 717 – 731. ISSN 0927-6505.
URL <http://dx.doi.org/https://doi.org/10.1016/j.astropartphys.2011.01.002>
- [432] J. Alvarez-Muniz, W. R. Carvalho, Jr., E. Zas. “Monte Carlo simulations of radio pulses in atmospheric showers using ZHAireS”. *Astropart. Phys.*, **vol. 35**, (2012) pp. 325–341. [1107.1189](https://doi.org/10.1016/j.astropartphys.2011.10.005).
URL <http://dx.doi.org/10.1016/j.astropartphys.2011.10.005>
- [433] K. D. de Vries, O. Scholten, K. Werner. “The air shower maximum probed by cherenkov effects from radio emission”. *Astroparticle Physics*, **vol. 45**, (2013) pp. 23 – 27. ISSN 0927-6505.
URL <http://dx.doi.org/https://doi.org/10.1016/j.astropartphys.2013.02.003>
- [434] T. Huege, C. W. James. “Full Monte Carlo simulations of radio emission from extensive air showers with CoREAS”. In “Proceedings, 33rd International Cosmic Ray Conference (ICRC2013): Rio de Janeiro, Brazil, July 2-9, 2013”, (2013), p. 0548. [1307.7566](https://doi.org/10.22323/1.236.0632).
URL <http://www.cbpf.br/%7Eicrc2013/papers/icrc2013-0548.pdf>
- [435] T. Huege. “The renaissance of radio detection of cosmic rays”. *Braz. J. Phys.*, **vol. 44**, (2014) pp. 520–529. [[1294\(2013\)](https://arxiv.org/abs/1294.1310)], [1310.6927](https://arxiv.org/abs/1310.6927).
URL <http://dx.doi.org/10.1007/s13538-014-0226-6>
- [436] Q. Gou. “R&D of EAS radio detection in China”. PoS, **vol. ICRC2015**, (2016) p. 632.
URL <http://dx.doi.org/10.22323/1.236.0632>
- [437] K. Kotera, D. Allard, A. V. Olinto. “Cosmogenic neutrinos: parameter space and detectability from PeV to ZeV”. *Journal of Cosmology and Astro-Particle Physics*, **vol. 2010**, 013. [1009.1382](https://doi.org/10.1088/1475-7516/2010/10/013).
URL <http://dx.doi.org/10.1088/1475-7516/2010/10/013>
- [438] G. T. Zatsepin, V. A. Kuzmin. “Upper limit of the spectrum of cosmic rays”. *JETP Lett.*, **vol. 4**, (1966) pp. 78–80. [*Pisma Zh. Eksp. Teor. Fiz.* 4, 114(1966)].
- [439] C. Kouveliotou, C. A. Meegan, *et al.*. “Identification of Two Classes of Gamma-Ray Bursts”. *ApJ*, **vol. 413**, (1993) p. L101.
URL <http://dx.doi.org/10.1086/186969>
- [440] B. P. Abbott, R. Abbott, *et al.*. “Gw170817: Observation of gravitational waves from a binary neutron star inspiral”. *Phys. Rev. Lett.*, **vol. 119**, (2017) p. 161101.
URL <http://dx.doi.org/10.1103/PhysRevLett.119.161101>
- [441] A. Goldstein, P. Veres, *et al.*. “An ordinary short gamma-ray burst with extraordinary implications: Fermi-GBM detection of GRB 170817a”. *The Astrophysical Journal*, **vol. 848**(2), (2017) p. L14.
URL <http://dx.doi.org/10.3847/2041-8213/aa8f41>
- [442] S. M. Matz, D. J. Forrest, *et al.*. “High-energy emission in gamma-ray bursts”. *ApJL*, **vol. 288**, (1985) pp. L37–L40.
URL <http://dx.doi.org/10.1086/184417>
- [443] K. Hurley, B. L. Dingus, *et al.*. “Detection of a γ -ray burst of very long duration and very high energy”. *Nature*, **vol. 372**, (1994) pp. 652–654.
URL <http://dx.doi.org/10.1038/372652a0>
- [444] M. Ackermann, M. Ajello, *et al.*. “Fermi-lat observations of the gamma-ray burst grb 130427a”. *Science*, **vol. 343**(6166), (2014) pp. 42–47. ISSN 0036-8075. <https://science.scienmag.org/content/343/6166/42.full.pdf>.
URL <http://dx.doi.org/10.1126/science.1242353>
- [445] K. Toma, X.-F. Wu, P. Mészáros. “An Up-Scattered Cocoon Emission Model of Gamma-Ray Burst High-Energy Lags”. *ApJ*, **vol. 707**(2), (2009) pp. 1404–1416. [0905.1697](https://doi.org/10.1088/0004-637X/707/2/1404).
URL <http://dx.doi.org/10.1088/0004-637X/707/2/1404>

- [446] A. M. Beloborodov, R. Hascoët, I. Vurm. “On the Origin of GeV Emission in Gamma-Ray Bursts”. *ApJ*, **vol. 788**(1), 36. [1307.2663](https://arxiv.org/abs/1307.2663).
URL <http://dx.doi.org/10.1088/0004-637X/788/1/36>
- [447] K. Asano, S. Guiriec, P. Mészáros. “Hadronic Models for the Extra Spectral Component in the Short GRB 090510”. *ApJ*, **vol. 705**(2), (2009) pp. L191–L194. [0909.0306](https://arxiv.org/abs/0909.0306).
URL <http://dx.doi.org/10.1088/0004-637X/705/2/L191>
- [448] S. Razzaque, C. D. Dermer, J. D. Finke. “Synchrotron Radiation from Ultra-High Energy Protons and the Fermi Observations of GRB 080916C”. *The Open Astronomy Journal*, **vol. 3**(1), (2010) pp. 150–155. [0908.0513](https://arxiv.org/abs/0908.0513).
URL <http://dx.doi.org/10.2174/1874381101003010150>
- [449] P. Kumar, R. Barniol Duran. “On the generation of high-energy photons detected by the Fermi Satellite from gamma-ray bursts”. *Mon. Not. R. Astron. Soc.*, **vol. 400**(1), (2009) pp. L75–L79. [0905.2417](https://arxiv.org/abs/0905.2417).
URL <http://dx.doi.org/10.1111/j.1745-3933.2009.00766.x>
- [450] Y.-C. Zou, Y.-Z. Fan, T. Piran. “The possible high-energy emission from GRB 080319B and origins of the GeV emission of GRBs 080514B, 080916C and 081024B”. *Mon. Not. R. Astron. Soc.*, **vol. 396**(2), (2009) pp. 1163–1170. [0811.2997](https://arxiv.org/abs/0811.2997).
URL <http://dx.doi.org/10.1111/j.1365-2966.2009.14779.x>
- [451] X. Wang, Y. H. Yan. “Monte Carlo simulations of a diffusive shock with multiple scattering angular distributions”. *Astron. Astrophys.*, **vol. 530**, A92.
URL <http://dx.doi.org/10.1051/0004-6361/201116791>
- [452] H.-N. He, X.-F. Wu, *et al.* “On the High-energy Emission of the Short GRB 090510”. *ApJ*, **vol. 733**(1), 22. [1009.1432](https://arxiv.org/abs/1009.1432).
URL <http://dx.doi.org/10.1088/0004-637X/733/1/22>
- [453] R.-Y. Liu, X.-Y. Wang, X.-F. Wu. “Interpretation of the Unprecedentedly Long-lived High-energy Emission of GRB 130427A”. *ApJ*, **vol. 773**(2), L20. [1306.5207](https://arxiv.org/abs/1306.5207).
URL <http://dx.doi.org/10.1088/2041-8205/773/2/L20>
- [454] B. Zhang, A. Pe'er. “Evidence of an Initially Magnetically Dominated Outflow in GRB 080916C”. *ApJ*, **vol. 700**(2), (2009) pp. L65–L68. [0904.2943](https://arxiv.org/abs/0904.2943).
URL <http://dx.doi.org/10.1088/0004-637X/700/2/L65>
- [455] Y. Lithwick, R. Sari. “Lower Limits on Lorentz Factors in Gamma-Ray Bursts”. *ApJ*, **vol. 555**(1), (2001) pp. 540–545. [astro-ph/0011508](https://arxiv.org/abs/astro-ph/0011508).
URL <http://dx.doi.org/10.1086/321455>
- [456] N. Gupta, B. Zhang. “Diagnosing the site of gamma-ray burst prompt emission with spectral cut-off energy”. *Mon. Not. R. Astron. Soc.*, **vol. 384**(1), (2008) pp. L11–L15. [0708.2763](https://arxiv.org/abs/0708.2763).
URL <http://dx.doi.org/10.1111/j.1745-3933.2007.00411.x>
- [457] W. B. Atwood, L. Baldini, *et al.* “New Fermi-LAT Event Reconstruction Reveals More High-energy Gamma Rays from Gamma-Ray Bursts”. *ApJ*, **vol. 774**(1), 76. [1307.3037](https://arxiv.org/abs/1307.3037).
URL <http://dx.doi.org/10.1088/0004-637X/774/1/76>
- [458] S. Razzaque, P. Mészáros, B. Zhang. “GeV and Higher Energy Photon Interactions in Gamma-Ray Burst Fireballs and Surroundings”. *ApJ*, **vol. 613**(2), (2004) pp. 1072–1078. [astro-ph/0404076](https://arxiv.org/abs/astro-ph/0404076).
URL <http://dx.doi.org/10.1086/423166>
- [459] N. Gehrels, E. Ramirez-Ruiz, D. B. Fox. “Gamma-Ray Bursts in the Swift Era”. *Annual Review of Astronomy and Astrophysics*, **vol. 47**(1), (2009) pp. 567–617. [0909.1531](https://arxiv.org/abs/0909.1531).
URL <http://dx.doi.org/10.1146/annurev.astro.46.060407.145147>
- [460] Icecube Collaboration, R. Abbasi, *et al.* “An absence of neutrinos associated with cosmic-ray acceleration in γ -ray bursts”. *Nature*, **vol. 484**(7394), (2012) pp. 351–354. [1204.4219](https://arxiv.org/abs/1204.4219).
URL <http://dx.doi.org/10.1038/nature11068>
- [461] G. Amelino-Camelia, F. Fiore, D. Guetta, S. Puccetti. “Quantum-spacetime scenarios and soft spectral lags of the remarkable GRB130427A”. *arXiv e-prints*, arXiv:1305.2626. [1305.2626](https://arxiv.org/abs/1305.2626).
- [462] G. Amelino-Camelia, J. Ellis, *et al.* “Tests of quantum gravity from observations of γ -ray bursts”. *Nature*, **vol. 393**(6687), (1998) pp. 763–765. [astro-ph/9712103](https://arxiv.org/abs/astro-ph/9712103).
URL <http://dx.doi.org/10.1038/31647>
- [463] J. Ellis, N. E. Mavromatos. “Probes of Lorentz violation”. *Astroparticle Physics*, **vol. 43**, (2013) pp. 50–55. [1111.1178](https://arxiv.org/abs/1111.1178).
URL <http://dx.doi.org/10.1016/j.astropartphys.2012.05.004>
- [464] J. Ellis, N. E. Mavromatos, D. V. Nanopoulos, A. S. Sakharov. “Quantum-gravity analysis of gamma-ray bursts using wavelets”. *Astron. Astrophys.*, **vol. 402**, (2003) pp. 409–424. [astro-ph/0210124](https://arxiv.org/abs/astro-ph/0210124).
URL <http://dx.doi.org/10.1051/0004-6361:20030263>
- [465] U. Jacob, T. Piran. “Lorentz-violation-induced arrival delays of cosmological particles”. *Journal of Cosmology and Astro-Particle Physics*, **vol. 2008**(1), 031. [0712.2170](https://arxiv.org/abs/0712.2170).

- URL <http://dx.doi.org/10.1088/1475-7516/2008/01/031>
- [466] S. Zhang, B.-Q. Ma. “Lorentz violation from gamma-ray bursts”. *Astroparticle Physics*, **vol. 61**, (2015) pp. 108–112. [1406.4568](https://arxiv.org/abs/1406.4568).
URL <http://dx.doi.org/10.1016/j.astropartphys.2014.04.008>
- [467] V. Vasileiou, A. Jacholkowska, *et al.*. “Constraints on Lorentz invariance violation from Fermi-Large Area Telescope observations of gamma-ray bursts”. *Phys. Rev. D*, **vol. 87**(12), 122001. [1305.3463](https://arxiv.org/abs/1305.3463).
URL <http://dx.doi.org/10.1103/PhysRevD.87.122001>
- [468] Y. Okazaki, A. Fushishita, *et al.*. “Drift Effects and the Cosmic Ray Density Gradient in a Solar Rotation Period: First Observation with the Global Muon Detector Network (GMDN)”. *ApJ*, **vol. 681**, (2008) pp. 693–707. [0802.2312](https://arxiv.org/abs/0802.2312).
URL <http://dx.doi.org/10.1086/588277>
- [469] B. Bartoli, P. Bernardini, *et al.*. “Radon contribution to single particle counts of the argo-ybj detector”. *Radiation Measurements*, **vol. 68**, (2014) pp. 42 – 48. ISSN 1350-4487.
URL <http://dx.doi.org/https://doi.org/10.1016/j.radmeas.2014.07.006>
- [470] S. Dasso, H. Asorey, Pierre Auger Collaboration. “The scalar mode in the Pierre Auger Observatory to study heliospheric modulation of cosmic rays”. *Advances in Space Research*, **vol. 49**, (2012) pp. 1563–1569. [1204.6196](https://arxiv.org/abs/1204.6196).
URL <http://dx.doi.org/10.1016/j.asr.2011.12.028>
- [471] B. Bartoli, *et al.*. “Observation of the Cosmic Ray Moon shadowing effect with ARGO-YBJ”. *Phys. Rev.*, **vol. D84**, (2011) p. 022003. [1107.4887](https://arxiv.org/abs/1107.4887).
URL <http://dx.doi.org/10.1103/PhysRevD.84.022003>
- [472] M. Amenomori, *et al.*. “Cosmic ray deficit from the directions of the moon and the sun detected with the Tibet Air Shower Array”. *Phys. Rev.*, **vol. D47**, (1993) pp. 2675–2681.
URL <http://dx.doi.org/10.1103/PhysRevD.47.2675>
- [473] M. Amenomori, Z. Cao, *et al.*. “Direct Evidence of the Interplanetary Magnetic Field Effect on the Cosmic-Ray Shadow by the Sun”. *ApJL*, **vol. 415**, (1993) p. L147.
URL <http://dx.doi.org/10.1086/187054>
- [474] M. Amenomori, B. Z. Dai, *et al.*. “Shadowing of Cosmic Rays by the Sun near Maximum or at the Declining Phase of Solar Activity”. *ApJ*, **vol. 464**, (1996) p. 954.
URL <http://dx.doi.org/10.1086/177382>
- [475] M. Amenomori, *et al.*. “Probe of the Solar Magnetic Field Using the “Cosmic-Ray Shadow” of the Sun”. *Phys. Rev. Lett.*, **vol. 111**(1), (2013) p. 011101. [1306.3009](https://arxiv.org/abs/1306.3009).
URL <http://dx.doi.org/10.1103/PhysRevLett.111.011101>
- [476] K. H. Schatten, J. M. Wilcox, N. F. Ness. “A model of interplanetary and coronal magnetic fields”. *Solar Physics*, **vol. 6**, (1969) pp. 442–455.
URL <http://dx.doi.org/10.1007/BF00146478>
- [477] K. Hakamada. “A Simple Method to Compute Spherical Harmonic Coefficients for the Potential Model of the Coronal Magnetic Field”. *Solar Physics*, **vol. 159**, (1995) pp. 89–96.
URL <http://dx.doi.org/10.1007/BF00733033>
- [478] T. J. Bogdan, B. C. Low. “The three-dimensional structure of magnetostatic atmospheres. II - Modeling the large-scale corona”. *ApJ*, **vol. 306**, (1986) pp. 271–283.
URL <http://dx.doi.org/10.1086/164341>
- [479] X. Zhao, J. T. Hoeksema. “Prediction of the interplanetary magnetic field strength”. *J. Geophys. Res.*, **vol. 100**, (1995) pp. 19–33.
URL <http://dx.doi.org/10.1029/94JA02266>
- [480] F. Zhu. “Five-year correlation of the Sun shadow in cosmic rays observed by ARGO-YBJ with the Interplanetary Magnetic Field variabilit”. PoS, **vol. ICRC2015**, (2016) p. 078.
URL <http://dx.doi.org/10.22323/1.236.0078>
- [481] G. Aielli, *et al.*. “Mean Interplanetary Magnetic Field Measurement Using the ARGO-YBJ Experiment”. *Astrophys. J.*, **vol. 729**, (2011) p. 113. [1101.4261](https://arxiv.org/abs/1101.4261).
URL <http://dx.doi.org/10.1088/0004-637X/729/2/113>
- [482] S. E. Forbush. “On the Effects in Cosmic-Ray Intensity Observed During the Recent Magnetic Storm”. *Physical Review*, **vol. 51**, (1937) pp. 1108–1109.
URL <http://dx.doi.org/10.1103/PhysRev.51.1108.3>
- [483] K. Nagashima, K. Fujimoto, *et al.*. “Local-time-dependent pre-imf-shock decrease and post-shock increase of cosmic rays, produced respectively by their imf-collimated outward and inward flows across the shock responsible for forbush decrease”. *Planetary and Space Science*, **vol. 40**(8), (1992) pp. 1109 – 1137. ISSN 0032-0633.
URL [http://dx.doi.org/https://doi.org/10.1016/0032-0633\(92\)90040-U](http://dx.doi.org/https://doi.org/10.1016/0032-0633(92)90040-U)
- [484] D. Ruffolo. “Transport and acceleration of energetic charged particles near an oblique shock”. *Astrophys. J.*, **vol. 515**, (1999) p. 787. [astro-ph/9812064](https://arxiv.org/abs/astro-ph/9812064).
URL <http://dx.doi.org/10.1086/307062>

- [485] K. Leerungnavarat, D. Ruffolo, J. W. Bieber. "Loss Cone Precursors to Forbush Decreases and Advance Warning of Space Weather Effects". *ApJ*, **vol. 593**, (2003) pp. 587–596.
URL <http://dx.doi.org/10.1086/376408>
- [486] K. Munakata, T. Kuwabara, *et al.*. "A "loss cone" precursor of an approaching shock observed by a cosmic ray muon hodoscope on october 28, 2003". *Geophysical Research Letters*, **vol. 32**(3). <https://agupubs.onlinelibrary.wiley.com/doi/pdf/10.1029/2004GL021469>.
URL <http://dx.doi.org/10.1029/2004GL021469>
- [487] A. Fushishita, T. Kuwabara, *et al.*. "Precursors of the Forbush Decrease on 2006 December 14 Observed with the Global Muon Detector Network (GMDN)". *ApJ*, **vol. 715**, (2010) pp. 1239–1247. [10.1088/0004-637X/715/2/1239](https://doi.org/10.1088/0004-637X/715/2/1239)
- [488] H. V. Cane. "Coronal mass ejections and forbush decreases". *Space Science Reviews*, **vol. 93**(1), (2000) pp. 55–77. ISSN 1572-9672.
URL <http://dx.doi.org/10.1023/A:1026532125747>
- [489] M. J. Jia, H. Y. and Wang, Y. G. Wang, J. L. Zhang, F. R. Zhu. "Observation of Forbush Decrease using YBJ-ARGO-spt". In "Proceedings, 29th International Cosmic Ray Conference (ICRC 2005) Pune, India", , vol. 1 (**2005**), pp. 137–140.
URL <https://cds.cern.ch/record/957320>
- [490] S. E. Forbush. "World-Wide Cosmic-Ray Variations, 1937-1952". *J. Geophys. Res.*, **vol. 59**, (1954) pp. 525–542.
URL <http://dx.doi.org/10.1029/JZ059i004p00525>
- [491] T. THAMBYAHILLAI, H. ELLIOT. "World-wide changes in the phase of the cosmic-ray solar daily variation". *Nature*, **vol. 171**(4360), (1953) pp. 918–920. ISSN 1476-4687.
URL <http://dx.doi.org/10.1038/171918b0>
- [492] J. R. Jokipii, E. H. Levy, W. B. Hubbard. "Effects of particle drift on cosmic-ray transport. I - General properties, application to solar modulation". *ApJ*, **vol. 213**, (1977) pp. 861–868.
URL <http://dx.doi.org/10.1086/155218>
- [493] M. Garcia-Munoz, P. Meyer, *et al.*. "The dependence of solar modulation on the sign of the cosmic ray particle charge". *J. Geophys. Res.*, **vol. 91**, (1986) pp. 2858–2866.
URL <http://dx.doi.org/10.1029/JA091iA03p02858>
- [494] J. W. Bieber, J. Chen. "Cosmic-ray diurnal anisotropy, 1936-1988 - Implications for drift and modulation theories". *ApJ*, **vol. 372**, (1991) pp. 301–313.
URL <http://dx.doi.org/10.1086/169976>
- [495] W. H. Fonger. "Cosmic radiation intensity-time variations and their origin. ii. energy dependence of 27-day variations". *Phys. Rev.*, **vol. 91**, (1953) pp. 351–361.
URL <http://dx.doi.org/10.1103/PhysRev.91.351>
- [496] K. Nagashima, K. Fujimoto, R. M. Jacklyn. "Galactic and heliotail-in anisotropies of cosmic rays as the origin of sidereal daily variation in the energy region $< 10^4$ GeV". *J. Geophys. Res.*, **vol. 103**, (1998) pp. 17429–17440.
URL <http://dx.doi.org/10.1029/98JA01105>
- [497] M. Amenomori. "Anisotropy and Corotation of Galactic Cosmic Rays". *Science*, **vol. 314**, (2006) pp. 439–443. [astro-ph/0610671](https://arxiv.org/abs/astro-ph/0610671).
URL <http://dx.doi.org/10.1126/SCIENCE.1131702>
- [498] G. Giacinti, G. Sigl. "Local magnetic turbulence and tev-pev cosmic ray anisotropies". *Phys. Rev. Lett.*, **vol. 109**, (2012) p. 071101.
URL <http://dx.doi.org/10.1103/PhysRevLett.109.071101>
- [499] M. Zhang, P. Zuo, N. Pogorelov. "HELIOSPHERIC INFLUENCE ON THE ANISOTROPY OF TeV COSMIC RAYS". *The Astrophysical Journal*, **vol. 790**(1), (2014) p. 5.
URL <http://dx.doi.org/10.1088/0004-637x/790/1/5>
- [500] M. Opher, J. F. Drake, B. Zieger, T. I. Gombosi. "Magnetized Jets Driven By the Sun: the Structure of the Heliosphere Revisited". *ApJ*, **vol. 800**, L28. [1412.7687](https://arxiv.org/abs/1412.7687).
URL <http://dx.doi.org/10.1088/2041-8205/800/2/L28>
- [501] K. Munakata, Y. Mizoguchi, *et al.*. "Solar Cycle Dependence of the Diurnal Anisotropy of 0.6 TeV Cosmic-ray Intensity Observed with the Matsushiro Underground Muon Detector". *ApJ*, **vol. 712**, (2010) pp. 1100–1106. [0911.1165](https://arxiv.org/abs/1011.1165).
URL <http://dx.doi.org/10.1088/0004-637X/712/2/1100>
- [502] U. R. Rao. "Solar modulation of galactic cosmic radiation". *Space Science Reviews*, **vol. 12**(6), (1972) pp. 719–809. ISSN 1572-9672.
URL <http://dx.doi.org/10.1007/BF00173071>
- [503] M. Amenomori, S. Ayabe, *et al.*. "Observation by an air-shower array in tibet of the multi-tev cosmic-ray anisotropy due to terrestrial orbital motion around the sun". *Phys. Rev. Lett.*, **vol. 93**, (2004) p. 061101.
URL <http://dx.doi.org/10.1103/PhysRevLett.93.061101>

- [504] J. E. Mazur, G. M. Mason, *et al.*. “Interplanetary magnetic field line mixing deduced from impulsive solar flare particles”. *The Astrophysical Journal*, **vol. 532**(1), (2000) pp. L79–L82.
URL <http://dx.doi.org/10.1086/312561>
- [505] J. Giacalone, J. R. Jokipii, J. E. Mazur. “Small-scale gradients and large-scale diffusion of charged particles in the heliospheric magnetic field”. *The Astrophysical Journal*, **vol. 532**(1), (2000) pp. L75–L78.
URL <http://dx.doi.org/10.1086/312564>
- [506] D. Ruffolo, W. H. Matthaeus, P. Chuychai. “Trapping of solar energetic particles by the small-scale topology of solar wind turbulence”. *The Astrophysical Journal*, **vol. 597**(2), (2003) pp. L169–L172.
URL <http://dx.doi.org/10.1086/379847>
- [507] J. T. Gosling, R. M. Skoug, D. J. McComas, J. E. Mazur. “Correlated dispersionless structure in suprathermal electrons and solar energetic ions in the solar wind”. *The Astrophysical Journal*, **vol. 614**(1), (2004) pp. 412–419.
URL <http://dx.doi.org/10.1086/423368>
- [508] J. E. Borovsky. “Flux tube texture of the solar wind: Strands of the magnetic carpet at 1 au?” *Journal of Geophysical Research: Space Physics*, **vol. 113**(A8). <https://agupubs.onlinelibrary.wiley.com/doi/pdf/10.1029/2007JA012684>
URL <http://dx.doi.org/10.1029/2007JA012684>
- [509] L. Trenchi, R. Bruno, *et al.*. “SOLAR ENERGETIC PARTICLE MODULATIONS ASSOCIATED WITH COHERENT MAGNETIC STRUCTURES”. *The Astrophysical Journal*, **vol. 770**(1), (2013) p. 11.
URL <http://dx.doi.org/10.1088/0004-637x/770/1/11>
- [510] D. Ruffolo, A. Seripienlert, *et al.*. “SQUEEZING OF PARTICLE DISTRIBUTIONS BY EXPANDING MAGNETIC TURBULENCE AND SPACE WEATHER VARIABILITY”. *The Astrophysical Journal*, **vol. 779**(1), (2013) p. 74.
URL <http://dx.doi.org/10.1088/0004-637x/779/1/74>
- [511] J. R. Jokipii, A. J. Owens. “Cross correlation between cosmic-ray fluctuations and interplanetary magnetic-field fluctuations”. *Geophysical Research Letters*, **vol. 1**(8), (1974) pp. 329–332. <https://agupubs.onlinelibrary.wiley.com/doi/pdf/10.1029/GL001i008p00329>
URL <http://dx.doi.org/10.1029/GL001i008p00329>
- [512] A. P. Jordan, H. E. Spence, *et al.*. “Multipoint, high time resolution galactic cosmic ray observations associated with two interplanetary coronal mass ejections”. *Journal of Geophysical Research: Space Physics*, **vol. 114**(A7). <https://agupubs.onlinelibrary.wiley.com/doi/pdf/10.1029/2008JA013891>
URL <http://dx.doi.org/10.1029/2008JA013891>
- [513] T. Mulligan, J. B. Blake, *et al.*. “Short-period variability in the galactic cosmic ray intensity: High statistical resolution observations and interpretation around the time of a forbush decrease in august 2006”. *Journal of Geophysical Research: Space Physics*, **vol. 114**(A7). <https://agupubs.onlinelibrary.wiley.com/doi/pdf/10.1029/2008JA013783>
URL <http://dx.doi.org/10.1029/2008JA013783>
- [514] J. W. Bieber, J. Clem, *et al.*. “GIANT GROUND LEVEL ENHANCEMENT OF RELATIVISTIC SOLAR PROTONS ON 2005 JANUARY 20. i. SPACESHIP EARTH OBSERVATIONS”. *The Astrophysical Journal*, **vol. 771**(2), (2013) p. 92.
URL <http://dx.doi.org/10.1088/0004-637x/771/2/92>
- [515] M. Amenomori, Z. Cao, *et al.*. “Antiproton Proton Ratio at 10^{13} eV Inferred from the Superposition of Sun Shadows Using the Tibet Air Shower”. *International Cosmic Ray Conference*, **vol. 3**, (1995) p. 84.
- [516] M. Ambrosio, R. Antolini, *et al.*. “Moon and sun shadowing effect in the macro detector”. *Astroparticle Physics*, **vol. 20**(2), (2003) pp. 145 – 156. ISSN 0927-6505.
URL [http://dx.doi.org/https://doi.org/10.1016/S0927-6505\(03\)00169-5](http://dx.doi.org/https://doi.org/10.1016/S0927-6505(03)00169-5)
- [517] J. Giacalone, D. Burgess, S. J. Schwartz, D. C. Ellison. “Ion injection and acceleration at parallel shocks - Comparisons of self-consistent plasma simulations with existing theories”. *ApJ*, **vol. 402**, (1993) pp. 550–559.
URL <http://dx.doi.org/10.1086/172157>
- [518] F. Guo, J. Giacalone. “The acceleration of thermal protons at parallel collisionless shocks: Three-dimensional hybrid simulations”. *The Astrophysical Journal*, **vol. 773**.
URL <http://dx.doi.org/10.1088/0004-637X/773/2/158>
- [519] O. Enriquez-Rivera, A. Lara. “The Galactic cosmic-ray Sun shadow observed by HAWC”. *PoS*, **vol. ICRC2015**, (2016) p. 099. [1508.07351](https://arxiv.org/abs/1508.07351).
URL <http://dx.doi.org/10.22323/1.236.0099>
- [520] X. Wang, N. Wang, Y. Yan. “THE RELATIONSHIP BETWEEN THE PARTICLE INJECTION RATE AND THE DISPERSION OF THE SCATTERING ANGULAR DISTRIBUTION”. *The Astrophysical Journal Supplement Series*, **vol. 209**(1), (2013) p. 18.
URL <http://dx.doi.org/10.1088/0067-0049/209/1/18>
- [521] D. C. Ellison, E. Moebius, G. Paschmann. “Particle injection and acceleration at earth’s bow shock - Comparison of upstream and downstream events”. *ApJ*, **vol. 352**, (1990) pp. 376–394.

- URL <http://dx.doi.org/10.1086/168544>
- [522] J. M. Knerr, J. R. Jokipii, D. C. Ellison. “A Dynamical Monte Carlo Simulation of a Collisionless Shock”. *ApJ*, **vol. 458**, (1996) p. 641.
URL <http://dx.doi.org/10.1086/176846>
- [523] X. Wang, Y.-H. Yan. “Analysis of the CME-driven shock from the SEP event that occurred on 2006 December 14”. *Research in Astronomy and Astrophysics*, **vol. 12**, (2012) pp. 1535–1548.
URL <http://dx.doi.org/10.1088/1674-4527/12/11/008>
- [524] X. Wang, Y. Yan, *et al.*. “Energy Spectral Property in an Isolated CME-driven Shock”. *Res. Astron. Astrophys.*, **vol. 16**(2), (2016) p. 032. [1509.04182](https://arxiv.org/abs/1509.04182).
URL <http://dx.doi.org/10.1088/1674-4527/16/2/032>
- [525] A. R. Bell. “Cosmic ray acceleration”. *Astroparticle Physics*, **vol. 43**, (2013) pp. 56–70.
URL <http://dx.doi.org/10.1016/j.astropartphys.2012.05.022>
- [526] A. M. Bykov, A. Brandenburg, M. A. Malkov, S. M. Osipov. “Microphysics of Cosmic Ray Driven Plasma Instabilities”. *Space Sci. Rev.*, **vol. 178**, (2013) pp. 201–232. [1304.7081](https://arxiv.org/abs/1304.7081).
URL <http://dx.doi.org/10.1007/s11214-013-9988-3>
- [527] P. Schneider. “Diffusive particle acceleration by an ensemble of shock waves”. *Astron. Astrophys.*, **vol. 278**, (1993) pp. 315–327.
- [528] D. B. Melrose, M. H. Pope. “Diffusive Shock Acceleration by Multiple Shocks”. *Proceedings of the Astronomical Society of Australia*, **vol. 10**, (1993) p. 222.
- [529] M. Amenomori, X. J. Bi, *et al.*. “Multi-TeV Gamma-Ray Observation from the Crab Nebula Using the Tibet-III Air Shower Array Finely Tuned by the Cosmic Ray Moon’s Shadow”. *ApJ*, **vol. 692**, (2009) pp. 61–72. [0810.3757](https://arxiv.org/abs/0810.3757).
URL <http://dx.doi.org/10.1088/0004-637X/692/1/61>
- [530] J. A. Eddy. “The Maunder Minimum”. *Science*, **vol. 192**, (1976) pp. 1189–1202.
URL <http://dx.doi.org/10.1126/science.192.4245.1189>
- [531] H. Svensmark, T. Bondo, J. Svensmark. “Cosmic ray decreases affect atmospheric aerosols and clouds”. *Geophysical Research Letters*, **vol. 36**(15). <https://agupubs.onlinelibrary.wiley.com/doi/pdf/10.1029/2009GL038429>.
URL <http://dx.doi.org/10.1029/2009GL038429>
- [532] J. Svensmark, M. B. Enghoff, H. Svensmark. “Effects of cosmic ray decreases on cloud microphysics”. *Atmospheric Chemistry and Physics Discussions*, **vol. 12**, (2012) pp. 3595–3617.
URL <http://dx.doi.org/10.5194/acpd-12-3595-2012>
- [533] T. Sloan, A. W. Wolfendale. “Testing the proposed causal link between cosmic rays and cloud cover”. *Environmental Research Letters*, **vol. 3**, 024001. [0803.2298](https://arxiv.org/abs/0803.2298).
URL <http://dx.doi.org/10.1088/1748-9326/3/2/024001>
- [534] —. “The contribution of cosmic rays to global warming”. *Journal of Atmospheric and Solar-Terrestrial Physics*, **vol. 73**, (2011) pp. 2352–2355. [1108.1047](https://arxiv.org/abs/1108.1047).
URL <http://dx.doi.org/10.1016/j.jastp.2011.07.013>
- [535] J. R. Dwyer, M. M. Schaal, *et al.*. “Observation of a gamma-ray flash at ground level in association with a cloud-to-ground lightning return stroke”. *Journal of Geophysical Research: Space Physics*, **vol. 117**(A10). <https://agupubs.onlinelibrary.wiley.com/doi/pdf/10.1029/2012JA017810>.
URL <http://dx.doi.org/10.1029/2012JA017810>
- [536] H. Tsuchiya, K. Hibino, *et al.*. “Observation of thundercloud-related gamma rays and neutrons in Tibet”. *Phys. Rev. D*, **vol. 85**, 092006. [1204.2578](https://arxiv.org/abs/1204.2578).
URL <http://dx.doi.org/10.1103/PhysRevD.85.092006>
- [537] Y. Stenkin, V. Alekseenko, *et al.*. “Seasonal and Lunar Month Periods Observed in Natural Neutron Flux at High Altitude”. *Pure and Applied Geophysics*, **vol. 174**(7), (2017) pp. 2763–2771. [1605.05406](https://arxiv.org/abs/1605.05406).
URL <http://dx.doi.org/10.1007/s00024-017-1545-7>
- [538] V. Alekseenko, F. Arneodo, *et al.*. “Decrease of atmospheric neutron counts observed during thunderstorms”. *Phys. Rev. Lett.*, **vol. 114**, (2015) p. 125003.
URL <http://dx.doi.org/10.1103/PhysRevLett.114.125003>
- [539] Y. V. Stenkin, V. V. Alekseenko, *et al.*. “Underground physics and the barometric pumping effect observed for thermal neutron flux underground”. *Soviet Journal of Experimental and Theoretical Physics*, **vol. 124**(5), (2017) pp. 718–721.
URL <http://dx.doi.org/10.1134/S106377611704015X>
- [540] D. R. Macgorman, W. D. Rust. *The Electrical Nature of Storms*, chap. Observations of the Electrical Characteristics of Thunderstorms, (Oxford University Press 1998). ISBN 0195073371, p. 422.
- [541] A. V. Gurevich, G. M. Milikh, R. Roussel-Dupre. “Runaway electron mechanism of air breakdown and preconditioning during a thunderstorm”. *Physics Letters A*, **vol. 165**, (1992) pp. 463–468.
URL [http://dx.doi.org/10.1016/0375-9601\(92\)90348-P](http://dx.doi.org/10.1016/0375-9601(92)90348-P)
- [542] V. V. Alexeyenko, A. E. Chudakov, V. G. Sborshikov, V. A. Tizengauzen. “Short Perturbations of Cosmic Ray

- Intensity and Electric Field in Atmosphere". International Cosmic Ray Conference, **vol. 5**, (1985) p. 352.
- [543] H. Tsuchiya, T. Enoto, *et al.* "Observation of an energetic radiation burst from mountain-top thunderclouds". Phys. Rev. Lett., **vol. 102**, (2009) p. 255003.
URL <http://dx.doi.org/10.1103/PhysRevLett.102.255003>
- [544] A. Chilingarian, G. Hovsepyan, A. Hovhannisyan. "Particle bursts from thunderclouds: Natural particle accelerators above our heads". Phys. Rev. D, **vol. 83**, (2011) p. 062001.
URL <http://dx.doi.org/10.1103/PhysRevD.83.062001>
- [545] A. Chilingarian, A. Daryan, *et al.* "Ground-based observations of thunderstorm-correlated fluxes of high-energy electrons, gamma rays, and neutrons". Phys. Rev. D, **vol. 82**, (2010) p. 043009.
URL <http://dx.doi.org/10.1103/PhysRevD.82.043009>
- [546] S. Buitink, T. Huege, *et al.* "Monte carlo simulations of air showers in atmospheric electric fields". Astroparticle Physics, **vol. 33**(1), (2010) pp. 1 – 12. ISSN 0927-6505.
URL <http://dx.doi.org/https://doi.org/10.1016/j.astropartphys.2009.10.006>
- [547] X. M. Zhou, N. Ye, *et al.* "Observing the Effect of the Atmospheric Electric Field Inside Thunderstorms on the EAS with the ARGO-YBJ Experiment". In "Proceedings, 32nd International Cosmic Ray Conference (ICRC 2011): Beijing, China, August 11-18, 2011", , vol. b (2011), p. 287.
URL <http://dx.doi.org/10.7529/ICRC2011/V11/0179>
- [548] Y. Zeng. "Correlations between cosmic ray flux and atmospheric electric field variations observed by the ARGO-YBJ experiment". In "Proceedings, 33rd International Cosmic Ray Conference (ICRC2013): Rio de Janeiro, Brazil, July 2-9, 2013", (2013), p. 0757.
URL <http://www.cbpf.br/%7Eicrc2013/papers/icrc2013-0757.pdf>
- [549] A. F. Bielajew. *Electron Transport in \vec{E} and \vec{B} Fields*, (Boston, MA: Springer US1988). ISBN 978-1-4613-1059-4, pp. 421–434.
URL http://dx.doi.org/10.1007/978-1-4613-1059-4_19
- [550] D. Liu, X. Yan, *et al.* "Distribution of lightning radiation sources in the squall line system and discussion of charge structure in the cloud (in chinese)". Physical Journal, **vol. 62**(21), 219201.
URL <http://dx.doi.org/10.7498/aps.62.219201>
- [551] V. Alexeenko, N. Khaerdinov, A. Lidvansky, V. Petkov. "Transient variations of secondary cosmic rays due to atmospheric electric field and evidence for pre-lightning particle acceleration". Physics Letters A, **vol. 301**(3), (2002) pp. 299 – 306. ISSN 0375-9601.
URL [http://dx.doi.org/https://doi.org/10.1016/S0375-9601\(02\)00981-7](http://dx.doi.org/https://doi.org/10.1016/S0375-9601(02)00981-7)
- [552] C. T. R. Wilson. "The acceleration of β -particles in strong electric fields such as those of thunderclouds". Mathematical Proceedings of the Cambridge Philosophical Society, **vol. 22**(4), (1925) pp. 534–538.
URL <http://dx.doi.org/10.1017/S0305004100003236>
- [553] T. C. Marshall, M. Stolzenburg, *et al.* "Observed electric fields associated with lightning initiation". Geophysical Research Letters, **vol. 32**(3). <https://agupubs.onlinelibrary.wiley.com/doi/pdf/10.1029/2004GL021802>.
URL <http://dx.doi.org/10.1029/2004GL021802>
- [554] T. C. Marshall, W. Rison, *et al.* "Rocket and balloon observations of electric field in two thunderstorms". Journal of Geophysical Research: Atmospheres, **vol. 100**(D10), (1995) pp. 20815–20828. <https://agupubs.onlinelibrary.wiley.com/doi/pdf/10.1029/95JD01877>.
URL <http://dx.doi.org/10.1029/95JD01877>
- [555] J. R. Dwyer. "A fundamental limit on electric fields in air". Geophysical Research Letters, **vol. 30**(20), (2003) p. 2055. <https://agupubs.onlinelibrary.wiley.com/doi/pdf/10.1029/2003GL017781>.
URL <http://dx.doi.org/10.1029/2003GL017781>
- [556] L. Vanyan, A. Chilingaryan. "Simulations of the relativistic runaway electron avalanches (rrea) in the thunderclouds above the aragats space environmental center (asec)". Proceedings of the 32nd International Cosmic Ray Conference, ICRC 2011, **vol. 11**, (2011) pp. 338–341.
URL <http://dx.doi.org/10.7529/ICRC2011/V11/0206>
- [557] D. M. Smith, L. I. Lopez, R. P. Lin, C. P. Barrington-Leigh. "Terrestrial gamma-ray flashes observed up to 20 mev". Science, **vol. 307**(5712), (2005) pp. 1085–1088. ISSN 0036-8075. <http://science.sciencemag.org/content/307/5712/1085.full.pdf>.
URL <http://dx.doi.org/10.1126/science.1107466>
- [558] A. Chilingarian, B. Mailyan, L. Vanyan. "Recovering of the energy spectra of electrons and gamma rays coming from the thunderclouds". Atmospheric Research, **vol. 114-115**, (2012) pp. 1–16.
URL <http://dx.doi.org/10.1016/j.atmosres.2012.05.008>
- [559] E. S. Cramer, J. R. Dwyer, *et al.* "An analytical approach for calculating energy spectra of relativistic runaway electron avalanches in air". Journal of Geophysical Research: Space Physics, **vol. 119**(9), (2014) pp. 7794–7823. <https://agupubs.onlinelibrary.wiley.com/doi/pdf/10.1002/2014JA020265>.

REFERENCES

- URL <http://dx.doi.org/10.1002/2014JA020265>
- [560] J.-F. Wang, X.-S. Qie, *et al.*. “Effect of thunderstorm electric field on intensity of cosmic ray muons (in chinese)”. *Acta Physica Sinica*, **vol. 61**(15), 159202.
URL <http://dx.doi.org/10.7498/aps.61.159202>
- [561] E. M. D. Symbalisty, R. A. Roussel-Dupre, V. A. Yukhimuk. “Finite volume solution of the relativistic boltzmann equation for electron avalanche studies”. *IEEE Transactions on Plasma Science*, **vol. 26**(5), (1998) pp. 1575–1582. ISSN 0093-3813.
URL <http://dx.doi.org/10.1109/27.736065>
- [562] L. Landau, E. Lifshitz. *Electrodynamics of Continuous Media*, (Pergamon, Oxford 1960).
- [563] A. Gurevich. “On the Theory of Runaway Electrons ”. *Soviet Journal of Experimental and Theoretical Physics*, **vol. 12**(5), (1961) p. 904.